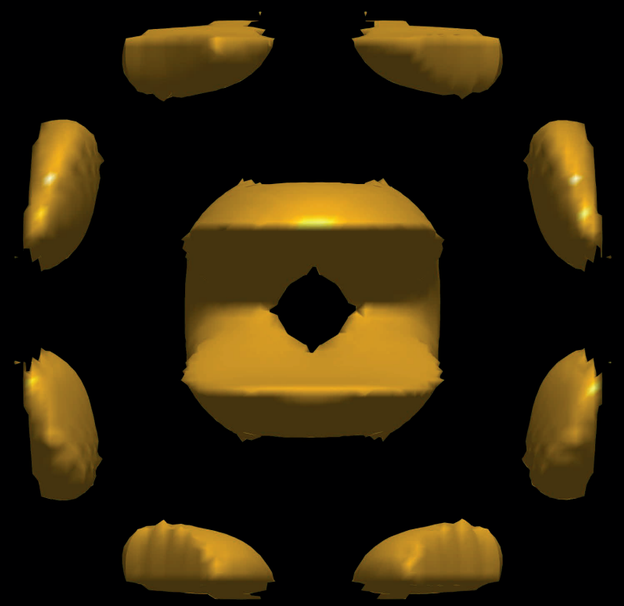

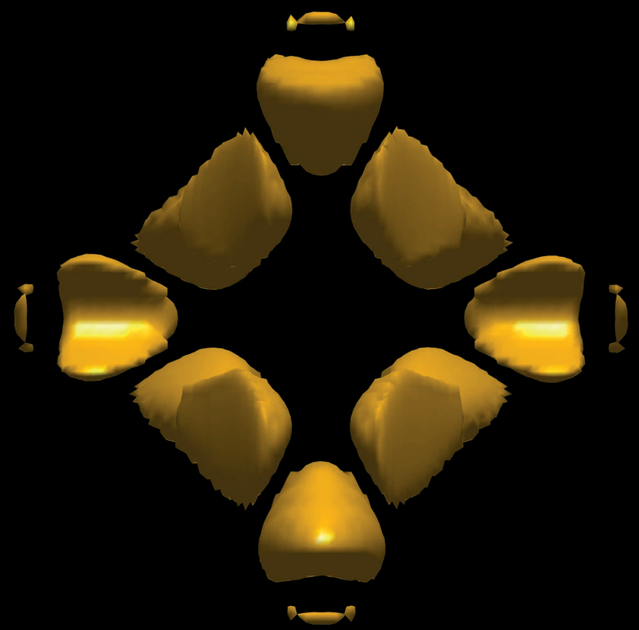

Theoretical and Computational Analysis of Wave Confinement in Periodic Media

Marek Kozoň

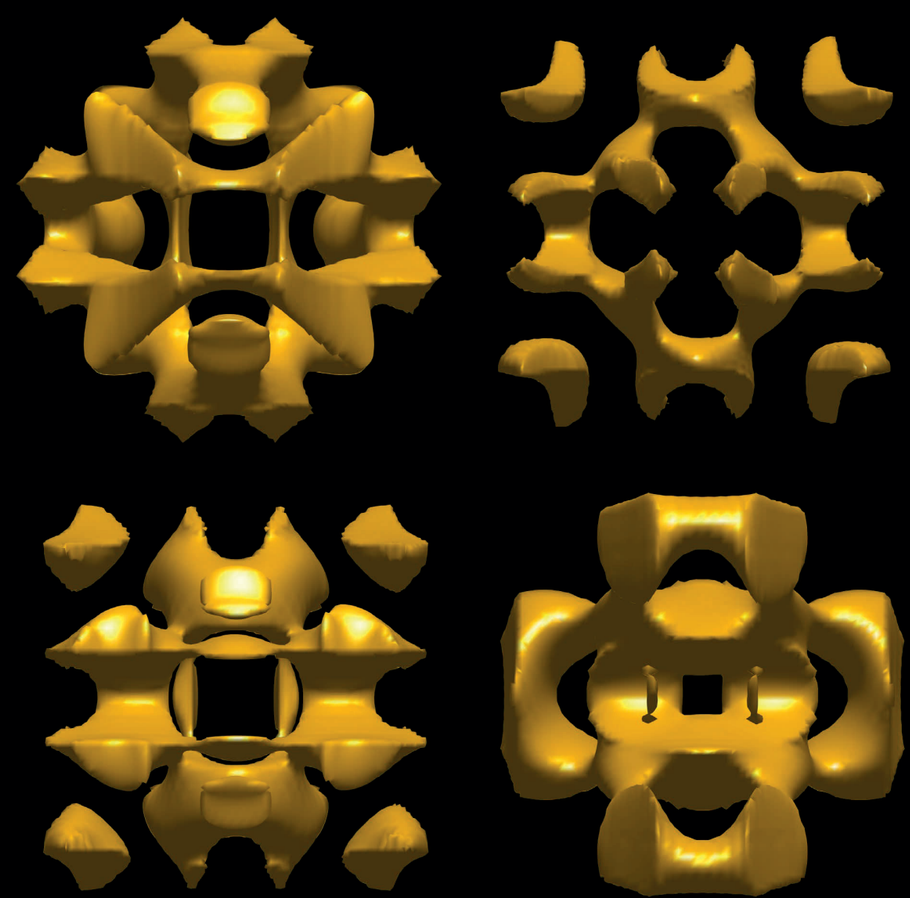

Theoretical and Computational Analysis of Wave Confinement in Periodic Media

Marek Kozoň

INVITATION

to the public defense of the doctoral dissertation:

Theoretical and Computational Analysis of Wave Confinement in Periodic Media

by

Marek Kozoň

Date: 26th of January 2023
Time: 14:30
Place: Prof. dr. G. Berkhoff-Zaal
Waaier
University of Twente

Paranymphs:
Shweta Pal
Ozan Akdemir

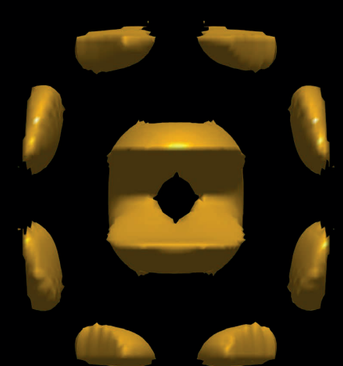

Theoretical and Computational Analysis of Wave Confinement in Periodic Media

Marek Kozoň

Theoretical and Computational Analysis of Wave Confinement in Periodic Media

DISSERTATION

to obtain
the degree of doctor at the University of Twente,
on the authority of the rector magnificus,
prof.dr.ir. A. Veldkamp,
on account of the decision of the graduation committee,
to be publicly defended
on Thursday the 26$^{\text{th}}$ of January 2023 at 14:45

by

Marek Kozoň

born on the 9$^{\text{th}}$ of February 1993
in Prešov, Slovakia.

This dissertation has been approved by:

Supervisors:
prof. dr. ir. J. J. W. van der Vegt
prof. dr. W. L. Vos

Co-supervisor:
dr. M. Schlottbom

Cover: Various confined bands of a 3D inverse woodpile photonic superlattice. Calculated using MIT Photonic Bands software and processed in Matlab by Marek Kozoň. The design conceptualized by Shweta Pal and Marek Kozoň.
Printed by: Gildeprint, Enschede, The Netherlands
ISBN: 978-90-365-5528-9
ISBN: 978-90-365-5529-6 (digital)
DOI: 10.3990/1.9789036555296
This thesis is also available on http://www.photonicbandgaps.com.

Graduation committee:

Chair/Secretary	prof. dr. J. N. Kok (University of Twente)
Supervisors	prof. dr. ir. J. J. W. van der Vegt (University of Twente) prof. dr. W. L. Vos (University of Twente)
Co-supervisor	dr. M. Schlottbom (University of Twente)
Committee Members	prof. dr. C. Rockstuhl (Karlsruhe Institute of Technology) prof. dr. A. F. Koenderink (AMOLF Institute) prof. dr. ir. W. L. IJzerman (TU Eindhoven) prof. dr. ir. I. M. Vellekoop (University of Twente) prof. dr. G. H. L. A. Brocks (University of Twente)

This work was financially supported by NWO-CSER program, project "Understanding the absorption of interfering light for improved solar cell efficiency" under the Project No. 680.93.14CSER035.

It was carried out at the
Complex Photonic Systems (COPS) chair,
Faculty of Science and Technology
and MESA+ Institute for Nanotechnology,
University of Twente, P.O. Box 217,
7500 AE Enschede, The Netherlands.

and the
Mathematics of Computational Science (MACS) chair,
Faculty of Electrical Engineering, Mathematics, and Computer Science
and MESA+ Institute for Nanotechnology,
University of Twente, P.O. Box 217,
7500 AE Enschede, The Netherlands.

Babke.
To my grandma.

"Nothing in life is to be feared, it is only to be understood.
Now is the time to understand more, so that we may fear less."
Maria Skłodowska-Curie

Contents

1 Introduction

1.1 Crystals and waves

The term *crystal* immediately brings up images of colorful minerals exhibiting curious, almost unnaturally sharp angles, or perhaps of gems, cut elaborately so that their faces reflect light in the most alluring fashion. These are already excellent examples of the nature's beauty. The term *crystal*, however, contains much more than just that. As we describe in the following, crystals encompass an immense variety of natural or man-made materials within frameworks of various physical systems.

From the physics point of view, a crystal, in the most general sense, is any periodic arrangement of matter on a lattice, *i.e.*, a crystal is made of constituents arranged in certain kind of a repeating pattern. In terms of minerals, we are speaking about the periodic arrangement of their constituent ions. This periodic arrangement within mineral crystals was first observed in 1912 by the father-and-son duo William H. Bragg and William L. Bragg [1, 2], who later shared a Nobel prize for this discovery. They found that the crystal periodicity had strong interference effects on X-rays passing through them, only reflecting rays with specific angles of incidence. This remarkable interaction between electromagnetic waves and crystals occurs because the wavelength of X-rays is similar to the spacing between the ions in the crystal structure.

X-rays are not the only type of waves heavily influenced by crystalline solids. The power of these materials fully showcases when we realize that electrons, thanks to their wave-particle duality, also have wavelength of the same order of magnitude as the distance between the ions in crystals [3]. In this case, it has been discovered that by disrupting the periodicity of a perfect crystal lattice, one can achieve the manipulation of waves for very specific purposes. This property is manifested especially powerfully in semiconductors, which allow for the control of the electron transport, thus enabling us to tune the conductivity of these materials. The most suitable semiconductors are used to build transistors on chips, thus becoming the true technological backbone of the modern society. It is therefore no exaggeration to say that at the heart of the digital revolution of the 20^{th} century are crystals that allow us to control electronic waves.

In a similar manner to ions in minerals, upon ordering materials with different optical properties on a periodic lattice, one may create a photonic crystal. In this case, it is not single atoms, but larger structures separated by distances comparable to the wavelength of visible or infrared light. Such a material then exhibits different colors and iridescence when viewed under different angles. This phenomenon is responsible for the iridescence of precious opals [4], as illustrated in Fig. 1.1(a). Photonic crystals also occur within living organisms, *e.g.*, on wings

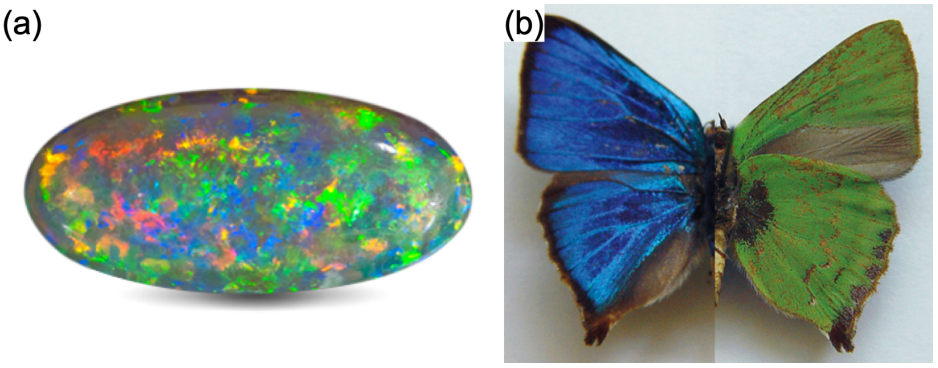

Figure 1.1: Photonic crystals in nature. (a) Opal gemstone. Source: [10]. (b) Wings of the butterfly *Cyanophrys remus*. Left side of the image depicts the dorsal (top) surface of the wings, while the right side shows the ventral (bottom) side. Source: [5].

of some butterflies [5] (see Fig. 1.1(b)), abdomens of spiders [6], exoskeletons of beetles [7], bodies of comb jellies [8], or peacock feathers [9], creating not only angular-dependent coloration, but also allowing for so-called structural colors that are hardly achievable by pigmentation.

One can extend the notion of controlling wave behavior by crystals to other physical realms as well. Magnonic crystals are able to control spin waves [11]. Phononic crystals have been developed to manipulate mechanical vibrations and sound [12]. Proposals have been made to build "seismic shields", giant crystals able to reflect earthquakes away from cities or vulnerable areas or to enhance building stability [13–16].

In this PhD thesis, we concentrate on the control of electromagnetic waves by photonic crystals as our main application. Many of our results are, however, very general and directly applicable to the control of other types of waves by crystals (Chapter 2 and Chapter 3), while some other provide essential ideas that can possibly be generalized to such media (Chapter 5).

1.2 Photonic crystals

The most important characteristic of photonic crystals from both the fundamental and applied point of view is the existence of band gaps in the spectrum of these materials. In a photonic crystal structure, the translational symmetry gives rise via interference effects to a *stop gap*, which is a range of frequencies for which light is not allowed to propagate inside the crystal for specific directions. Stop gaps are generally also polarization-dependent [4]. In three-dimensional (3D) photonic crystals, the interference effects are so strong and omnidirectional, that a 3D *photonic band gap* arises: a range of frequencies for which light is not allowed to propagate inside the crystal irrespective of its wave vector and polarization [4, 17, 18]. The phenomenon of stop gaps has been studied since lord Rayleigh in the 19^{th} century [19], and later by Russell [20] and Kawakami [21]. 3D periodic

photonic media were pioneered by Bykov [22, 23] and it were Yablonovitch and John [24, 25] who introduced the concept of a 3D band gap and of a photonic crystal into the modern scientific literature.

Photonic band gaps are a powerful phenomenon, allowing for radical control of light propagation and emission [4, 26–31] lending itself to a range of applications, such as the inhibition of spontaneous emission [24, 31–33], efficient reflectors [34, 35], absorption enhancement of thin silicon films such as solar cells [36], thermal emission control [37–39], and even cloaking [40].

Inclusion of defects in a photonic crystal disrupts the local symmetry of the crystal, resulting in a variety of bands appearing inside the band gap [4]. Certain frequencies of light can then become confined within these defects, shielded from the outside environment by the remainder of the band gap [4, 41–43]. This mechanism can be utilized for applications ranging from slow light [44], photon trapping [45], lasing [46–48], enhancement of solar cell absorption [49], detectors [50], enhanced spontaneous emission [51], to cavity quantum electrodynamics [52–55].

An especially interesting scattering behavior occurs when randomized defects are introduced into a photonic crystal, creating disorder [56]. This environment has been predicted to lead to Anderson localization [57–59], a state of light characterized by the lack of transport due to random scattering [25, 56, 60–62].

Throughout the years, a great number of photonic crystal structures have been proposed and fabricated. Ref. [29] provides a comprehensive analysis of these crystals, including a database of the gathered data. Among the variety of existing photonic crystals, the width of the band gap is a crucial factor to be considered for experiments and applications. A wide band gap is important in order to be robust with respect to fabrication disorder [63] and to effectively shield the defect states from the surrounding vacuum states [55]. Exceptionally wide band gaps are known to occur in crystals with diamond-like symmetry [64]. An example of these are the so-called inverse woodpile photonic crystals, consisting of two 2D arrays of nanopores etched perpendicularly to each other into a high-permittivity backbone medium [65, 66].

In the Complex Photonic Systems chair at the University of Twente, CMOS-compatible nanofabrication methods are used to etch nanopores into silicon, thus creating inverse woodpile photonic crystals [67–69]. The defect in these crystals is realized by altering the radius of two proximate orthogonal nanopores, thereby creating an excess of either air or silicon in their proximal region [42]. Over the years, extensive research has been done by COPS on these structures, both theoretical and experimental [35, 36, 42, 43, 63, 70–73]. The research presented in this PhD thesis is a part of this effort.

It is important to keep in mind that many properties of light inside photonic crystals are straightforwardly generalizable to other types of waves in different crystal types. Although most results of this PhD thesis are applicable to general wave systems, the ideas are often applied to the inverse woodpile structures in order to keep the explanation as intuitive as possible.

In order to understand the physical properties of any system, it is important to have a proper mathematical description of the specific phenomenon and its implications. Therefore, we continue this Section by describing the basic mathe-

matical concepts of light propagation in photonic crystals. In Subsection 1.2.1, we derive the key time-harmonic equation describing the light propagation through photonic crystals from the general Maxwell's equations of electrodynamics. Subsection 1.2.2 then introduces the mathematical notation for the description of crystals. Subsection 1.2.3 combines the previous two subsections to describe the behavior of light in photonic crystals. Subsection 1.2.4 introduces energy-related concepts for a better understanding of the physics of photonic crystals. Subsection 1.2.5 then applies the physical and mathematical insight gained in the previous subsections to describe the most important phenomena arising in photonic crystals, including the photonic band gap. Lastly, Subsection 1.2.7 introduces the inverse woodpile photonic crystal as the main means of application and illustration of ideas in this PhD thesis.

1.2.1 Maxwell's equations

The macroscopic behavior of light is described by *Maxwell's equations* [4, 74]:

$$\begin{aligned} \boldsymbol{\nabla} \cdot \mathbf{B}(\mathbf{r},t) &= 0, & \boldsymbol{\nabla} \times \mathbf{E}(\mathbf{r},t) + \frac{\partial \mathbf{B}(\mathbf{r},t)}{\partial t} &= 0, \\ \boldsymbol{\nabla} \cdot \mathbf{D}(\mathbf{r},t) &= \rho(\mathbf{r},t), & \boldsymbol{\nabla} \times \mathbf{H}(\mathbf{r},t) - \frac{\partial \mathbf{D}(\mathbf{r},t)}{\partial t} &= \mathbf{J}(\mathbf{r},t), \end{aligned} \tag{1.1}$$

where $\mathbf{E}, \mathbf{H}$, are electric and magnetic intensity, $\mathbf{D}, \mathbf{B}$, are electric and magnetic induction fields, and $\rho, \mathbf{J}$, are the free charge and current densities, respectively, $\mathbf{r}$ is the position vector and t is time. In this PhD thesis, we restrict ourselves to time-independent media with no sources of light, thus setting $\rho = 0$ and $\mathbf{J} = 0$.

The set of Eqs. (1.1) contains more variables than equations and as such needs to be supplemented by *constitutive relations*, relating some of the variables. We assume that all media we are considering are isotropic, the field strengths are small, and we neglect any frequency dependence of the permittivity, considering the materials at frequencies away from material resonances. Then, the constitutive relations are given by

$$\begin{aligned} \mathbf{B}(\mathbf{r},t) &= \mu_0 \mu(\mathbf{r}) \mathbf{H}(\mathbf{r},t), \\ \mathbf{D}(\mathbf{r},t) &= \varepsilon_0 \varepsilon(\mathbf{r}) \mathbf{E}(\mathbf{r},t), \end{aligned} \tag{1.2}$$

where ε_0, μ_0 are the vacuum permittivity and the vacuum permeability, and $\varepsilon(\mathbf{r}), \mu(\mathbf{r})$ are the relative permittivity and the relative permeability distribution within the system. We also assume that $\varepsilon(\mathbf{r})$ is purely real, *i.e.*, that all media are lossless, and that $\varepsilon(\mathbf{r}) > 0$.

We note that the speed of light in vacuum ν is given by

$$\nu = \frac{1}{\sqrt{\varepsilon_0 \mu_0}}, \tag{1.3}$$

and the refractive index n of a medium is equal to

$$n = \sqrt{\varepsilon \mu}. \tag{1.4}$$

In the following, we assume $\mu(\mathbf{r}) = 1$, which is a good approximation for many dielectric materials at optical frequencies. To simplify the notation, we will use units such that $\nu = \varepsilon_0 = \mu_0 = 1$.

Since Maxwell's equations (1.1) are linear, one can separate the time dependence from the spatial dependence by means of Fourier transforms, leading to a family of problems for monochromatic waves with frequency ω [4, 75]. The fields then obtain the *time-harmonic* form:

$$\begin{aligned} \mathbf{H}(\mathbf{r}, t) &= \mathbf{H}(\mathbf{r}) e^{\mathrm{i}\omega t} \\ \mathbf{E}(\mathbf{r}, t) &= \mathbf{E}(\mathbf{r}) e^{\mathrm{i}\omega t}, \end{aligned} \tag{1.5}$$

Combining (1.5) with the constitutive relations (1.2) and inserting these into Eqs. (1.1), we obtain the time-harmonic Maxwell's equations:

$$\boldsymbol{\nabla} \cdot \mathbf{H}(\mathbf{r}) = 0 \tag{1.6a}$$

$$\boldsymbol{\nabla} \cdot [\varepsilon(\mathbf{r}) \mathbf{E}(\mathbf{r})] = 0 \tag{1.6b}$$

$$\boldsymbol{\nabla} \times \mathbf{E} + \mathrm{i}\omega \mathbf{H}(\mathbf{r}) = 0 \tag{1.6c}$$

$$\boldsymbol{\nabla} \times \mathbf{H} - \mathrm{i}\omega \varepsilon(\mathbf{r}) \mathbf{E}(\mathbf{r}) = 0. \tag{1.6d}$$

Eqs. (1.6) still couple the electric and magnetic fields. However, the fields can be decoupled by taking the curl of Eq. (1.6c) and using the Eq. (1.6d) to eliminate $\mathbf{H}$. One thus obtains the equation for the electric field $\mathbf{E}$ only:

$$\boldsymbol{\nabla} \times \boldsymbol{\nabla} \times \mathbf{E}(\mathbf{r}) - \varepsilon(\mathbf{r}) \omega^2 \mathbf{E}(\mathbf{r}) = 0. \tag{1.7}$$

The magnetic field $\mathbf{H}$ is then obtained by inserting the computed $\mathbf{E}$ field back into Eq. (1.6c):

$$\mathbf{H}(\mathbf{r}) = \frac{\mathrm{i}}{\omega} \boldsymbol{\nabla} \times \mathbf{E}(\mathbf{r}). \tag{1.8}$$

Alternatively, one derives the equation for the magnetic field $\mathbf{H}$ only by taking the curl of Eq. (1.6d) and using the Eq. (1.6c) to eliminate $\mathbf{E}$:

$$\boldsymbol{\nabla} \times \frac{1}{\varepsilon(\mathbf{r})} \boldsymbol{\nabla} \times \mathbf{H}(\mathbf{r}) - \omega^2 \mathbf{H}(\mathbf{r}) = 0. \tag{1.9}$$

The electric field $\mathbf{E}$ is then obtained from $\mathbf{H}$ via

$$\mathbf{E}(\mathbf{r}) = -\frac{\mathrm{i}}{\varepsilon(\mathbf{r})\omega} \boldsymbol{\nabla} \times \mathbf{H}(\mathbf{r}). \tag{1.10}$$

Eqs. (1.7) and (1.9), supplemented by suitable boundary conditions on a given computational domain, are the standard differential equations used to describe the propagation of light through photonic crystals. Based on the specific solver or application, one of the equations may be more advantageous to use than the other. In the end, however, all results obtained for photonic crystals in this PhD thesis stem from these two equations.

1.2.2 Mathematical description of crystals

The periodicity of a crystal in three dimensions is mathematically expressed via the periodic lattice Λ, also called Bravais lattice [3], defined as

$$\Lambda \coloneqq \left\{ \sum_{j=1}^{3} n_j \mathbf{a}_j \,|\, n_j \in \mathbb{Z}, j = 1, 2, 3 \right\}, \tag{1.11}$$

where $\mathbf{a}_j \in \mathbb{R}^3$, for $j = 1, 2, 3$, are linearly independent lattice vectors. The lattice Λ thus consists of a point copied along the lattice vectors infinitely many times throughout the space. Thanks to this periodicity, one can fill the whole space $\mathbb{R}^3$ by taking a certain shape, called a *unit cell*, and repeating it over a subset of the vectors from Λ, such that they only overlap at the interfaces. In other words, if we take a unit cell and start placing it in some (but not necessarily all) lattice points, we will eventually cover the whole space.

The smallest possible unit cell for a given lattice, containing only one lattice point is called a *primitive unit cell* $\hat{\Omega}$. The primitive unit cell is not uniquely defined. A convenient choice is

$$\hat{\Omega} \coloneqq \left\{ \sum_{j=1}^{3} s_j \mathbf{a}_j \,|\, s_j \in \left[-\frac{1}{2}, \frac{1}{2} \right], j = 1, 2, 3 \right\}. \tag{1.12}$$

Alternatively, one may choose a *Wigner-Seitz* cell $\mathcal{W}$ as a primitive unit cell, defined as the region of space closer to a chosen lattice point than to any other lattice point [3]. If the lattice vectors $\mathbf{a}_j$ are orthogonal, the Wigner-Seitz cell $\mathcal{W}$ coincides with the parallellogram primitive cell $\hat{\Omega}$.

Let us now consider a plane wave

$$\mathbf{E}(\mathbf{r}) = \mathbf{E}_0 e^{\mathrm{i}\mathbf{k}\cdot\mathbf{r}+\mathrm{i}\omega t}, \tag{1.13}$$

propagating through the lattice Λ, with the amplitude $\mathbf{E}_0$ and wave vector $\mathbf{k}$. One can make a specific choice of the wave vector, so that the wave will have the same periodicity as the Bravais lattice Λ of the crystal. Such a wave vector $\mathbf{K}$ must then by definition satisfy

$$e^{\mathrm{i}\mathbf{K}\cdot(\mathbf{r}+\mathbf{R})} = e^{\mathrm{i}\mathbf{K}\cdot\mathbf{r}}, \tag{1.14}$$

where $\mathbf{R}$ is any linear combination of the lattice vectors

$$\mathbf{R} = n_1\mathbf{a}_1 + n_2\mathbf{a}_2 + n_3\mathbf{a}_3. \tag{1.15}$$

Eq. (1.14) corresponds to the following condition:

$$e^{\mathrm{i}\mathbf{K}\cdot\mathbf{R}} = 1. \tag{1.16}$$

The set of all wave vectors $\mathbf{K}$ satisfying Eq. (1.16) gives rise to a dual lattice to Λ, also known as the *reciprocal lattice* Λ^* [3]. Let us define the reciprocal lattice vectors $\mathbf{b}_i$, for $i = 1, 2, 3$ of Λ^* by

$$\mathbf{b}_i \cdot \mathbf{a}_j = 2\pi\delta_{ij}, \tag{1.17}$$

where δ_{ij} is the Kronecker delta. If we now write $\mathbf{K}$ as a linear combination of these reciprocal basis vectors

$$\mathbf{K} = k_1\mathbf{b}_1 + k_2\mathbf{b}_2 + k_3\mathbf{b}_3, \quad \text{for } k_1, k_2, k_3 \in \mathbb{Z}, \tag{1.18}$$

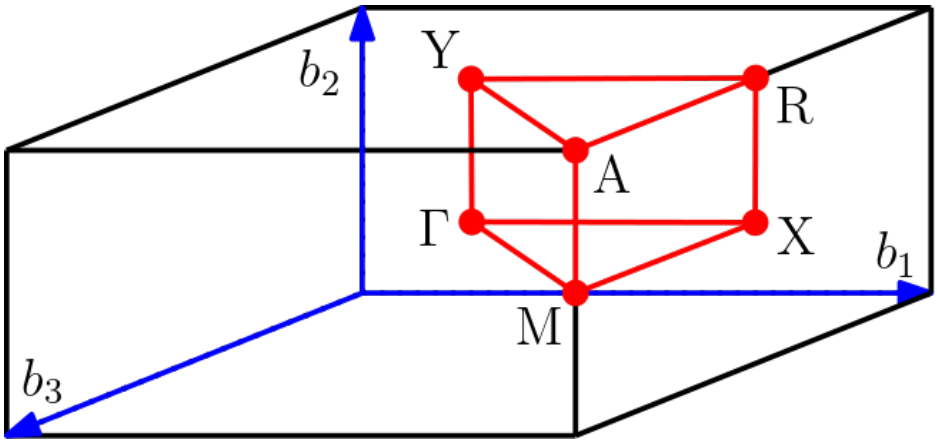

Figure 1.2: Brillouin zone of a tetragonal unit cell (black) with the corresponding irreducible Brillouin zone (red). The edges of the IRBZ represent the high-symmetry path, with the vertices labeled by convention, see, *e.g.*, Ref [77]. Γ represents the origin of the Brillouin zone. The basis vectors b_i, for $i = 1, 2, 3$ are depicted in blue and for convenience shifted away from the origin. For more details, see Ref. [77].

we immediately see that such a $\mathbf{K}$ satisfies the condition (1.16). The reciprocal lattice is thus defined as

$$\Lambda^* \coloneqq \left\{ \sum_{j=1}^{3} k_j \mathbf{b}_j \,|\, k_j \in \mathbb{Z}, j = 1, 2, 3 \right\}. \tag{1.19}$$

In analogy to the direct lattice Λ, the reciprocal lattice Λ^* gives rise to the reciprocal primitive unit cell, for example:

$$\hat{\Omega}^* \coloneqq \left\{ \sum_{j=1}^{3} s_j \mathbf{b}_j \,|\, s_j \in \left[-\frac{1}{2}, \frac{1}{2} \right], j = 1, 2, 3 \right\}. \tag{1.20}$$

One may again define a Wigner-Seitz cell on the reciprocal lattice, which is called the *first Brillouin zone* $\mathcal{B}$ [3]. In literature, the term Brillouin zone and the label $\mathcal{B}$ is sometimes used for a general reciprocal unit cell $\hat{\Omega}^*$ (see, *e.g.*, Ref. [76]) and in this PhD thesis we will employ the same nomenclature.

Finally, for each crystal lattice, the Brillouin zone has certain symmetries. One can reduce the Brillouin zone by all these symmetries to obtain a smaller volume, the so-called *irreducible Brillouin zone* (IRBZ). An example of the Brillouin zone and its irreducible counterpart for the tetragonal lattice is depicted in Fig. 1.2. The tetragonal Brillouin zone has three mirror planes cutting it in half along every axis and another two mirror planes given by the body diagonals of the tetragon. Upon applying these symmetries to the IRBZ, we obtain the full tetragonal Brillouin zone.

The edges of the IRBZ have more symmetries than the points inside its volume. A path along all these edges is referred to as the *high-symmetry path*. The vertices

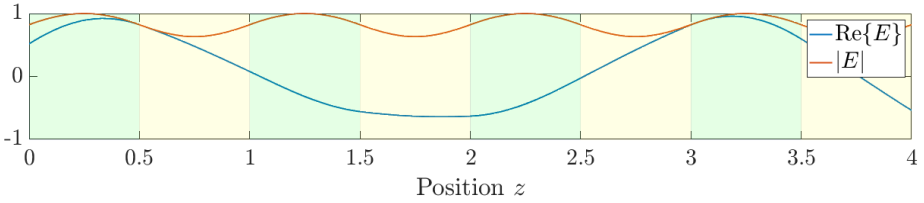

Figure 1.3: Transverse electric field amplitude E of a Bloch mode $\mathbf{E}_{\mathbf{k}}^{\mathrm{Bloch}} = (E, 0, 0)$ in a 1D photonic crystal, also called a Bragg stack. The structure consists of periodically stacked infinite slabs of permittivity $\varepsilon_1 = 13$ (green) and $\varepsilon_2 = 3$ (yellow). The blue curve shows the real part of the electric field amplitude E, while the red curve shows $|E|$, corresponding to the periodic component of the Bloch mode. The frequency is $\omega = 0.8a/\nu$.

of the IRBZ are the points with the most symmetries, appropriately referred to as the *high-symmetry points*, and are assigned conventional labels by capital letters, which generally depend on the specific lattice. For the description of high-symmetry paths for various 3D lattices, see Ref. [77].

1.2.3 Electromagnetic waves in photonic crystals

From the Bloch-Floquet theory (see, *e.g.*, Refs. [76, 78, 79]), it is known that the electric field $\mathbf{E}$ in a photonic crystal has the specific form of a *Bloch mode*

$$\mathbf{E}_{\mathbf{k}}^{\mathrm{Bloch}}(\mathbf{r}) \coloneqq \mathbf{E}_{\mathbf{k}}^{\mathrm{per}}(\mathbf{r}) e^{\mathrm{i}\mathbf{k}\cdot\mathbf{r}}. \tag{1.21}$$

Here, $\mathbf{E}_{\mathbf{k}}^{\mathrm{per}}$ is a periodic function on the lattice Λ and is thus fully determined by its values on the unit cell $\hat{\Omega}$ for each $\mathbf{k} \in \mathcal{B}$. An example of a Bloch mode in a 1D photonic crystal is illustrated in Fig. 1.3. We note that a Bloch mode $\mathbf{E}_{\mathbf{k}}^{\mathrm{Bloch}}(\mathbf{r})$ is not periodic in general, with the periodicity only appearing for the wave vector coinciding with the lattice points of the reciprocal lattice, *i.e.*, $\mathbf{k} \in \mathcal{B} \cap \Lambda^*$.

Upon inserting the form (1.21) into the equation (1.7), we obtain for each $\mathbf{k} \in \mathcal{B}$:

$$\boldsymbol{\nabla}_{\mathbf{k}} \times \boldsymbol{\nabla}_{\mathbf{k}} \times \mathbf{E}_{\mathbf{k}}^{\mathrm{per}}(\mathbf{r}) - \varepsilon(\mathbf{r})\omega^2 \mathbf{E}_{\mathbf{k}}^{\mathrm{per}}(\mathbf{r}) = 0, \qquad \text{for all } \mathbf{r} \in \hat{\Omega}, \tag{1.22}$$

with $E_{\mathbf{k}}^{\mathrm{per}}$ satisfying the boundary condition

$$\mathbf{E}_{\mathbf{k}}^{\mathrm{per}}(\mathbf{r} + \mathbf{R}) = \mathbf{E}_{\mathbf{k}}^{\mathrm{per}}(\mathbf{r}), \qquad \text{for all } \mathbf{R} \in \Lambda \text{ and } \mathbf{r} \in \partial\hat{\Omega}, \tag{1.23}$$

where

$$\boldsymbol{\nabla}_{\mathbf{k}} \coloneqq \boldsymbol{\nabla} + \mathrm{i}\mathbf{k}. \tag{1.24}$$

Eq. (1.22) can be conveniently written in the form of a generalized eigenvalue problem, see Refs. [4, 76], *i.e.*, for each $\mathbf{k} \in \mathcal{B}$ we look for the eigenpair $(E_{\mathbf{k}}^{\mathrm{per}}, \omega^2)$ such that

$$\hat{\Theta}_E \mathbf{E}_{\mathbf{k}}^{\mathrm{per}} = \omega^2 \hat{Z}_E \mathbf{E}_{\mathbf{k}}^{\mathrm{per}}, \tag{1.25}$$

with the operators $\hat{\Theta}_E = \boldsymbol{\nabla}_\mathbf{k} \times \boldsymbol{\nabla}_\mathbf{k}\times$ and $\hat{Z}_E = \varepsilon$. The periodic part $\mathbf{E}_\mathbf{k}^{\mathrm{per}}$ of the Bloch mode electric field can thus be seen as an eigenfunction of the problem (1.25), corresponding to the eigenvalue ω^2.

Alternatively, for the magnetic field of the Bloch modes

$$\mathbf{H}_\mathbf{k}^{\mathrm{Bloch}}(\mathbf{r}) \coloneqq \mathbf{H}_\mathbf{k}^{\mathrm{per}}(\mathbf{r}) e^{\mathrm{i}\mathbf{k}\cdot\mathbf{r}}, \tag{1.26}$$

one can derive the equation

$$\boldsymbol{\nabla}_\mathbf{k} \times \frac{1}{\varepsilon(\mathbf{r})} \boldsymbol{\nabla}_\mathbf{k} \times \mathbf{H}_\mathbf{k}^{\mathrm{per}}(\mathbf{r}) - \omega^2 \mathbf{H}_\mathbf{k}^{\mathrm{per}}(\mathbf{r}) = 0, \qquad \text{for all } \mathbf{r} \in \hat{\Omega}, \tag{1.27}$$

with $H_\mathbf{k}^{\mathrm{per}}$ satisfying the boundary condition

$$\mathbf{H}_\mathbf{k}^{\mathrm{per}}(\mathbf{r} + \mathbf{R}) = \mathbf{H}_\mathbf{k}^{\mathrm{per}}(\mathbf{r}), \qquad \text{for all } \mathbf{R} \in \Lambda \text{ and } \mathbf{r} \in \partial\hat{\Omega}. \tag{1.28}$$

Eq. (1.27) leads to a standard eigenvalue problem, similar to the one in Eq. (1.25): For each $\mathbf{k} \in \mathcal{B}$ find the eigenpair $(H_\mathbf{k}^{\mathrm{per}}, \omega^2)$ such that

$$\hat{\Theta}_H \mathbf{H}_\mathbf{k}^{\mathrm{per}} = \omega^2 \mathbf{H}_\mathbf{k}^{\mathrm{per}}, \tag{1.29}$$

with $\hat{\Theta}_H = \boldsymbol{\nabla}_\mathbf{k} \times \frac{1}{\varepsilon} \boldsymbol{\nabla}_\mathbf{k}\times$. The periodic part of the Bloch mode magnetic field $\mathbf{H}_\mathbf{k}^{\mathrm{per}}$ can be then seen as an eigenfunction of the problem (1.29), corresponding to the eigenvalue ω^2. We note that, despite leading to a simpler eigenvalue problem than (1.25), the formulation (1.29) may pose a disadvantage in some cases due to the permittivity ε appearing in the operator $\hat{\Theta}_H$. One therefore always needs to evaluate which of the two formulations is preferable for the specific problem and solution technique.

We note that the (generalized) eigenvalue problems (1.25) and (1.29) can also be formulated "in reverse", where for each frequency $\omega > 0$, one is looking for a corresponding wave vector $\mathbf{k}$, see, *e.g.*, Ref. [80] and Chapter 5 of this PhD thesis.

The relations between the periodic parts of the electric and magnetic Bloch mode fields can be derived by inserting the definitions (1.21) and (1.26) into Eqs. (1.8) and (1.10). We then obtain

$$\mathbf{H}_\mathbf{k}^{\mathrm{per}}(\mathbf{r}) = \frac{\mathrm{i}}{\omega} \boldsymbol{\nabla}_\mathbf{k} \times \mathbf{E}_\mathbf{k}^{\mathrm{per}}(\mathbf{r}) \tag{1.30}$$

and

$$\mathbf{E}_\mathbf{k}^{\mathrm{per}}(\mathbf{r}) = -\frac{\mathrm{i}}{\varepsilon(\mathbf{r})\omega} \boldsymbol{\nabla}_\mathbf{k} \times \mathbf{H}_\mathbf{k}^{\mathrm{per}}(\mathbf{r}). \tag{1.31}$$

1.2.4 Electromagnetic energy in photonic crystals

The time-averaged energy of the time-harmonic electric and the magnetic field, respectively, is given by [4, 74]:

$$\begin{aligned} U_{\mathrm{E}} &= \frac{1}{4} \int_{\hat{\Omega}} \varepsilon(\mathbf{r}) |\mathbf{E}_\mathbf{k}^{\mathrm{per}}(\mathbf{r})|^2 \mathrm{d}V, \\ U_{\mathrm{H}} &= \frac{1}{4} \int_{\hat{\Omega}} |\mathbf{E}_\mathbf{k}^{\mathrm{per}}(\mathbf{r})|^2 \mathrm{d}V. \end{aligned} \tag{1.32}$$

In time-harmonic modes the energy is periodically exchanged between the electric and the magnetic field, which means that for the time-averaged values $U_\mathrm{E} = U_\mathrm{H}$ (for a mathematical proof, see Ref. [4]). For a physical description of the Bloch modes, we could already settle with the expressions (1.32). Nevertheless, in order to gain deeper understanding of the phenomena occurring in photonic crystals, it is worthwhile to look at a more abstract concept of energy.

Variational theorems are powerful tools to understand the physics of any system and photonic crystals are no exception. We therefore introduce the energy functional (see Ref. [4]), also called Rayleigh quotient, for each $\mathbf{k} \in \mathcal{B}$:

$$\mathcal{U}(\mathbf{H}_\mathbf{k}^\mathrm{per}) \coloneqq \frac{(\mathbf{H}_\mathbf{k}^\mathrm{per}, \hat{\Theta}_H \mathbf{H}_\mathbf{k}^\mathrm{per})}{(\mathbf{H}_\mathbf{k}^\mathrm{per}, \mathbf{H}_\mathbf{k}^\mathrm{per})}, \tag{1.33}$$

where $(\mathbf{v}_1, \mathbf{v}_2) = \int_{\hat{\Omega}} \mathbf{v}_1 \cdot \mathbf{v}_2^* \,\mathrm{d}V$ denotes the scalar product of the vector fields $\mathbf{v}_1, \mathbf{v}_2$ and the * denotes complex conjugation. To simplify the notation, we will drop the "per" superscript in this subsection.

It can be shown that the function $\mathbf{H}_{\mathbf{k},0}$ minimizing the functional $\mathcal{U}(\mathbf{H}_\mathbf{k})$ corresponds to the lowest eigenvalue of $\hat{\Theta}_H$ and therefore to the lowest-frequency Bloch mode (see Ref. [4]). The Bloch mode with the second-lowest frequency then minimizes $\mathcal{U}(\mathbf{H}_\mathbf{k})$ in the subspace of functions orthogonal to $\mathbf{H}_{\mathbf{k},0}$, *etc.* Note that this approach is also known as the min-max theorem [81].

We can use the energy functional $\mathcal{U}(\mathbf{H}_\mathbf{k})$ to understand some crucial properties of the Bloch modes. In order to do so, we rewrite the functional defined by Eq. (1.33) in terms of $\mathbf{E}_\mathbf{k}$. Firstly, expressing the operator $\hat{\Theta}_H$ from its definition and substituting for $\mathbf{H}_\mathbf{k}$ from Eqs. (1.30) and (1.31), we have

$$\begin{aligned}
(\mathbf{H}_\mathbf{k}, \hat{\Theta}_H \mathbf{H}_\mathbf{k}) &= (\frac{\mathrm{i}}{\omega} \boldsymbol{\nabla}_\mathbf{k} \times \mathbf{E}_\mathbf{k}, \boldsymbol{\nabla} \times \frac{1}{\varepsilon} \boldsymbol{\nabla}_\mathbf{k} \times \mathbf{H}_\mathbf{k}) \\
&= (\frac{\mathrm{i}}{\omega} \boldsymbol{\nabla}_\mathbf{k} \times \mathbf{E}_\mathbf{k}, -\frac{\omega}{\mathrm{i}} \boldsymbol{\nabla}_\mathbf{k} \times \mathbf{E}_\mathbf{k}) \\
&= \int_{\hat{\Omega}} |\boldsymbol{\nabla}_\mathbf{k} \times \mathbf{E}_\mathbf{k}|^2 \mathrm{d}V.
\end{aligned} \tag{1.34}$$

Secondly, we use the definition of the eigenvalue problem (1.29) and (1.31) to obtain

$$\begin{aligned}
(\mathbf{H}_\mathbf{k}, \mathbf{H}_\mathbf{k}) &= (\mathbf{H}_\mathbf{k}, \frac{1}{\omega^2} \hat{\Theta}_H \mathbf{H}_\mathbf{k}) \\
&= \frac{1}{\omega^2} \int_{\hat{\Omega}} \mathbf{H}_\mathbf{k} \cdot \left(\boldsymbol{\nabla}_\mathbf{k} \times \frac{1}{\varepsilon} \boldsymbol{\nabla}_\mathbf{k} \times \mathbf{H}_\mathbf{k} \right)^* \mathrm{d}V \\
&= \frac{1}{\omega^2} \int_{\hat{\Omega}} \mathbf{H}_\mathbf{k} \cdot \left((\boldsymbol{\nabla} + \mathrm{i}\mathbf{k}) \times \frac{1}{\varepsilon} \boldsymbol{\nabla}_\mathbf{k} \times \mathbf{H}_\mathbf{k} \right)^* \mathrm{d}V \\
&= \frac{1}{\omega^2} \int_{\hat{\Omega}} (\boldsymbol{\nabla} + \mathrm{i}\mathbf{k}) \times \mathbf{H}_\mathbf{k} \cdot \left(\frac{1}{\varepsilon} \boldsymbol{\nabla}_\mathbf{k} \times \mathbf{H}_\mathbf{k} \right)^* \mathrm{d}V \\
&= \frac{1}{\omega^2} \int_{\hat{\Omega}} \boldsymbol{\nabla}_\mathbf{k} \times \mathbf{H}_\mathbf{k} \cdot \left(\frac{1}{\varepsilon} \boldsymbol{\nabla}_\mathbf{k} \times \mathbf{H}_\mathbf{k} \right)^* \mathrm{d}V \\
&= \int_{\hat{\Omega}} \varepsilon |\mathbf{E}_\mathbf{k}|^2 \mathrm{d}V.
\end{aligned} \tag{1.35}$$

In the fourth step in (1.35), we used the identities $\mathbf{A}\cdot(\mathbf{B}\times\mathbf{C}) = \mathbf{C}\cdot(\mathbf{A}\times\mathbf{B})$ and $\boldsymbol{\nabla}\cdot(\mathbf{F}\times\mathbf{G}) = (\boldsymbol{\nabla}\times\mathbf{F})\cdot\mathbf{G} - (\boldsymbol{\nabla}\times\mathbf{G})\cdot\mathbf{F}$, in combination with the divergence theorem, and neglected all the surface terms due to the periodicity of the fields.

Finally, inserting (1.34) and (1.35) into (1.33), we obtain the expression

$$\mathcal{U}(\mathbf{H}_\mathbf{k}) = \frac{\int_{\hat{\Omega}} |\boldsymbol{\nabla}_\mathbf{k}\times\mathbf{E}_\mathbf{k}|^2 \mathrm{d}V}{\int_{\hat{\Omega}} \varepsilon|\mathbf{E}_\mathbf{k}|^2 \mathrm{d}V}. \tag{1.36}$$

Let us now inspect the formula (1.36) more closely. We know that the physical Bloch mode minimizes the functional $\mathcal{U}(\mathbf{H}_\mathbf{k})$. Since $\mathbf{E}_\mathbf{k}$ are eigenfunctions, they can be normalized without loss of generality. If we normalize them so that $\int_{\hat{\Omega}} \varepsilon|\mathbf{E}_\mathbf{k}|^2 \mathrm{d}V = 1$, then the minimum of the energy functional $\mathcal{U}(\mathbf{H}_\mathbf{k})$ will correspond to the minimum of the numerator in (1.36). Since the numerator consists of $\boldsymbol{\nabla}_\mathbf{k}\times\mathbf{E}_\mathbf{k}$, each higher mode will have larger curl magnitude that the lower ones. In 1D, the curl reduces to simple derivative, directly corresponding to the amount of oscillation of the field and thus, in this case, higher modes will oscillate more. On the other hand, we may choose the normalization such that $\int_{\hat{\Omega}} |\boldsymbol{\nabla}\times\mathbf{E}_\mathbf{k}|^2 \mathrm{d}V = 1$. In this case, the minimum of $\mathcal{U}(\mathbf{H}_\mathbf{k})$ corresponds to the maximum of the denominator in (1.36), which is achieved when the electric field is concentrated in the high-permittivity regions. Since the denominator in (1.36) is proportional to the physical energy U_E, the physical mode minimizing $\mathcal{U}(\mathbf{H}_\mathbf{k})$ will have the highest physical energy among the modes with $\int_{\hat{\Omega}} |\boldsymbol{\nabla}\times\mathbf{E}_\mathbf{k}|^2 \mathrm{d}V = 1$.

At this point, we have sufficient mathematical basis to understand the behavior of photonic crystals, including their most exciting feature: the photonic band gap.

1.2.5 Photonic band structure and band gaps

A dispersion relation is the relation between the frequency of the wave and its wave vector $\omega = \omega(\mathbf{k})$. A homogeneous medium with permittivity ε satisfies the simple dispersion relation, see, *e.g.*, Ref. [82],

$$\omega = \frac{\nu}{\sqrt{\varepsilon}}|\mathbf{k}|. \tag{1.37}$$

The wave vector $\mathbf{k}$ belongs to the Brillouin zone $\mathcal{B}$ and its magnitude is therefore in the interval $[-\pi, \pi]$. Everything beyond this interval is a periodic repetition of the Brillouin zone, and it is possible to "fold" the dispersion relation for $\mathbf{k} \notin \mathcal{B}$ into $\mathcal{B}$ [3]. This way, the dispersion relation (1.37) is separated into lines corresponding to so-called *bands*, connecting at the end of the Brillouin zone. The set of such bands is called a *band structure*, and for a homogenous medium is illustrated in Fig. 1.4.

By solving the eigenproblem (1.25) or (1.29), we obtain the band structure of a photonic crystal. Let us consider an inverse woodpile photonic crystal, consisting of air pores within bulk silicon, described in detail in Subsection 1.2.7. Fig. 1.5 depicts a band structure for an inverse woodpile crystal with the pore radius $R = 0.24a$. Since in this nontrivial case $\omega = \omega(\mathbf{k})$ is a function of the direction of the wave vector and not only its magnitude, the issue of plotting the band

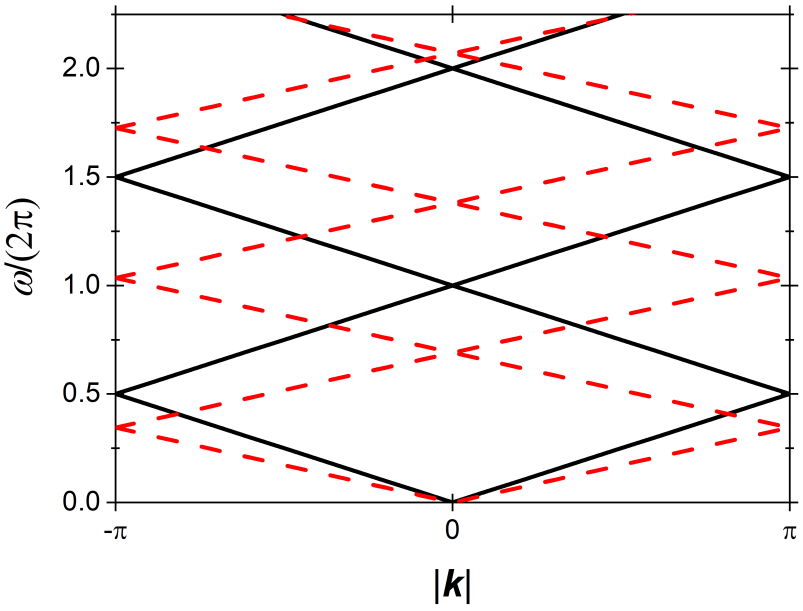

Figure 1.4: Band structure of a homogeneous medium. The solid black lines correspond to the vacuum and the dashed red lines represent a medium with permittivity $\varepsilon = 2.1$.

structure becomes nontrivial. It is a convention to plot the band structure only for the wave vectors belonging to the high-symmetry path. For the description of high-symmetry paths for various 3D lattices, see Ref. [77].

There are several interesting features in the band structure of Fig. 1.5. First of all, we see that the band structure is significantly more complicated than that of Fig. 1.4, due to the inhomogenous structure of the photonic crystal. Secondly, despite the differences, for low frequency $\tilde{\omega} = \omega a/(2\pi c) < 0.3$, the dispersion relation is effectively linear, as if the crystal was homogenous. This is the so-called long-wavelength limit. It can be interpreted as that the wavelength here is significantly longer than the periodicity of the crystal and the wave is thus unable to "see" the crystal structure. Instead, the wave behaves as if the crystal was a homogenous medium of some intermediate permittivity between that of air and silicon [83]. Thirdly, there is an interval of frequencies, between approximately $\tilde{\omega}^- = 0.5$ and $\tilde{\omega}^+ = 0.63$, devoid of any bands. This region corresponds to a 3D *photonic band gap* and it is the range of frequencies, for which no propagating wave is permitted in the crystal, irrespective of the direction of its propagation or its polarization.

The band gap is the most important characteristic of photonic crystals. But why does it appear at all? As discussed before, the physical field modes in a crystal are those minimizing the energy functional $\mathcal{U}(\mathbf{H}_\mathbf{k})$ defined by the Eq. (1.33), within the subspace orthogonal to all the lower modes. Upon reformulating the functional in terms of the electric field in Eq. (1.36), we found that a higher mode

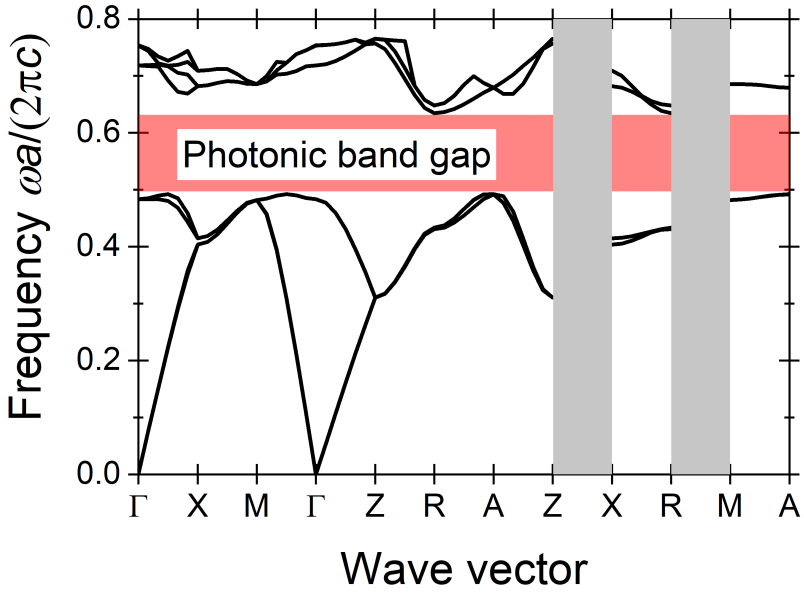

Figure 1.5: Band structure of an inverse woodpile photonic crystal with the pore radius $R = 0.24a$. The wave vector is described in terms of the high-symmetry path of the tetragonal unit cell, using the conventional notation for the high-symmetry points, as depicted in Fig. 1.2, and represents the direction of propagation of the given Bloch mode. The y-axis corresponds to the reduced frequency $\tilde{\omega} = \omega a/(2\pi c)$. For the discussion of the crystal structure, see Subsection 1.2.7.

tends to be more concentrated in the regions of lower permittivity ε than a lower mode. However, the fields in the crystal have to also satisfy the symmetry properties of the structure. Let us now assume a specific field mode $\mathbf{E}_\downarrow$ in a crystal, corresponding to an eigenvalue $\omega_\downarrow$, found by minimizing the functional $\mathcal{U}(\mathbf{H_k})$ in the subspace orthogonal to all the lower modes. To find the mode $E_\uparrow$ with the next lowest eigenvalue $\omega_\uparrow > \omega_\downarrow$, we now need to minimize $\mathcal{U}(\mathbf{H_k})$ again in the subspace orthogonal to all the lower modes and this time also to the mode $\mathbf{E}_\downarrow$. In some cases, the symmetry forces the mode $\mathbf{E}_\uparrow$ to have a significantly higher $\mathcal{U}(\mathbf{H}_\uparrow)$ than the mode $\mathbf{E}_\downarrow$. And since, by assumption, these two modes follow consecutively from the variational principle, no other modes are allowed between them and a band gap opens in this region [4, 76].

Intuitively, one could also see the gap-opening mechanism as the modes below and above the band gap having the same curl magnitude, *i.e.*, they are normalized so that $\int_{\hat{\Omega}} |\boldsymbol{\nabla} \times \mathbf{E_k}|^2 \mathrm{d}V = 1$, but their field peaks occurring in different dielectric media, resulting in the significant difference in $\mathcal{U}(\mathbf{H_k})$. To reiterate, the reason behind the existence of band gaps is a combination of the restrictions imposed by the crystal symmetry with the variational principle of minimizing the energy functional $\mathcal{U}(\mathbf{H_k})$. For more details on this mechanism, see Ref. [4]. Finally, the emergence of a 3D photonic band gap can be seen as the result of interference of 1D stop gaps along many different directions, which leads to band repulsion between Bloch states. For more details on this mechanism of multiple diffraction, see Refs. [17, 18].

It is important to realize that, despite the fact that no propagating wave is allowed within the band gap, so-called *evanescent waves* may appear at the band-gap frequencies. Evanescent waves have nonzero imaginary part of the wave vector $\mathbf{k} = \mathbf{k}_{\mathrm{real}} + \mathrm{i}\mathbf{k}_{\mathrm{imag}}$, with $\mathbf{k}_{\mathrm{real}} \in \mathcal{B}$ and $\mathbf{k}_{\mathrm{imag}} \in \mathbb{R}^3$. Simply by allowing such wave vectors in the Bloch mode definition (1.21), we can immediately see that the nonzero imaginary part corresponds to the decay of the wave with the distance it has traveled in the crystal:

$$\mathbf{E}_{\mathbf{k}}^{\mathrm{Bloch}}(\mathbf{r}) = \mathbf{E}_{\mathbf{k}}^{\mathrm{per}}(\mathbf{r}) e^{\mathrm{i}\mathbf{k}_{\mathrm{real}}\cdot\mathbf{r}} e^{-\mathbf{k}_{\mathrm{imag}}\cdot\mathbf{r}}. \tag{1.38}$$

Note that, in an infinite crystal model, a wave decaying in one direction will inherently increase in the opposite direction. Nevertheless, for realistic, finite crystals, only the decaying modes are physically meaningful.

We denote the width of the band gap as $\Delta\omega = \omega^+ - \omega^-$ and the band-gap center as $\omega_c = (\omega^+ + \omega^-)/2$, where ω^- and ω^+ are the bottom and top edges of the band gap, respectively. An important parameter is the relative width of the band gap, given as

$$\delta\omega = \frac{\Delta\omega}{\omega_c}. \tag{1.39}$$

It can be shown (see Refs. [4, 84]), that $\mathbf{k}_{\mathrm{imag}}$, and thus also the attenuation of the evanescent mode, will be the largest in the center of the band gap and that its magnitude is proportional to the relative band gap width $\delta\omega$. Furthermore, a wider band gap is also more interesting from the application point of view, since it offers control of light for a larger wavelength interval. As wide a band

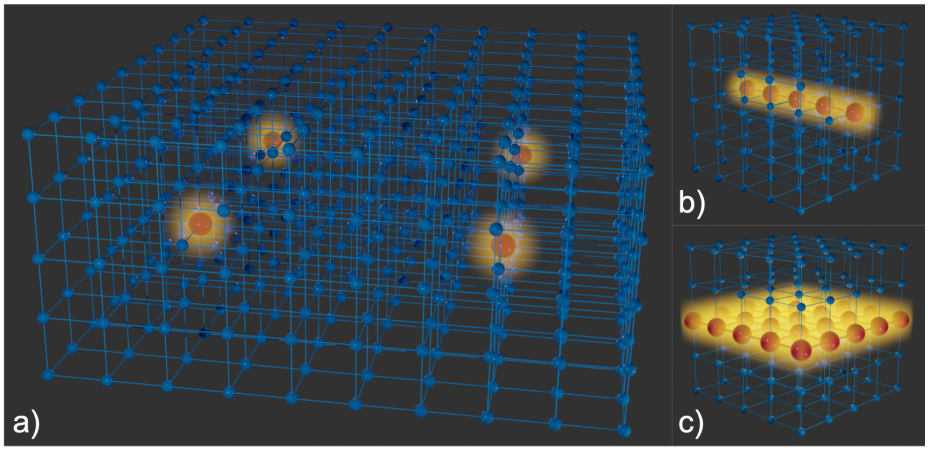

Figure 1.6: Illustration of supercells of size $N = 5$ in a 3D system with various types of defects. Blue spheres correspond to regular unit cells, unit cells containing defects are red and confined waves are represented by yellow. (a) Four supercells, each containing a point defect akin to a cavity [54], trap waves in all three dimensions. (b) Supercell with a linear defect, analogous to an optical waveguide or fiber. (c) Supercell with a planar defect, analogous to a 2D electron gas [85]. Note that in addition to the illustrated confined wave modes, extended modes are also possible in all of the depicted structures.

gap as possible is thus clearly one of the important goals to aim for, regarding successful applications of photonic crystals. It has been shown that the inverse woodpile photonic crystals have particularly large band gap and also exhibit good robustness against fabrication deviations [63].

1.2.6 Intentional defects and disorder in photonic crystals

Not all defects in a photonic crystal have to be undesirable. One can often utilize the presence of a band gap, in combination with a specific defect, to achieve exciting physical phenomena such as the manipulation and confinement of waves.

Both in experiments and in computational models it is often convenient to introduce the defects in a regular manner, such that, every few unperturbed unit cells, one unit cell containing a defect occurs. This can be also seen as superimposing the defect lattice on the unperturbed crystal lattice, giving rise to a crystal *superlattice*. The unit cell of such a superlattice is called a *supercell*. For notational simplicity, in this PhD thesis we assume that the supercells contain in each direction the same number N of unit cells. The number N then represents the linear size of the supercell. Supercells containing defects of various types are illustrated in Fig. 1.6.

Introducing the defect lattice into a perfectly periodic photonic crystal disrupts the crystal symmetry and thus also the band gap. As a result, several bands from

the outside of the gap move inside of it, creating a small number of allowed bands within the large forbidden regions. This effect makes it possible to trap the waves within the defects, as depicted in Fig 1.6, which are then shielded from the outside environment by the remainder of the band gap.

We distinguish two types of defects based on the analogy to semiconductors [86]: Donorlike defects correspond to doping the medium with a high-permittivity material and result in the bands from the top of the band gap shifting down inside the gap. Acceptorlike defects, on the other hand, are a result of removing a high-permittivity material and cause the bands from the bottom of the band gap to move up inside the gap.

Last but not least, the inevitable presence of random defects in real crystals, often called *disorder*, creates a speckle-like interference within the crystal. Even though in creation of periodic structures the disorder is often aimed to be suppressed, it may also lead to interesting phenomena. Namely, it is hypothesised to lead to Anderson localization, *i.e.*, confinement of waves by the means of interference in a disordered medium. For a detailed description of Anderson localization see, *e.g.*, [57–59]. For Anderson localization in photonic crystals, see Refs. [56, 61, 62].

1.2.7 Inverse woodpile photonic crystal

Inverse woodpile photonic crystals have a prominent place among the plethora of photonic structures, known for their wide band gap [63]. Most of the work in this PhD thesis is illustrated on or applied to the inverse woodpiles. It is therefore worthwhile to describe their structure in detail.

The inverse woodpile photonic crystal consists of bulk silicon ($\varepsilon = 12.1$, see Ref. [87]), in which nanopores of radius R filled with air ($\varepsilon = 1$) are etched along the x- and z-directions [31, 65]. The primitive unit cell of this structure is body-centered tetragonal, but for practical purposes it is convenient to work with the simple tetragonal lattice (see Fig. 1.2) with the lattice parameters a in the y-direction and $b = a/\sqrt{2}$ in the x- and z-directions. For a detailed description of both lattices, see [77]. The structure of an inverse woodpile crystal is depicted in Fig. 1.7(a).

Intentional defects can be incorporated in the inverse woodpile structure by altering the radius R' of two proximate nanopores, as illustrated in Fig. 1.7(b). This results in the creation of a region with excess silicon (donorlike, $R' < R$) or air (acceptorlike, $R' > R$) at the intersection of the two defect pores, serving as a point defect. We include one defect of this type per supercell.

1.3 Finite element methods for photonic crystals

The world around us and its behavior can be described by mathematical models and equations. However, solving these equations analytically is often too difficult, with the exception of the most simplified cases. This is where numerical methods come into play. They discretize the problem by describing it using a finite set of parameters and obtain the solution in terms of a finite set of values. The crucial

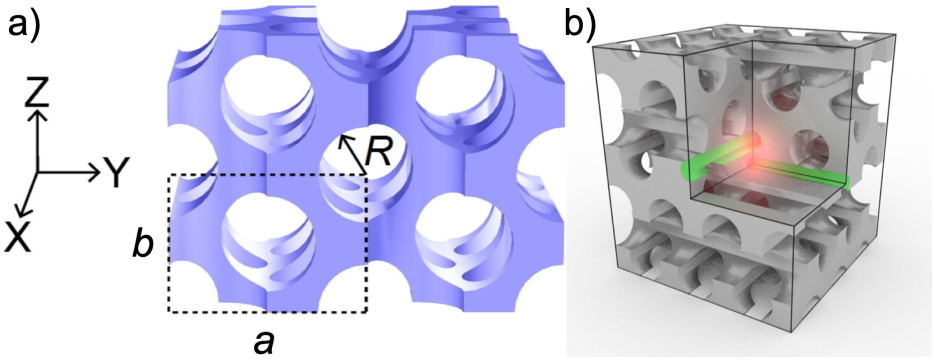

Figure 1.7: (a) Structure of an inverse woodpile photonic crystal. We use a tetragonal unit cell with lattice parameters a in the y direction and $b = a/\sqrt{2}$ in the x and z directions. The pore radius is denoted by R. The unit cell is designated by the dashed border. (b) Design of a defect in an inverse woodpile. The radius R' of two proximate defect pores (shown in green) is altered. At their intersection a region with excess of one material is created that serves as a point defect (red glow).

factor here is that the numerical solution must converge to the real solution, *i.e.*, the difference between the numerical solution and the real solution can be made arbitrarily small, just by increasing the number of discretization parameters. Moreover, this convergence must happen sufficiently fast for the method to be practically usable. Discretized problems can be directly translated into computer code and solved by the machine, where the discretization precision is only limited by the available processing power and memory.

There are several standard numerical methods used for solving the equation (1.7) for light propagation through photonic crystals (see Ref. [41]). The most notable ones are *plane-wave expansion* (PWE), expanding the dielectric function and the electromagnetic fields in terms of the reciprocal lattice vectors [88]; *finite-difference time-domain* (FDTD), replacing continuous derivatives by finite differences [89–91]; and *finite element methods* (FEM).

FEM are the most flexible of the computational methods, since they represent not one, but a whole class of approaches [92, 93] supported by a solid mathematical framework. Their broad applicability ranges from high-accuracy time-harmonic problems [35, 36, 70] to time-domain computations [94], to topology optimization [95].

Solving a problem via FEM constists of three main steps [41, 96]. Firstly, the equation is reformulated as a variational problem, which yields the so-called weak formulation. Secondly, the weak formulation is discretized. This is done by dividing the computational domain into finite elements, which standardly have the shape of triangles in 2D or tetrahedrons in 3D, albeit, in principle, arbitrary shapes are possible. Within each element, the solution of the problem is expanded as a linear combination of basis functions of a chosen approximation space. Thirdly, the discretized problem is transformed into a sparse system of linear equations, such that the coefficients of the linear combination from the

previous step form the solution.

The beauty and flexibility of FEM comes from the freedom of choosing the approximation space in which to look for the solution. If this space is chosen correctly, it can significantly alleviate the computational costs of the method. Typically, if there are no specific requirements on the approximation space, one chooses a simple space of hat functions, *i.e.*, polynomials with nonzero support only on a limited set of the elements. In this case, increasing the order of the polynomials increases the approximation accuracy. Typically, one assumes the approximating functions to be continuous across neighboring elements. This ensures the relative simplicity of the method, but places some restrictions on the approximation space. The *discontinuous Galerkin* framework removes the continuity requirement at the cost of additional terms in the approximation, expressed at the element boundaries.

1.4 Outline of this PhD thesis

In this PhD thesis, we study the propagation and behavior of waves in crystalline systems, with the emphasis on electromagnetic waves in photonic crystals and their confinement.

Chapter 2 introduces a general scaling theory of identification and classification of wave confinement in crystal superlattices. Starting from the confinement energy and the mode volume, we use finite-size scaling to find that ratios of these quantities raised to certain powers yield the confinement dimensionality of each band. Our classification has negligible additional computational costs compared to a band structure calculation and is valid for any type of wave, both quantum and classical, and in any dimension. In the quantum regime, we illustrate our method on electronic confinement in 2D hexagonal boron nitride with a nitrogen vacancy, in agreement with previous results. In the classical case, we study a three-dimensional inverse woodpile photonic band gap cavity superlattice, where we identify novel acceptor-like behavior.

In Chapter 3, we investigate the possibility of improving the accuracy of our scaling method for classification of wave confinement in very small supercells by means of machine learning. This is often the case for 3D photonic crystals, since light propagation through these structures is notoriously difficult to calculate and one is restricted to very small supercells in the computations. Moreover, small supercells are also often used in the experiments, making them an extremely important case to investigate. Unfortunately, due to the nature of scaling theories in general, small supercells are also those where the results of our scaling method are the least accurate. We therefore slightly reformulate the scaling theory of Chapter 2 and use it to implement two different clustering algorithms to classify wave confinement in photonic crystals. We compare the performance of the clustering algorithms with the results obtained by direct application of the scaling theory. We find that, under some circumstances, the clustering algorithms outperform the direct application of the scaling theory, but their applicability is limited. Therefore, we conclude that the use of clustering algorithms does not

supersede the direct scaling theory, but that they can be used as auxiliary tools to enhance the precision of the results for small supercells.

In Chapter 4, we employ the results of the previous chapters to analyze the light-confining properties of inverse woodpile photonic superlattices with respect to their structural parameters, namely the regular and defect pore radii. We create so-called confinement maps, depicting the dependence of the number and energy concentration of 3D confined bands on the crystal structural parameters. We find that certain minimal deviations between the two pore sizes are required for the appearance of 3D confined bands and larger deviations favor higher number of confined bands. Further, we investigate symmetries of selected bands and discuss their relation to electronic orbitals, suggesting that photonic structures offer greater variety of state geometries and symmetries than electronic systems, which can also be relatively easily controlled. Finally, we analyze the suitability of various inverse woodpile structures for cavity quantum electrodynamics applications. We find that the donorlike crystals with smaller defect pores than regular pores are more favorable for such applications as a result of their larger silicon volume around the cavities.

In Chapter 5 we investigate the problem of light propagation through realistically large photonic crystals - a notoriously computationally difficult task. To this end, we develop a size-robust discontinuous Galerkin finite element method, where we approximate the solution of a large but finite crystal by a set of Bloch modes, representing the solutions of an infinite crystal. We describe the construction in detail and numerically analyze the convergence and performance of our method.

We conclude in Chapter 6 by summarizing the results of this PhD thesis and providing suggestions for future research.

Bibliography

[1] W. H. Bragg. "X-Rays and Crystals". In: *Nature* 90.2243 (1912), pp. 219–219. ISSN: 0028-0836, 1476-4687. DOI: 10.1038/090219a0.

[2] W. H. Bragg and W. L. Bragg. "The Reflection of X-rays by Crystals". In: *Proc. R. Soc. Lond. A* 88.605 (1913), pp. 428–438. ISSN: 0950-1207, 2053-9150. DOI: 10.1098/rspa.1913.0040.

[3] N. W. Ashcroft and N. D. Mermin. *Solid State Physics*. New York: Holt, Rinehart and Winston, 1976. ISBN: 978-0-03-083993-1.

[4] J. D. Joannopoulos, S. G. Johnson, J. N. Winn, and R. D. Meade. *Photonic Crystals: Molding the Flow of Light*. Second. Princeton: Princeton University Press, 2008. ISBN: 978-0-691-12456-8.

[5] L. Biró, K. Kertész, Z. Vértesy, G. Márk, Z. Bálint, V. Lousse, and J.-P. Vigneron. "Living Photonic Crystals: Butterfly Scales — Nanostructure and Optical Properties". In: *Materials Science and Engineering: C* 27.5-8 (2007), pp. 941–946. ISSN: 09284931. DOI: 10.1016/j.msec.2006.09.043.

[6] B. D. Wilts, J. Otto, and D. G. Stavenga. "Ultra-Dense, Curved, Grating Optics Determines Peacock Spider Coloration". In: *Nanoscale Adv.* 2.3 (2020), pp. 1122–1127. ISSN: 2516-0230. DOI: 10.1039/C9NA00494G.

[7] J. P. Vigneron, J.-F. Colomer, N. Vigneron, and V. Lousse. "Natural Layer-by-Layer Photonic Structure in the Squamae of *Hoplia Coerulea* (Coleoptera)". In: *Phys. Rev. E* 72.6 (2005), p. 061904. ISSN: 1539-3755, 1550-2376. DOI: 10.1103/PhysRevE.72.061904.

[8] V. Welch, J. Vigneron, and A. Parker. "The Cause of Colouration in the Ctenophore Beroë Cucumis". In: *Current Biology* 15.24 (2005), R985–R986. ISSN: 09609822. DOI: 10.1016/j.cub.2005.11.060.

[9] S. R. Mouchet, S. Luke, L. T. McDonald, and P. Vukusic. "Optical Costs and Benefits of Disorder in Biological Photonic Crystals". In: *Faraday Discuss.* 223 (2020), pp. 9–48. ISSN: 1359-6640, 1364-5498. DOI: 10.1039/D0FD00101E.

[10] *Gemological Institute of America*. https://www.gia.edu/opal.

[11] S. O. Demokritov, ed. *Spin Wave Confinement: Propagating Waves*. Second edition. Singapur: Pan Stanford Publishing, 2017. ISBN: 978-981-4774-35-2 978-1-315-11082-0.

[12] M. Maldovan. "Sound and Heat Revolutions in Phononics". In: *Nature* 503.7475 (2013), pp. 209–217. ISSN: 0028-0836, 1476-4687. DOI: 10.1038/nature12608.

[13] B. B. Alagoz and S. Alagoz. "Towards Earthquake Shields: A Numerical Investigation of Earthquake Shielding with Seismic Crystals". In: *OJA* 01.03 (2011), pp. 63–69. ISSN: 2162-5786, 2162-5794. DOI: 10.4236/oja.2011.13008.

[14] S. Brûlé, S. Enoch, and S. Guenneau. "Role of Nanophotonics in the Birth of Seismic Megastructures". In: *Nanophotonics* 8.10 (2019), pp. 1591–1605. ISSN: 2192-8614. DOI: 10.1515/nanoph-2019-0106.

[15] M. Miniaci, A. Krushynska, F. Bosia, and N. M. Pugno. "Large Scale Mechanical Metamaterials as Seismic Shields". In: *New J. Phys.* 18.8 (2016), p. 083041. ISSN: 1367-2630. DOI: 10.1088/1367-2630/18/8/083041.

[16] D. Lee, J. H. Oh, I. S. Kang, and J. Rho. "Seismic Phononic Crystals by Elastodynamic Navier Equation". In: *Phys. Rev. E* 100.6 (2019), p. 063002. ISSN: 2470-0045, 2470-0053. DOI: 10.1103/PhysRevE.100.063002.

[17] W. L. Vos and H. M. van Driel. "Higher Order Bragg Diffraction by Strongly Photonic Fcc Crystals: Onset of a Photonic Bandgap". In: *Physics Letters A* 272.1-2 (2000), pp. 101–106. ISSN: 03759601. DOI: 10.1016/S0375-9601(00)00388-1.

[18] H. M. van Driel and W. L. Vos. "Multiple Bragg Wave Coupling in Photonic Band-Gap Crystals". In: *Phys. Rev. B* 62.15 (2000), pp. 9872–9875. ISSN: 0163-1829, 1095-3795. DOI: 10.1103/PhysRevB.62.9872.

[19] L. Rayleigh. "XXVI. *On the Remarkable Phenomenon of Crystalline Reflexion Described by* Prof. Stokes". In: *The London, Edinburgh, and Dublin Philosophical Magazine and Journal of Science* 26.160 (1888), pp. 256–265. ISSN: 1941-5982, 1941-5990. DOI: 10.1080/14786448808628259.

[20] P. S. J. Russell and L. Solymar. "Borrmann-like Anomalous Effects in Volume Holography". In: *Appl. Phys.* 22.4 (1980), pp. 335–353. ISSN: 0340-3793, 1432-0630. DOI: 10.1007/BF00901055.

[21] S. Kawakami. "Light Propagation along Periodic Metal–Dielectric Layers". In: *Appl. Opt.* 22.16 (1983), p. 2426. ISSN: 0003-6935, 1539-4522. DOI: 10.1364/AO.22.002426.

[22] V. P. Bykov. "Excited Molecules in a Medium with Negative Permittivity". In: *Soviet physics, JETP* (1973), pp. 646–650.

[23] V. P. Bykov. "Spontaneous Emission in a Periodic Structure". In: *Soviet physics, JETP* (1972), pp. 269–273.

[24] E. Yablonovitch. "Inhibited Spontaneous Emission in Solid-State Physics and Electronics". In: *Phys. Rev. Lett.* 58.20 (1987), pp. 2059–2062. DOI: 10.1103/PhysRevLett.58.2059.

[25] S. John. "Strong Localization of Photons in Certain Disordered Dielectric Superlattices". In: *Phys. Rev. Lett.* 58.23 (1987), pp. 2486–2489. ISSN: 0031-9007. DOI: 10.1103/PhysRevLett.58.2486.

[26] J. D. Joannopoulos, P. R. Villeneuve, and S. Fan. "Photonic Crystals: Putting a New Twist on Light". In: *Nature* 386.6621 (1997), pp. 143–149. ISSN: 0028-0836, 1476-4687. DOI: 10.1038/386143a0.

[27] C. López. "Materials Aspects of Photonic Crystals". In: *Adv. Mater.* 15.20 (2003), pp. 1679–1704. ISSN: 0935-9648, 1521-4095. DOI: 10.1002/adma.200300386.

[28] P. Lodahl, A. F. van Driel, I. S. Nikolaev, A. Irman, K. Overgaag, D. Vanmaekelbergh, and W. L. Vos. "Controlling the Dynamics of Spontaneous Emission from Quantum Dots by Photonic Crystals". In: *Nature* 430.7000 (2004), pp. 654–657. ISSN: 0028-0836, 1476-4687. DOI: 10.1038/nature02772.

[29] R. K. Cersonsky, J. Antonaglia, B. D. Dice, and S. C. Glotzer. "The Diversity of Three-Dimensional Photonic Crystals". In: *Nat. Commun.* 12.1 (2021), p. 2543. ISSN: 2041-1723. DOI: 10.1038/s41467-021-22809-6.

[30] A. F. Koenderink, A. Alu, and A. Polman. "Nanophotonics: Shrinking Light-Based Technology". In: *Science* 348.6234 (2015), pp. 516–521. ISSN: 0036-8075, 1095-9203. DOI: 10.1126/science.1261243.

[31] M. D. Leistikow, A. P. Mosk, E. Yeganegi, S. R. Huisman, A. Lagendijk, and W. L. Vos. "Inhibited Spontaneous Emission of Quantum Dots Observed in a 3D Photonic Band Gap". In: *Phys. Rev. Lett.* 107.19 (2011), p. 193903. ISSN: 0031-9007, 1079-7114. DOI: 10.1103/PhysRevLett.107.193903.

[32] S. Ogawa, M. Imada, S. Yoshimoto, M. Okano, and S. Noda. "Control of Light Emission by 3D Photonic Crystals". In: *Science* 305.5681 (2004), pp. 227–229. ISSN: 0036-8075, 1095-9203. DOI: 10.1126/science.1097968.

[33] A. F. Koenderink, L. Bechger, H. P. Schriemer, A. Lagendijk, and W. L. Vos. "Broadband Fivefold Reduction of Vacuum Fluctuations Probed by Dyes in Photonic Crystals". In: *Phys. Rev. Lett.* 88.14 (2002), p. 143903. ISSN: 0031-9007, 1079-7114. DOI: 10.1103/PhysRevLett.88.143903.

[34] D. Zhou and R. Biswas. "Photonic Crystal Enhanced Light-Trapping in Thin Film Solar Cells". In: *J. Appl. Phys.* 103.9 (2008), p. 093102. ISSN: 0021-8979, 1089-7550. DOI: 10.1063/1.2908212.

[35] D. Devashish, S. B. Hasan, J. J. W. van der Vegt, and W. L. Vos. "Reflectivity Calculated for a Three-Dimensional Silicon Photonic Band Gap Crystal with Finite Support". In: *Phys. Rev. B* 95.15 (2017), p. 155141. ISSN: 2469-9950, 2469-9969. DOI: 10.1103/PhysRevB.95.155141.

[36] D. Sharma, S. B. Hasan, R. Saive, J. J. W. van der Vegt, and W. L. Vos. "Enhanced Absorption in Thin and Ultrathin Silicon Films by 3D Photonic Band Gap Back Reflectors". In: *Opt. Express* 29.25 (2021), p. 41023. ISSN: 1094-4087. DOI: 10.1364/OE.435412.

[37] C. M. Cornelius and J. P. Dowling. "Modification of Planck Blackbody Radiation by Photonic Band-Gap Structures". In: *Phys. Rev. A* 59.6 (1999), pp. 4736–4746. ISSN: 1050-2947, 1094-1622. DOI: 10.1103/PhysRevA.59.4736.

[38] J. G. Fleming, S. Y. Lin, I. El-Kady, R. Biswas, and K. M. Ho. "All-Metallic Three-Dimensional Photonic Crystals with a Large Infrared Bandgap". In: *Nature* 417.6884 (2002), pp. 52–55. ISSN: 0028-0836, 1476-4687. DOI: 10.1038/417052a.

[39] S. E. Han, A. Stein, and D. J. Norris. "Tailoring Self-Assembled Metallic Photonic Crystals for Modified Thermal Emission". In: *Phys. Rev. Lett.* 99.5 (2007), p. 053906. ISSN: 0031-9007, 1079-7114. DOI: 10.1103/PhysRevLett.99.053906.

[40] T. Ergin, N. Stenger, P. Brenner, J. B. Pendry, and M. Wegener. "Three-Dimensional Invisibility Cloak at Optical Wavelengths". In: *Science* 328.5976 (2010), pp. 337–339. ISSN: 0036-8075, 1095-9203. DOI: 10.1126/science.1186351.

[41] K. Busch, G. von Freymann, S. Linden, S. Mingaleev, L. Tkeshelashvili, and M. Wegener. "Periodic Nanostructures for Photonics". In: *Phys. Rep.* 444.3-6 (2007), pp. 101–202. ISSN: 03701573. DOI: 10.1016/j.physrep.2007.02.011.

[42] L. A. Woldering, A. P. Mosk, and W. L. Vos. "Design of a Three-Dimensional Photonic Band Gap Cavity in a Diamondlike Inverse Woodpile Photonic Crystal". In: *Phys. Rev. B* 90.11 (2014), p. 115140. DOI: 10.1103/PhysRevB.90.115140.

[43] S. A. Hack, J. J. W. van der Vegt, and W. L. Vos. "Cartesian Light: Unconventional Propagation of Light in a Three-Dimensional Superlattice of Coupled Cavities within a Three-Dimensional Photonic Band Gap". In: *Phys. Rev. B* 99.11 (2019), p. 115308. ISSN: 2469-9950, 2469-9969. DOI: 10.1103/PhysRevB.99.115308.

[44] T. Baba. "Slow Light in Photonic Crystals". In: *Nat. Photonics* 2.8 (2008), pp. 465–473. ISSN: 1749-4893. DOI: 10.1038/nphoton.2008.146.

[45] S. Noda, A. Chutinan, and M. Imada. "Trapping and Emission of Photons by a Single Defect in a Photonic Bandgap Structure". In: *Nature* 407.6804 (2000), pp. 608–610. ISSN: 1476-4687. DOI: 10.1038/35036532.

[46] K. J. Vahala. "Optical Microcavities". In: *Nature* 424.6950 (2003), pp. 839–846. ISSN: 1476-4687. DOI: 10.1038/nature01939.

[47] A. Tandaechanurat, S. Ishida, D. Guimard, M. Nomura, S. Iwamoto, and Y. Arakawa. "Lasing Oscillation in a Three-Dimensional Photonic Crystal Nanocavity with a Complete Bandgap". In: *Nat. Photonics* 5.2 (2011), pp. 91–94. ISSN: 1749-4885, 1749-4893. DOI: 10.1038/nphoton.2010.286.

[48] R. Morita, T. Inoue, M. De Zoysa, K. Ishizaki, and S. Noda. "Photonic-Crystal Lasers with Two-Dimensionally Arranged Gain and Loss Sections for High-Peak-Power Short-Pulse Operation". In: *Nat. Photonics* 15.4 (2021), pp. 311–318. ISSN: 1749-4885, 1749-4893. DOI: 10.1038/s41566-021-00771-5.

[49] D. M. Callahan, K. A. W. Horowitz, and H. A. Atwater. "Light Trapping in Ultrathin Silicon Photonic Crystal Superlattices with Randomly-Textured Dielectric Incouplers". In: *Opt. Express* 21.25 (2013), p. 30315. ISSN: 1094-4087. DOI: 10.1364/OE.21.030315.

[50] J. Wang, F. Sciarrino, A. Laing, and M. G. Thompson. "Integrated Photonic Quantum Technologies". In: *Nat. Photonics* 14.5 (2020), pp. 273–284. ISSN: 1749-4885, 1749-4893. DOI: 10.1038/s41566-019-0532-1.

[51] J. M. Gérard, B. Sermage, B. Gayral, B. Legrand, E. Costard, and V. Thierry-Mieg. "Enhanced Spontaneous Emission by Quantum Boxes in a Monolithic Optical Microcavity". In: *Phys. Rev. Lett.* 81.5 (1998), pp. 1110–1113. DOI: 10.1103/PhysRevLett.81.1110.

[52] P. Michler, ed. *Single Quantum Dots: Fundamentals, Applications, and New Concepts*. Topics in Applied Physics v. 90. Berlin, Heidelberg, New York: Springer-Verlag, 2003. ISBN: 978-3-540-14022-1.

[53] T. Yoshie, A. Scherer, J. Hendrickson, G. Khitrova, H. M. Gibbs, G. Rupper, C. Ell, O. B. Shchekin, and D. G. Deppe. "Vacuum Rabi Splitting with a Single Quantum Dot in a Photonic Crystal Nanocavity". In: *Nature* 432.7014 (2004), pp. 200–203. ISSN: 1476-4687. DOI: 10.1038/nature03119.

[54] M. Aspelmeyer, T. J. Kippenberg, and F. Marquardt. "Cavity Optomechanics". In: *Rev. Mod. Phys.* 86.4 (2014), pp. 1391–1452. ISSN: 0034-6861, 1539-0756. DOI: 10.1103/RevModPhys.86.1391.

[55] W. L. Vos and L. A. Woldering. "Cavity Quantum Electrodynamics with Three-Dimensional Photonic Band Gap Crystals". In: *Light Localisation and Lasing: Random and Quasi-Random Photonic Structures*. Cambridge University Press, 2015, pp. 180–214. ISBN: 978-1-107-03877-6.

[56] A. F. Koenderink, A. Lagendijk, and W. L. Vos. "Optical Extinction Due to Intrinsic Structural Variations of Photonic Crystals". In: *Phys. Rev. B* 72.15 (2005), p. 153102. ISSN: 1098-0121, 1550-235X. DOI: 10.1103/PhysRevB.72.153102.

[57] P. W. Anderson. "Absence of Diffusion in Certain Random Lattices". In: *Phys. Rev.* 109.5 (1958), pp. 1492–1505. ISSN: 0031-899X. DOI: 10.1103/PhysRev.109.1492.

[58] P. W. Anderson. "The Question of Classical Localization A Theory of White Paint?" In: *Philos. Mag. B* 52.3 (1985), pp. 505–509. ISSN: 1364-2812, 1463-6417. DOI: 10.1080/13642818508240619.

[59] P. Sheng. *Introduction to Wave Scattering, Localization, and Mesoscopic Phenomena*. 2nd ed. Springer Series in Materials Science 88. Berlin; New York: Springer, 2006. ISBN: 978-3-540-29155-8.

[60] S. John. "Electromagnetic Absorption in a Disordered Medium near a Photon Mobility Edge". In: *Phys. Rev. Lett.* 53.22 (1984), pp. 2169–2172. ISSN: 0031-9007. DOI: 10.1103/PhysRevLett.53.2169.

[61] C. Conti and A. Fratalocchi. "Dynamic Light Diffusion, Three-Dimensional Anderson Localization and Lasing in Inverted Opals". In: *Nature Phys.* 4.10 (2008), pp. 794–798. ISSN: 1745-2473, 1745-2481. DOI: 10.1038/nphys1035.

[62] S. A. Hack. "Computational Nanophotonics in 3D". PhD thesis. Enschede, The Netherlands: University of Twente, 2019. ISBN: 9789036549080. DOI: 10.3990/1.9789036549080.

[63] L. A. Woldering, A. P. Mosk, R. W. Tjerkstra, and W. L. Vos. "The Influence of Fabrication Deviations on the Photonic Band Gap of Three-Dimensional Inverse Woodpile Nanostructures". In: *J. Appl. Phys.* 105.9 (2009), p. 093108. ISSN: 0021-8979, 1089-7550. DOI: 10.1063/1.3103777.

[64] M. Maldovan and E. L. Thomas. "Diamond-Structured Photonic Crystals". In: *Nat. Mater.* 3.9 (2004), pp. 593–600. ISSN: 1476-4660. DOI: 10.1038/nmat1201.

[65] K. M. Ho, C. T. Chan, C. M. Soukoulis, R. Biswas, and M. Sigalas. "Photonic Band Gaps in Three Dimensions: New Layer-by-Layer Periodic Structures". In: *Solid State Commun.* 89.5 (1994), pp. 413–416. ISSN: 0038-1098. DOI: 10.1016/0038-1098(94)90202-X.

[66] J. Schilling, J. White, A. Scherer, G. Stupian, R. Hillebrand, and U. Gösele. "Three-Dimensional Macroporous Silicon Photonic Crystal with Large Photonic Band Gap". In: *Appl. Phys. Lett.* 86.1 (2004), p. 011101. ISSN: 0003-6951. DOI: 10.1063/1.1842855.

[67] R. W. Tjerkstra, L. A. Woldering, J. M. van den Broek, F. Roozeboom, I. D. Setija, and W. L. Vos. "Method to Pattern Etch Masks in Two Inclined Planes for Three-Dimensional Nano- and Microfabrication". In: *J. Vac. Sci. Technol. B* 29.6 (2011), p. 061604. ISSN: 2166-2746. DOI: 10.1116/1.3662000.

[68] J. M. van den Broek, L. A. Woldering, R. W. Tjerkstra, F. B. Segerink, I. D. Setija, and W. L. Vos. "Inverse-Woodpile Photonic Band Gap Crystals with a Cubic Diamond-like Structure Made from Single-Crystalline Silicon". In: *Adv. Funct. Mater.* 22.1 (2012), pp. 25–31. ISSN: 1616-3028. DOI: 10.1002/adfm.201101101.

[69] D. A. Grishina, C. A. M. Harteveld, L. A. Woldering, and W. L. Vos. "Method for Making a Single-Step Etch Mask for 3D Monolithic Nanostructures". In: *Nanotechnology* 26.50 (2015), p. 505302. ISSN: 0957-4484. DOI: 10.1088/0957-4484/26/50/505302.

[70] D. Devashish, O. S. Ojambati, S. B. Hasan, J. J. W. van der Vegt, and W. L. Vos. "Three-Dimensional Photonic Band Gap Cavity with Finite Support: Enhanced Energy Density and Optical Absorption". In: *Phys. Rev. B* 99.7 (2019), p. 075112. ISSN: 2469-9950, 2469-9969. DOI: 10.1103/PhysRevB.99.075112.

[71] M. Adhikary, R. Uppu, C. A. M. Harteveld, D. A. Grishina, and W. L. Vos. "Experimental Probe of a Complete 3D Photonic Band Gap". In: *Opt. Express* 28.3 (2020), p. 2683. ISSN: 1094-4087. DOI: 10.1364/OE.28.002683.

[72] R. Uppu, M. Adhikary, C. A. M. Harteveld, and W. L. Vos. "Spatially Shaping Waves to Penetrate Deep inside a Forbidden Gap". In: *Phys. Rev. Lett.* 126.17 (2021), p. 177402. ISSN: 0031-9007, 1079-7114. DOI: 10.1103/PhysRevLett.126.177402.

[73] M. Kozoň, A. Lagendijk, M. Schlottbom, J. J. W. van der Vegt, and W. L. Vos. "Scaling Theory of Wave Confinement in Classical and Quantum Periodic Systems". In: *Phys. Rev. Lett.* 129.17 (2022), p. 176401. ISSN: 0031-9007, 1079-7114. DOI: 10.1103/PhysRevLett.129.176401.

[74] J. D. Jackson. *Classical Electrodynamics*. 3rd ed. New York: Wiley, 1999. ISBN: 978-0-471-30932-1.

[75] P. Monk. *Finite Element Methods for Maxwell's Equations*. Numerical Mathematics and Scientific Computation. Oxford : New York: Clarendon Press ; Oxford University Press, 2003. ISBN: 978-0-19-850888-5.

[76] W. Dörfler, A. Lechleiter, M. Plum, G. Schneider, and C. Wieners. *Photonic Crystals: Mathematical Analysis and Numerical Approximation*. Vol. 42. Oberwolfach Seminars. Basel: Springer Basel, 2011. ISBN: 978-3-0348-0112-6 978-3-0348-0113-3. DOI: 10.1007/978-3-0348-0113-3.

[77] W. Setyawan and S. Curtarolo. "High-Throughput Electronic Band Structure Calculations: Challenges and Tools". In: *Comput. Mater. Sci.* 49.2 (2010), pp. 299–312. ISSN: 09270256. DOI: 10.1016/j.commatsci.2010.05.010.

[78] P. Kuchment. "7. The Mathematics of Photonic Crystals". In: *Mathematical Modeling in Optical Science*. Ed. by G. Bao, L. Cowsar, and W. Masters. Society for Industrial and Applied Mathematics, 2001, pp. 207–272. ISBN: 978-0-89871-475-3 978-0-89871-759-4. DOI: 10.1137/1.9780898717594.ch7.

[79] P. Kuchment. "An Overview of Periodic Elliptic Operators". In: *Bull. Amer. Math. Soc.* 53.3 (2016), pp. 343–414. ISSN: 0273-0979, 1088-9485. DOI: 10.1090/bull/1528.

[80] H. Brandsmeier, K. Schmidt, and C. Schwab. "A Multiscale Hp-FEM for 2D Photonic Crystal Bands". In: *J. Comput. Phys.* 230.2 (2011), pp. 349–374. ISSN: 00219991. DOI: 10.1016/j.jcp.2010.09.018.

[81] E. H. Lieb and M. Loss. *Analysis*. 2nd ed. Graduate Studies in Mathematics v. 14. Providence, RI: American Mathematical Society, 2001. ISBN: 978-0-8218-2783-3.

[82] L. Novotny and B. Hecht. *Principles of Nano-Optics*. Cambridge: Cambridge University Press, 2006. ISBN: 978-0-511-81353-5.

[83] S. Datta, C. T. Chan, K. M. Ho, and C. M. Soukoulis. "Effective Dielectric Constant of Periodic Composite Structures". In: *Phys. Rev. B* 48.20 (1993), pp. 14936–14943. ISSN: 0163-1829, 1095-3795. DOI: 10.1103/PhysRevB.48.14936.

[84] A. Yariv and P. Yeh. *Optical Waves in Crystals: Propagation and Control of Laser Radiation*. Wiley classics library ed. Wiley Classics Library. Hoboken, N.J: John Wiley and Sons, 2003. ISBN: 978-0-471-43081-0.

[85] T. Ando, A. B. Fowler, and F. Stern. "Electronic Properties of Two-Dimensional Systems". In: *Rev. Mod. Phys.* 54.2 (1982), pp. 437–672. ISSN: 0034-6861. DOI: 10.1103/RevModPhys.54.437.

[86] P. R. Villeneuve, S. Fan, and J. D. Joannopoulos. "Microcavities in Photonic Crystals: Mode Symmetry, Tunability, and Coupling Efficiency". In: *Phys. Rev. B* 54.11 (1996), pp. 7837–7842. DOI: 10.1103/PhysRevB.54.7837.

[87] R. Hillebrand, S. Senz, W. Hergert, and U. Gösele. "Macroporous-Silicon-Based Three-Dimensional Photonic Crystal with a Large Complete Band Gap". In: *J. Appl. Phys.* 94.4 (2003), pp. 2758–2760. ISSN: 0021-8979, 1089-7550. DOI: 10.1063/1.1593796.

[88] S. G. Johnson and J. D. Joannopoulos. "Block-Iterative Frequency-Domain Methods for Maxwell's Equations in a Planewave Basis". In: *Opt. Express* 8.3 (2001), p. 173. ISSN: 1094-4087. DOI: 10.1364/OE.8.000173.

[89] K. Yee. "Numerical Solution of Initial Boundary Value Problems Involving Maxwell's Equations in Isotropic Media". In: *IEEE Trans. Antennas Propagat.* 14.3 (1966), pp. 302–307. ISSN: 0018-926X. DOI: 10.1109/TAP.1966.1138693.

[90] A. Taflove and S. C. Hagness. *Computational Electrodynamics: The Finite-Difference Time-Domain Method*. 3rd ed. Artech House Antennas and Propagation Library. Boston: Artech House, 2005. ISBN: 978-1-58053-832-9.

[91] S. G. Johnson, A. Oskooi, and A. Taflove, eds. *Advances in FDTD Computational Electrodynamics: Photonics and Nanotechnology*. Artech House Antennas and Propagation Series. Boston: Artech House, 2013. ISBN: 978-1-60807-170-8.

[92] J.-M. Jin. *The Finite Element Method in Electromagnetics*. Third edition. Hoboken. New Jersey: John Wiley & Sons Inc, 2014. ISBN: 978-1-118-84202-7 978-1-118-84198-3.

[93] S. Burger, R. Klose, A. Schaedle, F. Schmidt, and L. W. Zschiedrich. "FEM Modeling of 3D Photonic Crystals and Photonic Crystal Waveguides". In: *Integrated Optoelectronic Devices 2005*. Ed. by Y. Sidorin and C. A. Waechter. San Jose, California, United States, 2005, p. 164. DOI: 10.1117/12.585895.

[94] L. Petersson and J.-M. Jin. "A Three-Dimensional Time-Domain Finite-Element Formulation for Periodic Structures". In: *IEEE Trans. Antennas Propagat.* 54.1 (2006), pp. 12–19. ISSN: 0018-926X. DOI: 10.1109/TAP.2005.861547.

[95] P. I. Borel, A. Harpøth, L. H. Frandsen, M. Kristensen, P. Shi, J. S. Jensen, and O. Sigmund. "Topology Optimization and Fabrication of Photonic Crystal Structures". In: *Opt. Express* 12.9 (2004), p. 1996. ISSN: 1094-4087. DOI: 10.1364/OPEX.12.001996.

[96] J. van Kan, G. Segal, and F. Vermolen. *Numerical Methods in Scientific Computing*. VSSD, 2010. ISBN: 978-90-6562-179-5.

2 Scaling Theory of Wave Confinement in Classical and Quantum Periodic Systems

2.1 Introduction

Completely controlling wave propagation in periodic media is a key challenge that is essential for a large variety of applications [1–15]. An especially interesting type of control is wave confinement achieved by introducing disorder and functional defects into an otherwise periodic medium. The interference of waves in such an altered structure may result in a strong concentration of the energy density inside a small sub-volume of the medium. Wave confinement has been investigated for different types of waves and in various settings, *e.g.*, classical mechanics [16], photonics [9, 10, 17–19], solid state physics [20–24], or magnonics [25, 26]. Its applications include sensors, controlled spontaneous emission, and enhanced interactions between hybrid wave-types such as sound and light [27–35].

The analysis of spatial concentration of energy in physical systems is in photonics traditionally done via the mode volume [18, 36–39] or in condensed matter physics via the participation ratio [16, 23, 40]. Bands with small mode volume or participation ratio are considered to be confined while, conversely, bands with large mode volume or participation ratio are taken to be extended [16, 18, 19, 22–24, 41]. However, the notion of what specifically is 'large' and 'small' is in each case determined subjectively as there are no rigorous boundaries imposed by nature.

An alternative method to analyze the wave confinement, multifractality analysis [42–44], is based on the scaling of the participation ratio in the limit of infinitely large supercells. Unfortunately, this approach requires impractically large supercells, which is further compounded by its inability to deal with band folding, see Appendices 2.A and 2.B.

Therefore, in this chapter[1] we present a rigorous, derived method to determine the confinement of waves in periodic structures with defects, based on finite-size scaling [46–48]. Rather than extending the supercells towards impractically large sizes, our method determines confinement in moderately large supercells by comparing them to smaller ones. As a consequence, our approach requires only minimal computational overhead and its results are directly applicable to experimentally relevant finite systems. Our technique can be viewed as a more

[1] This chapter is based on the publication by Kozoň *et al.* [45].

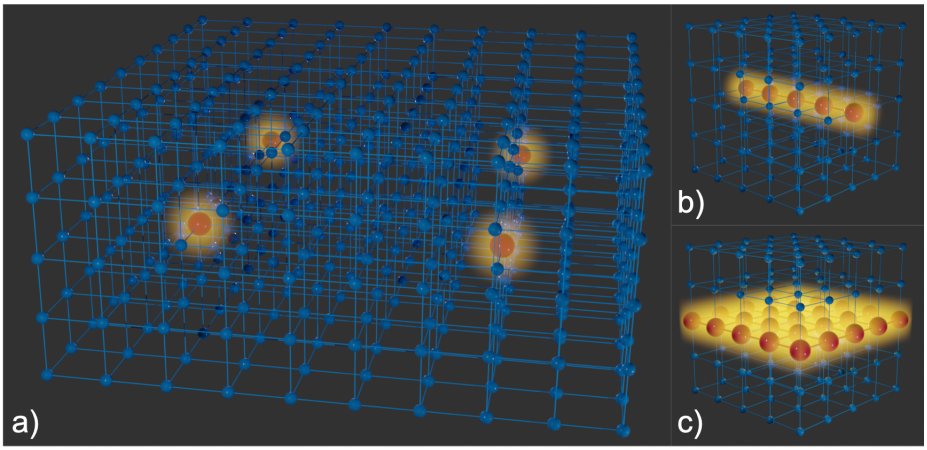

Figure 2.1: Illustration of supercells of size $N = 5$ in a $D = 3$ system with various wave confinement dimensionalities c induced by defect geometries of dimensionalities d. Blue spheres correspond to regular unit cells, unit cells containing defects are red and confined waves are represented by yellow. (a) Four supercells, each containing a point defect akin to a cavity [11], trap waves in all three dimensions, $d = 0$, $c = 3$. (b) Supercell with a linear defect, analogous to an optical waveguide or fiber, $d = 1$, $c = 2$. (c) Supercell with a planar defect, analogous to a 2D electron gas [52], $d = 2$, $c = 1$.

accessible and practical extension of the multifractality concept and is even suited for automated classification, *e.g.*, via machine learning (see Chapter 3).

2.2 Defect Superlattices

Superimposing a defect lattice on an unperturbed crystal lattice gives rise to a defect superlattice [6, 22, 23, 49–51]. A unit cell of such a superlattice that contains N^D unit cells, with D the system dimension, is referred to as a supercell of linear size N. For simplicity, we keep here the number of unit cells per supercell the same for all directions, but this is not necessary for our theory to work. Based on the geometric dimensionality d of the defects, wave bands with different confinement dimensionality c arise in the spectrum, as shown in Fig. 2.1 for an $N = 5$ supercell in $D = 3$ dimensions. The confinement dimensionality c of a wave determines the number of dimensions in which the wave is confined and mathematically corresponds to the codimension of the defect dimensionality: $c = D - d$. We note that introducing defects in every unit cell of the supercell is equivalent to a new periodic structure with no defects ($d = 3$) that supports only extended, unconfined waves ($c = 0$).

Fig. 2.1 represents highly idealized examples of simple defects. Real structures often contain multiple defects of various geometries oriented along different directions. Such complex defect configurations allow for several different confinement dimensionalities c and the problem of assigning the correct c to a given band thus

becomes highly nontrivial. In order to understand the confinement in these real structures, a systematic method of identification and classification of confined bands is needed.

2.3 Key confinement quantities

To analyze the confinement of waves, one must first determine the physical quantity corresponding to the notion of wave confinement for the given type of physical wave. Without loss of generality, one can make this a real, non-negative quantity. For example, in electromagnetic systems this quantity could be the energy density, in electronic systems the charge density, and analogously for other waves. We denote this spatially dependent confinement quantity by $W(\mathbf{x})$. To keep the description of our method general, we assume in the following that $W(\mathbf{x})$ has been identified and can be calculated for every band of interest.

For scientifically interesting structures of moderate supercell sizes, the number of bands to be analyzed quickly reaches several hundreds, see, *e.g.*, Refs. [18, 19]. It is therefore impractical to analyze the confinement by visually inspecting the spatial distribution of $W(\mathbf{x})$, as has been done before by ,*e.g.*, Ref. [18], for each band. These limitations call for a quantitative, automatable method to analyze wave confinement.

We employ $W(\mathbf{x})$ to define the two key quantities for our scaling analysis. First, we consider the mode volume [18, 36–39] defined as

$$V_{\mathrm{M}} := \frac{\int\limits_{V_{\mathrm{S}}} W(\mathbf{x})\mathrm{d}V}{\max\limits_{\mathbf{x}\in V_{\mathrm{S}}}\{W(\mathbf{x})\}}, \tag{2.1}$$

where the integration is over the supercell volume V_{S}. The mode volume intuitively corresponds to the *volume in which the wave is confined*. Alternatively, the participation ratio [16, 40] can be used, see Appendix 2.C.

Secondly, it is important to also consider the problem from the converse point of view: *How much energy of the wave is stored in a certain volume*? To quantify this notion, we define the confinement energy

$$E_{\mathrm{C}} := \int\limits_{V_{\mathrm{C}}} W(\mathbf{x})\mathrm{d}V, \tag{2.2}$$

with the integration volume V_{C} taken as the volume of one unit cell, centered around the defect (*cf.* Appendix 2.A). An analogous quantity, termed SAW-likeness coefficient, has been introduced by Ref. [53] to analyze the confinement of surface acoustic waves (SAW). We note that by referring to the quantity E_{C} as the confinement energy we employ the nomenclature from photonics, where the quantity W represents the energy density and its spatial integral corresponds to the energy. In physical systems that employ different W, the quantity E_{C} does not necessarily represent energy. Nevertheless, due to the absence of a more general term, we stick to the photonic terminology in this chapter.

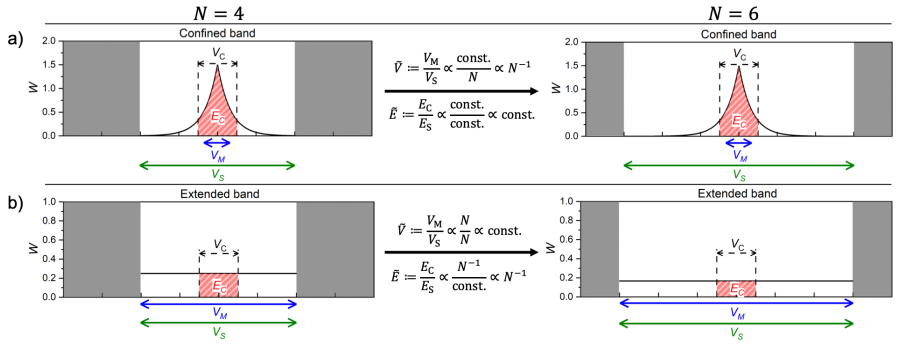

Figure 2.2: Illustration of our scaling argument in the didactic case of $D = 1$. An $N = 4$ supercell is transformed into an $N = 6$ supercell by adding unit cells to its boundary. We investigate how the characteristic quantities $\widetilde{V}$ and $\widetilde{E}$ evolve upon this transition and obtain scaling relations for them. While scaling, we keep the total amount of energy E_S within the supercell constant. (a) Confined band. (b) Extended band.

We employ normalized quantities

$$\widetilde{V} := \frac{V_\mathrm{M}}{V_\mathrm{S}}, \qquad \widetilde{E} := \frac{E_\mathrm{C}}{E_\mathrm{S}}, \tag{2.3}$$

where E_S denotes the total amount of energy in the supercell.

For a wave confined within a cavity we expect simultaneously a low $\widetilde{V}$ and a high $\widetilde{E}$, while the opposite (high $\widetilde{V}$, low $\widetilde{E}$) is expected for a fully extended band. Nevertheless, there are no natural thresholds on how low $\widetilde{V}$ and how high $\widetilde{E}$ should be for a band to be identified as confined. To overcome this ambiguity, we analyze the behaviour of $\widetilde{V}$ and $\widetilde{E}$ with respect to the variation of the supercell size N, instead of their values themselves. This technique is known as finite-size scaling [46–48].

2.4 Scaling

Our scaling argument is illustrated with the didactic 1D model in Fig. 2.2. Let us consider a linear supercell with $N = 4$ with a cavity in its center. For a specific band with certain $\widetilde{V}$ and $\widetilde{E}$, we are interested in how adding more unit cells to the supercell boundary changes these values, and how these changes differ for a confined band as opposed to an extended band. Therefore, we increase the supercell size to $N = 6$.

A band of confined states is depicted in Fig. 2.2(a), with its energy density decaying away from the cavity in the supercell center. Since the size of the cavity to which the wave is confined does not change, it follows that the mode volume V_M also remains constant while scaling. However, the supercell volume V_S increases proportionally to N, hence, the normalized quantity $\widetilde{V}$ decreases for the confined band as N^{-1}. Since the wave is confined within the cavity, it only 'feels' that additional unit cells have been added through its decaying tail. This

response clearly approaches zero in the limit of $N \to \infty$ and, thus, in this limit $\widetilde{E} = \text{const}$.

A band of extended states is illustrated in Fig. 2.2(b) by a constant energy density throughout the whole supercell. In this case, the behavior described above is the converse: The volume occupied by the wave in the supercell grows proportionally to the supercell volume, resulting in the scaling $\widetilde{V} = \text{const}$. The energy density extends homogeneously throughout the whole supercell and will further spread into the added unit cells as N increases. This leakage decreases the amount of confinement energy E_C within V_C as N^{-1}.

It is straightforward to extend the above scaling analysis to a D-dimensional system. A band with a given confinement dimensionality $0 \leq c \leq D$ obeys the following scaling relations, in the limit of $N \to \infty$:

$$\widetilde{V} = AN^{-c}, \qquad \widetilde{E} = BN^{c-D}. \tag{2.4}$$

Here, A and B are constants independent of N. For the proper derivation of Eqs. (2.4), see Appendix 2.D.

One can calculate $\widetilde{V}$ and $\widetilde{E}$ from Eqs. (2.1)-(2.3) for each band, but because the constants A, B are not known *a priori*, Eqs. (2.4) cannot be easily inverted to obtain c. To accurately obtain c from our scaling relations, we combine the two equations in (2.4) into a ratio of the normalized mode volume raised to a judiciously chosen power $\alpha > 0$ and the normalized confinement energy:

$$\frac{\widetilde{V}^\alpha}{\widetilde{E}} = CN^\kappa, \tag{2.5}$$

where the exponent κ is given by

$$\kappa = -(\alpha + 1)c + D. \tag{2.6}$$

By suitably choosing the power α, we can adjust the value of κ so that it is negative for bands with certain c and positive for the other bands. The value of κ, in turn, influences the scaling behavior of these bands as per Eq. (2.5).

Our technique is illustrated in Fig. 2.3. Investigating the confinement in a supercell of size N, for every $0 < j \leq D$, we have chosen α so that $\kappa < 0$ for all $c \geq j$ and $\kappa > 0$ for all $c < j$. Hence, we are now able to distinguish between the bands with $c < j$ and $c \geq j$ by simply tracking the behavior of $\widetilde{V}^\alpha/\widetilde{E}$ as the supercell grows from a smaller reference size N_0 to the investigated size N. The bands with negative κ will move downwards in the graph, while the bands with positive κ will shift upwards, in accordance with the Eq. (2.5). By varying j over all the integer values $0 < j \leq D$, this approach allows us to completely classify all wave bands in the spectrum based on their confinement dimensionality.

Eq. (2.5) strictly holds only in the limit of very large N, with sub-leading order terms in N present for finite supercell sizes. By following the procedure as outlined in the previous paragraph, there is still some freedom remaining in the choice of the auxiliary power α. This freedom can be utilized to effectively reduce the contribution of these sub-leading terms, thereby allowing confinement

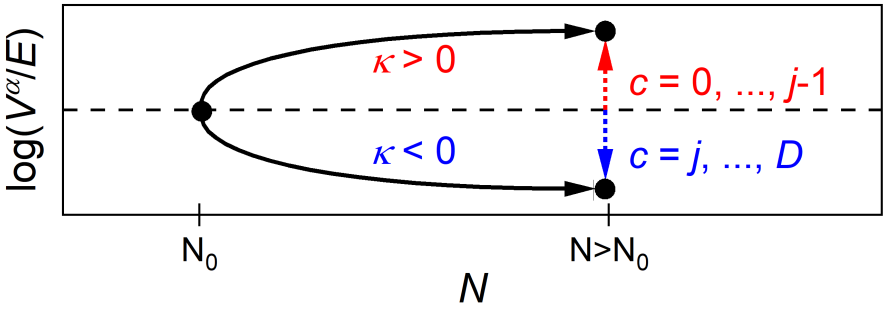

Figure 2.3: Flow diagram to identify bands confined in $c \geq j$ dimensions in a D-dimensional medium: The ratio $\widetilde{V}^{\alpha}/\widetilde{E}$ versus the system size N. The auxiliary power α is chosen so that $\kappa < 0$ for all $c \geq j$ and $\kappa > 0$ for all $c < j$. The sign of κ determines if $\widetilde{V}^{\alpha}/\widetilde{E}$ increases or decreases with growing supercell size.

identification already for very small supercells. Nevertheless, since the coefficients corresponding to the sub-leading terms are generally not known, one cannot eliminate their effect completely, which may show up as misidentification of some bands for small supercells, as we illustrate in an example below. The unique values of α to maximize the accuracy of our technique for $D = 1, 2, 3$ are listed in Table 2.1. For their calculation, see Appendix 2.E.

		D		
		1	2	3
j	3	–	–	$1/5$
	2	–	$1/3$	1
	1	1	3	5

Table 2.1: Auxiliary powers α to classify the confinement in systems of various dimension D. The value of $j \leq D$ indicates the confinement dimensionality being identified, as per Fig. 2.3.

In case of the 1D example from Fig. 2.2, if we choose $\alpha = 1$, corresponding to $D = 1$ and $j = 1$ from Table 2.1, upon plotting $\tilde{V}/\tilde{E}$ versus the supercell size N we will observe that the $c = 1$ confined band moves down, while the $c = 0$ extended band moves up in the flow diagram, analogously to Fig. 2.3.

2.5 Application examples

We now demonstrate our method on an atomic crystal confinint electronic quantum waves, namely a 2D hexagonal BN with a nitrogen vacancy representing a point-like defect [54]. Specifically, we investigate electronic confinement in a supercell of size $N = 5$. The band structure and charge densities of this quantum system were calculated using density functional theory [55] implemented in the

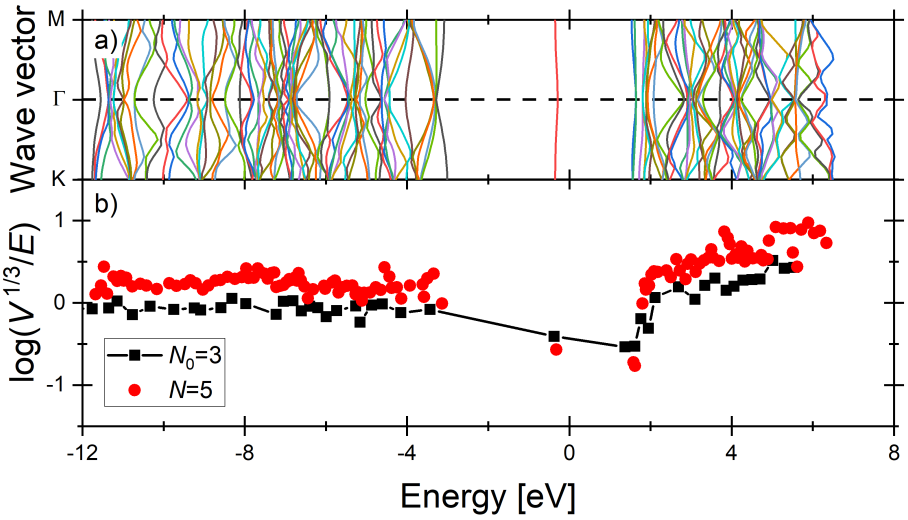

Figure 2.4: Our confinement analysis applied to a 2D quantum system: electronic waves in a hexagonal BN with nitrogen deficiency. Zero energy is set at the Fermi level. (a) Band structure of the $N = 5$ supercell, flipped to have an energy abscissa. Bands are distinguished by colors. (b) Scaling analysis of confinement: every band is represented by a point. As the supercell size increases from $N_0 = 3$ to $N = 5$, extended bands move upwards, while the three point-confined bands closest to zero energy shift down.

VASP code v6.1.1 [56]. For details on the methodology, see Appendix 2.F.

The band structure of the system is shown in Fig. 2.4(a). Since the defect in our $D = 2$ system has point geometry, we only expect two different confinement dimensionalities to appear: the point-confined ($c = 2$) and the extended ($c = 0$) bands. To distinguish between these, we choose $\alpha = 1/3$ from Table 2.1 and use a reference supercell of size $N_0 = 3$. The plot of $\log\left(\widetilde{V}^{1/3}/\widetilde{E}\right)$ for each band in Fig. 2.4(b) clearly shows that the majority of bands move upwards, identifying them as extended ($c = 0$), according to our framework. Additionally, three bands near zero energy move downwards and thus correspond to point-confined ($c = 2$), in agreement with the findings of Huang and Lee [54].

In our second example, we demonstrate our technique on light confinement in an $N = 4$ supercell of a 3D inverse woodpile photonic crystal with two proximate line defects [18, 19, 57, 58]. The crossing point of these line defects represents a point defect. We study the acceptor-like structure investigated by Ref. [18]. The defects in this case have more complicated geometry than in the previous example: The system sustains point-confined ($c = 3$) bands, line-confined ($c = 2$) bands and extended ($c = 0$) bands. The band structure and the energy densities were calculated using the MPB code [59]. For details on the methodology, see Appendix 2.G.

Fig. 2.5 depicts the results of our analysis. We unambiguously identify the con-

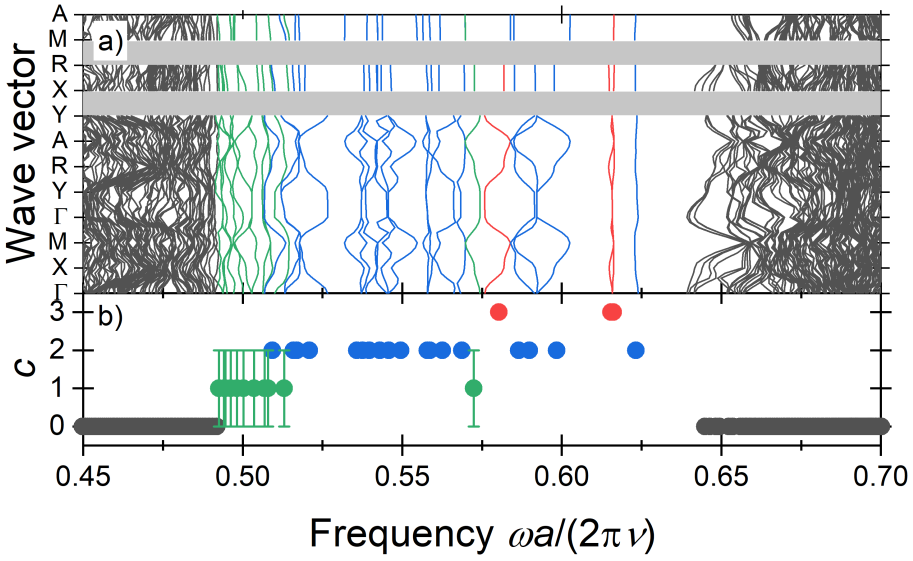

Figure 2.5: Scaling analysis of wave confinement in an $N = 4$ supercell of a 3D inverse woodpile photonic crystal with two proximate line defects. The horizontal axis displays the reduced frequency $\tilde{\omega} := \omega a/(2\pi\nu)$, where a is the lattice constant in the y direction and ν denotes the speed of light. (a) Band structure. In the M-A region degenerate bands overlap. (b) Confinement dimensionalities determined by our method for each band. Error bars denote bands assigned to $c = 1$, which should not occur in our structure but appears due to the small size of the supercell.

finement dimensionality c of most bands. At frequencies outside the band gap ($\tilde{\omega} < 0.49$ and $\tilde{\omega} > 0.64$), all bands have $c = 0$ and are thus three-dimensionally extended. Within the gap, most bands have $c = 2$, that is waveguide-like behavior. This is the first time that such guiding states have been identified in inverse woodpile photonic crystals, even though their presence was naively expected based on the defect geometry involving defect pores. Additionally, several bands, mostly near $\tilde{\omega} \approx 0.5$, appear to be plane-confined ($c = 1$). We know, however, that our defect geometry is linear and thus it does not support plane-confined bands. We attribute this discrepancy to the small size of the studied supercell (see Appendix 2.G). Nevertheless, our analysis is the first that distinguishes $c = 2$ bands from those with $c = 0$ in a 3D photonic superlattice. Remarkably, we also find three bands (red) with $c = 3$. Visual inspection confirms the point-confined character of the two bands at $\tilde{\omega} \approx 0.62$. We therefore discover point-confined bands in an acceptor-like 3D inverse woodpile structure, thus disproving earlier claims by Woldering *et al.* [18] that such bands do not exist. For a detailed discussion of the third red band, see Appendix 2.G.

Hack *et al.* [19] have shown that in higher dimensional structures such as 3D inverse woodpiles there is no direct correlation between dispersion and coupling in a given direction and thus one cannot assess confinement by analyzing band dispersion. Our method is able to analyze confinement in such structures where the dispersion arguments fail. Furthermore, our technique is not limited to 'defect' superlattices in terms of 'impurity'. Any superlattice superimposed on another lattice can be analyzed by our technique. This is the case for, *e.g.*, Lieb lattices or other so-called flat-band lattices [60, 61]. Our technique is also directly applicable to quasicrystals by analyzing their periodic approximants, which, based on Refs. [62, 63], exhibit defect properties virtually identical to their parent quasicrystals.

2.6 Conclusion

In this chapter we describe a systematic scaling theory to analyze wave confinement in periodic superlattices, applicable to any type of physical waves. Already in one of the studied examples our technique uncovers physically new results, namely photonic acceptor behavior, thus showcasing its power. Our method is directly applicable to actively researched periodic and quasiperiodic structures and for optimization algorithms aiming to minimize or maximize specific types of wave confinement.[2]

[2]The data used for this chapter are available [64] via the open-access repository Zenodo that is developed under the European OpenAIRE program and operated by CERN.

Appendices

2.A Basic considerations

When numerically calculating band structures, the frequencies ω are computed for discrete wave vectors $\mathbf{k}$ within the Brillouin zone and subsequently connected to form bands. Correctly connecting the discrete values becomes nontrivial at points where multiple bands intersect. Since each band represents an eigenstate of the Maxwell problem, it is possible to utilize the orthogonality of different bands together with their continuity in $\mathbf{k}$ and symmetry properties to perform these connections correctly at every point, see, *e.g.*, Dörfler [65]. It is obviously crucial for the band structures used as the input into our method to be correctly connected, otherwise the whole concept of a 'band' as such is spoiled. In our examples, we use in each case the corresponding band-computation software to perform these connections.

The larger the supercell gets, the more bands it contains in the given frequency range, thus making one-to-one comparison between increasing supercells impossible. This effect is known as band-folding and it is a fundamental property of the Brillouin zone. Several ways of 'unfolding' the band structure have been proposed in the literature, see, *e.g.*, Refs [66, 67]. Nevertheless, it is still very hard to draw direct relations of any type between bands from different supercells as the band-folding effects seem to also depend on the confinement dimensionality of the bands. Our approach circumvents this problem by not requiring such direct relations between different supercells. Namely, in the $\widetilde{V}^{\alpha}/\widetilde{E}$ plots for large enough $N > N_0$, each band of the investigated N supercell is clearly either above or below *all* the bands with similar frequencies of the reference N_0 supercell.

Our method can be viewed as an extension of the multifractality techniques, which are usually formulated for scaling of the participation ratio [42–44]. In the first step of our framework we also perform a similar scaling for the mode volume in Eq. (2.4). However, by limiting oneself to only this scaling behavior, it would require very large supercell size N to draw conclusive results for the whole spectrum, as described below and illustrated in Fig. 2.6. To complicate the matter even more, due to the band folding effects, translating the results obtained for this large N to experimentally interesting supercells of moderate size would be extremely complicated, if at all possible. By subsequently introducing the confinement energy as another analyzed quantity with different scaling exponent than the mode volume and the auxiliary power parameter α, our method allows for the determination of confinement throughout the whole spectrum for relatively small supercell sizes and, as described in the previous paragraph, free of complications related to band folding.

In our definition of E_{C} in Eq (2.2) we choose the volume V_{C} to be centered around the cavity, where the confinement is expected. Nevertheless, this is not a strict requirement. Choosing the volume V_{C} at a different location within the supercell will still yield correct scaling results, albeit possibly affecting the convergence of the method and thus requiring larger supercell sizes N, N_0 to

properly classify the whole spectrum. It is however necessary, after V_C is selected, to keep this volume constant throughout the scaling, so that the exponent $c - D$ appears in the scaling relation for $\widetilde{E}$ in Eq. (2.4), since this is crucial to tune the exponent κ as needed.

The dimension of the supercell used to model the system may differ from the system dimensionality D in some cases. For example, in 2D electronic materials $D = 2$, but the charge density usually extends slightly into the third dimension and, moreover, can be zero in the 2D plane where the atomic nuclei are positioned. This case is therefore traditionally modeled by a 3D supercell and thus the integration in Eqs. (2.1) and (2.2) must be performed over three-dimensional volumes, *i.e.*, the volumes V_S and V_C will be three-dimensional. Nevertheless, since the structure of the material is still two-dimensional, the subsequent scaling analysis of confinement can be performed in $D = 2$ dimensions with the third dimension kept constant, *i.e.*, adding unit cells only along the planar material, as we did in the example of a hexagonal BN with N vacancy.

In this chapter we are only concerned with integer defect dimensionalities d in systems of dimension $D \leq 3$, as these are the most relevant for experiments. It is, however, straightforward to extend our technique to also include fractal defects with fractional dimensionalities and higher dimensional spaces. One can directly apply the derivations in this Supplemental material to find the optimal values of the auxiliary power α in case of fractional d or arbitrarily high D. These possibilities further emphasize the generality of our scaling theory.

In both the theory and examples in this chapter, we restrict ourselves to cases with two superposed lattices. One could readily devise an example of a structure in which more than two lattices are superposed, for example a system containing two different defect superlattices or a Lieb lattice with an impurity superlattice [60, 61]. We expect it to be straightforward to generalize the essence of our method to such multiple-lattice cases, however, there will likely also appear several details that one will need to address, such as correct extension of one superlattice when scaling the other. Therefore, this is an interesting area for further research.

We note that to get additional overview of band confinement properties, one can construct maximally localized Wannier functions and analyze their behavior. For details on this, see Refs. [68, 69].

2.B Shortcoming of multifractality

In the main text we claim that our method surpasses multifractality analysis because it is able to identify confinement of bands in much smaller supercells than is possible by multifractality. We illustrate this by applying the simple multifractality scaling to our example of 3D inverse woodpile photonic crystal with two linear defects used in the main text. We analyze the $N = 4$ supercell and use the $N_0 = 2$ supercell as a reference. We scale either the mode volume $\widetilde{V}$, in Fig. 2.6(a), or the confinement energy $\widetilde{E}$, in Fig. 2.6(b).

From Fig. 2.6(a), we observe that for some bands the value of $\widetilde{V}$ decreases

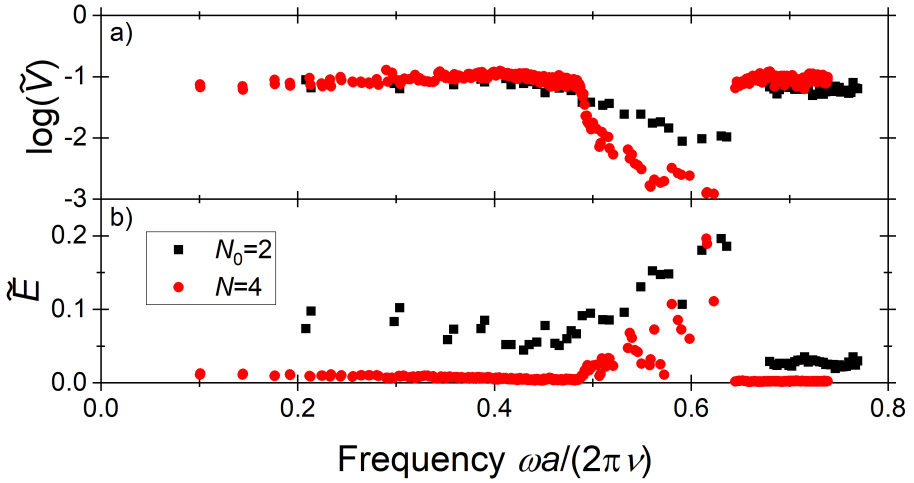

Figure 2.6: Failure of the standard multifractality approach to identify confined bands for small supercell sizes. Each band is represented by a point. (a) Scaling of the normalized mode volume. (b) Scaling of the normalized confinement energy. For some bands the values change significantly when scaling from $N_0 = 2$ to $N = 4$ while for others they remain approximately constant. This variety of behaviors indicates that different confinement dimensionalities c are present in the band spectrum, as predicted by the multifractality. Nevertheless, from each of these plots on its own, it is not possible to clearly assign confinement dimensionalities to specific bands and there is thus a need to move beyond the traditional multifractality method. One can, albeit, infer interesting information on confinement properties upon analyzing both plots simultaneously, which already brings us close to the essence of our technique of scaling the ratio of $\widetilde{V}^{\alpha}/\widetilde{E}$.

significantly as the supercell grows and for some it stays roughly constant. One would immediately expect the bands with constant $\widetilde{V}$ to be extended, according to Eq. (2.4). However, differentiating between the $c = 2$ and $c = 3$ bands is basically impossible. Moreover, even the distinction between the 'decreasing' and 'constant' mode volume can be rather unclear, for example around the frequencies $\tilde{\omega} \approx 0.5$.

Similarly, in Fig. 2.6(b), for some bands the value of $\widetilde{E}$ decreases significantly as the supercell grows and for some it stays roughly constant. In this case, the distinction between the various confinement dimensionalities is even blurrier than for the mode volume.

As it is suggestively implied by the combined Fig. 2.6, looking at the scaling of both $\widetilde{V}$ and $\widetilde{E}$ at the same time and comparing these yields more information than analyzing only one of them as does the traditional multifractality approach. This already brings us very close to our confinement analysis method as described in the main text, which represents a systematic approach to the simultaneous scaling of both $\widetilde{V}$ and $\widetilde{E}$.

2.C Sparsity measures: Analogies of mode volume and participation ratio

In our confinement analysis, we employ the mode volume V_{M} as one of two key quantities, defined in Eq. (2.1). We note that in literature the definitions of the mode volume may differ for various applications [18, 36–39], which is usually manifested in modifications of the integration volume in Eq. (2.1). In our case of a superlattice, it seems physically obvious to choose the supercell volume V_{S} as the integration domain. Moreover, irrespective of the physical meaning of the quantity V_{M}, integrating over V_{S} is crucial to obtain the correct scaling behavior in Eq. (2.5). Mode volume is, however, not the only possible choice, and a whole class of quantities can be substituted for V_{M} in our confinement identification method.

Hurley and Rickard [70] were the first to rigorously define the so-called *measures of sparsity*. In the most simple terms, measures of sparsity are functions quantifying the inequality of distribution of values within a given set. One such measure, for the set of values $\{m_1, \ldots, m_M\} \in \mathbb{R}^M$, is a pq-mean:

$$\mu_{p,q} := \frac{\left(\frac{1}{M} \sum_{j=1}^{M} m_j^p \right)^{1/p}}{\left(\frac{1}{M} \sum_{j=1}^{M} m_j^q \right)^{1/q}}. \tag{2.7}$$

Ref. [70] has shown that, for $p < q < \infty$, $\mu_{p,q}$ is indeed a viable measure of sparsity.

There is clear correspondence between the inequality of $W(\mathbf{x})$ over the volume V_{S} for a given band and its confinement: For a confined band, $W(\mathbf{x})$ is very high in certain parts of V_{S} but low everywhere else, while for an extended band $W(\mathbf{x})$ is approximately equally distributed over the whole V_{S}. To see this quantitatively, we write the straightforward continuous generalization of Eq. (2.7) to quantify the inequality of $W(\mathbf{x})$ over the volume V_{S} as

$$U_{p,q} := \frac{\left(\frac{1}{V_{\mathrm{S}}} \int_{V_{\mathrm{S}}} W^p(\mathbf{x}) \mathrm{d}V \right)^{1/p}}{\left(\frac{1}{V_{\mathrm{S}}} \int_{V_{\mathrm{S}}} W^q(\mathbf{x}) \mathrm{d}V \right)^{1/q}}. \tag{2.8}$$

Our normalized mode volume $\widetilde{V}$, as defined by Eq. (2.3), turns out to be a continuous version of the pq-mean with $p = 1$ and $q = \infty$, *i.e.*, $\widetilde{V} = U_{1,\infty}$. Note that, strictly speaking, the value of $q = \infty$ means that $\widetilde{V}$ has slightly weaker properties [3] than what is required for a sparsity measure as defined by Ref. [70]. This detail is, however, unimportant for our confinement identification purposes.

[3] Namely, it does not strictly satisfy the "Robin Hood" property that redistributing the values

For the purpose of confinement analysis, one can substitute any other pq-mean $U_{p,q}$ for $\widetilde{V}$ and our method will still work properly, albeit possibly with different scaling power than we obtained for $\widetilde{V}$ in Eq. (2.4). Specifically, substituting $p = 1$, $q = 2$ yields

$$U_{1,2} := \frac{\int\limits_{V_\mathrm{S}} W(\mathbf{x})\mathrm{d}V}{\sqrt{V_\mathrm{S}}\sqrt{\int\limits_{V_\mathrm{S}} W^2(\mathbf{x})\mathrm{d}V}}. \tag{2.9}$$

The quantity $U_{1,2}$ corresponds to the square root of normalized participation ratio:

$$U_{1,2} = \sqrt{\frac{P}{V_\mathrm{S}}}, \tag{2.10}$$

where the participation ratio P [16, 23, 40] is given by

$$P := \frac{\left(\int_{V_\mathrm{S}} W(\mathbf{x})\mathrm{d}V\right)^2}{\int_{V_\mathrm{S}} W^2(\mathbf{x})\mathrm{d}V}. \tag{2.11}$$

Finally, since the pq-mean is a non-negative dimensionless quantity, its various powers are equivalent in characterizing confinement and thus one can use $U_{1,2}^2$ instead of $U_{1,2}$. This illustrates that, in our approach, instead of normalized mode volume $\widetilde{V}$, normalized participation ratio can be used as well, similarly to any other pq-mean $U_{p,q}$.

2.D Derivation of the scaling equation

In a homogeneous D-dimensional system, waves propagate freely in all directions. Adding a periodic structure with no defects may restrict some ways of propagation, but the waves will still be extended, *i.e.*, they can propagate from any given unit cell to any other one. Upon introducing a defect of dimensionality $d \leq D$, some waves may couple to this defect and only propagate within it, thus never being able to achieve the non-defect unit cells. A wave coupled to a defect of dimension d has confinement dimensionality $c = D - d$, *i.e.*, it is confined in c dimensions. This effect is very strongly observable upon scaling of the system size. To analyze the confinement dimensionality of waves, one can utilize the scaling of mode volume and confinement energy.

Mathematically, the behavior of mode volume, defined by (2.1), for such a wave is given by

$$\begin{aligned} V_\mathrm{M} &= AN^d + \mathcal{O}(N^{d-1}) \\ &= AN^{D-c} + \mathcal{O}(N^{D-c-1}), \end{aligned} \tag{2.12}$$

where A is a constant independent of N. In fact, A is actually a functional depending on the permittivity distribution $\epsilon(\mathbf{x})$ and the band number. Eq. (2.12)

by decreasing the large ones and increasing the small ones ("stealing from the rich and giving to the poor") decreases sparsity. In the case of $q = \infty$, only decreasing the largest value will decrease the sparsity measure.

holds beyond the localization length of a given wave and expresses the fact that the mode volume of a confined wave can only grow within the geometrical constraints of the defect, with a small contribution of decaying waves in other directions. Upon normalization by $V_\mathrm{S} = N^D$, we obtain

$$\widetilde{V} = AN^{-c} + \mathcal{O}(N^{-c-1}). \tag{2.13}$$

Similarly, the normalized confinement energy, defined by Eqs. (2.2) and (2.4), behaves as

$$\begin{aligned}\widetilde{E} &= BN^{-d} + \mathcal{O}(N^{-d-1}) \\ &= BN^{c-D} + \mathcal{O}(N^{c-D-1}),\end{aligned} \tag{2.14}$$

where B is a constant independent of N. Analogously to A, B is a functional depending on the permittivity distribution $\epsilon(\mathbf{x})$ and the band number. Eq. (2.14) holds beyond the localization length of the given wave and expresses the fact that the confinement energy of a confined wave can only escape from the volume V_0 in ways that obey the geometrical constraints of the defect. There can also be additional, fast decaying, leakage expressed by the term $\mathcal{O}(N^{c-D-1})$.

We combine the Eqs. (2.13) and (2.14) and, upon neglecting the big-$\mathcal{O}$ contributions, we obtain for a wave with the confinement dimensionality c in the limit $N \to \infty$:

$$\frac{\widetilde{V}^\alpha}{\widetilde{E}} = \frac{(AN^{-c})^\alpha}{BN^{c-D}} = CN^{-(\alpha+1)c+D}, \tag{2.15}$$

where $C = A^\alpha/B$. Eq. (2.15) represents exactly our scaling relation in Eq. (2.5).

2.E Determining the auxiliary powers α

In our method, we are able to distinguish between the bands with $c < j$ and $c \geq j$ by tracking the behavior of $\widetilde{V}^\alpha/\widetilde{E}$ according to Eq. (2.5), as the supercell size changes from a smaller reference size N_0 to the investigated size N. By varying j over all the values $0 < j \leq D$, this approach allows us to completely classify all wave bands in the spectrum based on their confinement dimensionality. For this approach to work, the power α has to be chosen so that $\kappa < 0$ for all $c \geq j$ and $\kappa > 0$ for all $c < j$, where κ is given by Eq. (2.6). This condition, however, still allows for some freedom in the choice of α, which can be used to reduce the influence of the sub-leading orders to the Eq. (2.5).

These sub-leading orders are represented by the big-$\mathcal{O}$ contributions in Eqs. (2.13) and (2.14) and, especially for small supercells, can change the behavior of certain bands from what would be expected based on Eq. (2.5). Since we determine the confinement dimensionality by analyzing the change of $\widetilde{V}^\alpha/\widetilde{E}$ with respect to the reference supercell, the bands most susceptible to the sub-leading order effects will be the bands where the smallest leading-order change is expected. According to Eq. (2.5), these are the bands, for which κ is close to zero, *i.e.*, for every j, the bands with $c = j$ and $c = j - 1$. Because we generally do not know the contribution of the sub-leading orders to the overall scaling result, the most reasonable choice is to maximize the leading-order movement, *i.e.*, that

of the $c = j$ bands downwards and that of the $c = j - 1$ bands upwards, at the same time.

Since $\kappa := -(\alpha + 1)c + D$ is a linear function of c, the desired leading-order movements will be maximal if $\kappa = 0$ at the middle point, *i.e.*, for $c = j - 1/2$. Thus, for each $0 < j \leq D$, we solve the equation

$$-(\alpha + 1)(j - \frac{1}{2}) + D = 0. \tag{2.16}$$

The solution to (2.16) is

$$\alpha = \frac{2D}{2j - 1} - 1. \tag{2.17}$$

By choosing α according to (2.17) for each D, j, we ensure the effective minimization of the sub-leading order contributions to our scaling analysis and thus the best precision of our method. The powers α obtained this way for each j for $D = 1, 2, 3$ are tabulated in Table 2.1.

2.F Electronic band computation

For our analysis of the 2D hexagonal BN crystal with a nitrogen vacancy, we calculated the band structure and charge densities using the density functional theory [55] implemented in the VASP code v6.1.1 [56]. We use the PBE exchange-correlation functional [71] and represent the electron-ion interaction via the PAW potentials [72], specifically via the B and N potential files recommended by VASP. The cutoff energy was set to 550 eV.

We modeled the material using a 3D supercell with periodic boundary conditions, starting each geometry optimization with the vacuum layer of 12.56 Å perpendicular to the material layer to eliminate the effects of periodic boundary conditions in this direction. For geometry optimization and computation of the charge densities, we used 11×11 Γ-centered k-point grid. Geometry optimization was performed via the conjugate gradient algorithm until the residual atomic forces were smaller than 10 meV/Å. For the computation of the band structure in Fig. 2.4(a), we interpolated each segment of the high-symmetry path with 13 k-points, in addition to the two high-symmetry points.

For completeness, we include the plot for $j = 1$, which was omitted in the main text, in Fig. 2.7. These results confirm the three point-confined bands ($c = 2$ in a $D = 2$ system) around the Fermi level. At the same time, some other bands of the $N = 5$ supercell seem to be slightly under the reference values. Naively, this could indicate $c = 1$ confinement dimensionality for those bands, however, in this case we attribute this effect to be most likely caused by the sub-leading order effects in the scaling. This would be remedied by using larger supercell sizes N and N_0. This conclusion is confirmed by looking at the standard deviation of the $c \neq 2$ bands for the $N = 5$ supercell (green area in Fig. 2.7(b)), which is higher than the separation of the questionable bands from their reference line, in each case. Fig. 2.7 exemplifies that our framework can offer rigorous and cost-effective scaling analysis, but, especially for small supercell sizes, its results must still be critically evaluated to avoid the sub-leading order effects of scaling.

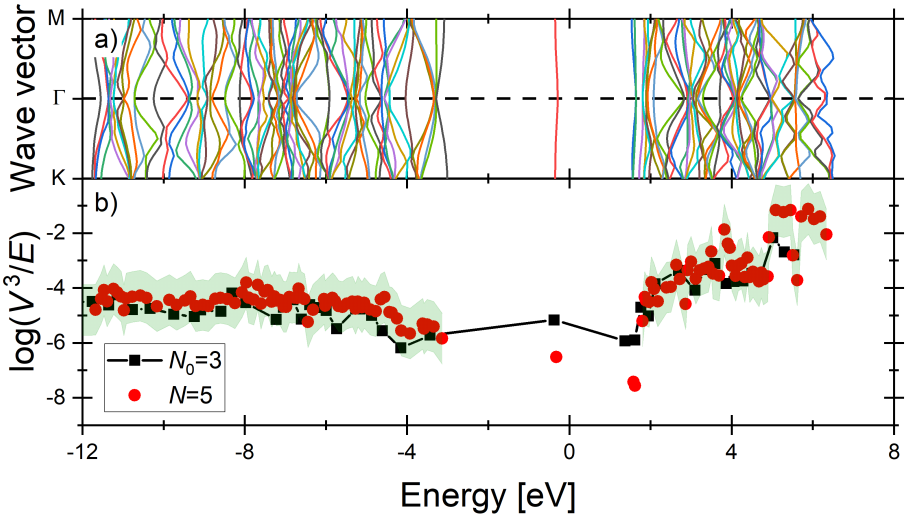

Figure 2.7: Confinement analysis applied to electronic waves in a 2D hexagonal BN with nitrogen deficiency, $j = 1$. Zero energy is set at the Fermi level. (a) Band structure of the $N = 5$ supercell, flipped to have an energy abscissa. Different bands are shown with different color for clarity. (b) Scaling analysis of confinement. Every band is represented by a point. These results confirm the three point-confined bands around the Fermi level. However, compared to Fig. 2.4, several other bands appear slightly under the reference line. We attribute this effect to be most likely caused by the sub-leading order contributions in the scaling and would be remedied for larger supercell sizes. This conclusion is enhanced by the fact that the standard deviation for these bands (green area) is higher than their separation from the reference line.

2.G Photonic band computation

In the main text we analyze light confinement in a 3D inverse woodpile photonic band gap superlattice with two proximate linear defects. The photonic band gap crystal consists of bulk silicon ($\varepsilon = 12.1$, see Ref. [73]), in which nanopores of radius R filled with air ($\varepsilon = 1$) are etched [57, 74]. We model the unperturbed crystal using a tetragonal unit cell with lattice parameters a in the y direction and $b = a/\sqrt{2}$ in the x and z directions. This unperturbed structure is depicted in Fig. 2.8(a).

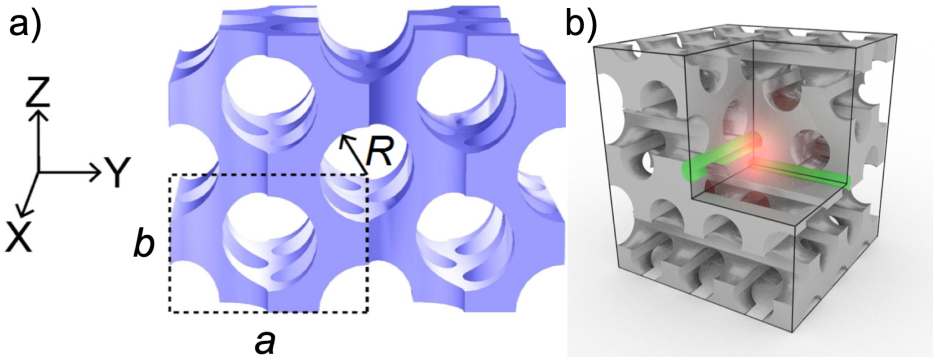

Figure 2.8: (a) Structure of an unperturbed inverse woodpile photonic crystal. We use a tetragonal unit cell with lattice parameters a in the y direction and $b = a/\sqrt{2}$ in the x and z directions. The pore radius is denoted by R. The figure shows an $N = 2$ supercell, with one unit cell designated by the dashed border. (b) Design of the defect. The radius R' of two proximate defect pores (shown in green) is altered. At their intersection a region with excess of one material is created that serves as a point defect (red glow).

A defect can be incorporated in the structure by altering the radius R' of two proximate nanopores, as illustrated in Fig. 2.8(b). In our example from the main text we use the unperturbed pores of the radius $R = 0.24a$ and the defect pores with the increased radius $R' = 0.35a > R$. This results in creation of a region with excess air at the intersection of the two defect pores, serving as a point defect. We include one defect of this type per supercell. Such a defect results in splitting of the defect bands from the bottom edge of the band gap, in analogy with acceptor-doped lattices in solid state physics.

We investigate the confinement of $N = 4$ supercell and use $N_0 = 2$ as a reference. The spectrum of the investigated cavity superlattice is computed by the plane-wave expansion method using the well-known MPB code [59] and is depicted in the main text in Fig. 2.5(a). For the band structure, we follow the high-symmetry path of the tetragonal unit cell (see Ref. [75]), as depicted in Fig. 2.9.

We perform scaling analysis to identify the confinement dimensionality c of each band, as described by our theory introduced in this chapter. Each step of the analysis for this $D = 3$-dimensional system is described in Fig. 2.10. We

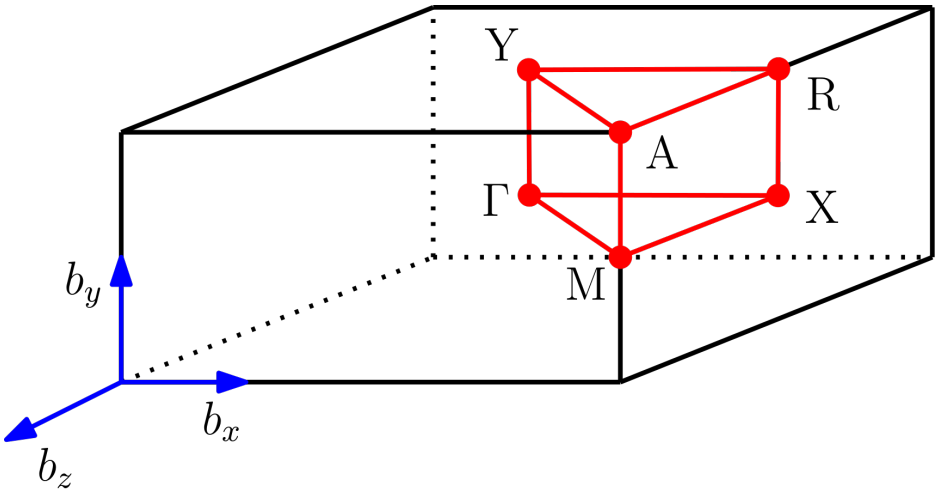

Figure 2.9: Brillouin zone of a tetragonal unit cell (black) with the corresponding high-symmetry path (red). The Cartesian basis vectors (blue) are denoted by b_x, b_y, b_z. For more details, see Ref. [75].

choose the auxiliary powers α based on Table 2.1.

Fig. 2.10(a) describes $j = 3$, with $\alpha = 1/5$. Out of the whole spectrum of unidentified bands, three bands around $\tilde{\omega} = 0.6$ decrease in value of $\log\left(V^{1/5}/E\right)$ with respect to the reference supercell. Visual inspection of energy density confirms the point-confined character of the two bands at $\tilde{\omega} \approx 0.62$. We thus confidently identify these two bands as having $c = 3$ confinement dimensionality. This is in stark contrast with the statement made in Ref. [18] that no point-confined bands exist in acceptor-like 3D inverse woodpile crystals.

The visual inspection of the energy density also shows that the band at $\tilde{\omega} \approx 0.58$ is confined in at least two dimensions, however it is visually not clear if the confinement is $c = 2$ or $c = 3$ and we are thus unable to confirm the correctness of the result for this band. This band also appears to be degenerate in the M-A region with the bands to its right, see Fig. 2.5(a) in the main text. It is therefore likely that all of these bands have the same c and either the blue ones or the red one are misindentified as a result of sub-leading order effects due to the small supercell sizes.

Fig. 2.10(b) describes $j = 2$, with $\alpha = 1$. In this case, several additional bands between roughly $\tilde{\omega} = 0.5$ and $\tilde{\omega} = 0.6$ drop below the values of the reference supercell. These newly separated bands are therefore identified as having $c = 2$ confinement dimensionality. This marks the first time such $c = 2$ bands are distinguished from fully extended bands in a 3D inverse woodpile photonic structure.

Fig. 2.10(c) describes $j = 1$, with $\alpha = 5$. There are several more bands dropping below the reference line. According to our framework, this would mean that they are plane-confined, *i.e.*, having $c = 1$. Nevertheless, we know that

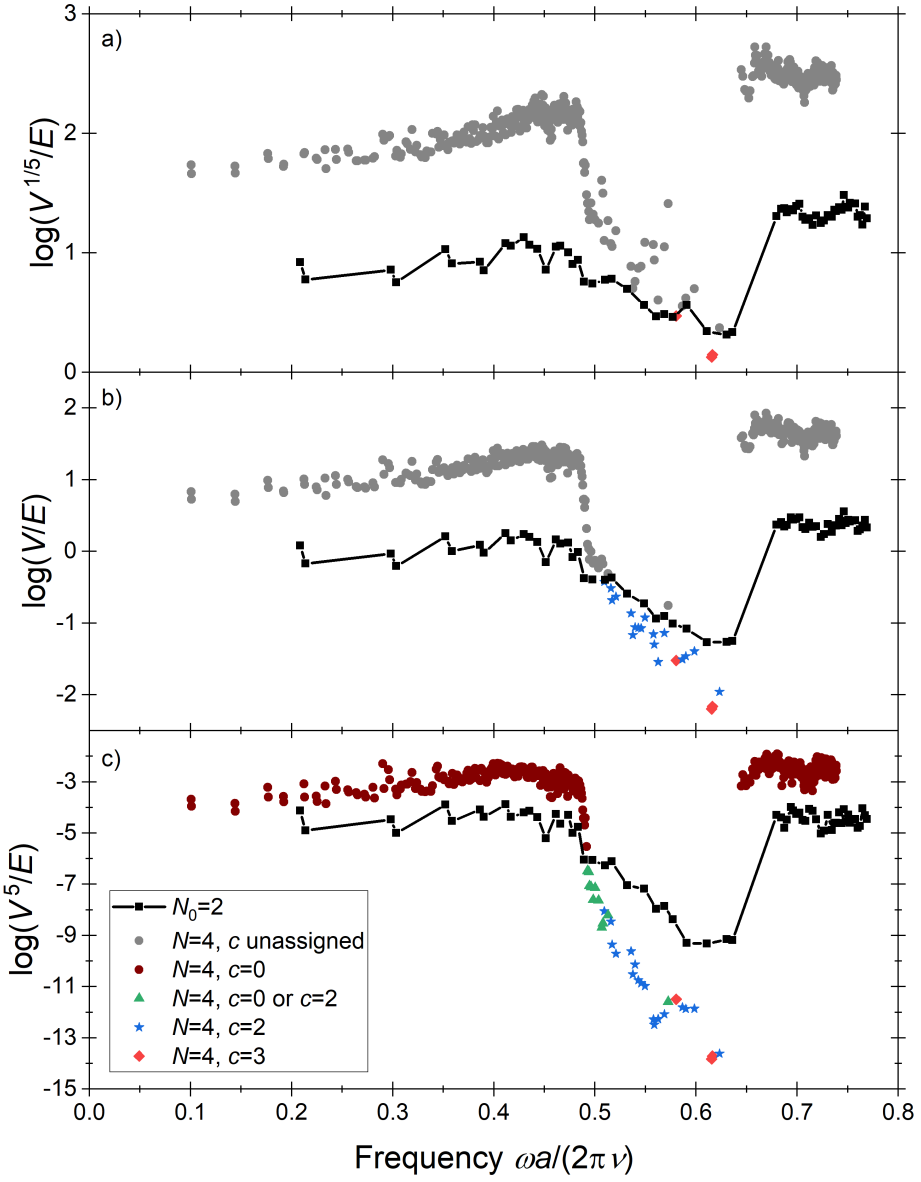

Figure 2.10: Step-by-step confinement analysis of bands in a supercell of size $N = 4$, for a 3D inverse woodpile photonic crystal with two proximate line defects. As a reference, supercell of size $N_0 = 2$ is taken. Every band is represented by a point. The parameter values are (a) $j = 3, \alpha = 1/5$, (b) $j = 2, \alpha = 1$, (c) $j = 1, \alpha = 5$, as per Table 2.1. We note that the slight shift in frequency between the bands from $N_0 = 2$ and $N = 4$ is due to different effective refractive index of the supercells and tends to zero for larger supercells.

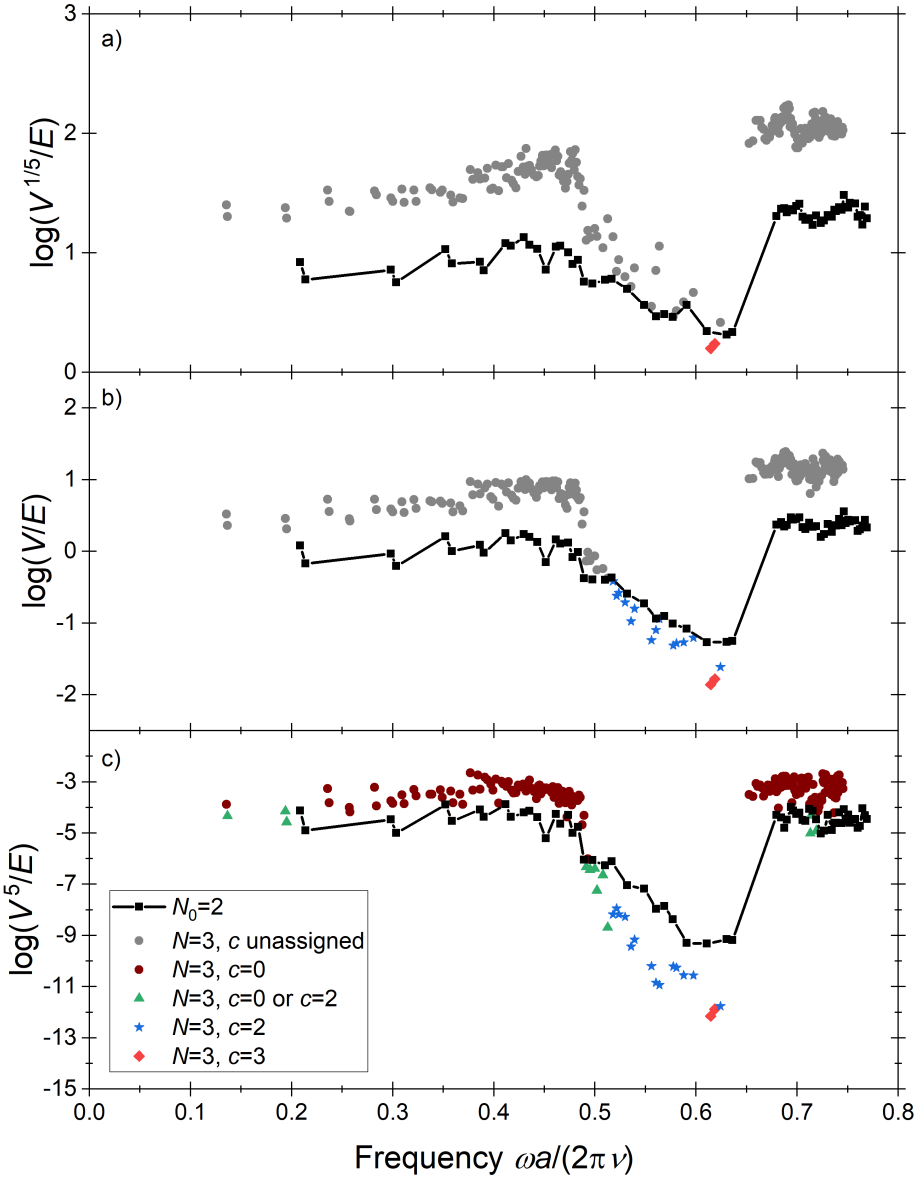

Figure 2.11: Step-by-step confinement analysis of bands in a supercell of size $N = 3$, for a 3D inverse woodpile photonic crystal with two proximate line defects. As a reference, supercell of size $N_0 = 2$ is taken. Every band is represented by a point. The parameter values are (a) $j = 3, \alpha = 1/5$, (b) $j = 2, \alpha = 1$, (c) $j = 1, \alpha = 5$, as per Table 2.1.

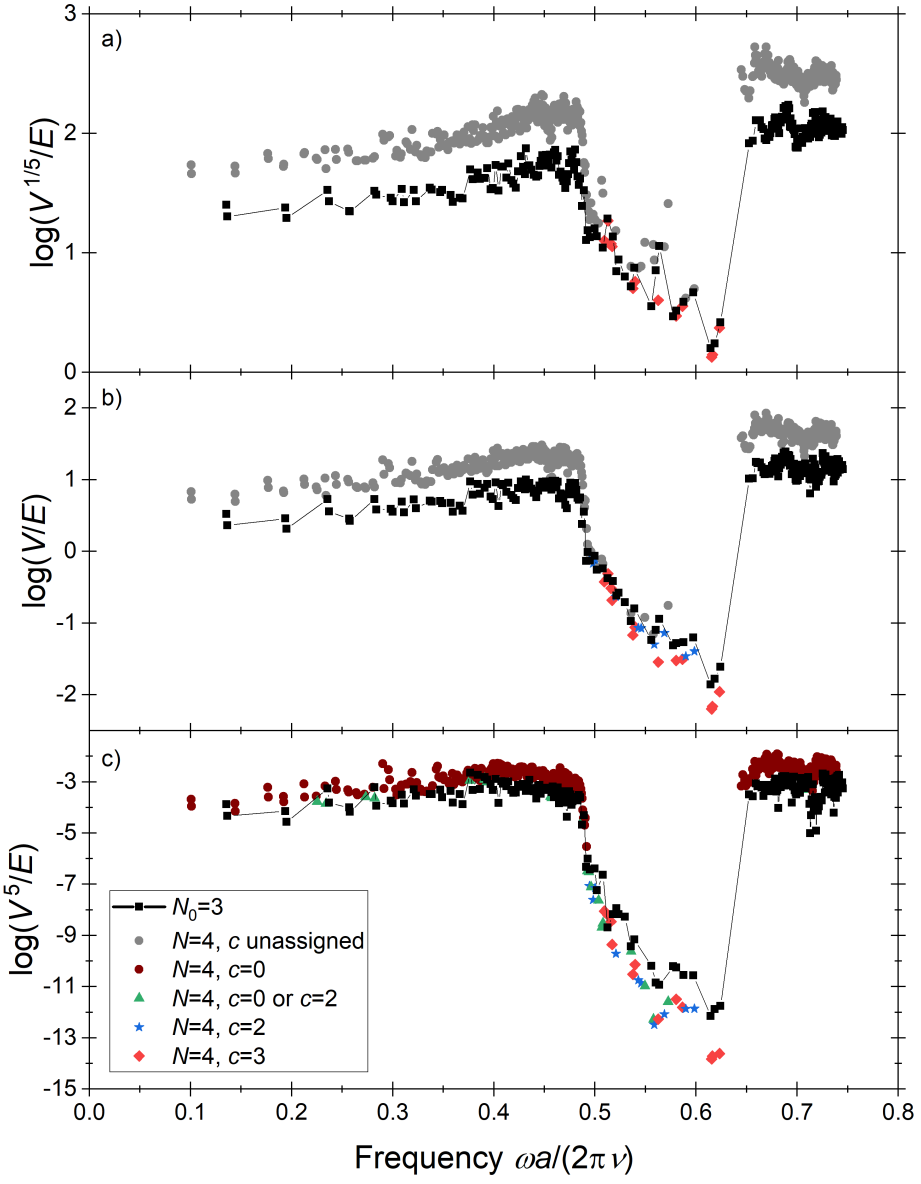

Figure 2.12: Step-by-step confinement analysis of bands in a supercell of size $N = 4$, for a 3D inverse woodpile photonic crystal with two proximate line defects. As a reference, supercell of size $N_0 = 3$ is taken. Every band is represented by a point. The parameter values are (a) $j = 3, \alpha = 1/5$, (b) $j = 2, \alpha = 1$, (c) $j = 1, \alpha = 5$, as per Table 2.1.

our defect geometry is linear and therefore cannot support plane-confined bands. These bands must thus either have $c = 2$ or $c = 0$.

The misidentification for bands that should have $c = 2$ is due to the fact that the size of the (reference) supercell is still below the localization length in the plane where the linear defects are positioned. However, the scaling Eq. (2.5) holds only for supercell sizes larger than the localization length. Therefore it is understandable that our method identifies these bands as plane-confined. Simply put, for the given supercell size, the information about confinement of these bands is not yet available in the calculated energy density and thus cannot be extracted from it by any means, unless implementing some additional knowledge, for example about the defect geometry.

The misidentified bands that should have $c = 0$ are caused by the fact that for the given supercell size the effects of the sub-leading order terms on Eq. (2.5) are still too large. This is an issue of the convergence of our technique and it would also be corrected for larger supercell sizes. In this case, it hypothetically could be possible to devise some alternative way to improve the convergence since, unlike in the case of the previous paragraph, the information about the confinement may be available in the calculated energy density data - this remains, however, beyond the scope of this chapter.

We note that many of these misidentified bands (green in Fig. 2.5) seem to be flat in the Γ-Y, X-R, and M-A regions, which could naively imply their confinement. Nevertheless, all of these regions correspond to the wave-vector shift in the y-direction and, as it has been shown by Ref. [19], the coupling coefficients in this direction are much weaker than in the x, y-directions due to the geometrical properties of the inverse-woodpile structure and can be tuned by changing the relative distances of neighboring cavities. Therefore the apparent flatness in these regions is not a reason enough to claim their confinement.

Lastly, all the bands remaining above the reference values in Fig. 2.10(c) are identified as extended, *i.e.*, with $c = 0$.

Unfortunately, we do not have enough computational power available to illustrate the convergence of our method by analyzing the larger $N = 5$ supercell. However, we analyzed two cases using different supercells than in our main example. The analysis of $N = 3$ supercell using $N_0 = 2$ as a reference is illustrated in Fig. 2.11 and the analysis of $N = 4$ supercell using the reference $N_0 = 3$ is in Fig. 2.12. It is immediately clear that the separation of bands between the reference and the investigated supercell in both of these cases is significantly smaller than in the main case of $N = 4$ and $N_0 = 2$. This becomes problematic especially in Fig. 2.11(c) and the whole Fig. 2.12, since in these cases the separation between the supercells is clearly smaller than the spread of the bands within one supercell. This, for example in Figs. 2.11(c) and. 2.12(c), results in several bands at both ends of the spectrum (around $\tilde{\omega} < 0.3$ and $\tilde{\omega} > 0.7$) being identified as $c = 1$. However, it can be easily confirmed by looking at the energy-density profile of these bands that they are extended ($c = 0$). Since these misindentifications do not appear in the $N = 4, N_0 = 2$ case, this example clearly shows not only that the accuracy of our method increases with larger supercells, but that it is also important to maintain large enough size difference between N and N_0.

We note that it might be possible to devise some kind of Richardson-like extrapolation argument [76] to enhance the convergence of our method, by comparing results for various supercell sizes N. Nevertheless, this is nontrivial, especially due to the fact that band folding clearly affects the bands of different c differently. For now, such an extension remains out of the scope of this chapter.

Our method is especially powerful for experimentally interesting supercells of moderate size. These supercell sizes are, however, in a range where possible inaccuracies due to finite-size scaling can occur and therefore, naturally, the results need to be critically evaluated. The presented photonic example further illustrates the strength and novelty of our method. Our framework has enabled the discovery of 3D-confined acceptor-like bands previously thought non-existent and, for the first time ever in an inverse woodpile structure, distinguished 2D-confined bands from the extended ones. It is therefore clear that our technique enables direct access to previously inaccessible confinement information.

Bibliography

[1] P. Markoš and C. M. Soukoulis. *Wave Propagation: From Electrons to Photonic Crystals and Left-Handed Materials*. Princeton ; Oxford: Princeton University Press, 2008. ISBN: 978-0-691-13003-3.

[2] M. Fink, D. Cassereau, A. Derode, C. Prada, P. Roux, M. Tanter, J.-L. Thomas, and F. Wu. "Time-Reversed Acoustics". In: *Rep. Prog. Phys.* 63.12 (2000), pp. 1933–1995. ISSN: 0034-4885, 1361-6633. DOI: 10.1088/0034-4885/63/12/202.

[3] Z. Liu, X. Zhang, Y. Mao, Y. Y. Zhu, Z. Yang, C. T. Chan, and P. Sheng. "Locally Resonant Sonic Materials". In: *Science* 289.5485 (2000), pp. 1734–1736. ISSN: 0036-8075, 1095-9203. DOI: 10.1126/science.289.5485.1734.

[4] M. Maldovan. "Sound and Heat Revolutions in Phononics". In: *Nature* 503.7475 (2013), pp. 209–217. ISSN: 0028-0836, 1476-4687. DOI: 10.1038/nature12608.

[5] S. A. Cummer, J. Christensen, and A. Alù. "Controlling Sound with Acoustic Metamaterials". In: *Nat. Rev. Mater.* 1.3 (2016), p. 16001. ISSN: 2058-8437. DOI: 10.1038/natrevmats.2016.1.

[6] V. V. Kruglyak, S. O. Demokritov, and D. Grundler. "Magnonics". In: *J. Phys. D* 43.26 (2010), p. 264001. ISSN: 0022-3727, 1361-6463. DOI: 10.1088/0022-3727/43/26/264001.

[7] K. Wagner, A. Kákay, K. Schultheiss, A. Henschke, T. Sebastian, and H. Schultheiss. "Magnetic Domain Walls as Reconfigurable Spin-Wave Nanochannels". In: *Nat. Nanotechnol.* 11.5 (2016), pp. 432–436. ISSN: 1748-3387, 1748-3395. DOI: 10.1038/nnano.2015.339.

[8] K. Klyukin, L. L. Tao, E. Y. Tsymbal, and V. Alexandrov. "Defect-Assisted Tunneling Electroresistance in Ferroelectric Tunnel Junctions". In: *Phys. Rev. Lett.* 121.5 (2018), p. 056601. ISSN: 0031-9007, 1079-7114. DOI: 10.1103/PhysRevLett.121.056601.

[9] D. M. Callahan, K. A. W. Horowitz, and H. A. Atwater. "Light Trapping in Ultrathin Silicon Photonic Crystal Superlattices with Randomly-Textured Dielectric Incouplers". In: *Opt. Express* 21.25 (2013), p. 30315. ISSN: 1094-4087. DOI: 10.1364/OE.21.030315.

[10] A. Tandaechanurat, S. Ishida, D. Guimard, M. Nomura, S. Iwamoto, and Y. Arakawa. "Lasing Oscillation in a Three-Dimensional Photonic Crystal Nanocavity with a Complete Bandgap". In: *Nat. Photonics* 5.2 (2011), pp. 91–94. ISSN: 1749-4885, 1749-4893. DOI: 10.1038/nphoton.2010.286.

[11] M. Aspelmeyer, T. J. Kippenberg, and F. Marquardt. "Cavity Optomechanics". In: *Rev. Mod. Phys.* 86.4 (2014), pp. 1391–1452. ISSN: 0034-6861, 1539-0756. DOI: 10.1103/RevModPhys.86.1391.

[12] A. F. Koenderink, A. Alu, and A. Polman. "Nanophotonics: Shrinking Light-Based Technology". In: *Science* 348.6234 (2015), pp. 516–521. ISSN: 0036-8075, 1095-9203. DOI: 10.1126/science.1261243.

[13] W. Li and S. Fan. "Nanophotonic Control of Thermal Radiation for Energy Applications". In: *Opt. Express* 26.12 (2018), p. 15995. ISSN: 1094-4087. DOI: 10.1364/OE.26.015995.

[14] J. Wang, F. Sciarrino, A. Laing, and M. G. Thompson. "Integrated Photonic Quantum Technologies". In: *Nat. Photonics* 14.5 (2020), pp. 273–284. ISSN: 1749-4885, 1749-4893. DOI: 10.1038/s41566-019-0532-1.

[15] R. Uppu, M. Adhikary, C. A. M. Harteveld, and W. L. Vos. "Spatially Shaping Waves to Penetrate Deep inside a Forbidden Gap". In: *Phys. Rev. Lett.* 126.17 (2021), p. 177402. ISSN: 0031-9007, 1079-7114. DOI: 10.1103/PhysRevLett.126.177402.

[16] F. Arceri and E. I. Corwin. "Vibrational Properties of Hard and Soft Spheres Are Unified at Jamming". In: *Phys. Rev. Lett.* 124.23 (2020), p. 238002. ISSN: 0031-9007, 1079-7114. DOI: 10.1103/PhysRevLett.124.238002.

[17] K. Busch, G. von Freymann, S. Linden, S. Mingaleev, L. Tkeshelashvili, and M. Wegener. "Periodic Nanostructures for Photonics". In: *Phys. Rep.* 444.3-6 (2007), pp. 101–202. ISSN: 03701573. DOI: 10.1016/j.physrep.2007.02.011.

[18] L. A. Woldering, A. P. Mosk, and W. L. Vos. "Design of a Three-Dimensional Photonic Band Gap Cavity in a Diamondlike Inverse Woodpile Photonic Crystal". In: *Phys. Rev. B* 90.11 (2014), p. 115140. DOI: 10.1103/PhysRevB.90.115140.

[19] S. A. Hack, J. J. W. van der Vegt, and W. L. Vos. "Cartesian Light: Unconventional Propagation of Light in a Three-Dimensional Superlattice of Coupled Cavities within a Three-Dimensional Photonic Band Gap". In: *Phys. Rev. B* 99.11 (2019), p. 115308. ISSN: 2469-9950, 2469-9969. DOI: 10.1103/PhysRevB.99.115308.

[20] E. N. Economou. *The Physics of Solids*. Graduate Texts in Physics. Berlin, Heidelberg: Springer Berlin Heidelberg, 2010. ISBN: 978-3-642-02068-1 978-3-642-02069-8. DOI: 10.1007/978-3-642-02069-8.

[21] G. Shao. "Electronic Structures of Manganese-Doped Rutile TiO $_2$ from First Principles". In: *J. Phys. Chem. C* 112.47 (2008), pp. 18677–18685. ISSN: 1932-7447, 1932-7455. DOI: 10.1021/jp8043797.

[22] C. Pashartis and O. Rubel. "Localization of Electronic States in III-V Semiconductor Alloys: A Comparative Study". In: *Phys. Rev. Appl.* 7.6 (2017), p. 064011. ISSN: 2331-7019. DOI: 10.1103/PhysRevApplied.7.064011.

[23] C. Pashartis and O. Rubel. "Alloying Strategy for Two-Dimensional GaN Optical Emitters". In: *Phys. Rev. B* 96.15 (2017), p. 155209. ISSN: 2469-9950, 2469-9969. DOI: 10.1103/PhysRevB.96.155209.

[24] J. Zhang, C.-Z. Wang, Z. Z. Zhu, and V. V. Dobrovitski. "Vibrational Modes and Lattice Distortion of a Nitrogen-Vacancy Center in Diamond from First-Principles Calculations". In: *Phys. Rev. B* 84.3 (2011), p. 035211. ISSN: 1098-0121, 1550-235X. DOI: 10.1103/PhysRevB.84.035211.

[25] S. O. Demokritov, ed. *Spin Wave Confinement: Propagating Waves*. Second edition. Singapur: Pan Stanford Publishing, 2017. ISBN: 978-981-4774-35-2 978-1-315-11082-0.

[26] E. V. Tartakovskaya, M. Pardavi-Horvath, and R. D. McMichael. "Spin-Wave Localization in Tangentially Magnetized Films". In: *Phys. Rev. B* 93.21 (2016), p. 214436. ISSN: 2469-9950, 2469-9969. DOI: 10.1103/PhysRevB.93.214436.

[27] E. Krioukov, D. J. W. Klunder, A. Driessen, J. Greve, and C. Otto. "Sensor Based on an Integrated Optical Microcavity". In: *Opt. Lett.* 27.7 (2002), pp. 512–514. ISSN: 1539-4794. DOI: 10.1364/OL.27.000512.

[28] T. Baba. "Slow Light in Photonic Crystals". In: *Nat. Photonics* 2.8 (2008), pp. 465–473. ISSN: 1749-4893. DOI: 10.1038/nphoton.2008.146.

[29] S. Noda, A. Chutinan, and M. Imada. "Trapping and Emission of Photons by a Single Defect in a Photonic Bandgap Structure". In: *Nature* 407.6804 (2000), pp. 608–610. ISSN: 1476-4687. DOI: 10.1038/35036532.

[30] J. M. Gérard, B. Sermage, B. Gayral, B. Legrand, E. Costard, and V. Thierry-Mieg. "Enhanced Spontaneous Emission by Quantum Boxes in a Monolithic Optical Microcavity". In: *Phys. Rev. Lett.* 81.5 (1998), pp. 1110–1113. DOI: 10.1103/PhysRevLett.81.1110.

[31] P. Michler, ed. *Single Quantum Dots: Fundamentals, Applications, and New Concepts*. Topics in Applied Physics v. 90. Berlin, Heidelberg, New York: Springer-Verlag, 2003. ISBN: 978-3-540-14022-1.

[32] J. P. Reithmaier, G. Sęk, A. Löffler, C. Hofmann, S. Kuhn, S. Reitzenstein, L. V. Keldysh, V. D. Kulakovskii, T. L. Reinecke, and A. Forchel. "Strong Coupling in a Single Quantum Dot–Semiconductor Microcavity System". In: *Nature* 432.7014 (2004), pp. 197–200. ISSN: 1476-4687. DOI: 10.1038/nature02969.

[33] T. Yoshie, A. Scherer, J. Hendrickson, G. Khitrova, H. M. Gibbs, G. Rupper, C. Ell, O. B. Shchekin, and D. G. Deppe. "Vacuum Rabi Splitting with a Single Quantum Dot in a Photonic Crystal Nanocavity". In: *Nature* 432.7014 (2004), pp. 200–203. ISSN: 1476-4687. DOI: 10.1038/nature03119.

[34] E. Peter, P. Senellart, D. Martrou, A. Lemaître, J. Hours, J. M. Gérard, and J. Bloch. "Exciton-Photon Strong-Coupling Regime for a Single Quantum Dot Embedded in a Microcavity". In: *Phys. Rev. Lett.* 95.6 (2005), p. 067401. DOI: 10.1103/PhysRevLett.95.067401.

[35] P. Russell, E. Marin, A. Diez, S. Guenneau, and A. Movchan. "Sonic Band Gaps in PCF Preforms: Enhancing the Interaction of Sound and Light". In: *Opt. Express* 11.20 (2003), p. 2555. ISSN: 1094-4087. DOI: 10.1364/OE.11.002555.

[36] O. Painter, R. K. Lee, A. Scherer, A. Yariv, J. D. O'Brien, P. D. Dapkus, and I. Kim. "Two-Dimensional Photonic Band-Gap Defect Mode Laser". In: *Science* 284.5421 (1999), pp. 1819–1821. ISSN: 0036-8075, 1095-9203. DOI: 10.1126/science.284.5421.1819.

[37] C. Sauvan, J. P. Hugonin, I. S. Maksymov, and P. Lalanne. "Theory of the Spontaneous Optical Emission of Nanosize Photonic and Plasmon Resonators". In: *Phys. Rev. Lett.* 110.23 (2013), p. 237401. ISSN: 0031-9007, 1079-7114. DOI: 10.1103/PhysRevLett.110.237401.

[38] P. T. Kristensen, R.-C. Ge, and S. Hughes. "Normalization of Quasinormal Modes in Leaky Optical Cavities and Plasmonic Resonators". In: *Phys. Rev. A* 92.5 (2015), p. 053810. ISSN: 1050-2947, 1094-1622. DOI: 10.1103/PhysRevA.92.053810.

[39] E. A. Muljarov and W. Langbein. "Exact Mode Volume and Purcell Factor of Open Optical Systems". In: *Phys. Rev. B* 94.23 (2016), p. 235438. ISSN: 2469-9950, 2469-9969. DOI: 10.1103/PhysRevB.94.235438.

[40] R. G. S. El-Dardiry, S. Faez, and A. Lagendijk. "Snapshots of Anderson Localization beyond the Ensemble Average". In: *Phys. Rev. B* 86.12 (2012), p. 125132. ISSN: 1098-0121, 1550-235X. DOI: 10.1103/PhysRevB.86.125132.

[41] K. J. Vahala. "Optical Microcavities". In: *Nature* 424.6950 (2003), pp. 839–846. ISSN: 1476-4687. DOI: 10.1038/nature01939.

[42] H. Aoki. "Critical Behaviour of Extended States in Disordered Systems". In: *J. Phys. C: Solid State Phys.* 16.6 (1983), pp. L205–L208. ISSN: 0022-3719. DOI: 10.1088/0022-3719/16/6/007.

[43] M. Janssen. "Statistics and Scaling in Disordered Mesoscopic Electron Systems". In: *Phys. Rep.* 295.1-2 (1998), pp. 1–91. ISSN: 03701573. DOI: 10.1016/S0370-1573(97)00050-1.

[44] S. Faez, A. Strybulevych, J. H. Page, A. Lagendijk, and B. A. van Tiggelen. "Observation of Multifractality in Anderson Localization of Ultrasound". In: *Phys. Rev. Lett.* 103.15 (2009), p. 155703. ISSN: 0031-9007, 1079-7114. DOI: 10.1103/PhysRevLett.103.155703.

[45] M. Kozoň, A. Lagendijk, M. Schlottbom, J. J. W. van der Vegt, and W. L. Vos. "Scaling Theory of Wave Confinement in Classical and Quantum Periodic Systems". In: *Phys. Rev. Lett.* 129.17 (2022), p. 176401. ISSN: 0031-9007, 1079-7114. DOI: 10.1103/PhysRevLett.129.176401.

[46] E. Abrahams, P. W. Anderson, D. C. Licciardello, and T. V. Ramakrishnan. "Scaling Theory of Localization: Absence of Quantum Diffusion in Two Dimensions". In: *Phys. Rev. Lett.* 42.10 (1979), pp. 673–676. ISSN: 0031-9007. DOI: 10.1103/PhysRevLett.42.673.

[47] P. Sheng. *Introduction to Wave Scattering, Localization, and Mesoscopic Phenomena*. 2nd ed. Springer Series in Materials Science 88. Berlin; New York: Springer, 2006. ISBN: 978-3-540-29155-8.

[48] K. Slevin, P. Markoš, and T. Ohtsuki. "Reconciling Conductance Fluctuations and the Scaling Theory of Localization". In: *Phys. Rev. Lett.* 86.16 (2001), pp. 3594–3597. ISSN: 0031-9007, 1079-7114. DOI: 10.1103/PhysRevLett.86.3594.

[49] W. L. Bragg and E. J. Williams. "The Effect of Thermal Agitation on Atomic Arrangement in Alloys". In: *Proc. R. Soc. Lond. A* 145.855 (1934), pp. 699–730. ISSN: 0950-1207, 2053-9150. DOI: 10.1098/rspa.1934.0132.

[50] H. A. Bethe. "Statistical Theory of Superlattices". In: *Proc. R. Soc. Lond. A* 150.871 (1935), pp. 552–575. ISSN: 0080-4630, 2053-9169. DOI: 10.1098/rspa.1935.0122.

[51] H. T. Grahn, ed. *Semiconductor Superlattices: Growth and Electronic Properties*. Singapore ; River Edge, NJ: World Scientific, 1995. ISBN: 978-981-02-2061-7.

[52] T. Ando, A. B. Fowler, and F. Stern. "Electronic Properties of Two-Dimensional Systems". In: *Rev. Mod. Phys.* 54.2 (1982), pp. 437–672. ISSN: 0034-6861. DOI: 10.1103/RevModPhys.54.437.

[53] D. Nardi, F. Banfi, C. Giannetti, B. Revaz, G. Ferrini, and F. Parmigiani. "Pseudosurface Acoustic Waves in Hypersonic Surface Phononic Crystals". In: *Phys. Rev. B* 80.10 (2009), p. 104119. ISSN: 1098-0121, 1550-235X. DOI: 10.1103/PhysRevB.80.104119.

[54] B. Huang and H. Lee. "Defect and Impurity Properties of Hexagonal Boron Nitride: A First-Principles Calculation". In: *Phys. Rev. B* 86.24 (2012), p. 245406. ISSN: 1098-0121, 1550-235X. DOI: 10.1103/PhysRevB.86.245406.

[55] P. Kratzer and J. Neugebauer. "The Basics of Electronic Structure Theory for Periodic Systems". In: *Front. Chem.* 7:106 (2019). ISSN: 2296-2646. DOI: 10.3389/fchem.2019.00106.

[56] G. Kresse and J. Furthmüller. "Efficiency of Ab-Initio Total Energy Calculations for Metals and Semiconductors Using a Plane-Wave Basis Set". In: *Comput. Mater. Sci.* 6.1 (1996), pp. 15–50. ISSN: 09270256. DOI: 10.1016/0927-0256(96)00008-0.

[57] K. M. Ho, C. T. Chan, C. M. Soukoulis, R. Biswas, and M. Sigalas. "Photonic Band Gaps in Three Dimensions: New Layer-by-Layer Periodic Structures". In: *Solid State Commun.* 89.5 (1994), pp. 413–416. ISSN: 0038-1098. DOI: 10.1016/0038-1098(94)90202-X.

[58] D. Devashish, O. S. Ojambati, S. B. Hasan, J. J. W. van der Vegt, and W. L. Vos. "Three-Dimensional Photonic Band Gap Cavity with Finite Support: Enhanced Energy Density and Optical Absorption". In: *Phys. Rev. B* 99.7 (2019), p. 075112. ISSN: 2469-9950, 2469-9969. DOI: 10.1103/PhysRevB.99.075112.

[59] S. G. Johnson and J. D. Joannopoulos. "Block-Iterative Frequency-Domain Methods for Maxwell's Equations in a Planewave Basis". In: *Opt. Express* 8.3 (2001), p. 173. ISSN: 1094-4087. DOI: 10.1364/OE.8.000173.

[60] S. Mukherjee, A. Spracklen, D. Choudhury, N. Goldman, P. Öhberg, E. Andersson, and R. R. Thomson. "Observation of a Localized Flat-Band State in a Photonic Lieb Lattice". In: *Phys. Rev. Lett.* 114.24 (2015), p. 245504. ISSN: 0031-9007, 1079-7114. DOI: 10.1103/PhysRevLett.114.245504.

[61] D. Leykam, A. Andreanov, and S. Flach. "Artificial Flat Band Systems: From Lattice Models to Experiments". In: *Adv. Phys.: X* 3.1 (2018), p. 1473052. ISSN: 2374-6149. DOI: 10.1080/23746149.2018.1473052.

[62] K. Wang, S. David, A. Chelnokov, and J. M. Lourtioz. "Photonic Band Gaps in Quasicrystal-Related Approximant Structures". In: *J. Mod. Opt.* 50.13 (2003), pp. 2095–2105. ISSN: 0950-0340, 1362-3044. DOI: 10.1080/09500340308235260.

[63] D. N. Chigrin and A. V. Lavrinenko. "Photonic Applications of Two-Dimensional Quasicrystals". In: *Applications of Metamaterials*. Ed. by F. Capolino. Boca Raton, FL: CRC Press, 2009. ISBN: 978-1-4200-5423-1.

[64] 10.5281/zenodo.6783107.

[65] W. Dörfler. "Photonic Bandstructure Calculations". In: *Photonic Crystals: Mathematical Analysis and Numerical Approximation*. Oberwolfach Seminars 42. Basel: Springer Basel, 2011. ISBN: 978-3-0348-0112-6 978-3-0348-0113-3.

[66] W. Ku, T. Berlijn, and C.-C. Lee. "Unfolding First-Principles Band Structures". In: *Phys. Rev. Lett.* 104.21 (2010), p. 216401. ISSN: 0031-9007, 1079-7114. DOI: 10.1103/PhysRevLett.104.216401.

[67] S. G. Mayo, F. Yndurain, and J. M. Soler. "Band Unfolding Made Simple". In: *J. Phys. Condens. Matter* 32.20 (2020), p. 205902. ISSN: 0953-8984, 1361-648X. DOI: 10.1088/1361-648X/ab6e8e.

[68] K. Busch, S. F. Mingaleev, A. Garcia-Martin, M. Schillinger, and D. Hermann. "The Wannier Function Approach to Photonic Crystal Circuits". In: *J. Phys.: Condens. Matter* 15.30 (2003), R1233–R1256. ISSN: 0953-8984, 1361-648X. DOI: 10.1088/0953-8984/15/30/201.

[69] N. Marzari, A. A. Mostofi, J. R. Yates, I. Souza, and D. Vanderbilt. "Maximally Localized Wannier Functions: Theory and Applications". In: *Rev. Mod. Phys.* 84.4 (2012), pp. 1419–1475. ISSN: 0034-6861, 1539-0756. DOI: 10.1103/RevModPhys.84.1419.

[70] N. Hurley and S. Rickard. "Comparing Measures of Sparsity". In: *IEEE Trans. Inform. Theory* 55.10 (2009), pp. 4723–4741. ISSN: 0018-9448, 1557-9654. DOI: 10.1109/TIT.2009.2027527.

[71] J. P. Perdew, K. Burke, and M. Ernzerhof. "Generalized Gradient Approximation Made Simple". In: *Phys. Rev. Lett.* 77.18 (1996), pp. 3865–3868. ISSN: 0031-9007, 1079-7114. DOI: 10.1103/PhysRevLett.77.3865.

[72] G. Kresse and D. Joubert. "From Ultrasoft Pseudopotentials to the Projector Augmented-Wave Method". In: *Phys. Rev. B* 59.3 (1999), pp. 1758–1775. ISSN: 0163-1829, 1095-3795. DOI: 10.1103/PhysRevB.59.1758.

[73] R. Hillebrand, S. Senz, W. Hergert, and U. Gösele. "Macroporous-Silicon-Based Three-Dimensional Photonic Crystal with a Large Complete Band Gap". In: *J. Appl. Phys.* 94.4 (2003), pp. 2758–2760. ISSN: 0021-8979, 1089-7550. DOI: 10.1063/1.1593796.

[74] M. D. Leistikow, A. P. Mosk, E. Yeganegi, S. R. Huisman, A. Lagendijk, and W. L. Vos. "Inhibited Spontaneous Emission of Quantum Dots Observed in a 3D Photonic Band Gap". In: *Phys. Rev. Lett.* 107.19 (2011), p. 193903. ISSN: 0031-9007, 1079-7114. DOI: 10.1103/PhysRevLett.107.193903.

[75] W. Setyawan and S. Curtarolo. "High-Throughput Electronic Band Structure Calculations: Challenges and Tools". In: *Comput. Mater. Sci.* 49.2 (2010), pp. 299–312. ISSN: 09270256. DOI: 10.1016/j.commatsci.2010.05.010.

[76] L. F. Richardson and J. A. Gaunt. "VIII. The Deferred Approach to the Limit". In: *Phil. Trans. R. Soc. Lond. A* 226.636-646 (1927), pp. 299–361. ISSN: 0264-3952, 2053-9258. DOI: 10.1098/rsta.1927.0008.

3 Machine Learning for Wave Confinement Analysis

3.1 Introduction

Completely controlling wave propagation in periodic media is a key challenge that is essential for a large variety of applications [1–15]. An especially interesting type of control is wave confinement achieved by introducing disorder and functional defects into an otherwise periodic medium. The interference of waves in such an altered structure may result in a strong concentration of the energy density inside a small sub-volume of the medium. Wave confinement has been investigated for different types of waves and in various settings, *e.g.*, classical mechanics [16], photonics [9, 10, 17–19], solid state physics [20–24], or magnonics [25, 26]. Its applications include sensors, controlled spontaneous emission, and enhanced interactions between hybrid wave-types such as sound and light [27–35].

Recently, we have described a rigorous method of determining confinement of waves in periodic media with defects and in superlattices in general [36]. We first introduced a so-called confinement dimensionality, quantifying the intuitive term of "confinement" and then proceeded to develop a scaling theory to determine confinement dimensionality of every band in a given system. This scaling theory is valid for any type of physical wave (acoustic, electromagnetic, electronic, spin, *etc.*), in both quantum and classical setting, and for systems in any dimension, and is readily usable in computer algorithms.

Nevertheless, the theory of Ref. [36] requires, for every investigated superlattice, a smaller *reference* superlattice, so that one can observe the scaling behavior of the key quantities when changing the supercell size. Generally, obtaining the data for the reference supercell is significantly less computationally demanding than performing the calculations for the investigated supercell of interest. On the other hand, this requirement for a reference supercell makes the scaling approach of Ref. [36] inapplicable in case the reference supercell is not available for any reason. Furthermore, the scaling theory is exact only in the case of infinitely large supercells and thus for experimentally relevant small supercells inaccuracies may occur, as also described by Ref. [36]. Since the reference supercell is smaller than the investigated one, it is clear that eliminating the reference supercell from the confinement determination provides an immediate advantage in terms of accuracy of the scaling method.

Assigning the confinement dimensionality to each band in a spectrum is a typical classification task, which is among the most typical problems solved by unsupervised machine learning [37, 38]. A prominent approach within unsuper-

vised learning are clustering algorithms, which aim to partition the dataset into several clusters in such a way that "similar" data points are grouped together in the same cluster [39, 40].

In this chapter[1], we investigate the application of clustering algorithms to improve the precision of confinement identification for small supercells. Specifically, we employ two clustering algorithms to partition the bands of interest in the two-dimensional parameter space of mode volume and confinement energy, so that each resulting cluster corresponds to a specific value of confinement dimensionality. First is the well-known k-means algorithm [42] with improved initialization [43], which measures the "similarity" between the bands by their distance in the parameter space. This is a standard algorithm, which, however, does not take into account any specific physical properties of our system and, as we show, this results in lesser accuracy in some cases. Alternatively, we implement our own model-based clustering algorithm (MBC), which uniquely merges clustering with the physical model behind the wave confinement, measuring the "similarity" between the bands by their distance from the scaling curves predicted by Ref. [36]. The MBC algorithm shows improved accuracy in the cases where k-means fails.

We conclude that, even though the clustering approach brings specific complications on its own, it can be used to enhance the precision of confinement identification for small supercells, especially if used in addition to the directly applied scaling method of Ref. [36]. In terms of computational complexity, the additional clustering step is negligible, taking mere seconds for the cases presented in this chapter.

The remainder of this chapter is organized as follows: The second section of this chapter contains definitions of crucial terms and a brief review of scaling theory of wave confinement. In the third section, we reformulate the scaling equation for wave confinement into a more machine-learning friendly form. The fourth section deals with the evaluation of the accuracy of the clustering algorithms, while in the fifth section we describe our model-based clustering algorithm. In the sixth section, we compare the performance of the k-means clustering algorithm, our MBC algorithm, and the standard scaling approach using a reference supercell.

3.2 Superlattices and scaling

Superimposing a periodic lattice of defects on another underlying crystal lattice gives rise to a so-called superlattice [36]. A unit cell of such a superlattice is called a supercell. Fig. 3.1 depicts supercells containing various types of defects. This is a traditional model for, *e.g.*, defects in periodic materials. A supercell of linear size N in a D-dimensional system contains N^D unit cells. A defect of dimensionality d can confine waves in $c = D - d$ dimensions, as illustrated in Fig. 3.1. The number c is referred to as confinement dimensionality.

Ref. [36] has recently developed a general scaling theory of wave confinement. This method relies on the confinement quantity $W(\mathbf{r})$ as an input. This quantity

[1] This work is building upon the bachelor thesis of R. Schrijver [41].

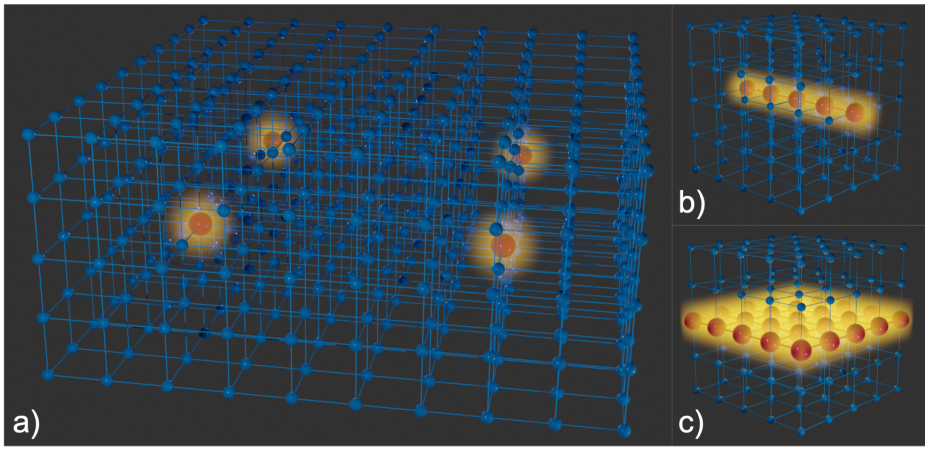

Figure 3.1: Illustration of supercells containing various defects. Blue spheres represent unperturbed unit cells, red spheres correspond to defect unit cells and confined waves are depicted in yellow. (a) Four supercells containing point defects. (b) Supercell containing a line defect. (c) Supercell containing a plane defect.

depends on the investigated system and represents what is intuitively understood as confinement. It can be, *e.g.*, the energy density in photonic systems, or the charge density in electronic systems. From $W(\mathbf{r})$, two other quantities are calculated; the relative confinement energy

$$\widetilde{E} = E_{\mathrm{C}} := \frac{\int_{V_{\mathrm{C}}} W(\mathbf{r})\mathrm{d}V}{E_{\mathrm{S}}}, \tag{3.1}$$

and the relative mode volume

$$\widetilde{V} = V_{\mathrm{M}} := \frac{\int_{V_{\mathrm{C}}} W(\mathbf{r})\mathrm{d}V}{V_{\mathrm{S}} \max\limits_{\mathbf{r}\in V_{\mathrm{S}}}\{W(\mathbf{r})\}}. \tag{3.2}$$

In the above, V_{S} is the supercell volume and V_{C} a specific integration volume, usually chosen so that it contains a part of the defect. The quantity E_{S} represents the total energy in the supercell. The quantities defined by Eqs. (3.1) and (3.2) have the following scaling behavior in the limit $N \to \infty$:

$$\widetilde{V} = AN^{-c}, \qquad \widetilde{E} = BN^{c-D}, \tag{3.3}$$

with A, B constants that are independent of N.

Ref. [36] and Chapter 2 of this PhD thesis show that by observing the scaling behavior of the combined quantity

$$\frac{\widetilde{V}^{\alpha}}{\widetilde{E}} = CN^{\kappa} \tag{3.4}$$

with respect to the supercell size N, for judiciously chosen auxiliary powers α, one can determine the confinement dimensionality c for each band of states of a

given system. Here, the constant $C = A^{\alpha}/B$ is *a priori* unknown and may depend on various system parameters and the specific investigated band. Although this scaling approach is rigorously valid only for sufficiently large N, it has been observed in [36] that it works for several smaller systems as well, which is unusual for scaling theories. However, the method sometimes also yielded unphysical results for some bands in these small supercells, necessitating critical evaluation of the results.

In this chapter, we present an alternative scaling approach and employ machine learning algorithms to enhance the precision of the method of Ref [36] and Chapter 2 of this PhD thesis. Although this approach introduces an additional step in the confinement analysis, this step is computationally cheap and, as we show, it can improve the accuracy of the results for small supercells. Moreover the clustering analysis still maintains its wide range of applicability to different physical systems introduced.

3.3 Machine-learning approach to scaling

Instead of combining the quantities in Eqs. (3.1) and (3.2) into the ratio (3.4), one can express the mode volume as a function of confinement energy, in the limit $N \to \infty$:

$$\widetilde{V} = \widetilde{C}\widetilde{E}^{\frac{-c}{c-D}}, \tag{3.5}$$

where

$$\widetilde{C} = \frac{A}{B^{\frac{-c}{c-D}}}. \tag{3.6}$$

Eq. (3.5) represents a different form of scaling behavior than Eq. (3.4), this time with respect to $\widetilde{E}$. Of course, from Eq. (3.3), it is clear that $\widetilde{E}$ also changes with the system size N.

The band behavior based on Eq. (3.5) is graphically illustrated in Fig. 3.2. For small supercell sizes N, the bands are more or less concentrated in the upper right corner with relatively high $\widetilde{E}$ and $\widetilde{V}$. As the supercell size increases, the bands start to follow a path corresponding to their confinement dimensionality c. Eventually, bands with the same c form clusters as depicted in Fig. 3.2. The bands in a D dimensional system will form at most $D+1$ clusters, corresponding to all possible values of the confinement dimensionality c.

The immediate advantage of this approach compared to the one presented in Ref. [36] and Chapter 2 is that this method does not require a smaller reference supercell, but one can directly analyze which bands belong to which cluster for the supercell size of interest. Nevertheless, since Eq. (3.5) strictly holds only for $N \to \infty$, the clusters will be clearly distinguishable only for sufficiently large supercells. In both computations and experiments, one is realistically constrained to relatively low N and it thus may become difficult to distinguish the clusters from each other. To improve the accuracy of confinement determination, we suggest the employment of a clustering algorithm, which divides the data into clusters quantitatively and automatically.

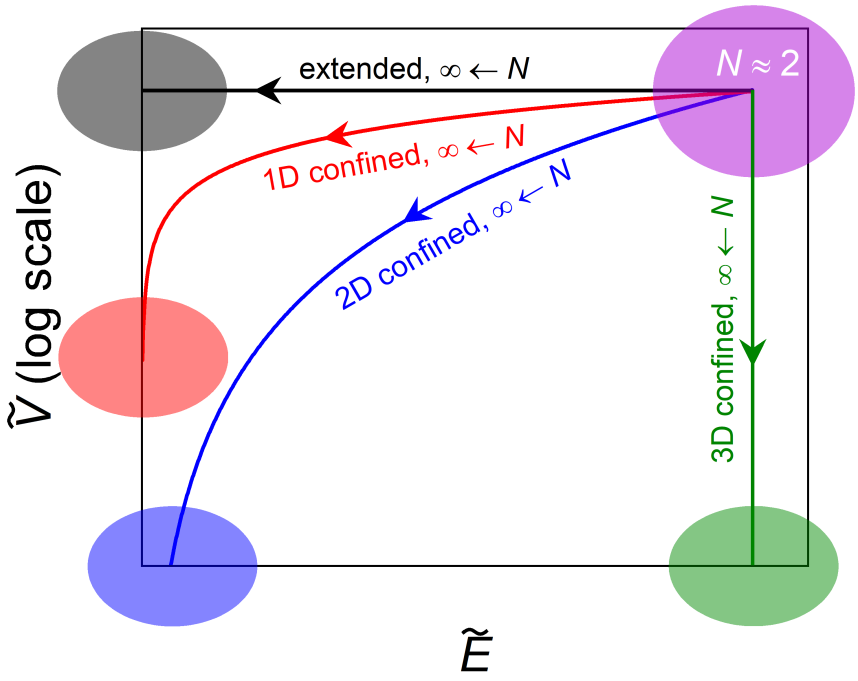

Figure 3.2: Schematic of the scaling behavior of the bands according to Eq. (3.5). Mode volume versus the confinement energy. For small supercell size N all the bands are grouped together, but, for larger N, they spread over the parameter space, forming clusters in accordance with their confinement dimensionality c.

Data clustering is one of the staple problems of machine learning techniques [37, 38] and it can thus be reasonably expected that such techniques could enhance the precision of confinement identification. In order to formulate the band confinement identification as a clustering problem, we define, for a given supercell size N, the dataset $\mathcal{X}_{N,0} \in \mathbb{R}^{M_N \times 2}$, containing the logarithm of mode volumes $\log \widetilde{V}_i$ and the confinement energies $\widetilde{E}_i$ for each band $i = 1, \ldots, M_N$, where M_N is the total number of bands for the corresponding supercell. To ensure that both $\log_{10} \widetilde{V}_i$ and $\widetilde{E}_i$ are treated with equal importance and thus neither of them dominates the clustering, we renormalize the data once again, so that both variables have the same range of values, prior to the clustering. The renormalization is performed for each dataset separately as follows:

$$\mathcal{E}_i = \frac{\widetilde{E}_i}{\max\limits_{1 \leq j \leq M_N} \left\{ \widetilde{E}_j \right\} - \min\limits_{1 \leq j \leq M_N} \left\{ \widetilde{E}_j \right\}}, \tag{3.7}$$

$$\mathcal{V}_i = \frac{\log_{10} \widetilde{V}_i}{\max\limits_{1\leq j\leq M_N} \left\{\log_{10} \widetilde{V}_j\right\} - \min\limits_{1\leq j\leq M_N} \left\{\log_{10} \widetilde{V}_j\right\}}. \tag{3.8}$$

The normalized dataset used for the clustering is thus $\mathcal{X}_N = \{\mathbf{x}_i \coloneqq (\mathcal{E}_i, \mathcal{V}_i) \,|\, i = 1, \ldots, M_N\}$.

The goal of a clustering algorithm is to subdivide the data in $\mathcal{X}_N$ among K clusters, such that "similar" data points are assigned to the same cluster $C_k = \{\mathbf{x}_j^k \,|\, j = 1, \ldots, M_k\}$, where $k = 1, \ldots, K$. In total, each cluster will contain $M_k \geq 1$ data points, such that $\sum_{k=1}^{K} M_k = M$. We refer to the specific distribution of the data points within the clusters as a *partition*, denoting it as $\mathcal{C}_K = \{C_1, \ldots, C_K\}$. The centroid $\mathbf{c}_k$ of the cluster C_k is defined as the mean of its constituent points, *i.e.*, $\mathbf{c}_k = (\sum_{j=1}^{M_k} \mathbf{x}_j^k)/M_k$. We denote the set of all possible partitions of the dataset $\mathcal{X}_N$ into K clusters as $\mathcal{P}_K$.

In this chapter we explore two different ways of clustering the data for the purpose of confinement identification: A standard k-means++ algorithm implemented in the Python library *scikit-learn* [44] and our own MBC algorithm utilizing the physical insight to perform the clustering. Each of them utilizes a slightly different notion of what it means for two data points to be "similar", and therefore employs a different approach to obtain the resulting partition, as we will describe below.

3.3.1 The k-means++ algorithm

The standard and most well-known clustering algorithm is the k-means algorithm [42], which considers two data points to be "similar" if their Euclidean distance in the data space is small. Therefore, it aims to group such points together in one cluster. Within a given partition $\mathcal{C}_K$, this notion of similarity can be measured via the cost function $\Psi : \mathcal{P}_K \to \mathbb{R}$ representing the sum of distances of each data point from the centroid of its cluster:

$$\Psi(\mathcal{C}_K) \coloneqq \sum_{k=1}^{K} \sum_{\mathbf{x}\in C_k} \|\mathbf{x} - \mathbf{c}_k\|^2, \tag{3.9}$$

where $\|\cdot\|$ denotes the Euclidean norm. The k-means algorithm aims to minimize the cost function Ψ over all possible partitions. The partition $\tilde{\mathcal{C}}_K$, for which Ψ attains its minimum is considered the best partition of the dataset:

$$\Psi(\tilde{\mathcal{C}}_K) \coloneqq \min_{\mathcal{C}_K\in\mathcal{P}_K} \Psi(\mathcal{C}_K). \tag{3.10}$$

The k-means algorithm is summarized in Algorithm 1.

Algorithm 1 will always converge to a local minimum of the cost function Ψ (see Ref. [45]). There is, however, a likelihood that this local minimum does not coincide with the global minimum. As a result, the output of the algorithm may depend on the specific initialisation choice.

Algorithm 1 k-means algorithm

Input: Data array $\mathcal{X}_N \subset \mathbb{R}^2$, number of clusters $K \in \mathbb{N}$

Output: Division of the data into K clusters corresponding to various confinement dimensionalities c, such that the cost function Ψ is minimized.

1. Arbitrarily select the initial centroids $\mathbf{c}_k$ for each $k = 1, \ldots, K$.

2. Assign each data point $\mathbf{x}_i \in \mathcal{X}_N$ to its nearest centroid using the Euclidean metric. In case of equality of the nearest centroids, the data point is assigned to either cluster.

3. Recalculate the centroid of each cluster as the mean of all its constituent data points.

4. Repeat the steps 2 and 3 with the new centroids until the termination criterion (usually certain degree of convergence) is reached.

One can improve the probability of reaching the global minimum by applying the algorithm multiple times with different random initializations and choosing the result with the smallest cost function Ψ. Alternatively, one can choose a more sophisticated method of the cluster centroid initialization, as described by the k-means++ algorithm [43]. Here, instead of choosing the initial centroids in Step 1 of Algorithm 1 at random, we choose the first centroid randomly from the dataset $\mathcal{X}_N$, with a uniform probability distribution. Then, we continue to choose each subsequent centroid $\mathbf{c}_k, 1 < k \leq K$ randomly from the dataset $\mathcal{X}_N$ with the adjusted probability distribution

$$P_k(\mathbf{x}) = \frac{D_k^2(\mathbf{x})}{\sum_{\mathbf{x}' \in \mathcal{X}_N} D_k^2(\mathbf{x}')}, \tag{3.11}$$

where

$$D_k(\mathbf{x}) = \min_{1 \leq j < k} \{\|\mathbf{x} - \mathbf{c}_j\|\} \tag{3.12}$$

is the shortest distance of the point $\mathbf{x}$ to the closest centroid that has already been determined. The remaining part of the k-means++ algorithm is the same as for the standard k-means algorithm, described in Algorithm 1.

3.4 Clustering accuracy

Clustering of the bands based on their confinement dimensionality is complicated by the fact that there is no known ground truth, *i.e.*, there is no reference solution against which we can assess the accuracy of the clustering process and evaluate its validity. This is an important hurdle for the clustering approach, since the k-means++ algorithm requires the number of clusters K as an input,

which is, however, not known *a priori*. One can, of course, run the algorithms for all possible values of K, but how can we determine that we have found the correct number of clusters? Since the cost function Ψ defined by Eq. (3.9) is, by definition, a decreasing function of cluster numbers, it cannot be used to determine the correct K. We therefore need another type of clustering accuracy measure and this is where the concept of cluster validity indices (CVIs) comes into play.

Cluster validity indices, as the name implies, are quantitative measures to determine the validity of the clustering results. A plethora of CVIs has been proposed in the literature, employing various approaches to measuring the clustering accuracy [46]. Based on the definition of each CVI, better clustering results correspond to either lower or higher values of the index and thus the most accurate clustering out of a set of results is the one achieving the optimum of the CVI, *i.e.*, either the minimum or the maximum.

CVIs can be divided into two categories in a rather straightforward manner: external indices, comparing the clustering result against the ground truth, and internal indices, analyzing only the partitioned data without the need for any external information [47]. It is clear that for our purposes we are interested in the CVIs of the internal type. Most CVIs measure *cluster cohesion* and *cluster separation* of the data, in some sense. Cluster cohesion describes to what extent the entities inside a cluster are alike, whereas cluster separation evaluates how well different clusters are separated.

The behaviour of the CVIs largely depends on the context and the setting [46]. This is why numerical tests have to be conducted to convincingly select the CVI providing the correct measure of accuracy in the given context [46]. This obviously also applies to clustering for wave-confinement analysis. Therefore, in this section, we perform analysis of selected CVIs, in order to find the ultimate clustering accuracy measure for our specific problem.

3.4.1 Methodology

In order to limit the number of CVIs to be tested, we pick five of the best-performing CVIs from the review in Ref. [46]. These are the Silhouette coefficient (Sil), the Calinski-Harabasz (CH), the Davies-Bouldin(DB) including its slight variation (DB*), the COP and the S_Dbw indices. Sil, CH, and DB were implemented via the package library *scikit-learn*, S_Dbw was implemented via the package library *S_Dbw*, and DB* and COP were implemented directly by ourselves. For the overview of the CVIs and their definitions, see Appendix 3.B.

The testing procedure was executed in an identical fashion for each CVI. As the reference system we used a 3D inverse woodpile photonic band gap crystal with two proximate defects [48], described in detail in Appendix 3.A and Chapter 1 of this PhD thesis. Specifically, we employ the well-researched structure with regular pores of radius $R = 0.24a$, with a being the lattice parameter, and defect pores of radius $R' = 0.5R$ [18, 19, 49]. This system represents a suitable model due to its relatively complex arrangement of linear defects, creating a cavity at their crossover. We know that, as a result, the system exhibits extended

($c = 0$), line-confined ($c = 2$), and point-confined ($c = 3$) bands which need to be distinguished, corresponding to the total number of $K = 3$ clusters. On the other hand, we know from physics that the system does not support plane-confined ($c = 1$) bands and those should therefore not appear in the correct clustering result. We employ the range of supercell sizes $N = 2, 3, 4$, exhausting what is feasible in a reasonable computing time. For every supercell size N, we used the plane-wave expansion method implemented via the well-known MPB code [50] to obtain the values of mode volume and energy density for each band.

To find the CVI that provides the best accuracy measure, we run the clustering algorithm for various total number of clusters K and subsequently compute the value of each CVI for that partition. The global optimum (minimum or maximum, depending on the CVI definition) should then be attained for the correct number of clusters $K = 3$. For this analysis, we choose the range of $K = 2, \ldots, 25$. This range exceeds the number of clusters expected in the context of wave confinement, but such a broad range of values may provide additional information on the accuracy of the CVIs. Note that we do not use $K = 1$ since the value of the CVIs is not defined for only one cluster, see their definitions in Appendix 3.B. It is important to note that the choice of clustering algorithm should not affect the CVI performance, since CVIs only evaluate the intrinsic clustering outcome [51, 52]. This is why, for the purpose of the CVI analysis, we stick to only the k-means++ algorithm.

According to the supercell scaling method the distance between the clusters of different levels of confinement should increase as the supercell size N grows. Taking also into account that we always renormalize the dataset to a unit domain, we expect the well-behaved CVIs to display better result, *i.e.*, lower minimum or higher maximum, every time N is incremented. In other words, the CVI must be a monotonically increasing or decreasing function of N, depending on the CVI definition. We refer to this as the convergence property of the CVI.

Thus, in this section, we are looking for the best performing CVI for our specific setting of wave confinement analysis. The suitable CVI has to satisfy the following criteria:

1. For the reference structure, the maximum or minimum of the CVI must be obtained at $K = 3$ clusters.

2. The CVI should be a monotonically increasing or decreasing function of the supercell size N, exhibiting convergence.

3.4.2 Results and discussion

Fig. 3.3 contains obtained CVI values as a function of the input number of cluster K, for the reference structure. For the supercell size $N = 2$, none of the indices achieve their respective optimum for $K = 3$. This is not surprising, as this is an extremely small supercell and the scaling properties are not yet well developed, for this size. In the case of $N = 3$, the only CVI achieving correctly its optimum is DB* (green) at $K = 3$. Finally, for $N = 4$, both DB (blue) and DB* (green) achieve their minimum for the correct $K = 3$. DB and DB* also

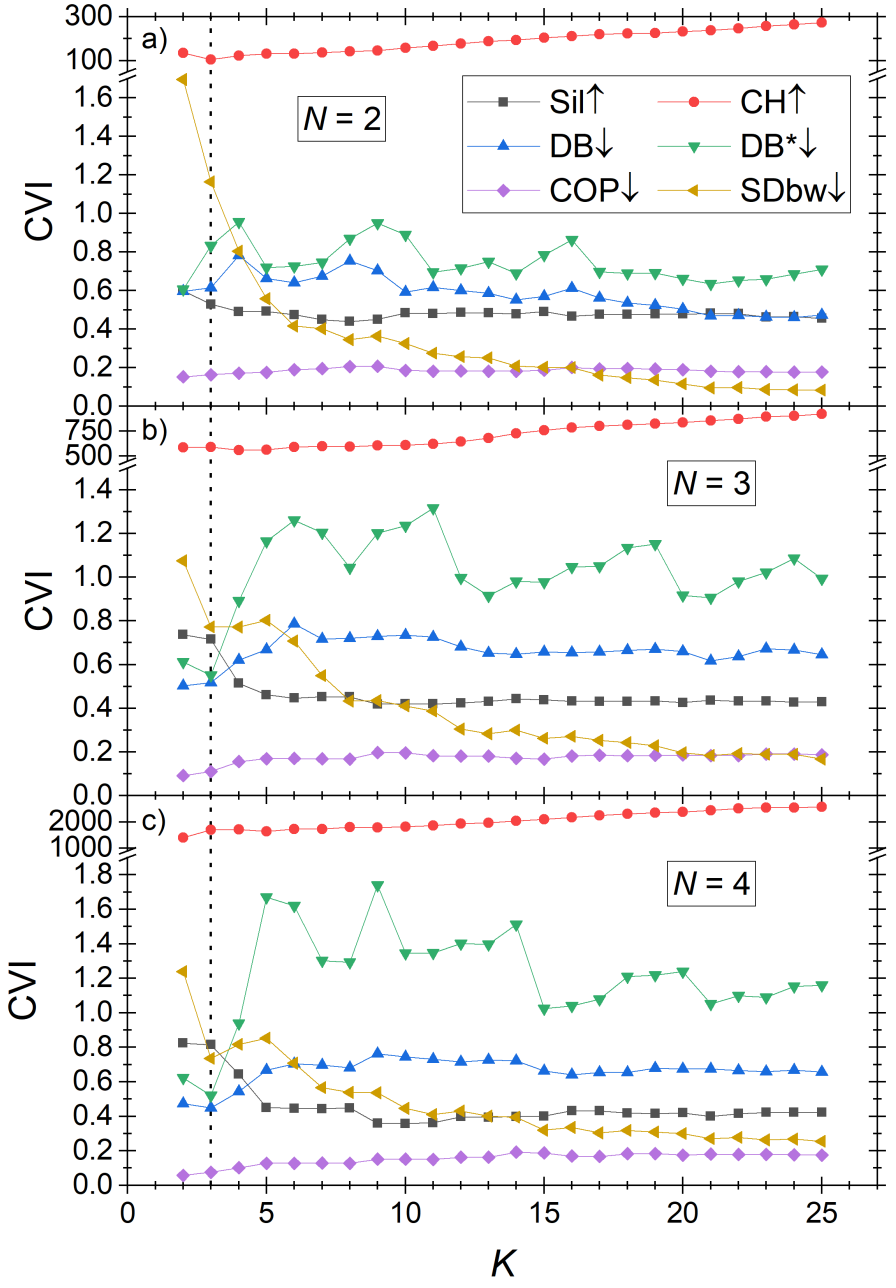

Figure 3.3: CVI values as a function of the number of clusters K. The arrows in the legend indicate if the optimum of a specific CVI is a minimum (down arrow) or a maximum (up arrow). The suitable CVI should attain its respective optimum at the correct number of clusters $K = 3$, highlighted with the dotted vertical line. Note that for $K = 1$ the CVIs are undefined. (a) $N = 2$ supercell. (b) $N = 3$ supercell. (c) $N = 4$ supercell.

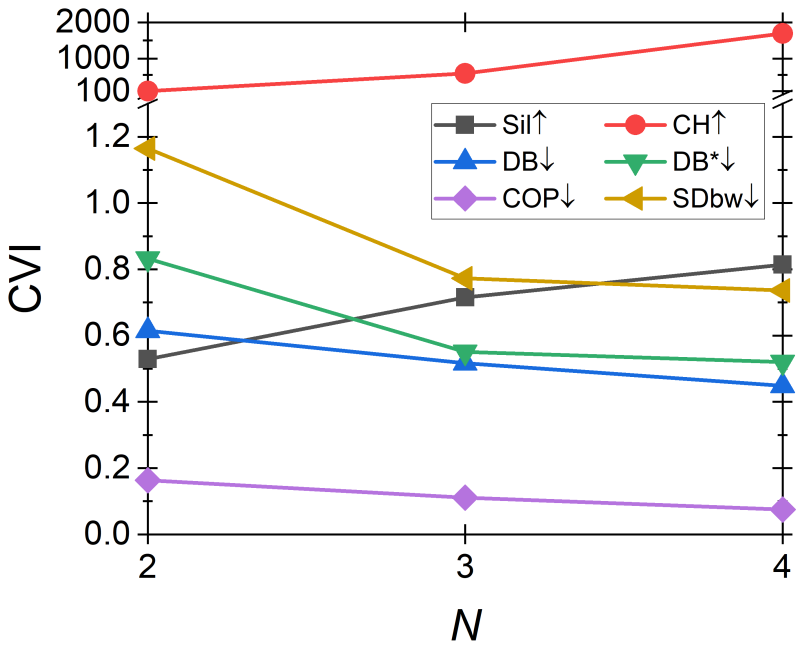

Figure 3.4: CVI values as a function of the supercell size N for the correct number of clusters $K = 3$. The arrows in the legend indicate if the optimum of a specific CVI is a minimum (down arrow) or a maximum (up arrow). The suitable CVI is expected to decrease (increase) with growing N, if its optimum is a minimum (maximum).

exhibit very similar behavior with respect to the number of clusters K and certain qualitative difference between them is only visible in the regime of large K, where DB stays mostly constant around a value relatively close to its minimum, whereas DB* oscillates around a value much greater than its minimum. The other CVIs exhibit rather erratic behaviour. CH (red) and S_Dbw (yellow) exhibit local, but not global optima at $K = 3$, whereas Sil (black) and COP (purple) do not even exhibit local optima at the correct number of clusters.

Fig. 3.4 shows the convergence behavior of CVIs with respect to the supercell size N. Here, it seems clear that all the indices obey the required property of monotonic convergence.

Based on our analysis, we thus conclude that, out of our tested sample of CVIs, DB* is the only CVI to satisfy the requirements for a good clustering accuracy measure in our setting for both $N = 3$ and $N = 4$ supercell sizes. Therefore, we will continue to work only with this CVI. We note aside that for the larger supercell size $N = 4$, DB also seems to be well-behaved and thus might be suitable as a CVI for larger supercell sizes.

3.5 Model-based clustering

The k-means clustering algorithm is a standard and easy-to-implement process. However, it simply clusters the data without any account for the underlying physics. That is why we present here our model-based clustering (MBC) algorithm, a unique mix of clustering and a model-based regression method.

As discussed in Section 3.3, bands in a superlattice analysis follow certain trajectories in the $(\widetilde{E}, \log_{10} \widetilde{V})$ space based on their confinement dimensionalities c, forming clusters as depicted in Fig. 3.2. Mathematically, upon transforming Eq. (3.5) from the $(\widetilde{E}, \widetilde{V})$ to $(\widetilde{E}, \log_{10} \widetilde{V})$ space, the trajectory of a band with confinement dimensionality c will be given by

$$\log_{10} \widetilde{V} = \log_{10} \tilde{C} + \frac{-c}{c-D} \log_{10} \widetilde{E}. \tag{3.13}$$

Note that the further renormalization given by Eqs. (3.7) and (3.8), only adds a constant to the right-hand side of Eq. (3.13), which can be absorbed by the unknown constant $\tilde{C}$. We can thus directly write

$$\mathcal{V} = \log_{10} \tilde{C} + \frac{-c}{c-D} \log_{10} \mathcal{E}. \tag{3.14}$$

In the MBC method, instead of evaluating the distance of a data point to the centroid of its cluster, we evaluate the distance of a point to the curve given by Eq. (3.14). For $0 < c < D$, we define the distance Δ_c of a point $\mathbf{x}_0 = (\mathcal{E}_0, \mathcal{V}_0)$ to a point $\mathbf{x} = (\mathcal{E}, \mathcal{V})$ on the curve (3.14) as their Euclidean distance $\|\mathbf{x}_0 - \mathbf{x}\|$. This distance can be evaluated for any $\mathbf{x}$ on the curve as

$$\Delta_c(\mathcal{E}) = \sqrt{(\mathcal{E} - \mathcal{E}_0)^2 + (\log_{10} \tilde{C} + \frac{-c}{c-D} \log_{10} \mathcal{E} - \mathcal{V}_0)^2}. \tag{3.15}$$

The distance of a point $(\mathcal{E}_0, \mathcal{V}_0)$ to the curve is then defined as $\Delta_c(\mathcal{E}^*)$, where $\mathcal{E}^*$ is such that

$$\frac{\mathrm{d}\Delta_c}{\mathrm{d}\mathcal{E}}(\mathcal{E}^*) = 0. \tag{3.16}$$

For the degenerate cases of $c = 0$ and $c = D$, the distance is simply given by the difference of the $\mathcal{V}$ and $\mathcal{E}$ values, respectively.

In the MBC method, we calculate the distance of each data point to each curve corresponding to different values of c and assign the data point to the cluster corresponding to the smallest distance. Upon clustering the whole data set, we recalculate the curve positions by calculating the centroid of each dataset. We then force the corresponding curve to pass through this centroid by adjusting the value of $\tilde{C}$ accordingly. Since our curves have a strict ordering from left to right, as can be seen from the Fig. 3.2, there does not seem to be any significant reason for repeated random iteration, especially since this would complicate the algorithm. As initialization values, we simply set all the centroids at the point $(\max_{i=1}^{M_N} \mathcal{E}, \max_{i=1}^{M_N} \mathcal{V})$, corresponding to the top-right corner of the clustering dataset in Fig. 3.2.

The MBC algorithm is summarized in Algorithm 2. We note that, while the

Algorithm 2 Model-based clustering algorithm

Input: Data array $\mathcal{X}_N \subset \mathbb{R}^2$, values of K confinement dimensionalities, corresponding to different clusters.

Output: Division of the data into clusters corresponding to various confinement dimensionalities c, such that the distance from each point to its corresponding curve is minimized.

1. Set the initial centroids to (1,0) for each curve.

2. Assign each data point $\mathbf{x}_i = (\mathcal{E}_i, \mathcal{V}_i) \in \mathcal{X}_N$ to its nearest curve using the distance measure (3.15). In case of equality of the nearest centroids, the data point is assigned to either cluster.

3. Recalculate the centroid of each cluster as the mean of all its constituent data points and adjust the corresponding curve to pass through the new centroid.

4. Repeat the steps 2 and 3 with the new curves until a termination criterion (usually certain degree of convergence) is reached.

k-means algorithm only performs the clustering and one needs to manually assign the corresponding confinement dimensionality c to each cluster, MBC does this inherently and automatically, which is an additional advantage of this approach.

Again, we use DB* as a CVI to determine the correct number of clusters. We stress here that for MBC, the input is not only the number of clusters, but also their specific confinement dimensionalities. The set of K clusters can thus include different combination of c values, yielding different partitions. In such a case, DB* can sometimes prefer a physically impossible partition, such as plane-confined bands in a structure with no plane defects. Nevertheless, if we restrict ourselves to only sets of physically meaningful confinement dimensionalities, the performance of DB* is comparable to the case of the k-means algorithm. This is inherently a shortcoming of DB* applied to our problem, as it does not measure the validity with respect to the theory, but only based on clustering cohesion and separation, as discussed in more detail in Appendix 3.B. There would thus be a clear benefit in devising a model-based CVI along with our model-based clustering algorithm. This is, however, beyond the scope of this chapter. Moreover, as we discuss below, our computations suggest that the best accuracy in the confinement identification can be achieved by finding the correct set of confinement dimensionalities via the scaling method of Ref. [36] combined with physical insight. The use of a CVI can thus be skipped if one is able to perform the scaling and has some information about the physics of the investigated structure.

Fig. 3.5 shows the resulting clusters obtained by the MBC algorithm for the $N = 4$ supercell of the inverse woodpile photonic crystal with the same unper-

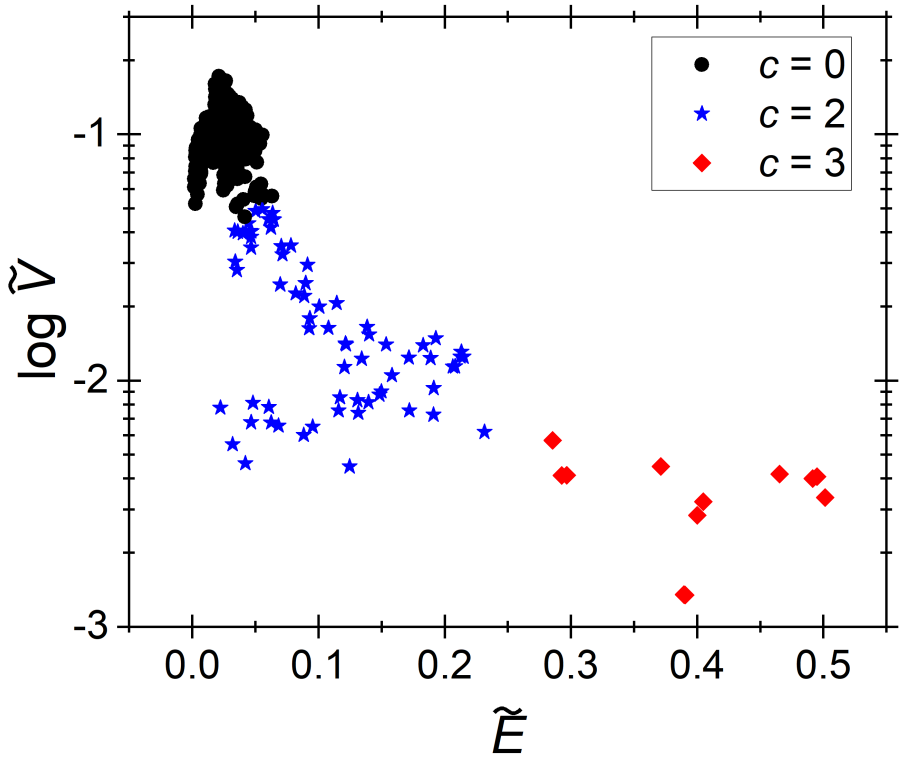

Figure 3.5: Clusters corresponding to different confinement dimensionalities c obtained by our MBC algorithm for an $N = 4$ supercell of an inverse woodpile photonic superlattice (see Appendix 3.A) with parameters $R = 0.24a$, $R' = 0.5R$.

turbed pore size $R = 0.24a$, and defect pore size $R' = 0.5R$, see Appendix 3.A. The clusters correspond to the expectation illustrated in Fig. 3.2, but, even for $N = 4$ as the largest computationally achievable supercell, we see that especially the $c = 2$ and $c = 0$ clusters are not very well separated yet and it would be difficult to distinguish them visually without a quantitative method.

3.6 Performance analysis in confinement determination

In this section, we compare the results obtained by our MBC algorithm and by the k-means++ algorithm with the results obtained by direct application of the scaling method described in Ref. [36] with reference supercell size $N_0 = 2$. We do this by applying the methods to several inverse woodpile structures with different properties. The absence of the ground truth information for these problems complicates the analysis and therefore we attempt to somewhat alleviate this issue

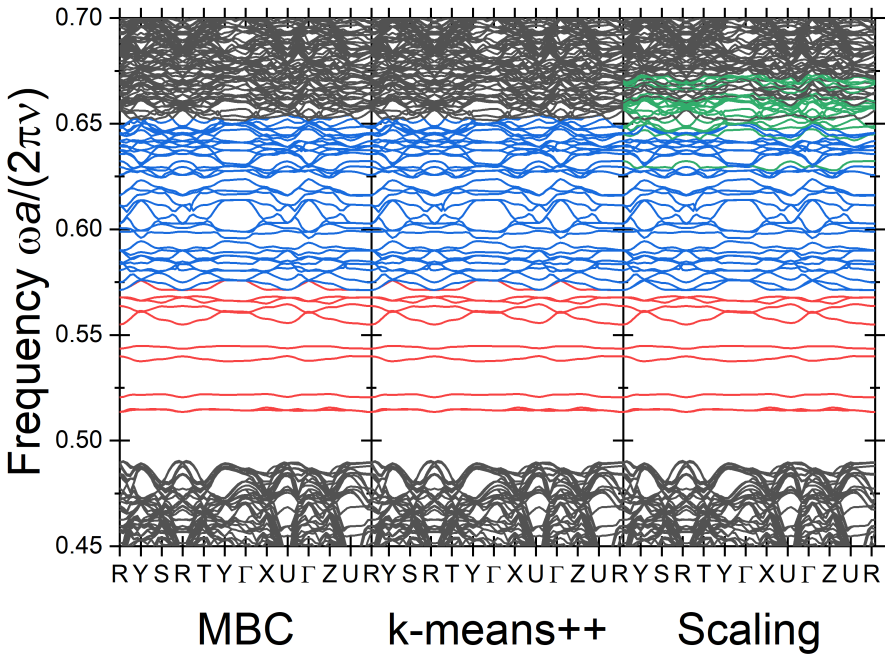

Figure 3.6: Band structure of an $N = 3$ supercell of an inverse woodpile photonic crystal (see Appendix 3.A) with parameters $R = 0.24a$, $R' = 0.5R$, with bands color-coded to indicate the confinement dimensionalities c of each band. Red color corresponds to point-confined $c = 3$, blue to line-confined $c = 2$, green to plane-confined $c = 1$ and black to extended $c = 0$. The vertical axis is given in the reduced frequency $\tilde{\omega} = \omega a/(2\pi\nu)$, with a being the lattice constant and ν the speed of light. The left panel shows the confinement classification for the MBC clustering, the central panel for the k-means++ clustering, and the right panel for the direct application of the scaling approach from Ref. [36].

by visually inspecting the energy-density distribution $W(\mathbf{r})$ of selected bands. Note, however, that this visual inspection is a qualitative tool and often it is not completely clear from it how well the band is confined, either.

Fig. 3.6 shows the results of confinement identification on an $N = 3$ supercell of the most studied inverse woodpile photonic crystal case with unperturbed pore size $R = 0.24a$, and defect pore size $R' = 0.5R$, see Appendix 3.A and Refs. [18, 19, 49]. In this case, both clustering algorithms yield the same solution, which almost perfectly coincides with the direct scaling approach. It is remarkable that all three methods independently agree on the presence of at least 9 bands with $c = 3$, between $\tilde{\omega} \approx 0.52$ and $\tilde{\omega} \approx 0.57$, instead of the 5 previously identified by qualitative guesswork by Refs. [18, 19, 49]. Some of these bands have been shown to demonstrate 3D coupled cavity behavior also in the recent experiments of Ref. [53]. The direct scaling approach of Ref. [36], however, identified several bands, mostly near $\tilde{\omega} \approx 0.65$, as $c = 1$ plane-confined modes, which is unphysical,

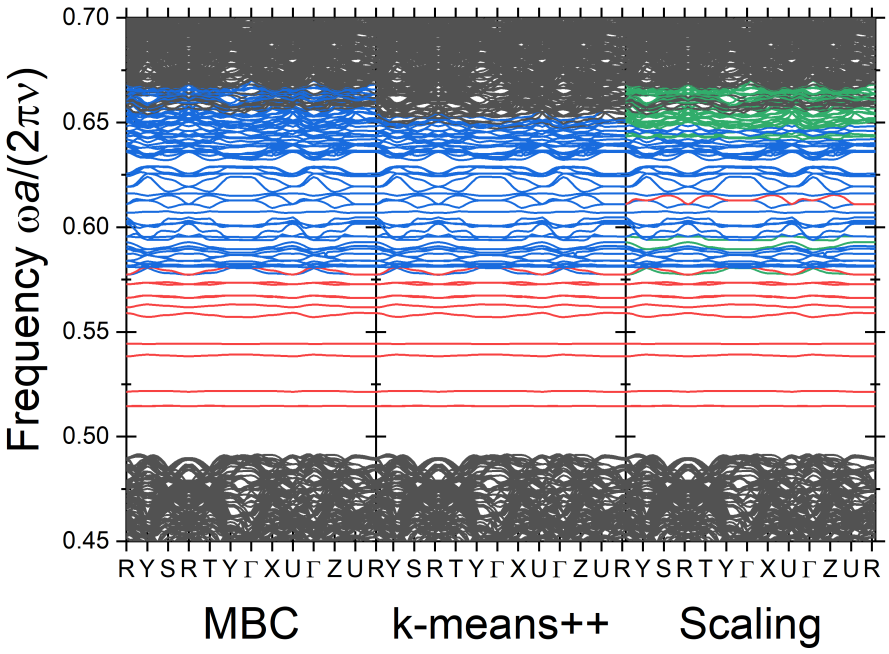

Figure 3.7: Band structure of an $N = 4$ supercell of an inverse woodpile photonic crystal (see Appendix 3.A) with parameters $R = 0.24a$, $R' = 0.5R$, with bands color-coded to indicate the confinement dimensionalities c of each band. Red color corresponds to point-confined $c = 3$, blue to line-confined $c = 2$, green to plane-confined $c = 1$ and black to extended $c = 0$. The left panel shows the confinement classification for the MBC clustering, the central panel for the k-means++ clustering, and the right panel for the direct application of the scaling approach from Ref. [36].

since the structure does not contain planar defects. Thanks to the fact that the clustering algorithms do not require a smaller reference supercell, but work only with the larger investigated supercell, the clustering approach successfully avoids these unphysical results. In this case, we therefore conclude that the clustering approaches are superior to the direct scaling.

Fig. 3.7 shows the results of our confinement identification on an $N = 4$ supercell of the inverse woodpile photonic crystal with the same unperturbed pore size $R = 0.24a$, and defect pore size $R' = 0.5R$ as in the previous paragraph. Note that all approaches agree that a higher number of $c = 3$ bands is present here than for the $N = 3$ supercell of the same structure. This clearly illustrates the problem with small supercells: the localization length of some confined bands is too large to be identifiable in the small supercells and only becomes clear for larger ones. In this case, the clustering approach again avoids the unphysical plane-confined bands ($c = 1$) obtained by the direct scaling application near $\tilde{\omega} \approx 0.65$. The k-means algorithm classifies the $c = 2$ and the $c = 3$ bands in a very similar way to the direct scaling approach. The direct scaling approach, however, contains

a unique red ($c = 3$) band at $\tilde{\omega} \approx 0.61$ and several green ($c = 2$) bands around $\tilde{\omega} \approx 0.58$, within the area filled with blue $c = 2$ bands. The red $c = 3$ band seems to be degenerate with a blue $c = 2$ band, which seems physically implausible and is similar to the issue observed by Ref. [36]. The more robustly grouped result of the clustering approach thus seem to be more physically plausible also in this case.

The MBC approach offers another remarkable insight, namely, it assigns the green $c = 1$ bands from the scaling approach to the blue $c = 2$ group. Even by the visual inspection of energy density distribution W it is hard to judge if the bands in question are $c = 2$ or $c = 0$ as concluded by the MBC and the k-means algorithm, respectively. There does not seem to be a significant qualitative difference between the energy density distributions for the bands around $\tilde{\omega} \approx 0.65$ and the bands around $\tilde{\omega} \approx 0.67$, when visually compared. All of them have W extended throughout the whole supercell, but also with certain peaks at the defect positions. Those peaks are, nevertheless, noticeably lower than the bands between $\tilde{\omega} \approx 0.52$ and $\tilde{\omega} \approx 0.60$. The correct classification of the bands above $\tilde{\omega} \approx 0.65$ thus remains unclear for now.

Fig. 3.8 shows the results of confinement identification on an $N = 3$ supercell of the inverse woodpile photonic crystal with different structural parameters, namely the unperturbed pore size $R = 0.24a$, and larger defect pore size $R' = 0.8R$. The results of the clustering algorithms are almost identical, here, again avoiding unphysical cases. The direct scaling approach found two degenerate unphysical $c = 1$ bands below the band gap at $\tilde{\omega} \approx 0.47$. However, the visual inspection of the energy density indicates that these two bands are unconfined ($c = 0$), which was concluded by the clustering algorithms. There are several other bands, between $\tilde{\omega} \approx 0.62$ and $\tilde{\omega} \approx 0.67$, that the scaling approach identifies as having $c = 1$. Some of these bands are assigned $c = 2$ (among the other blue bands), while others $c = 0$ (above the other black bands) by the clustering algorithms, which seems a lot more consistent. Thus, also in this case, the clustering performs better than the direct scaling approach.

Fig. 3.9 shows the results of confinement identification on an $N = 3$ supercell of the inverse woodpile photonic crystal with unperturbed pore size $R = 0.15a$, and defect pore size $R' = 0.5R$. In this parameter set, the main pores are smaller than optimal, a situation typical of the experiments [15, 54, 55]. In this case, the results obtained by clustering algorithm almost coincide again. The direct scaling approach again shows several unphysical green $c = 1$ bands. Some of these bands are classified by the clustering algorithms as $c = 2$ and some as $c = 0$. Visual inspection of the energy density indicates that the $c = 1$ bands around $\tilde{\omega} \approx 0.41$, resulting from the direct scaling approach, are in fact $c = 0$. This has been also identified by the clustering algorithms. We thus again conclude that the clustering algorithms outperform the direct scaling approach. The black $c = 0$ band at $\tilde{\omega} = 0.36$, resulting from the scaling and the MBC algorithm has similar energy-density distribution properties to its neighboring bands and therefore it looks like it should have been also labelled as $c = 1$, which has been done only by the k-means algorithm.

Fig. 3.10 shows the results of confinement identification on an $N = 3$ super-

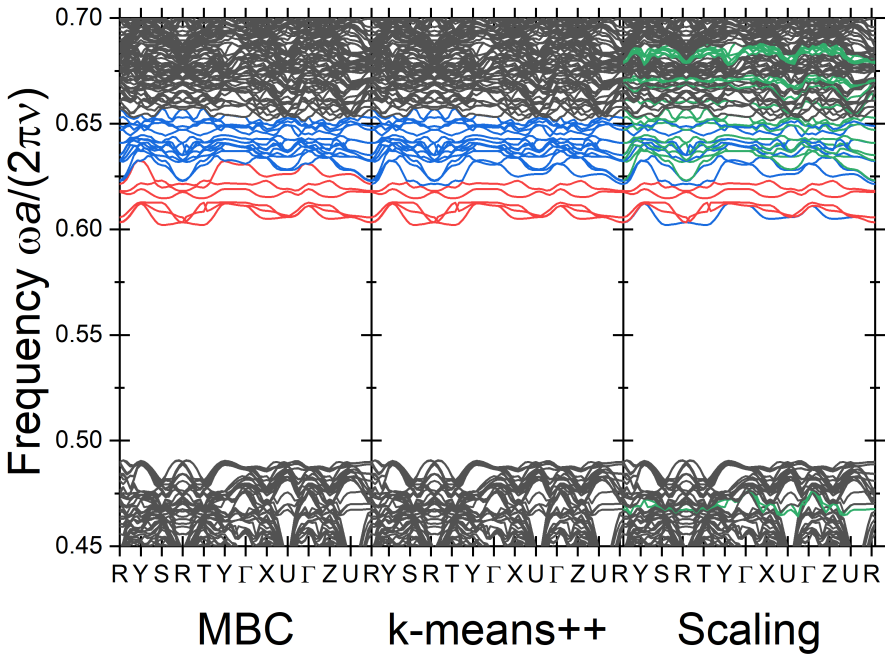

Figure 3.8: Band structure of an $N = 3$ supercell of an inverse woodpile photonic crystal (see Appendix 3.A) with parameters $R = 0.24a$, $R' = 0.8R$, with bands color-coded to indicate the confinement dimensionalities c of each band. Red color corresponds to point-confined $c = 3$, blue to line-confined $c = 2$, green to plane-confined $c = 1$ and black to extended $c = 0$. The left panel shows the confinement classification for the MBC clustering, the central panel for the k-means++ clustering, and the right panel for the direct application of the scaling approach from Ref. [36].

cell of the inverse woodpile photonic crystal with large unperturbed pores with $R = 0.29a$, and defect pores with $R' = 0.5R$. This is the only of the investigated cases where the direct scaling application overcomes the clustering. Visual investigation of the energy-density distribution W clearly shows that there are $c = 3$ bands present in this system, such as those around $\tilde{\omega} \approx 0.77$. The clustering algorithms with the help of DB* as a CVI thus clearly failed to identify the correct number of clusters here.

Fig. 3.11 shows the clustering results where we have explicitly stated the number of clusters $K = 3$ for the k-means++ algorithm and the possible confinement dimensionalities $c = 0, 2, 3$ for the MBC. Now, both clustering algorithms identified $c = 3$ bands similarly to the scaling algorithm. Here, we can see much better agreement regarding the $c = 3$ bands among all three approaches. The clustering algorithms again circumvent the unphysical $c = 1$ bands, this time by explicitly inputting the number of clusters and the confinement dimensionalities before the analysis. In this case, there is a remarkable difference between the line-confined $c = 2$ bands identified by the k-means++ and the MBC algorithms.

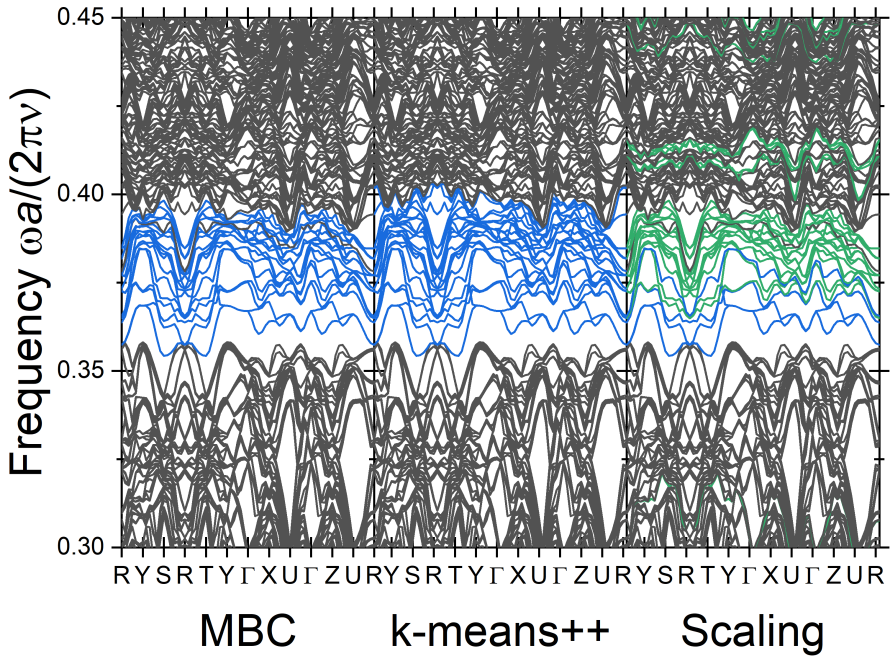

Figure 3.9: Band structure of an $N = 3$ supercell of an inverse woodpile photonic crystal (see Appendix 3.A) with parameters $R = 0.15a$, $R' = 0.5R$, with bands color-coded to indicate the confinement dimensionalities c of each band. Red color corresponds to point-confined $c = 3$, blue to line-confined $c = 2$, green to plane-confined $c = 1$ and black to extended $c = 0$. The left panel shows the confinement classification for the MBC clustering, the central panel for the k-means++ clustering, and the right panel for the direct application of the scaling approach from Ref. [36].

The k-means++ found a large number of these bands, especially also below the band gap of an unperturbed structure $\tilde{\omega} < 0.72$, which seems physically highly implausible. The visual inspection of the energy density of some of these bands indeed indicates that they are $c = 0$. Note that MBC also classified a few bands below the gap as $c = 2$. To our surprise, the visual inspection of the energy density for some of these bands shows that, despite not being truly spatially confined, these bands do exhibit some confinement patterns at the defect cross-sections. Therefore, MBC outperforms the other approaches here.

In this section, we investigated the confinement-classification performance of MBC, k-means++ and the direct scaling application methods on small supercells of various inverse woodpile structures. The clustering algorithms clearly outperform the direct scaling approach if the implemented CVI identifies the correct number of clusters to use as the input to the algorithms. To avoid errors in the cases when the CVI fails, we found it valuable to first directly employ the scaling analysis of Ref. [36] to identify the correct set of physically plausible confinement dimensionalities and then use that as the input for the clustering algorithms.

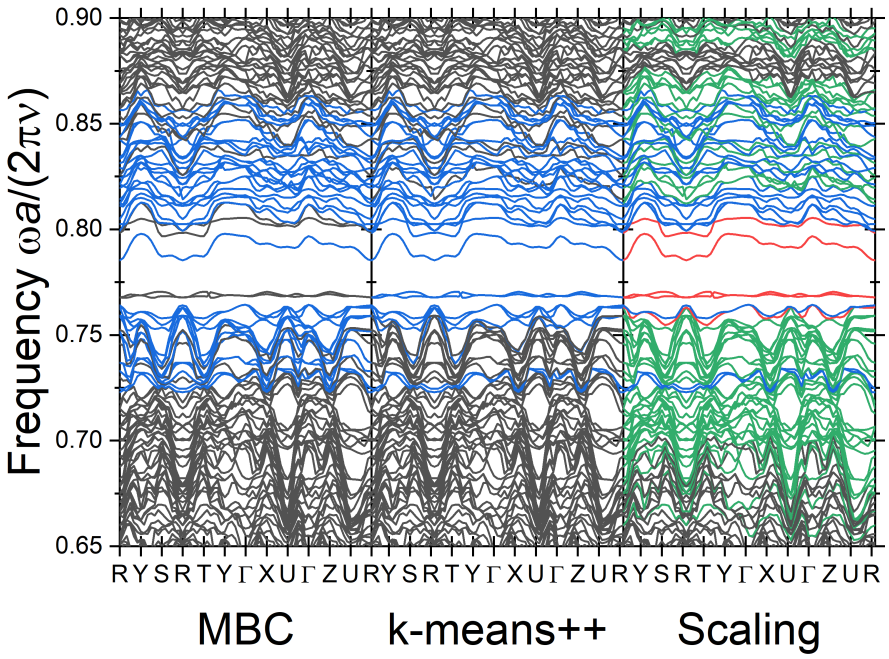

Figure 3.10: Band structure of an $N = 3$ supercell of an inverse woodpile photonic crystal (see Appendix 3.A) with parameters $R = 0.29a$, $R' = 0.5R$, with bands color-coded to indicate the confinement dimensionalities c of each band. Red color corresponds to point-confined $c = 3$, blue to line-confined $c = 2$, green to plane-confined $c = 1$ and black to extended $c = 0$. The left panel shows the confinement classification for the MBC clustering, the central panel for the k-means++ clustering, and the right panel for the direct application of the scaling approach from Ref. [36].

The performance of the two clustering algorithms is in most cases very similar. Nevertheless, the MBC algorithm takes into account the underlying physics behind the clustering, which may prove beneficial in some cases, such as the one illustrated in Fig. 3.11. Moreover, MBC has an additional advantage of immediately assigning the clusters to their corresponding confinement dimensionalities, offering an additional advantage over the k-means++ algorithm, where one has to assign the dimensionalities to the clusters manually. Our final recommendation for confinement identification in small supercells is thus to employ the scaling analysis of Ref. [36] to identify the correct set of confinement dimensionalities and subsequently use the MBC algorithm to properly classify each band.

3.7 Conclusion

In this chapter we investigated the application of machine-learning based clustering algorithms to increase the accuracy of band confinement identification for

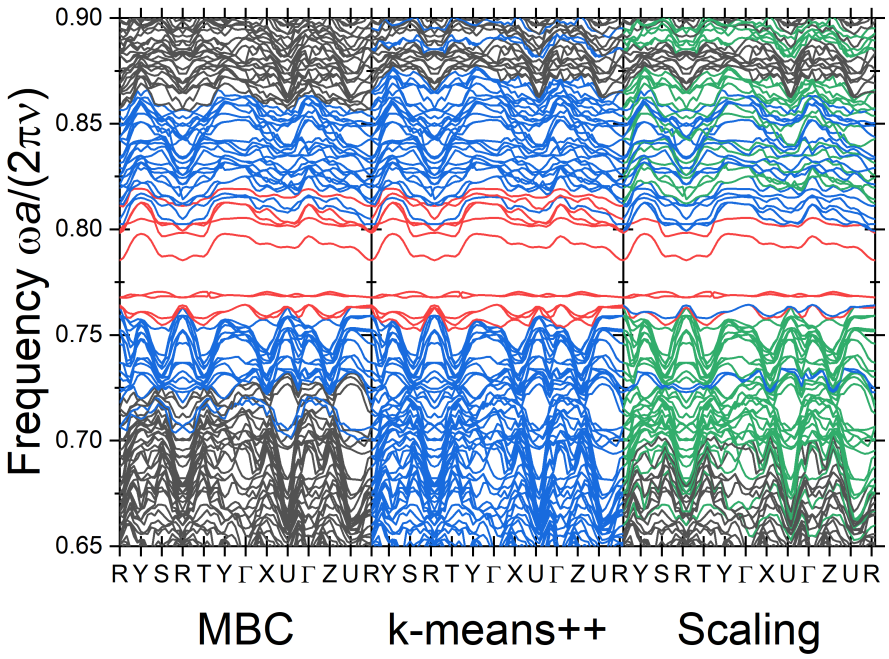

Figure 3.11: Band structure of an $N = 3$ supercell of an inverse woodpile photonic crystal (see Appendix 3.A) with parameters $R = 0.29a$, $R' = 0.5R$, with bands color-coded to indicate the confinement dimensionalities c of each band. Red color corresponds to point-confined $c = 3$, blue to line-confined $c = 2$, green to plane-confined $c = 1$ and black to extended $c = 0$. The left panel shows the confinement classification for the MBC clustering, the central panel for the k-means++ clustering, and the right panel for the direct application of the scaling approach from Ref. [36]. Here, we have explicitly chosen the number of cluster for the k-means++ algorithm and the clusterin curves for the MBC, based on the direct scaling results.

small supercells. To overcome the lack of a ground truth, we employed cluster validity indices as a measure of partition correctness and as a way to find the correct number of clusters. We analyzed several CVIs to find that the most suitable validity measure for our application is the DB* variant of the Davies-Bouldin index.

We further proposed two different algorithms to be used for band confinement identification: the k-means++ and our own model-based clustering (MBC). We analyzed the performance of these two algorithms in comparison to the direct application of scaling without clustering and found that the addition of clustering improves the accuracy of identification if the number of clusters is correctly found. Nevertheless, we also found that even with the use of the CVI, the clustering algorithms are not always able to find the correct number of clusters. To overcome this issue, we propose to first directly apply scaling to find the number of physically valid clusters and then use that number as an input for the

clustering algorithms to find the best band confinement classification.

Even though, as we have shown, both the k-means++ and our MBC algorithm usually perform well, in some cases the MBC algorithm is able to provide better results than the k-means++ algorithm. Combined with the fact that MBC assigns confinement dimensionalities to the clusters inherently and automatically without any need for external input, we suggest the use of this algorithm over the k-means++ algorithm

In the future, it would be beneficial to devise a model-based CVI, measuring the cluster validity not only in terms of cohesion and separation but also with respect to the adherence to the scaling theory of confinement, in a similar manner as our model-based clustering algorithm works. Furthermore, it would be interesting to explore the application of fuzzy clustering in order to include an error measure of assigning each point to its cluster [40].

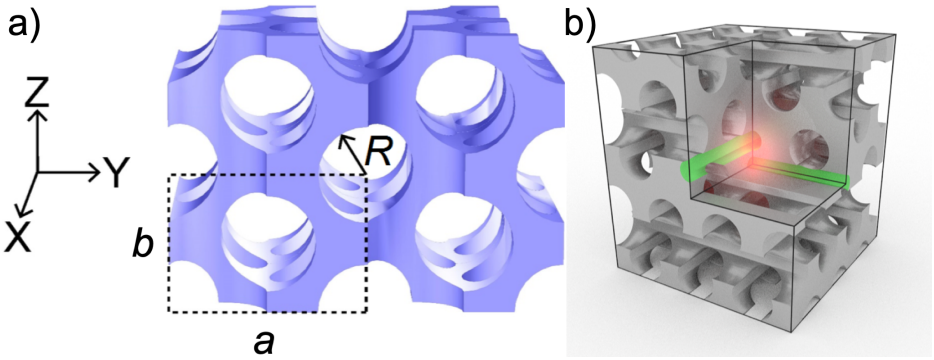

Figure 3.12: (a) Structure of an unperturbed inverse woodpile photonic crystal. We use a tetragonal unit cell with lattice parameters a in the y direction and $b = a/\sqrt{2}$ in the x and z directions. The pore radius is denoted by R. The figure shows an $N = 2$ supercell, with one unit cell designated by the dashed border. (b) Design of the defect. The radius R' of two proximate defect pores (shown in green) is altered. At their intersection a region with excess of one material is created that serves as a point defect (red glow).

Appendices

3.A The inverse woodpile structure

The 3D inverse woodpile photonic band gap crystal consists of bulk silicon ($\varepsilon = 12.1$, see Ref. [56]), in which nanopores of radius R filled with air ($\varepsilon = 1$) are etched [48, 54]. We model the unperturbed crystal using a tetragonal unit cell with lattice parameters a in the y direction and $b = a/\sqrt{2}$ in the x and z directions. This unperturbed structure is depicted in Fig. 3.12(a).

A defect can be incorporated in the structure by altering the radius R' of two proximate nanopores, as illustrated in Fig. 3.12(b). This results in creation of a region with excess of either air ($R' > R$) or silicon ($R' < R$) at the intersection of the two defect pores, serving as a point defect. We include one defect of this type per supercell.

3.B Overview of the used CVIs

Here, the mathematical definition for each CVI is provided along with some intuitive explanation of each formula, mainly in terms of cluster cohesion and cluster separation. For a more comprehensive review, see Ref. [46]. We denote the centroid of the dataset $\mathcal{X}$ containing M data points as $\mathbf{X} = \frac{1}{M}\sum_{\mathbf{x}_i \in \mathcal{X}} x_i$.

3.B.1 Silhouette

The Silhouette index [51] is defined as

$$\mathrm{Sil}(\mathcal{C}) \coloneqq \frac{1}{M} \sum_{C_i \in \mathcal{C}} \sum_{\mathbf{x}_j \in C_i} \frac{b(\mathbf{x}_j, C_i) - a(\mathbf{x}_j, C_i)}{\max\{a(\mathbf{x}_j, C_i), b(\mathbf{x}_j, C_i)\}} \tag{3.17}$$

and is aimed to be maximized for the best clustering outcome. Here,

$$a(\mathbf{x}_i, C_k) \coloneqq \frac{1}{M_i} \sum_{\mathbf{x}_j \in C_k} \|\mathbf{x}_j - \mathbf{x}_i\|^2, \quad \text{for } \mathbf{x}_i \in C_k, \tag{3.18}$$

represents the cohesion of the cluster C_k given as a distance between a chosen point $\mathbf{x}_i \in C_k$ and all the other points in the given cluster. Clearly, the smaller a is, the better the cluster cohesion. Furthermore, the function

$$b(\mathbf{x}_i, C_k) \coloneqq \min_{C_l \in \mathcal{C} \setminus C_k} \left\{ \frac{1}{M_l} \sum_{\mathbf{x}_j \in C_l} \|\mathbf{x}_j - \mathbf{x}_l\|^2 \right\}, \quad \text{for } \mathbf{x}_i \in C_k, \tag{3.19}$$

represents the separation of the cluster in terms of nearest neighbor distance from the other clusters $C_l, l \neq k$ to the point $\mathbf{x}_i \in C_k$. The larger b is, the further apart different clusters are from each other and thus the better the cluster separation is.

3.B.2 Calinski-Harabasz

The Calinski-Harabasz index [57] is given as

$$\mathrm{CH}(\mathcal{C}) \coloneqq \frac{M - K}{K - 1} \frac{\sum_{C_i \in \mathcal{C}} M_i \|\mathbf{c}_i - \mathbf{X}\|^2}{\sum_{C_i \in \mathcal{C}} \sum_{\mathbf{x}_j \in C_i} \|\mathbf{x}_j - \mathbf{c}_i\|^2}. \tag{3.20}$$

A high value of CH is assumed to corresponds to better data clustering.

Intuitively, the distance between the global centroid $\mathbf{X}$ and the cluster centroids $\mathbf{c}_i$ in the numerator acts as a cluster separation measure, with larger number corresponding to better separation. The cluster cohesion is represented by the denominator as the sum of distances between the cluster centroids and their constituent data points. Smaller distances between the cluster centroid and the cluster data obviously correspond to a more cohesive cluster. For a good clustering, one thus aims for maximizing the numerator and minimizing the denominator of CH, thus maximizing its overall value.

3.B.3 Davies-Bouldin

The Davies-Bouldin index [52] is defined as

$$\mathrm{DB}(\mathcal{C}) \coloneqq \frac{1}{K} \sum_{C_i \in \mathcal{C}} \max_{C_j \in \mathcal{C} \setminus C_i} \left\{ \frac{S(C_i) + S(C_j)}{\|\mathbf{c}_i - \mathbf{c}_j\|^2} \right\}, \tag{3.21}$$

where

$$S(C_i) \coloneqq \frac{1}{M_i} \sum_{\mathbf{x}_j \in C_i} \|\mathbf{x}_j - \mathbf{c}_i\|^2. \tag{3.22}$$

DB is expected to decrease with better partioning.

Here, the cohesion of the cluster C_i is gauged by the function $S(C_i)$ in the numerator, as the sum of the intracluster distances, *i.e.*, the sum of the distance of each data point assigned to the cluster C_i to the cluster centroid. The separation is measured in the denominator simply as the distance between the cluster centroids. A good clustering result will have a small numerator and a large denominator, thus resulting in a small value of DB.

3.B.4 Davies-Bouldin*

This variant on the Davies-Bouldin algorithm, described in Ref. [58], is defined as

$$\mathrm{DB}^*(\mathcal{C}) \coloneqq \frac{1}{K} \sum_{C_i \in \mathcal{C}} \frac{\max_{C_j \in \mathcal{C} \setminus C_i} \{S(C_i) + S(C_j)\}}{\min_{C_j \in \mathcal{C} \setminus C_i} \{\|\mathbf{c}_i - \mathbf{c}_j\|^2\}} \tag{3.23}$$

and is expected to attain low values for good clustering outcomes. The fact that the standard DB minimizes the maximum of the ratio of cluster cohesion and cluster separation can lead to pathological cases, as described by Ref. [58]. To remedy this, DB* instead maximizes the cluster cohesion and minimizes the cluster separation independently.

3.B.5 COP

The COP index [59] is given as

$$COP(\mathcal{C}) \coloneqq \frac{1}{M} \sum_{C_i \in \mathcal{C}} M_i \frac{\frac{1}{M_i} \sum_{\mathbf{x}_j \in C_i} \|\mathbf{x}_j - \mathbf{c}_i\|^2}{\min_{\mathbf{x}_j \notin C_i} \max_{\mathbf{x}_k \in C_i} \{\|\mathbf{x}_j - \mathbf{x}_k\|^2\}} \tag{3.24}$$

and is expected to be small for good clustering results. Here, the cluster cohesion is measured in the numerator as the average of intracluster distances and the cluster separation is measured by minimizing the furthest-neighbor distance to a given cluster in the denominator. One aims to minimize the numerator and maximize the denominator, thus maximizing the value of COP. We note here that, due to the furthest-neighbor distance measure, long and thin cluster can possibly skew this measure by overestimating the actual separation between the clusters.

3.B.6 S_Dbw index

The S_Dbw index [60] is defined as

$$\begin{aligned}\text{S\_Dbw}(\mathcal{C}) \coloneqq &\frac{1}{K}\sum_{C_i\in\mathcal{C}}\frac{\|\sigma(C_i)\|}{\|\sigma(X)\|}\\ &+\frac{1}{K(K-1)}\sum_{C_i\in\mathcal{C}}\sum_{C_j\in\mathcal{C}\setminus C_i}\frac{\rho(C_i,C_j)}{\max\{\rho(C_i),\rho(C_j)\}}\end{aligned} \tag{3.25}$$

and is expected to attain small values for good partitions. Here, $\boldsymbol{\sigma}(\mathcal{X})$ is the variance of each component of the data set $\mathcal{X}$. Its p-th component is defined as

$$\sigma^p(\mathcal{X}) \coloneqq \frac{1}{|X|}\sum_{\mathbf{x}_j\in\mathcal{X}}(x_j^p - X^p)^2, \tag{3.26}$$

Furthermore, $\tau(\mathcal{C})$ is the standard deviation of the partition $\mathcal{C}$, defined as

$$\tau(\mathcal{C}) \coloneqq \frac{1}{K}\sqrt{\sum_{C_i\in\mathcal{C}}\|\boldsymbol{\sigma}(C_i)\|}. \tag{3.27}$$

We further define the terms

$$\rho(C_i) \coloneqq \sum_{\mathbf{x}_j\in C_i}\theta(\mathbf{x}_j,\mathbf{c}_i), \tag{3.28}$$

and

$$\rho(C_i,C_j) \coloneqq \sum_{\mathbf{x}_k\in C_i\cup C_j}\theta\left(\mathbf{x}_k,\frac{\mathbf{c}_i+\mathbf{c}_j}{2}\right), \tag{3.29}$$

where

$$\theta(\mathbf{x}_j,C_i) \coloneqq \begin{cases}0 & \text{if } \|\mathbf{x}_j-\mathbf{c}_i\| > \tau(\mathcal{C})\\ 1 & \text{else}\end{cases}. \tag{3.30}$$

The term $\rho(C_i)$ evaluates the number of points in a cluster C_i within the standard deviation of the partition and the term $\rho(C_i,C_j)$ evaluates the number of points at the midpoint between the centers of C_i and C_j. A good clustering corresponds to large $\rho(C_i),\rho(C_j)$ and small $\rho(C_i,C_j)$ for each $i,j\leq K, i\neq j$, which translates into a small value of the second term in (3.25). The first term in (3.25) is termed intracluster variance and is a measure of the cluster cohesion in terms of a mean cluster variance.

The first term in Eq. (3.25) thus corresponds to the cluster cohesion and the second term represents the cluster separation [60]. Unlike all the other CVIs described in this chapter, S_Dbw relates these two terms by addition, instead of a ratio. Overall S_Dbw aims to minimize both of these terms for a good clustering result.

Bibliography

[1] P. Markoš and C. M. Soukoulis. *Wave Propagation: From Electrons to Photonic Crystals and Left-Handed Materials*. Princeton ; Oxford: Princeton University Press, 2008. ISBN: 978-0-691-13003-3.

[2] M. Fink, D. Cassereau, A. Derode, C. Prada, P. Roux, M. Tanter, J.-L. Thomas, and F. Wu. "Time-Reversed Acoustics". In: *Rep. Prog. Phys.* 63.12 (2000), pp. 1933–1995. ISSN: 0034-4885, 1361-6633. DOI: 10.1088/0034-4885/63/12/202.

[3] Z. Liu, X. Zhang, Y. Mao, Y. Y. Zhu, Z. Yang, C. T. Chan, and P. Sheng. "Locally Resonant Sonic Materials". In: *Science* 289.5485 (2000), pp. 1734–1736. ISSN: 0036-8075, 1095-9203. DOI: 10.1126/science.289.5485.1734.

[4] M. Maldovan. "Sound and Heat Revolutions in Phononics". In: *Nature* 503.7475 (2013), pp. 209–217. ISSN: 0028-0836, 1476-4687. DOI: 10.1038/nature12608.

[5] S. A. Cummer, J. Christensen, and A. Alù. "Controlling Sound with Acoustic Metamaterials". In: *Nat. Rev. Mater.* 1.3 (2016), p. 16001. ISSN: 2058-8437. DOI: 10.1038/natrevmats.2016.1.

[6] V. V. Kruglyak, S. O. Demokritov, and D. Grundler. "Magnonics". In: *J. Phys. D* 43.26 (2010), p. 264001. ISSN: 0022-3727, 1361-6463. DOI: 10.1088/0022-3727/43/26/264001.

[7] K. Wagner, A. Kákay, K. Schultheiss, A. Henschke, T. Sebastian, and H. Schultheiss. "Magnetic Domain Walls as Reconfigurable Spin-Wave Nanochannels". In: *Nat. Nanotechnol.* 11.5 (2016), pp. 432–436. ISSN: 1748-3387, 1748-3395. DOI: 10.1038/nnano.2015.339.

[8] K. Klyukin, L. L. Tao, E. Y. Tsymbal, and V. Alexandrov. "Defect-Assisted Tunneling Electroresistance in Ferroelectric Tunnel Junctions". In: *Phys. Rev. Lett.* 121.5 (2018), p. 056601. ISSN: 0031-9007, 1079-7114. DOI: 10.1103/PhysRevLett.121.056601.

[9] D. M. Callahan, K. A. W. Horowitz, and H. A. Atwater. "Light Trapping in Ultrathin Silicon Photonic Crystal Superlattices with Randomly-Textured Dielectric Incouplers". In: *Opt. Express* 21.25 (2013), p. 30315. ISSN: 1094-4087. DOI: 10.1364/OE.21.030315.

[10] A. Tandaechanurat, S. Ishida, D. Guimard, M. Nomura, S. Iwamoto, and Y. Arakawa. "Lasing Oscillation in a Three-Dimensional Photonic Crystal Nanocavity with a Complete Bandgap". In: *Nat. Photonics* 5.2 (2011), pp. 91–94. ISSN: 1749-4885, 1749-4893. DOI: 10.1038/nphoton.2010.286.

[11] M. Aspelmeyer, T. J. Kippenberg, and F. Marquardt. "Cavity Optomechanics". In: *Rev. Mod. Phys.* 86.4 (2014), pp. 1391–1452. ISSN: 0034-6861, 1539-0756. DOI: 10.1103/RevModPhys.86.1391.

[12] A. F. Koenderink, A. Alu, and A. Polman. "Nanophotonics: Shrinking Light-Based Technology". In: *Science* 348.6234 (2015), pp. 516–521. ISSN: 0036-8075, 1095-9203. DOI: 10.1126/science.1261243.

[13] W. Li and S. Fan. "Nanophotonic Control of Thermal Radiation for Energy Applications". In: *Opt. Express* 26.12 (2018), p. 15995. ISSN: 1094-4087. DOI: 10.1364/OE.26.015995.

[14] J. Wang, F. Sciarrino, A. Laing, and M. G. Thompson. "Integrated Photonic Quantum Technologies". In: *Nat. Photonics* 14.5 (2020), pp. 273–284. ISSN: 1749-4885, 1749-4893. DOI: 10.1038/s41566-019-0532-1.

[15] R. Uppu, M. Adhikary, C. A. M. Harteveld, and W. L. Vos. "Spatially Shaping Waves to Penetrate Deep inside a Forbidden Gap". In: *Phys. Rev. Lett.* 126.17 (2021), p. 177402. ISSN: 0031-9007, 1079-7114. DOI: 10.1103/PhysRevLett.126.177402.

[16] F. Arceri and E. I. Corwin. "Vibrational Properties of Hard and Soft Spheres Are Unified at Jamming". In: *Phys. Rev. Lett.* 124.23 (2020), p. 238002. ISSN: 0031-9007, 1079-7114. DOI: 10.1103/PhysRevLett.124.238002.

[17] K. Busch, G. von Freymann, S. Linden, S. Mingaleev, L. Tkeshelashvili, and M. Wegener. "Periodic Nanostructures for Photonics". In: *Phys. Rep.* 444.3-6 (2007), pp. 101–202. ISSN: 03701573. DOI: 10.1016/j.physrep.2007.02.011.

[18] L. A. Woldering, A. P. Mosk, and W. L. Vos. "Design of a Three-Dimensional Photonic Band Gap Cavity in a Diamondlike Inverse Woodpile Photonic Crystal". In: *Phys. Rev. B* 90.11 (2014), p. 115140. DOI: 10.1103/PhysRevB.90.115140.

[19] S. A. Hack, J. J. W. van der Vegt, and W. L. Vos. "Cartesian Light: Unconventional Propagation of Light in a Three-Dimensional Superlattice of Coupled Cavities within a Three-Dimensional Photonic Band Gap". In: *Phys. Rev. B* 99.11 (2019), p. 115308. ISSN: 2469-9950, 2469-9969. DOI: 10.1103/PhysRevB.99.115308.

[20] E. N. Economou. *The Physics of Solids*. Graduate Texts in Physics. Berlin, Heidelberg: Springer Berlin Heidelberg, 2010. ISBN: 978-3-642-02068-1 978-3-642-02069-8. DOI: 10.1007/978-3-642-02069-8.

[21] G. Shao. "Electronic Structures of Manganese-Doped Rutile TiO $_2$ from First Principles". In: *J. Phys. Chem. C* 112.47 (2008), pp. 18677–18685. ISSN: 1932-7447, 1932-7455. DOI: 10.1021/jp8043797.

[22] C. Pashartis and O. Rubel. "Localization of Electronic States in III-V Semiconductor Alloys: A Comparative Study". In: *Phys. Rev. Appl.* 7.6 (2017), p. 064011. ISSN: 2331-7019. DOI: 10.1103/PhysRevApplied.7.064011.

[23] C. Pashartis and O. Rubel. "Alloying Strategy for Two-Dimensional GaN Optical Emitters". In: *Phys. Rev. B* 96.15 (2017), p. 155209. ISSN: 2469-9950, 2469-9969. DOI: 10.1103/PhysRevB.96.155209.

[24] J. Zhang, C.-Z. Wang, Z. Z. Zhu, and V. V. Dobrovitski. "Vibrational Modes and Lattice Distortion of a Nitrogen-Vacancy Center in Diamond from First-Principles Calculations". In: *Phys. Rev. B* 84.3 (2011), p. 035211. ISSN: 1098-0121, 1550-235X. DOI: 10.1103/PhysRevB.84.035211.

[25] S. O. Demokritov, ed. *Spin Wave Confinement: Propagating Waves*. Second edition. Singapur: Pan Stanford Publishing, 2017. ISBN: 978-981-4774-35-2 978-1-315-11082-0.

[26] E. V. Tartakovskaya, M. Pardavi-Horvath, and R. D. McMichael. "Spin-Wave Localization in Tangentially Magnetized Films". In: *Phys. Rev. B* 93.21 (2016), p. 214436. ISSN: 2469-9950, 2469-9969. DOI: 10.1103/PhysRevB.93.214436.

[27] E. Krioukov, D. J. W. Klunder, A. Driessen, J. Greve, and C. Otto. "Sensor Based on an Integrated Optical Microcavity". In: *Opt. Lett.* 27.7 (2002), pp. 512–514. ISSN: 1539-4794. DOI: 10.1364/OL.27.000512.

[28] T. Baba. "Slow Light in Photonic Crystals". In: *Nat. Photonics* 2.8 (2008), pp. 465–473. ISSN: 1749-4893. DOI: 10.1038/nphoton.2008.146.

[29] S. Noda, A. Chutinan, and M. Imada. "Trapping and Emission of Photons by a Single Defect in a Photonic Bandgap Structure". In: *Nature* 407.6804 (2000), pp. 608–610. ISSN: 1476-4687. DOI: 10.1038/35036532.

[30] J. M. Gérard, B. Sermage, B. Gayral, B. Legrand, E. Costard, and V. Thierry-Mieg. "Enhanced Spontaneous Emission by Quantum Boxes in a Monolithic Optical Microcavity". In: *Phys. Rev. Lett.* 81.5 (1998), pp. 1110–1113. DOI: 10.1103/PhysRevLett.81.1110.

[31] P. Michler, ed. *Single Quantum Dots: Fundamentals, Applications, and New Concepts*. Topics in Applied Physics v. 90. Berlin, Heidelberg, New York: Springer-Verlag, 2003. ISBN: 978-3-540-14022-1.

[32] J. P. Reithmaier, G. Sęk, A. Löffler, C. Hofmann, S. Kuhn, S. Reitzenstein, L. V. Keldysh, V. D. Kulakovskii, T. L. Reinecke, and A. Forchel. "Strong Coupling in a Single Quantum Dot–Semiconductor Microcavity System". In: *Nature* 432.7014 (2004), pp. 197–200. ISSN: 1476-4687. DOI: 10.1038/nature02969.

[33] T. Yoshie, A. Scherer, J. Hendrickson, G. Khitrova, H. M. Gibbs, G. Rupper, C. Ell, O. B. Shchekin, and D. G. Deppe. "Vacuum Rabi Splitting with a Single Quantum Dot in a Photonic Crystal Nanocavity". In: *Nature* 432.7014 (2004), pp. 200–203. ISSN: 1476-4687. DOI: 10.1038/nature03119.

[34] E. Peter, P. Senellart, D. Martrou, A. Lemaître, J. Hours, J. M. Gérard, and J. Bloch. "Exciton-Photon Strong-Coupling Regime for a Single Quantum Dot Embedded in a Microcavity". In: *Phys. Rev. Lett.* 95.6 (2005), p. 067401. DOI: 10.1103/PhysRevLett.95.067401.

[35] P. Russell, E. Marin, A. Diez, S. Guenneau, and A. Movchan. "Sonic Band Gaps in PCF Preforms: Enhancing the Interaction of Sound and Light". In: *Opt. Express* 11.20 (2003), p. 2555. ISSN: 1094-4087. DOI: 10.1364/OE.11.002555.

[36] M. Kozoň, A. Lagendijk, M. Schlottbom, J. J. W. van der Vegt, and W. L. Vos. "Scaling Theory of Wave Confinement in Classical and Quantum Periodic Systems". In: *Phys. Rev. Lett.* 129.17 (2022), p. 176401. ISSN: 0031-9007, 1079-7114. DOI: 10.1103/PhysRevLett.129.176401.

[37] D. M. Dutton and G. V. Conroy. "A Review of Machine Learning". In: *Knowl. Eng. Rev.* 12.4 (1997), pp. 341–367. ISSN: 0269-8889, 1469-8005. DOI: 10.1017/S026988899700101X.

[38] B. Mahesh. "Machine Learning Algorithms - A Review". In: *Int.J.Sci.Res.* 9.1 (2018), p. 6.

[39] A. K. Jain and R. C. Dubes. *Algorithms for Clustering Data*. Prentice Hall Advanced Reference Series. Englewood Cliffs, N.J: Prentice Hall, 1988. ISBN: 978-0-13-022278-7.

[40] A. K. Jain, M. N. Murty, and P. J. Flynn. "Data Clustering: A Review". In: *ACM Comput. Surv.* 31.3 (1999), pp. 264–323. ISSN: 0360-0300, 1557-7341. DOI: 10.1145/331499.331504.

[41] R. Schrijver. "Machine-Learning Algorithms in Wave-Confinement Analysis". PhD thesis. 2021.

[42] J. Macqueen. "Some Methods for Classification and Analysis of Multivariate Observations". In: *Proceedings of the Fifth Berkeley Symposium on Mathematical Statistics and Probability*. Ed. by L. Lecam and J. Neyman. Vol. 1. 1967, pp. 281–297.

[43] D. Arthur and S. Vassilvitskii. "K-Means++: The Advantages of Careful Seeding". In: *Proceedings of the Eighteenth Annual ACM-SIAM Symposium on Discrete Algorithms*. 2007, p. 9.

[44] F. Pedregosa, G. Varoquaux, A. Gramfort, V. Michel, B. Thirion, O. Grisel, M. Blondel, P. Prettenhofer, R. Weiss, V. Dubourg, J. Vanderplas, A. Passos, D. Cournapeau, M. Brucher, M. Perrot, and É. Duchesnay. "Scikit-Learn: Machine Learning in Python". In: *Journal of Machine Learning Research* 12.85 (2011), pp. 2825–2830. ISSN: 1533-7928.

[45] V. Piccialli, A. M. Sudoso, and A. Wiegele. "SOS-SDP: An Exact Solver for Minimum Sum-of-Squares Clustering". In: *INFORMS J. Comput.* 34.4 (2022), pp. 2144–2162. ISSN: 1091-9856, 1526-5528. DOI: 10.1287/ijoc.2022.1166.

[46] O. Arbelaitz, I. Gurrutxaga, J. Muguerza, J. M. Pérez, and I. Perona. "An Extensive Comparative Study of Cluster Validity Indices". In: *Pattern Recognition* 46.1 (2013), pp. 243–256. ISSN: 00313203. DOI: 10.1016/j.patcog.2012.07.021.

[47] A. Saxena, M. Prasad, A. Gupta, N. Bharill, O. P. Patel, A. Tiwari, M. J. Er, W. Ding, and C.-T. Lin. "A Review of Clustering Techniques and Developments". In: *Neurocomputing* 267 (2017), pp. 664–681. ISSN: 09252312. DOI: 10.1016/j.neucom.2017.06.053.

[48] K. M. Ho, C. T. Chan, C. M. Soukoulis, R. Biswas, and M. Sigalas. "Photonic Band Gaps in Three Dimensions: New Layer-by-Layer Periodic Structures". In: *Solid State Commun.* 89.5 (1994), pp. 413–416. ISSN: 0038-1098. DOI: 10.1016/0038-1098(94)90202-X.

[49] D. Devashish, O. S. Ojambati, S. B. Hasan, J. J. W. van der Vegt, and W. L. Vos. "Three-Dimensional Photonic Band Gap Cavity with Finite Support: Enhanced Energy Density and Optical Absorption". In: *Phys. Rev. B* 99.7 (2019), p. 075112. ISSN: 2469-9950, 2469-9969. DOI: 10.1103/PhysRevB.99.075112.

[50] S. G. Johnson and J. D. Joannopoulos. "Block-Iterative Frequency-Domain Methods for Maxwell's Equations in a Planewave Basis". In: *Opt. Express* 8.3 (2001), p. 173. ISSN: 1094-4087. DOI: 10.1364/OE.8.000173.

[51] P. J. Rousseeuw. "Silhouettes: A Graphical Aid to the Interpretation and Validation of Cluster Analysis". In: *Journal of Computational and Applied Mathematics* 20 (1987), pp. 53–65. ISSN: 03770427. DOI: 10.1016/0377-0427(87)90125-7.

[52] D. L. Davies and D. W. Bouldin. "A Cluster Separation Measure". In: *IEEE Trans. Pattern Anal. Mach. Intell.* PAMI-1.2 (1979), pp. 224–227. ISSN: 0162-8828, 2160-9292. DOI: 10.1109/TPAMI.1979.4766909.

[53] M. Adhikary, M. Kozoň, R. Uppu, and W. L. Vos. "Observation of Light Propagation through a Three-Dimensional (3D) Superlattice of Cavities in a 3D Photonic Band Gap". In preparation.

[54] M. D. Leistikow, A. P. Mosk, E. Yeganegi, S. R. Huisman, A. Lagendijk, and W. L. Vos. "Inhibited Spontaneous Emission of Quantum Dots Observed in a 3D Photonic Band Gap". In: *Phys. Rev. Lett.* 107.19 (2011), p. 193903. ISSN: 0031-9007, 1079-7114. DOI: 10.1103/PhysRevLett.107.193903.

[55] M. Adhikary, R. Uppu, C. A. M. Harteveld, D. A. Grishina, and W. L. Vos. "Experimental Probe of a Complete 3D Photonic Band Gap". In: *Opt. Express* 28.3 (2020), p. 2683. ISSN: 1094-4087. DOI: 10.1364/OE.28.002683.

[56] R. Hillebrand, S. Senz, W. Hergert, and U. Gösele. "Macroporous-Silicon-Based Three-Dimensional Photonic Crystal with a Large Complete Band Gap". In: *J. Appl. Phys.* 94.4 (2003), pp. 2758–2760. ISSN: 0021-8979, 1089-7550. DOI: 10.1063/1.1593796.

[57] T. Calinski and J. Harabasz. "A Dendrite Method for Cluster Analysis". In: *Comm. in Stats. - Theory & Methods* 3.1 (1974), pp. 1–27. ISSN: 0361-0926. DOI: 10.1080/03610927408827101.

[58] M. Kim and R. Ramakrishna. "New Indices for Cluster Validity Assessment". In: *Pattern Recognition Letters* 26.15 (2005), pp. 2353–2363. ISSN: 01678655. DOI: 10.1016/j.patrec.2005.04.007.

[59] I. Gurrutxaga, I. Albisua, O. Arbelaitz, J. I. Martín, J. Muguerza, J. M. Pérez, and I. Perona. "SEP/COP: An Efficient Method to Find the Best Partition in Hierarchical Clustering Based on a New Cluster Validity Index". In: *Pattern Recognition* 43.10 (2010), pp. 3364–3373. ISSN: 00313203. DOI: 10.1016/j.patcog.2010.04.021.

[60] M. Halkidi and M. Vazirgiannis. "Clustering Validity Assessment: Finding the Optimal Partitioning of a Data Set". In: *Proceedings 2001 IEEE International Conference on Data Mining*. San Jose, CA, USA: IEEE Comput. Soc, 2001, pp. 187–194. ISBN: 978-0-7695-1119-1. DOI: 10.1109/ICDM.2001.989517.

4 Photonic Confinement in 3D Inverse Woodpile Photonic Superlattices: Symmetry and "Orbitals"

4.1 Introduction

The confinement of light is a prominent branch of nanophotonics [1, 2]. To achieve and exploit this phenomenon, a variety of devices has been designed such as micropillars [3, 4], microdisks [5], toroidal rings [6], plasmonic cavities [7, 8] and point defects in two-dimensional photonic crystals [9]. Light confinement has been practically utilized in applications ranging from sensing [10], to slowing down or trapping of photons [11, 12], to enhanced spontaneous emission [3] and cavity quantum electrodynamics (cQED) [4, 5, 13, 14].

Of particular significance are cavities embedded in three-dimensional (3D) photonic crystals [15, 16] as these are capable of confining light in *all three dimensions* simultaneously [17]. In a perfect photonic crystal structure, the translational symmetry gives rise via interference effects to a 3D *photonic bandgap*, which is a range of frequencies for which light is not allowed to propagate inside the crystal irrespective of its wave vector and polarization. Introduction of a cavity in the structure disrupts the local symmetry of the crystal, resulting in a variety of states appearing inside the band gap. Some of these states may correspond to a resonance, *i.e.*, light confined in all three directions simultaneously.

The width of the band gap is a crucial factor in order to make the band gap robust with respect to fabrication disorder [18] and to effectively shield the 3D cavity states from the surrounding vacuum states [19]. Exceptionally wide band gaps are known to occur in crystals with diamond-like symmetry [20]. An example of these are the so-called inverse-woodpile photonic crystals, consisting of two 2D arrays of nanopores [21]. These structures have been realized using various nanofabrication techniques and high-index backbones [22]. In the Complex Photonic Systems chair at the University of Twente, CMOS-compatible nanofabrication methods are used to etch pores into silicon [23–26]. The cavity in these crystals is realized by altering the radius of two proximate orthogonal *defect* pores, thereby creating an excess of one type of material in their proximal region [27].

Inverse woodpile photonic crystals with and without defects have been investigated both theoretically [27–31] and experimentally [18, 22, 32–36]. 3D confined

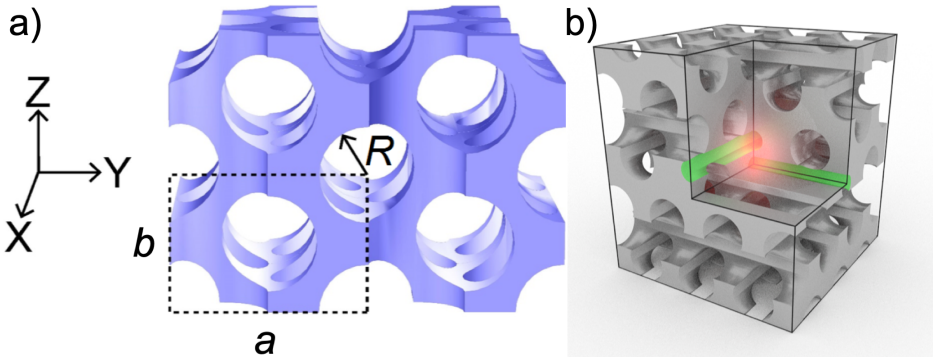

Figure 4.1: (a) Structure of the perfect inverse woodpile photonic crystal. We use a tetragonal unit cell with lattice constants b and a, and the pore radius is denoted by R. The figure shows a $2 \times 2 \times 2$ supercell. (b) Design of a cavity. The radius of two proximal defect pores (shown in green) is altered, resulting in a region with excess of either silicon or air, which behaves as a cavity confining the light (orange glow).

states in these structures have great potential for, *e.g.*, cavity QED and Anderson localization of light. To properly interpret the experimental data and provide guidance for fabrication, it is crucial to understand the dependence of the crystal properties on its structural parameters, namely the regular and defect pore sizes. Therefore, in this chapter, we perform a thorough computational characterization of light confined in photonic crystals with respect to both pore sizes. We create so-called confinement maps by keeping one of the radii constant and varying another one. Subsequently we analyze the symmetry of selected structures and investigate their potential for cavity quantum electrodynamics applications.

4.2 Methodology

We study three-dimensional (3D) cavity superlattices embedded in 3D inverse woodpile photonic band gap crystals. The inverse woodpile crystal structure consists of two perpendicular 2D arrays of nanopores with radius R in a high-refractive-index medium such as silicon [21], as illustrated in Fig. 4.1(a). The normal plane to each 2D pore array corresponds to the (110) crystal face of a conventional diamond structure. We employ a tetragonal unit cell with lattice parameters b (in the x- and z- directions) and a (in the y- direction). We set $a/b = \sqrt{2}$, which ensures a cubic crystal structure. Varying the ratio R/a results in tuning of both the center frequency and the bandwidth of the band gap, as depicted in Fig. 4.2. It has been found that the widest band gap is obtained for the ideal radius $R/a = 0.24$ [18, 28]. We note that throughout this chapter we give the frequency in its reduced form $\tilde{\omega} = \omega a/(2\pi\nu)$, where ν is the speed of light.

We introduce a defect in an inverse woodpile photonic crystal by decreasing the radius $R' \neq R$ of two proximate perpendicular *defect pores* [27], as shown

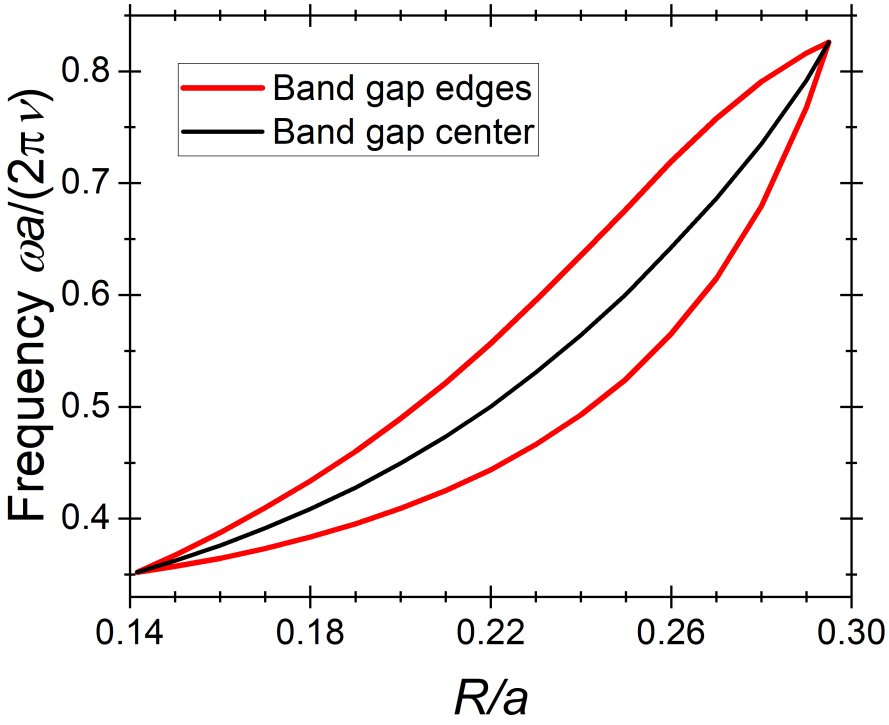

Figure 4.2: Band gap frequencies as a function of pore radius R in an inverse woodpile photonic crystal. The band gap is open for pore radii $0.15 \leq R/a \leq 0.29$, with the maximum width at $R/a \approx 0.24$.

in Fig. 4.1(b). We introduce a defect pore as every third pore of the crystal, giving rise to a defect superlattice of linear size $N = 3$. The introduction of a defect superlattice causes some of the bands to move into the band gap of the perfect crystal. The states of these bands may then become confined in various dimensions, depending on the geometry of the defect. We denote the number of dimensions in which a band of states is confined as the *confinement dimensionality* c. For more discussion on defect superlattices and wave confinement dimensionalities, see Chapter 2 of this PhD thesis and Ref. [37].

In this chapter, we aim to find point-confined ($c = 3$) bands and investigate their dependence on the structural parameters of the inverse woodpile photonic crystal. To this end, we employ the scaling analysis of Ref. [37] and Chapter 2 of this PhD thesis, supplemented by the MBC clustering algorithm presented in Chapter 3 of this PhD thesis. Specifically, we utilize the scaling to identify the set of confinement dimensionalities c present in the structure, which is then supplemented as an input to the MBC clustering algorithm. Note that the scaling analysis, for small supercells, tends to identify several bands as plane-confined ($c = 1$), which is unphysical, since our structure does not contain plane defects.

We thus automatically exclude the $c = 1$ bands from the input into the MBC algorithm. We note that, even though the power of this analysis method exceeds any other known method of confinement classification, it is known to be not fully accurate for small supercells [37], so a few out of many bands may end up being misidentified.

Our confinement analysis requires knowledge of the energy-density distribution $W(\mathbf{r})$ in the structure. We have calculated the energy densities as functions of the crystal pore radius R/a and the defect pore radius R'/R using the plane-wave expansion method implemented in the MPB code [38]. We normalize each band so that $\int_{V_S} W \mathrm{d}V = 1$. The band structure of the crystal with $R/a = 0.24$ and $R' = 0.5R$ in Fig. 4.8 has also been computed using the MPB code. In the isosurface plots, we always chose to plot the isosurface corresponding to the third of the maximum of the energy density $W(\mathbf{r}) = \max_{V_S} W(\mathbf{r})/3$ as a representative gauge. For applications in spontaneous emission control, we also investigate the maximum energy density of each band, defining $\Omega := \max_{V_S} W(\mathbf{r})$. High Ω then corresponds to high concentration of energy in the cavity.

4.3 Confinement maps

Fig. 4.3 depicts the map of $c = 3$ point-confined bands in an inverse woodpile superlattice with regular pore radius $R = 0.24a$, while varying radius R' of the defect pore. We observe several interesting features. Firstly, there is a minimal deviation of the defect pore radius from the regular one necessary for the 3D confined bands to be present. In this case this restriction appears to be $R' \leq 0.8R$ or $R' \geq 1.2R$.

Secondly, we observe that for $R' < R$, the confined bands descend into the band gap from its top edge, while for $R' > R$, the confined bands ascend from the bottom edge. This is in agreement with the analysis of Ref. [39] and with the semiconductor analogy, where $R' < R$ corresponds to donor doping, while $R' > R$ is analogous to acceptor doping [40]. In the photonic case, we can interpret this behavior using the energy functional

$$\mathcal{U}(\mathbf{E_k}) = \frac{\int_{V_S} |\boldsymbol{\nabla}_\mathbf{k} \times \mathbf{E_k}|^2 \mathrm{d}V}{\int_{V_S} \varepsilon |\mathbf{E_k}|^2 \mathrm{d}V}, \tag{4.1}$$

where $\boldsymbol{\nabla}_\mathbf{k} := \boldsymbol{\nabla} + \mathrm{i}\mathbf{k}$, V_S denotes the superlattice volume and $\mathbf{E_k}$ is the periodic part of a specific mode corresponding to the wave-vector $\mathbf{k}$. It is known that each higher-frequency mode $\mathbf{E_k}$ minimizes the functional $\mathcal{U}(\mathbf{E_k})$ in the space orthogonal to all the lower-frequency modes, see Chapter 1 of this PhD thesis and Ref. [17]. The band gap appears if there is a large frequency difference between two consecutive modes. Decreasing the size of the defect pores $R' < R$, results in added silicon in the crystal, which provides more opportunity to concentrate the electromagnetic energy in the high-index material and thus allowing for the minimum of the energy functional at lower frequency, pushing the bands from the top of the band gap downwards. On the other hand, increasing the size of the defect pores $R' > R$ results in more air in the structure and thus restricts

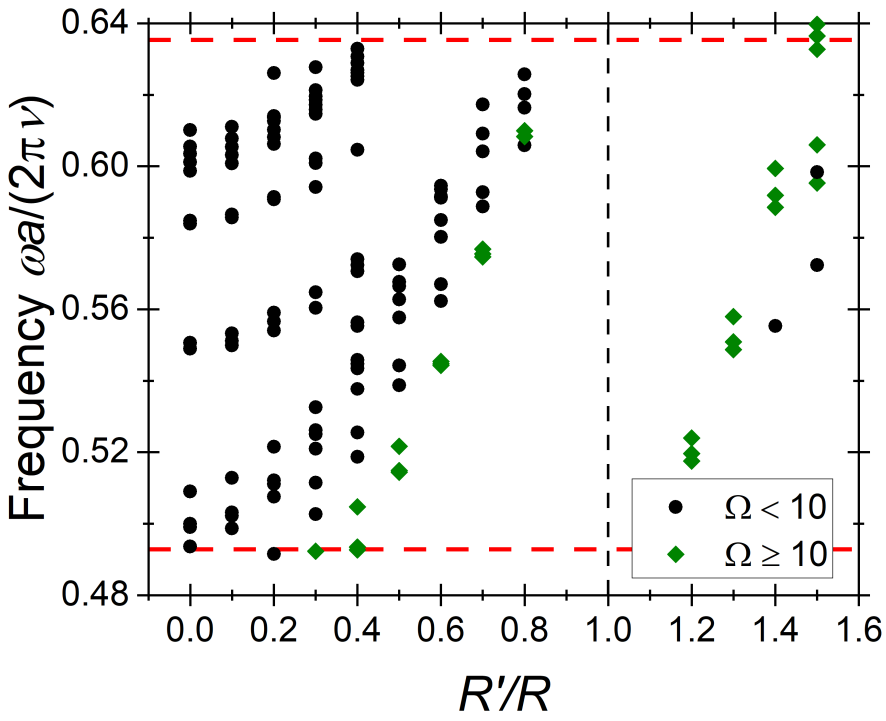

Figure 4.3: Confinement map of point-confined $c = 3$ bands in an inverse woodpile superlattice with regular pore radius $R = 0.24a$ and varying radius R' of the crossing defect pores. The case of the unperturbed crystal corresponds to $R'/R = 1$ and is denoted by the dashed vertical line. Each point represents the average reduced frequency of a point-confined band and the dashed red lines represent the edges of the band gap of an unperturbed crystal. The color and shape of the symbols correspond to their values of maximum energy density Ω, as described in the legend.

the freedom of concentrating the energy in the high-index material for the bands below the band gap, thereby pushing them upwards into the gap. In this regard, it is also worth noting that larger deviations of the defect pore radius R' from the regular pore radius R provide more 3D confined bands.

Thirdly, the confined bands exhibit a clear upward moving trend with increasing R'/R, until they disappear in the top edge of the band gap, creating groups separated by frequency gaps. It is worth noting that even though there are more confined bands for small defect pore sizes, only the large enough defect radii $R' \geq 0.3R$ provide the value of $\Omega > 10$, corresponding to large energy concentration.

Finally, these defect bands do not abruptly disappear at the edges of the band gap, but sometimes extend slightly beyond them, specifically, some confined bands cross the bottom edge of the gap for $R' < R$, whereas certain bands cross the top gap edge for $R' > R$. This is because the decrease of the defect pore radius increases the total silicon volume fraction of the medium, thus effectively shifting the whole band structure slightly downwards for $R' < R$, whereas the opposite happens for $R' > R$, where the lower silicon volume fraction shifts the band structure slightly upwards.

We note that the specific case of $R = 0.24a, R' = 0.5R$ has been previously investigated by means of a somewhat naive band structure analysis by Refs. [27, 30, 31], all of which found only five 3D confined bands. Using our novel confinement identification method from Ref. [37], and Chapters 2 and 3 of this PhD thesis, we discovered in total 10 3D confined bands in the same setting.

Fig. 4.4 depicts the map of $c = 3$ point-confined bands in an inverse woodpile superlattice with larger regular pore radius $R = 0.27a$, while varying the radius R' of the defect pore. The behavior of bands here is similar to that in Fig. 4.3, with groups of bands moving from the bottom edge of the band gap upwards and disappearing at the top edge, as R'/R increases. There are, however, three qualitative differences. Firstly, in this case, $c = 3$ defect bands are observed already for $R' = 1.1R$, thus reducing the minimal relative deviation of the defect pore radius compared to the case of $R = 0.24a$. Secondly, the bands with high energy concentration $\Omega > 10$ are now sprinkled across the whole plot, suggesting that energy concentration prefers larger pore radii R.

Thirdly, we see here several bands exceeding the top of the band gap for $R' < R$, which cannot be explained by the differences in silicon volume fraction. These bands are indeed 3D confined, as confirmed by visually inspecting their energy density distribution, so this is not an artifact of the employed method. This observation confirms what has been already hinted at by the results of Chapter 3 of this PhD thesis, namely that the confinement does not suddenly stop at the top edge of the band gap, for $R' < R$. At frequencies above the point-confined $c = 3$ bands, linearly confined $c = 2$ bands appear, as seen in Chapter 3. It follows from this observation that the bands at the top of the band gap only seem to lose their confinement properties gradually, transitioning from $c = 3$ through $c = 2$ until they become extended $c = 0$ bands. In contrast to this, the bottom edge appears to be a much stricter boundary, even when the slight shift with respect to the change in the silicon volume fraction is accounted for. This

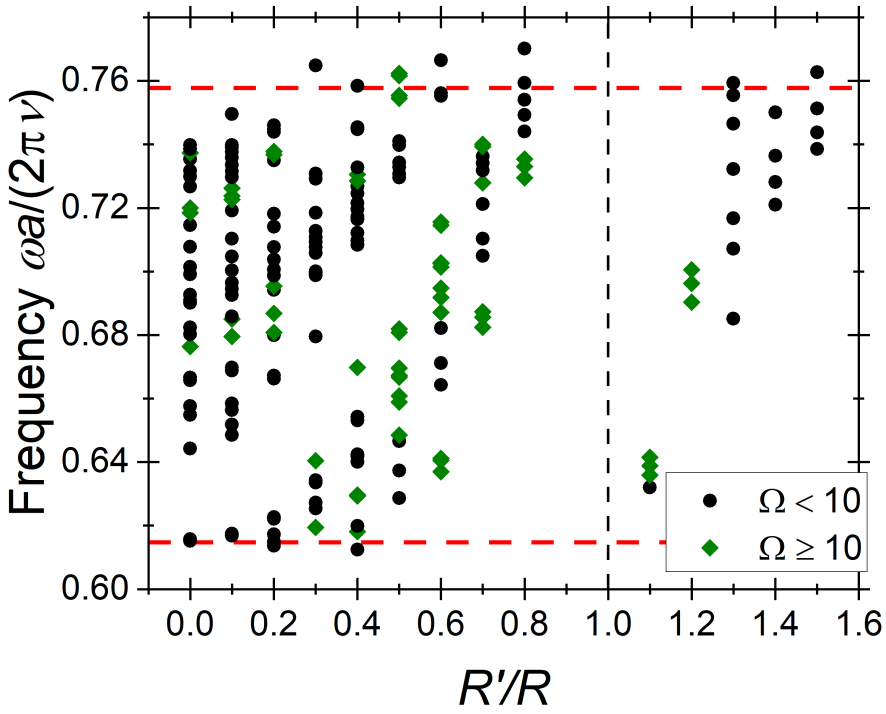

Figure 4.4: Confinement map of point-confined $c = 3$ bands in an inverse woodpile superlattice with regular pore radius $R = 0.27a$ and varying radius R' of the crossing defect pores. The case of the unperturbed crystal corresponds to $R'/R = 1$ and is denoted by the dashed vertical line. Each point represents the average reduced frequency of a point-confined band and the dashed red lines represent the edges of the band gap of an unperturbed crystal. The color and shape of the symbols correspond to their values of maximum energy density Ω, as described in the legend.

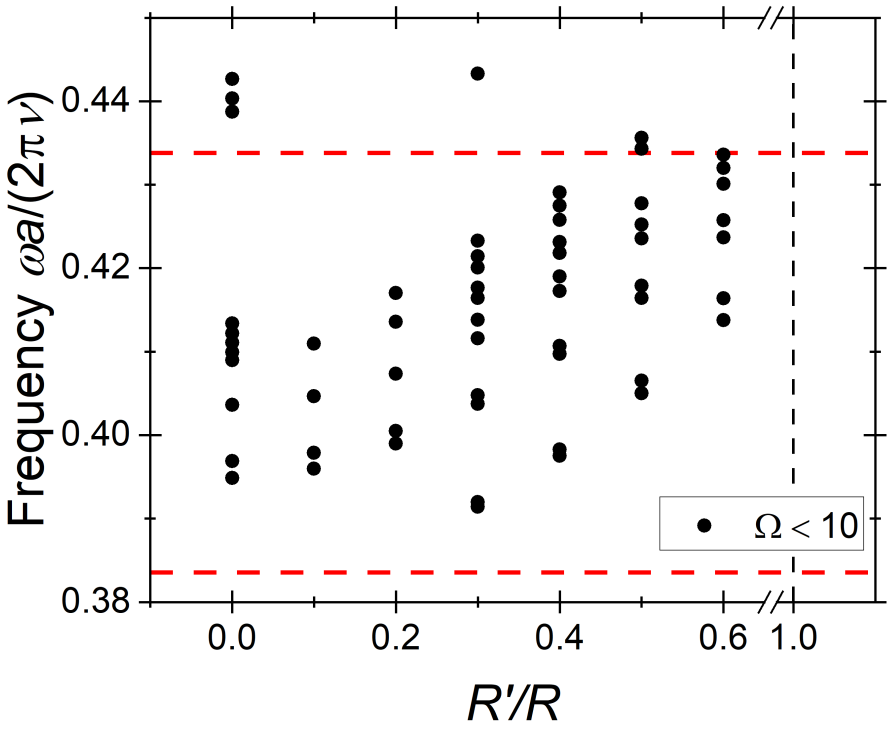

Figure 4.5: Confinement map of point-confined $c = 3$ bands in an inverse woodpile superlattice with regular pore radius $R = 0.18a$ and varying radius R' of the crossing defect pores. The case of the unperturbed crystal corresponds to $R'/R = 1$ and is denoted by the dashed vertical line. Each point represents the average reduced frequency of a point-confined band and the dashed red lines represent the edges of the band gap of an unperturbed crystal. The color and shape of the symbols correspond to their values of maximum energy density Ω, as described in the legend.

has been also observed in experiments, where the position of this edge provided great help when analyzing the wave confinement and connecting the experiments with the theory [34]. Analogously, the role of the band edges is exchanged, and for $R' > R$, the top edge of the band gap acts as a hard boundary, only slightly shifted by the change in the silicon volume fraction, while at the bottom edge, the bands seem to lose their confinement properties only gradually.

Fig. 4.5 depicts the map of $c = 3$ point-confined bands in an inverse woodpile superlattice with small regular pores of the radius $R = 0.18a$, while varying the radius R' of the defect pore. Once again, we observe groups of bands emerging from the top of the band gap and descending into the gap with decreasing pore radius. A crucial observation here is that no 3D confined bands have been found for the defect pore radii $R' > 0.6R$, including no confined acceptor-like bands for $R' > 0.6R$. Notably, there is also a lack of bands with $\Omega > 10$, which means that

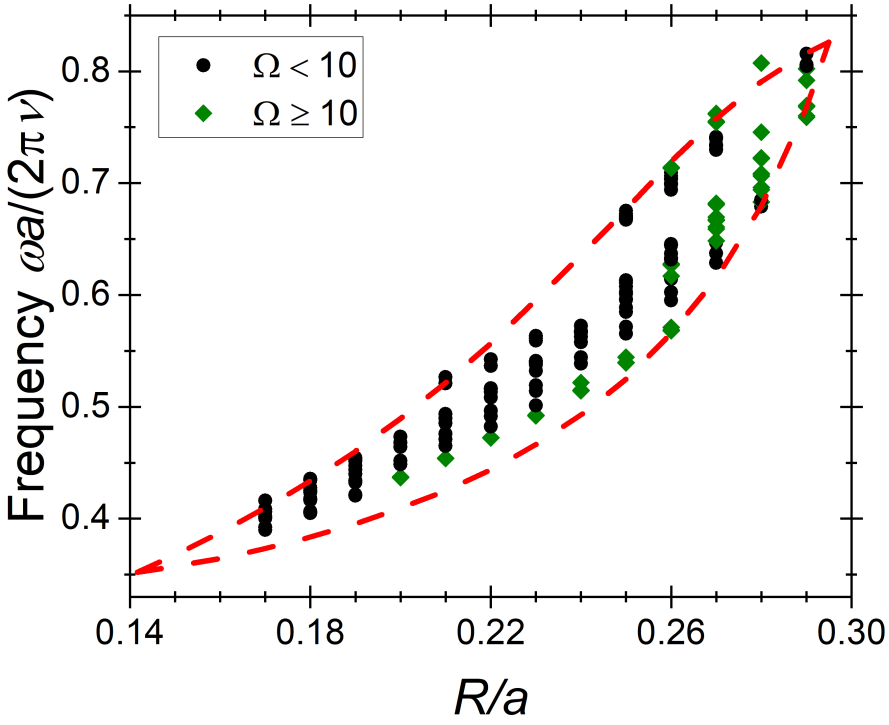

Figure 4.6: Confinement map of point-confined $c = 3$ bands in an inverse woodpile superlattice with varying regular pore radius R and constant ratio $R'/R = 0.5$. Each point represents the average reduced frequency of a point-confined band and the dashed red lines represent the edges of the band gap of an unperturbed crystal. The color and shape of the symbols correspond to their values of maximum energy density Ω, as described in the legend.

for $R = 0.18a$ the energy concentration is in general weaker than in the case of larger pores. There seems to be a significant preference for both the existence and the strength of 3D confinement in structures with larger regular pores. This discovery is of considerable practical importance, since in real photonic crystal fabrication there is a propensity towards smaller pores. Our research thus offers important guidelines for manufacturing inverse woodpile superlattices for confinement experiments and applications.

Fig. 4.6 depicts the map of $c = 3$ point-confined bands in an inverse woodpile superlattice from an alternative point of view, where the ratio between the defect and the regular pore radius $R'/R = 0.5$ is kept constant, while R is altered. For viewing convenience, we also replotted this data in Fig. 4.7, where we subtracted the band gap center frequency ω_c for each R from the band frequencies.

First of all, it is interesting that, despite the band gap having nonzero width, there are no 3D confined bands for $R = 0.15a$ and $R = 0.16a$. This is not the case

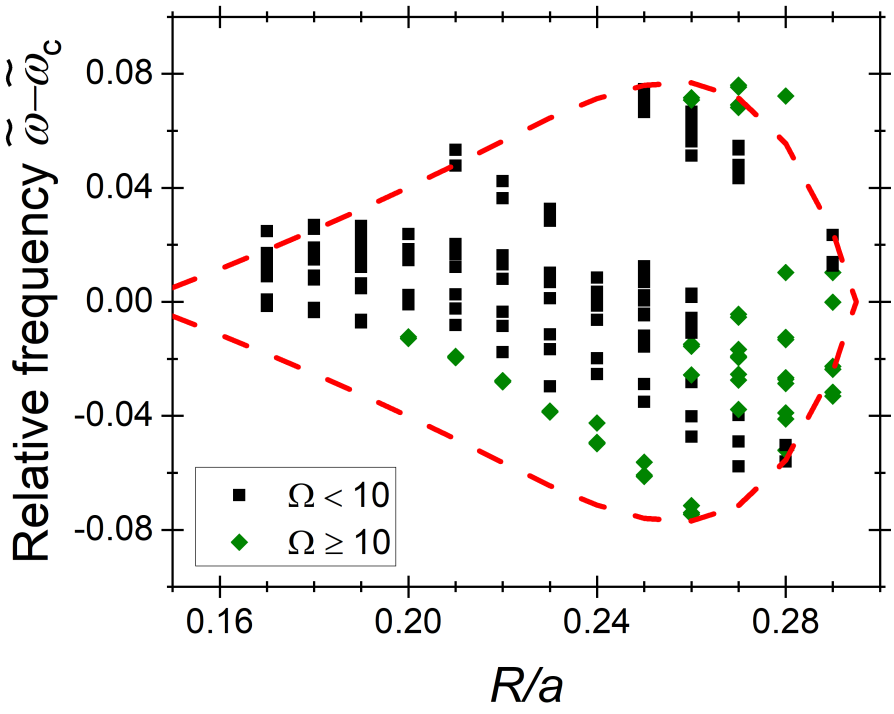

Figure 4.7: Confinement map of point-confined $c = 3$ bands in an inverse woodpile superlattice with varying regular pore radius R and constant ratio $R'/R = 0.5$. This plot shows the same data as Fig. 4.6, but the frequency of each structure has been adjusted by subtracting the center of the band gap for each regular pore radius R. Each point represents the average relative frequency of a point-confined band and the dashed red lines represent the edges of the band gap of an unperturbed crystal. The color and shape of the symbols correspond to their values of maximum energy density Ω, as described in the legend.

at the opposite side of the band gap, where 3D confined bands appear even very close to its closing at $R = 0.29a$. Similarly to the other studied cases, we observe that $\Omega > 10$ appears only in structures with larger radius $R \geq 0.20a$. This is all in agreement with our statement above that the strongly confined bands are more abundant in structures with larger pores. There is also visible movement of the confined bands from the top of the band gap towards its bottom, as R/a increases. These bands again form groups, which get more separated in frequency from each other as the band gap becomes wider.

4.4 Photonic states beyond quasiatomic orbitals

Here, we investigate more closely the energy-density profiles of some of the confined bands presented above. We specifically concentrate on the structure

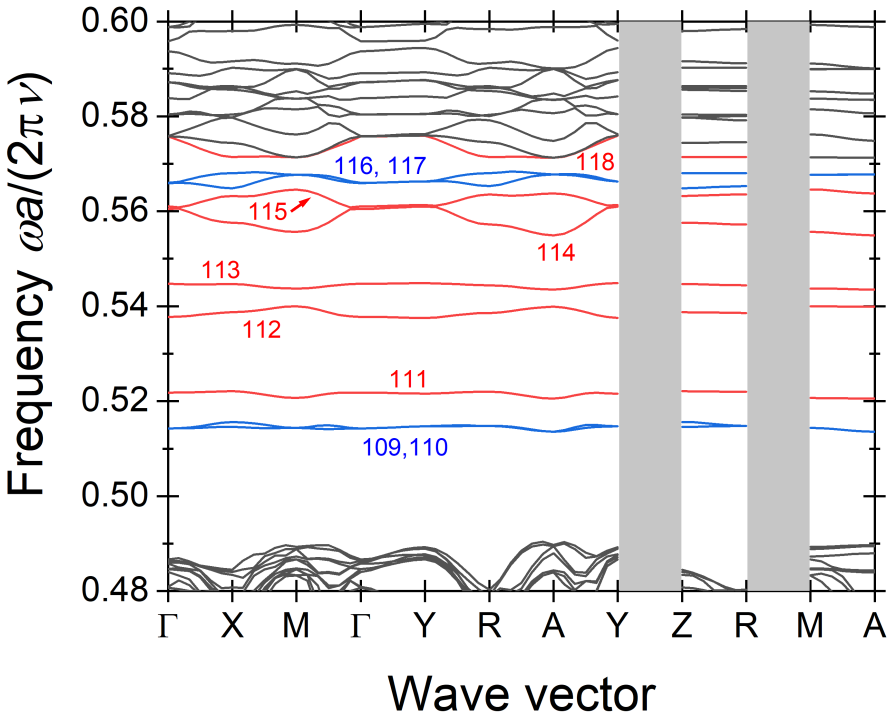

Figure 4.8: Band structure of an inverse woodpile crystal with regular pore radius $R = 0.24a$, and the defect pore radius $R' = 0.5R$. Bands that are identified as $c = 3$ confined are colored, with red designating individual bands and blue pairs of degenerate bands. The bands are also labeled by their band number N_b.

with $R = 0.24a$, $R' = 0.5R$, but as we will see, the main results can be easily generalized to inverse woodpile structures in general. Some useful properties, such as band degeneracies, are best observed from the photonic band structure. Fig. 4.8 shows the band structure of an inverse woodpile crystal with $R = 0.24a$, $R' = 0.5R$. The bands that are identified to have $c = 3$ confinement above (see Fig. 4.3), have been colored to be easily recognizable. For convenience, we distinguish the bands by their band number N_b, ordering the bands ascendingly according to their frequencies.

First, we analyze the energy-density profile of the $N_b = 111$ band, which has been investigated in detail by Refs. [27, 30, 31]. Specifically, Ref. [30], based also on data published by Ref. [27], concluded that this band represents a quadrupole, analogous to a 3d electronic orbital. Here we will explain that the analogy between inverse woodpile photonic crystals and atomic orbitals is misleading and that the inverse woodpile photonic structure actually presents a new challenge in symmetry description.

Fig. 4.9(a) depicts a 3D view of the energy-density profile of the band $N_b = 111$, confined within the cavity created by the defect pores. One can immediately see

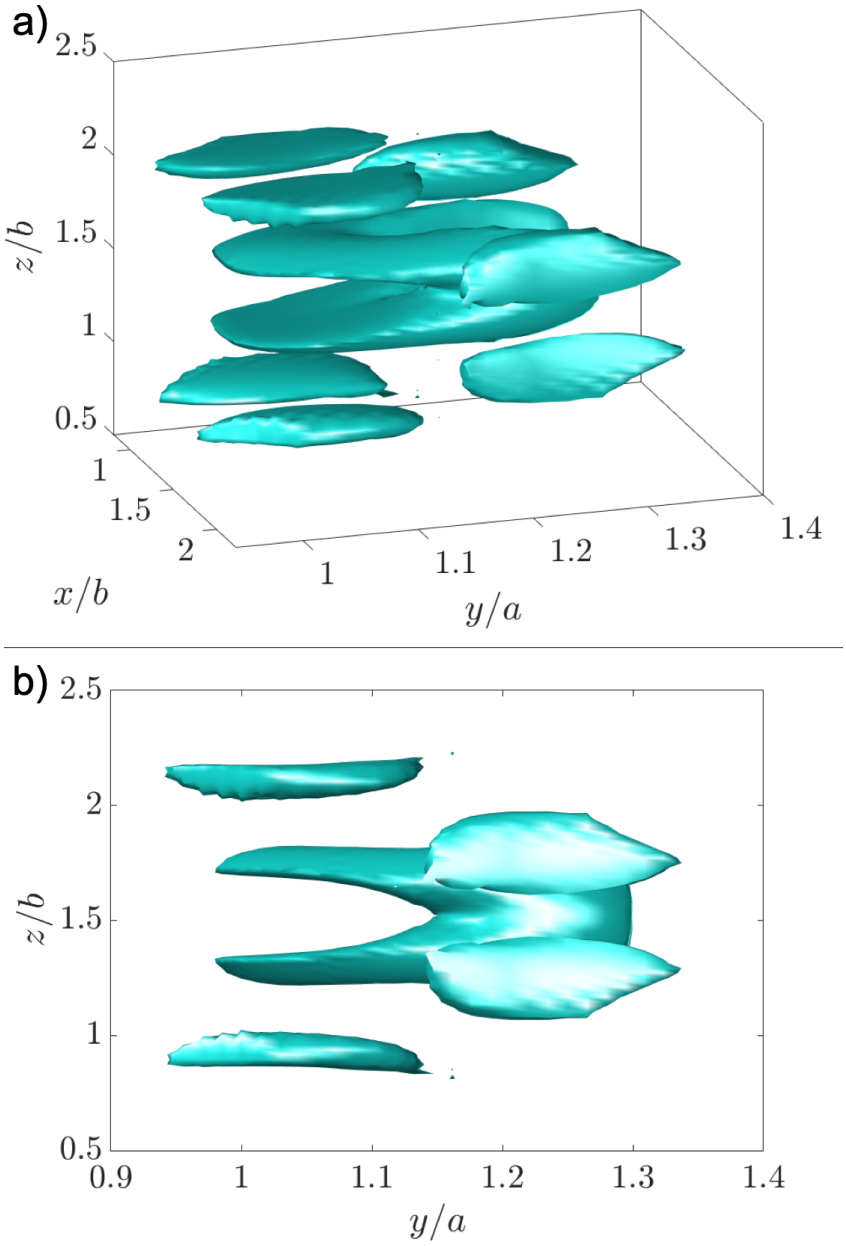

Figure 4.9: 3D isosurface plot of the energy density in the confined band $N_b = 111$ in an inverse woodpile crystal with the regular pore radius $R = 0.24a$, and defect pore radius $R' = 0.5R$. The energy profile exhibits specific symmetries inherited from the parent defect superlattice. Besides the mirror symmetries along the $z/b \approx 1.5$ and $x/b \approx 1.5$ planes, it is also symmetric with respect to mirroring with according to the $y/a \approx 1.15$ plane combined with 90° rotation about the $(x/b, z/b) \approx (1.5, 1.5)$ axis. The a) 3D view from an arbitrary angle. b) View of the y-z plane.

that the symmetries here are highly influenced by the defect-pore symmetry in Fig. 4.1(b). There is a high-field volume around $x/b = 1.5, y/a = 1.15, z/b = 1.5$. The volume can be divided by the plane $y/a \approx 1.15$ into two half-spaces, where it contains a dent in each of these half-spaces. For $y/a < 1.15$, the dent is along the x direction and is surrounded in the same half-space by two smaller regions at both $z/b < 1.5$ and $z/b > 1.5$. For $y/a > 1.15$, the second dent in the central volume spreads in the z direction and is surrounded by two smaller regions at both $x/b < 1.5$ and $x/b > 1.5$. The energy-density profile exhibits mirror symmetries along the $z/b \approx 1.5$ and $x/b \approx 1.5$ plane, but not along any plane of constant y/a, similarly to the parent superlattice.

From the view in Fig. 4.9(a), it is clear that the energy density does not have the quadrupolar profile as in a 3d electronic orbital, since it lacks the 90° rotational symmetry required for the 3d electronic orbital. However, one can argue that the actual band symmetry is even more interesting than that of the 3d orbital. Fig. 4.9(b) depicts the y-z plane view of the energy density for the same band $N_b = 111$. From this view, it becomes clear that the confined band actually exhibits mirror symmetry with respect to the plane $y/a \approx 1.15$ combined with a 90° rotation about the $(x/b, z/b) \approx (1.5, 1.5)$ axis.

This discovery brings us to an extremely interesting fundamental question. Instead of striving for strict analogies in symmetries between the electronic orbitals and photonic bands, photonic structures could be utilized to create photonic analogies of "orbitals" with a much greater variety of geometries and symmetries than would be feasible in spherical atoms [41], and controllable in more complicated electronic systems. Since there is a great diversity of photonic crystals of various geometries and a plethora of options for introducing defects of different kinds in them (see, *e.g.*, Refs. [17, 20]), it seems highly plausible that the set of symmetries achievable by "photonic orbitals" could be much more plentiful than that achievable in electronic orbitals. Since it is well known from atomic solid-state physics that the symmetries of atomic orbitals are closely tied to the appearance of the band structure and even to the macroscopic behavior of materials, such as their placement in the periodic table [40], it would be exciting to investigate to what extent the symmetries in "photonic orbitals" translate to the macroscopic behavior of "photonic solid-state matter" and how their great variety could be utilized.

4.5 Symmetry and degeneracy

Fig. 4.10 depicts the x-z view of all the nondegenerate 3D confined bands in Fig. 4.8. It appears that the band $N_b = 118$ is degenerate with the band $N_b = 119$, which has not been identified as confined. This is likely due to the decreased accuracy of the employed scaling method for small supercells, as described in more detail in Ref. [37], and Chapters 2 and 3 of this PhD thesis.

All bands depicted appear to have unrelated spatial energy-density profiles, which is in agreement with the fact that these bands are nondegenerate. Even though they appear to have 90° rotational symmetries, this is just an illusion

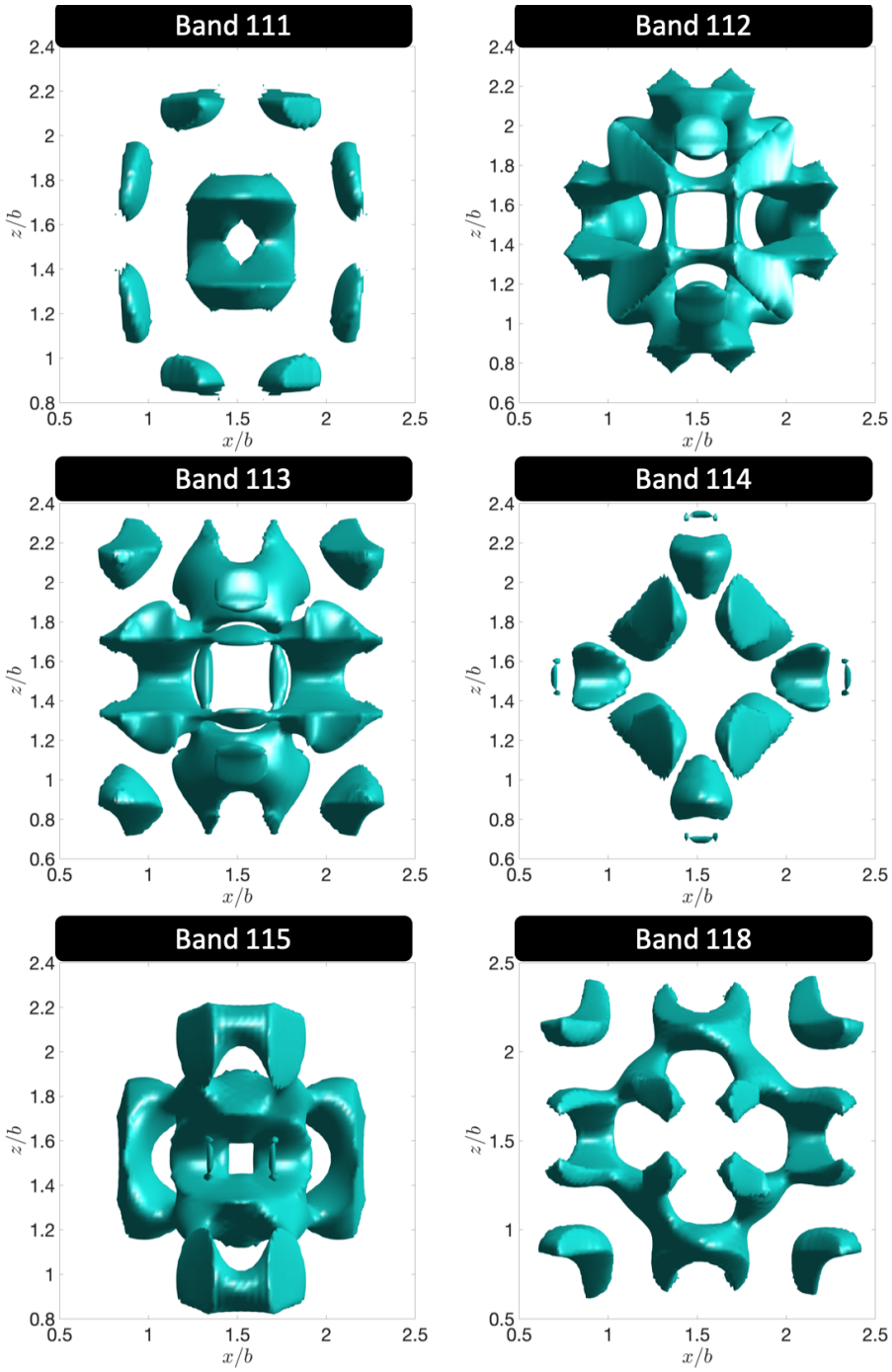

Figure 4.10: The x-z plane profile of the energy-density distribution of the nondegenerate 3D confined bands in an inverse woodpile crystal with the regular pore radius $R = 0.24a$, and the defect pore radius $R' = 0.5R$. The plane view may give an impression of the 90° rotational symmetry of these profiles, but that is misleading, as is easily verified by looking at the 3D profile of the band $N_b = 111$ in Fig. 4.9.

created by the plane-view of the plots, as is clearly seen by inspecting different views of band $N_b = 111$ in Figs. 4.10 and 4.9. Nevertheless, it is important to stress that these profiles exhibit mirror symmetries with respect to the $x/b = 1.5$ and $z/b = 1.5$ planes, passing through the axes of each defect pore, respectively.

Fig. 4.11 depicts the two pairs of degenerate bands $N_b = 109, 110$ and $N_b = 116, 117$. These bands are related to each other by the mirror symmetries along the planes $x/b \approx 1.5$ and $z/b \approx 1.5$. In solid-state physics, atomic orbitals are categorized as different spherical multipoles. This is possible due to the spherical symmetry of the atomic geometry, with each multipole exhibiting a lesser than spherical symmetry. One thus obtains three mutually orthogonal dipoles, each exhibiting a 180° rotational symmetry along every plane. The inverse woodpile structure does not have spherical symmetry, albeit a lower one. Namely, only the x-z plane is rotationally symmetric with respect to 180°. This symmetry thus only allows for two mutually orthogonal dipoles, which are both symmetric with respect to 180° rotation in the x-z plane. Exactly this property is exhibited by the band pairs $N_b = 109, 110$ and $N_b = 116, 117$. We therefore interpret these two pairs of degenerate pores as generalized dipoles for the case of the inverse woodpile structural symmetry. Moreover, within the limited set of the energy-density profiles that we have visually investigated, it seems that if the energy-density profile of a band is not symmetric with respect to both the mirror planes $x/b = 1.5$ and $z/b = 1.5$, the band turns out to be degenerate with another band which then complements these mirror symmetries. This symmetry relation could therefore be used to spot or confirm the presence of degenerate bands in the inverse woodpile photonic band structure and possibly even be generalized to other situations.

Finally, Fig. 4.12 depicts the evolution of the band $N_b = 111$ in structures with increasing pore radii R, while maintaining the ratio R'/R. The energy-density maximum of the band is changing with R, which makes it difficult to plot the same isosurface every time. Nevertheless, the mode seems to maintain a similar symmetric profile shape with strongly varying pore radius. This visualisation confirms the results from Fig. 4.7, that for the radii $R = 0.15a$ and $R = 0.27a$ this band is not 3D confined, since in both cases the profile extends throughout the whole supercell, at least in the x-z plane. It is remarkable that even for $R = 0.27a$, the shape of the central volume still resembles the confined profile seen for lower radii. Overall, Fig. 4.12 offers an interesting observation that, for a given band, its energy-density profile is conserved for strongly varying structural parameters of the inverse woodpile structure.

4.6 Enhancement of the local density of states

It is known that, in thermodynamic equilibrium, the time-averaged energy density $\overline{W_\omega}$ of the electromagnetic field of the frequency ω corresponds to [2]

$$\overline{W_\omega(\mathbf{r}, \omega)} = \overline{w}(\omega, T) N(\mathbf{r}, \omega), \tag{4.2}$$

where $\overline{w}(\omega, T)$ is the average energy per mode, $N(\mathbf{r}, \omega)$ is the local density of states (LDOS), and T is the temperature. Expression (4.2) suggests that by

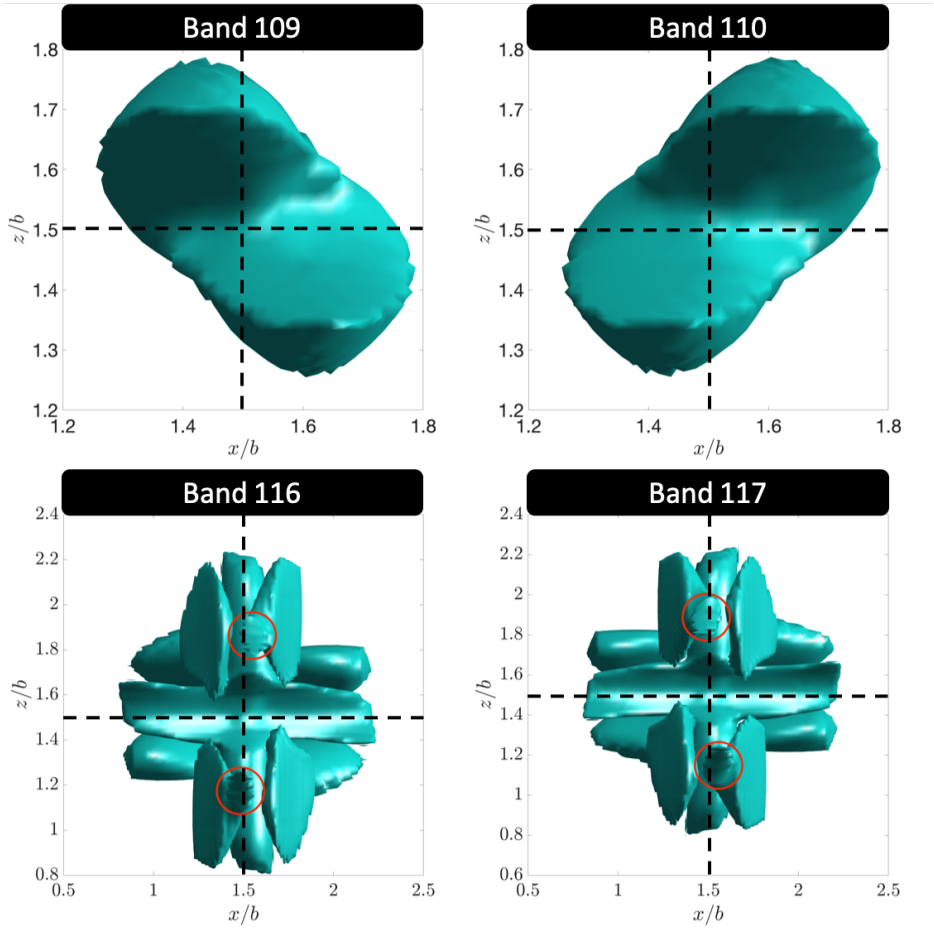

Figure 4.11: The x-z plane profile of the energy-density distribution of the degenerate pairs of 3D confined bands in an inverse woodpile crystal with regular pore radius $R = 0.24a$, and defect pore radius $R' = 0.5R$. The dashed lines indicate the planes of the mirror symmetry between these bands and the red circles for the bands $N_b = 116, 117$ indicate the profile parts where the mirror symmetries can be easily spotted.

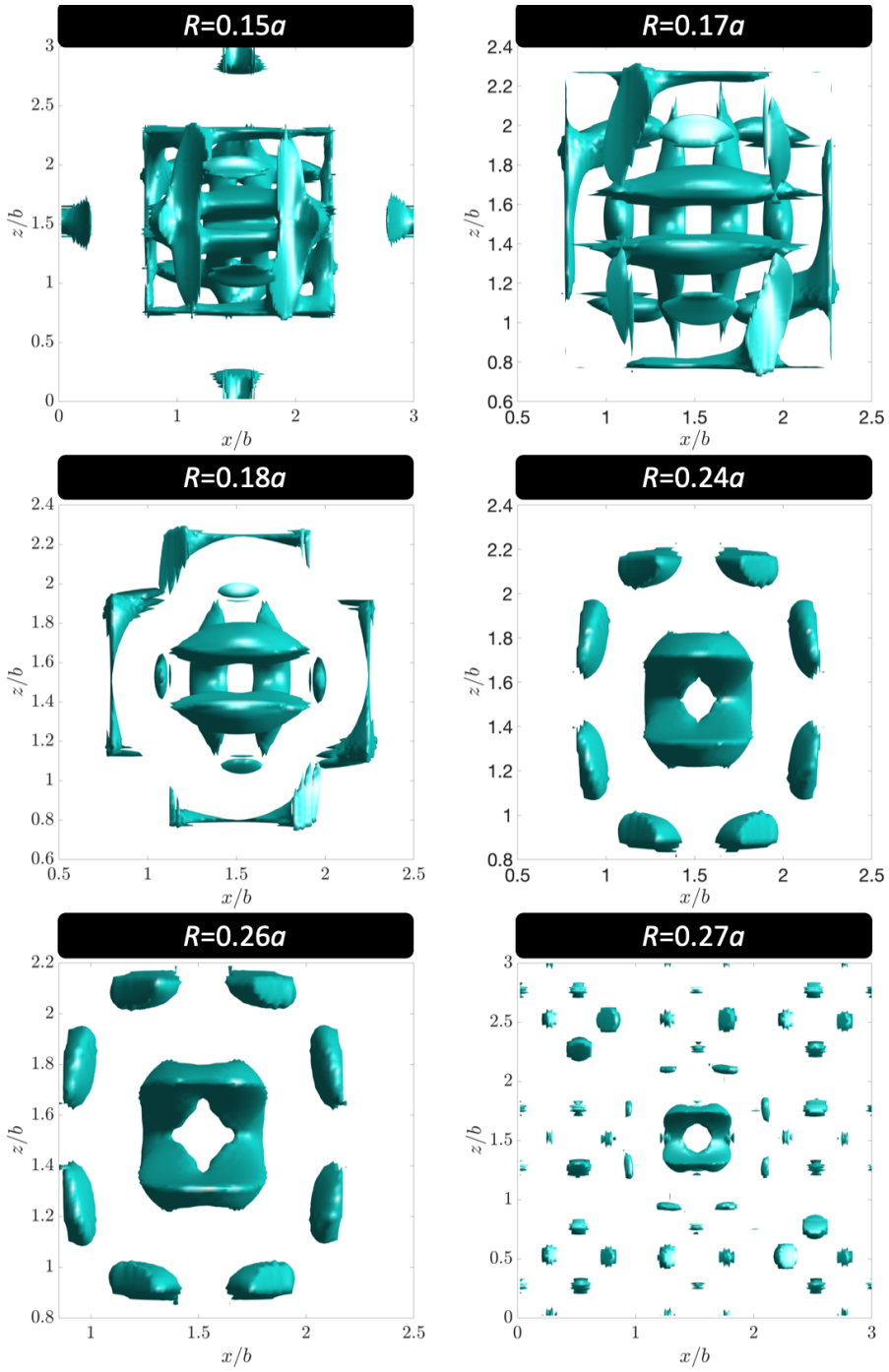

Figure 4.12: The x-z plane profile of the energy-density distribution of the $N_b = 111$ band in an inverse woodpile crystal with varying regular pore radius R, and the defect pore radius $R' = 0.5R$.

manipulating the energy density W, we can influence the LDOS, which is a crucial quantity in cQED [2]. Large LDOS is favorable for cQED applications, at first for enhanced spontaneous emission and, at even larger LDOS, for cQED strong coupling whereby quantum matter states are hybridized with photonic states. By positioning quantum dots within the pores of inverse woodpile photonic crystal superlattices [42] and coupling them to the right electromagnetic frequencies, it is possible to observe these cQED phenomena. It is therefore important to investigate the energy-density enhancement properties of the inverse woodpile photonic crystals with respect to their structural parameters.

In Section 4.3, we have already employed Figs. 4.3-4.7 to analyze the energy enhancement for different bands in superlattices of varying pore radii. We concluded that larger pore radii R are generally more favorable towards large enhancements. Out of all the investigated bands, $N_b = 108$ in the case of the $R = 0.27a, R' = 1.2a$ structure has the largest maximum of the energy density $\Omega = 29.6$. We therefore investigate the energy profile of this acceptor-like band in greater detail.

Fig. 4.13(a) shows the cross-section of the permittivity of the investigated structure in the plane $y/a = 1$. Fig. 4.13(c) then depicts the energy density distribution W of the band $N_b = 108$. To investigate the energy density more quantitatively, we plot W along the red line in the figure, corresponding to $(x/b, y/a) = (0.87, 1)$, resulting in the plot in Fig. 4.13(c). Fig. 4.13(e) also contains an extended band $N_b = 54$ for reference, to help us establish the vacuum energy density level by looking at its value of W in the air regions. This vacuum energy density turns out to be around $W = 0.03$. From this graph, it is clear that the band $N_b = 108$ has large energy-density peaks but these are restricted to the regions of high permittivity. In the central cavity region, the distribution of W within the large pore varies considerably and is an order of magnitude greater at the pore walls than at the pore center. Taking into account that quantum dots embedded in a crystal usually stick to the silicon walls, this structure could provide an LDOS enhancement of around one order of magnitude compared to the vacuum level. Nevertheless, overall, it appears that the lack of silicon and air regions that are too large significantly restrict the energy density distribution in the acceptor-like structure, thus making it a sub-par candidate for cQED applications.

To observe the influence of donor-like structures with $R' < R$ on the energy density enhancement, we investigate the band $N_b = 209$ in the superlattice with regular pore radius $R = 0.26a$ and $R' = 0.5R$, which exhibits the maximum of the energy density $\Omega = 25.7$ that is the largest among the investigated donor-like structures. The permittivity distribution of this structure in the plane $y/a = 1.13$ is depicted in Fig. 4.13(b) and the energy density profile of the band $N_b = 209$ in the same plane is in Fig. 4.13(d). Fig. 4.13(f) shows the energy density profile along the red line in Fig. 4.13(d), given by $(x/b, y/a) = (1.60, 1)$. Again, we depict also an extended band $N_b = 54$ for reference. In this case, since the air volume is much smaller compared to the amount of silicon around the cavity, the energy density within the central defect pore drops only slightly compared to its values in the surrounding silicon. Overall, even in the center of the defect

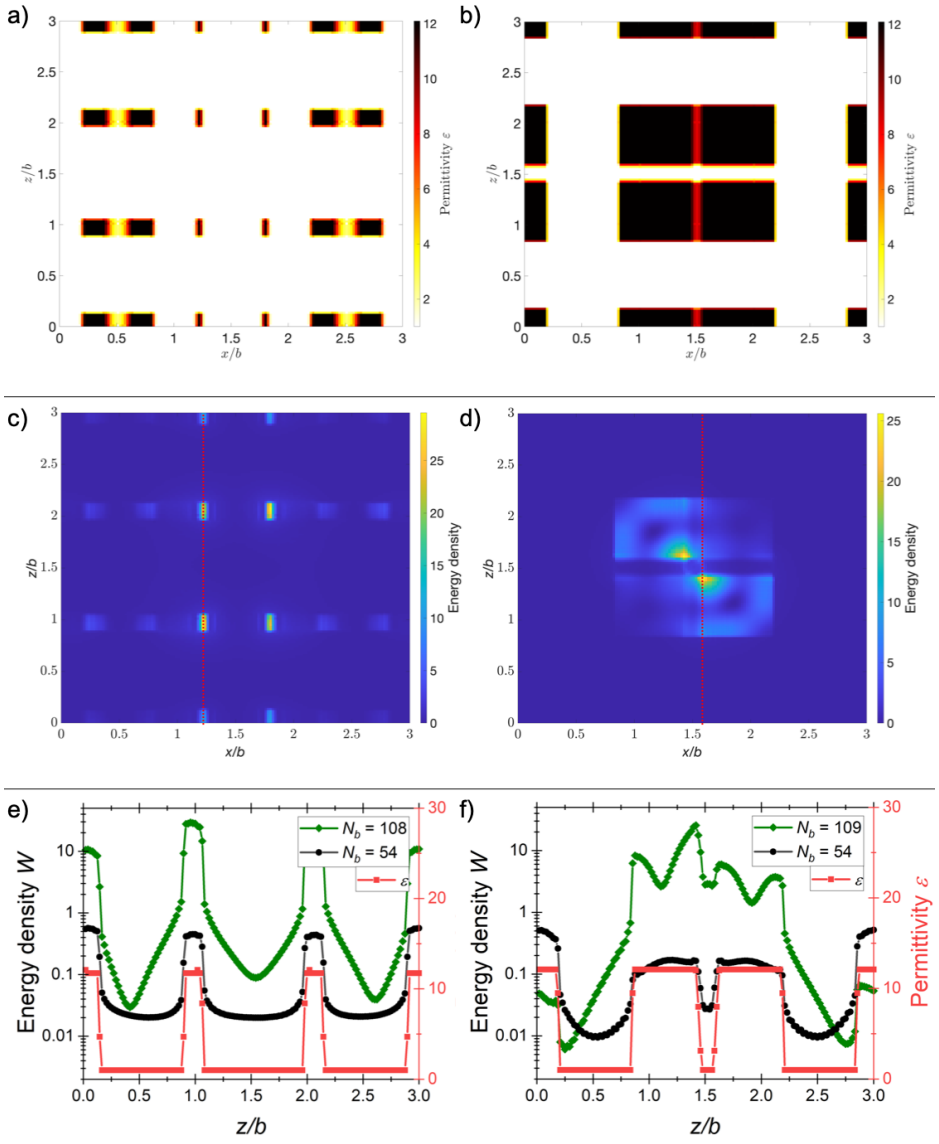

Figure 4.13: Energy enhancement in two different inverse woodpile structures. (a), (c), (e) Acceptor-like structure with the regular pore radius $R = 0.27a$, defect pore radius $R' = 1.2R$, band number $N_b = 108$. (b), (d), (f) Donor-like structure with the regular pore radius $R = 0.26a$, defect pore radius $R' = 0.5R$, band number $N_b = 109$. (a) Permittivity distribution of the acceptor-like structure in the $y/a = 1$ plane. (b) Permittivity distribution of the donor-like structure in the $y/a = 1.13$ plane. (c) Energy density distribution of the acceptor-like band $N_b = 108$ in the $y/a = 1$ plane. (d) Energy density distribution of the donor-like band $N_b = 109$ in the $y/a = 1.13$ plane. (e) Cross-section of the energy density distribution for the $(x/b, y/a) = (0.87, 1)$ line, denoted by the red line in (c). Depicted is the confined band $N_b = 108$ and a reference extended band $N_b = 54$. (f) Cross-section of the energy density distribution for the $(x/b, y/a) = (1.60, 1)$ line, denoted by the red line in (d). Depicted is the confined band $N_b = 109$ and a reference extended band $N_b = 54$.

pore where W is the smallest, the energy-density enhancement compared to the vacuum level at $W = 0.01$, and therefore also the LDOS enhancement, is more than two orders of magnitude.

To conclude, we observed three competing phenomena with regard to cQED applications: Firstly, donor-like cavities are preferable for cQED due to larger silicon and smaller air regions. Secondly, larger defect pore deviations, *i.e.*, smaller defect pore radii R' for donor-like structures, favor the appearance of more confined bands. Thirdly, larger defect pore radii R', appear to favor more concentrated energy density. From our investigation it therefore seems that a good balance between these three requirements could be around the defect pore radius $R' \approx 0.6R$ slightly above half the regular pore radius R. We also further reiterate our finding that larger regular pore sizes R overall help to enhance both the number of 3D confined bands and the energy concentration.

4.7 Conclusion

In this chapter we performed computational characterization of light confined in 3D inverse woodpile photonic superlattices with respect to their structural parameters, namely the regular and the defect pore radii. We created maps of 3D confined bands via various cross sections through the parameter space of the two pore radii and used these to analyze the influence of the superlattice structure on the confinement. We found that larger regular pore radii favor more confined bands and these bands also tend to have more concentrated energy densities.

Further, we analyzed symmetries of chosen 3D confined bands in 3D inverse woodpile photonic superlattices. We concluded that the inverse woodpile photonic crystal bands exhibit very different symmetries compared to electronic orbitals, which is caused by the underlying crystal structure. We propose that attention should be given to confined band symmetries in "photonic solid-state matter" and their influence on the properties of these materials.

Finally, we analyzed the potential of the inverse woodpile photonic structures for cavity QED applications. To this end, large concentration of energy density, proportional to LDOS, must be present in the defect-pore region. We found that even though the acceptor-like structures with defect pores larger than the regular pores may offer higher energy concentration, this energy is mostly concentrated in small regions of silicon and decays rapidly in air. On the other hand, the investigated donor-like structure, despite exhibiting less concentrated energy density, provides overall higher values of energy density within the cavity due to larger silicon and smaller air volumes inside. Therefore, donor-like structures seem to be more favorable for spontaneous emission control.

In the future, more data should be gathered and analyzed to obtain even deeper understanding of the confinement behavior of the inverse woodpile superlattices. This investigation should be extended to encompass not only 3D confined bands, but also 2D confined ones, which have been previously shown to be present in these structures as well. Finally, this investigation should be extended to other types of photonic superlattices.

Bibliography

[1] K. J. Vahala. "Optical Microcavities". In: *Nature* 424.6950 (2003), pp. 839–846. ISSN: 1476-4687. DOI: 10.1038/nature01939.

[2] L. Novotny and B. Hecht. *Principles of Nano-Optics*. Cambridge: Cambridge University Press, 2006. ISBN: 978-0-511-81353-5.

[3] J. M. Gérard, B. Sermage, B. Gayral, B. Legrand, E. Costard, and V. Thierry-Mieg. "Enhanced Spontaneous Emission by Quantum Boxes in a Monolithic Optical Microcavity". In: *Phys. Rev. Lett.* 81.5 (1998), pp. 1110–1113. DOI: 10.1103/PhysRevLett.81.1110.

[4] J. P. Reithmaier, G. Sęk, A. Löffler, C. Hofmann, S. Kuhn, S. Reitzenstein, L. V. Keldysh, V. D. Kulakovskii, T. L. Reinecke, and A. Forchel. "Strong Coupling in a Single Quantum Dot–Semiconductor Microcavity System". In: *Nature* 432.7014 (2004), pp. 197–200. ISSN: 1476-4687. DOI: 10.1038/nature02969.

[5] E. Peter, P. Senellart, D. Martrou, A. Lemaître, J. Hours, J. M. Gérard, and J. Bloch. "Exciton-Photon Strong-Coupling Regime for a Single Quantum Dot Embedded in a Microcavity". In: *Phys. Rev. Lett.* 95.6 (2005), p. 067401. DOI: 10.1103/PhysRevLett.95.067401.

[6] D. K. Armani, T. J. Kippenberg, S. M. Spillane, and K. J. Vahala. "Ultra-High- Q Toroid Microcavity on a Chip". In: *Nature* 421.6926 (2003), pp. 925–928. ISSN: 1476-4687. DOI: 10.1038/nature01371.

[7] H. T. Miyazaki and Y. Kurokawa. "Squeezing Visible Light Waves into a 3-Nm-Thick and 55-Nm-Long Plasmon Cavity". In: *Phys. Rev. Lett.* 96.9 (2006), p. 097401. DOI: 10.1103/PhysRevLett.96.097401.

[8] R. Chikkaraddy, B. de Nijs, F. Benz, S. J. Barrow, O. A. Scherman, E. Rosta, A. Demetriadou, P. Fox, O. Hess, and J. J. Baumberg. "Single-Molecule Strong Coupling at Room Temperature in Plasmonic Nanocavities". In: *Nature* 535.7610 (2016), pp. 127–130. ISSN: 1476-4687. DOI: 10.1038/nature17974.

[9] Y. Akahane, T. Asano, B.-S. Song, and S. Noda. "High- Q Photonic Nanocavity in a Two-Dimensional Photonic Crystal". In: *Nature* 425.6961 (2003), pp. 944–947. ISSN: 1476-4687. DOI: 10.1038/nature02063.

[10] E. Krioukov, D. J. W. Klunder, A. Driessen, J. Greve, and C. Otto. "Sensor Based on an Integrated Optical Microcavity". In: *Opt. Lett.* 27.7 (2002), pp. 512–514. ISSN: 1539-4794. DOI: 10.1364/OL.27.000512.

[11] T. Baba. "Slow Light in Photonic Crystals". In: *Nat. Photonics* 2.8 (2008), pp. 465–473. ISSN: 1749-4893. DOI: 10.1038/nphoton.2008.146.

[12] S. Noda, A. Chutinan, and M. Imada. "Trapping and Emission of Photons by a Single Defect in a Photonic Bandgap Structure". In: *Nature* 407.6804 (2000), pp. 608–610. ISSN: 1476-4687. DOI: 10.1038/35036532.

[13] P. Michler, ed. *Single Quantum Dots: Fundamentals, Applications, and New Concepts*. Topics in Applied Physics v. 90. Berlin, Heidelberg, New York: Springer-Verlag, 2003. ISBN: 978-3-540-14022-1.

[14] T. Yoshie, A. Scherer, J. Hendrickson, G. Khitrova, H. M. Gibbs, G. Rupper, C. Ell, O. B. Shchekin, and D. G. Deppe. "Vacuum Rabi Splitting with a Single Quantum Dot in a Photonic Crystal Nanocavity". In: *Nature* 432.7014 (2004), pp. 200–203. ISSN: 1476-4687. DOI: 10.1038/nature03119.

[15] E. Yablonovitch. "Inhibited Spontaneous Emission in Solid-State Physics and Electronics". In: *Phys. Rev. Lett.* 58.20 (1987), pp. 2059–2062. DOI: 10.1103/PhysRevLett.58.2059.

[16] S. John. "Strong Localization of Photons in Certain Disordered Dielectric Superlattices". In: *Phys. Rev. Lett.* 58.23 (1987), pp. 2486–2489. ISSN: 0031-9007. DOI: 10.1103/PhysRevLett.58.2486.

[17] J. D. Joannopoulos, S. G. Johnson, J. N. Winn, and R. D. Meade. *Photonic Crystals: Molding the Flow of Light*. Second. Princeton: Princeton University Press, 2008. ISBN: 978-0-691-12456-8.

[18] L. A. Woldering, A. P. Mosk, R. W. Tjerkstra, and W. L. Vos. "The Influence of Fabrication Deviations on the Photonic Band Gap of Three-Dimensional Inverse Woodpile Nanostructures". In: *J. Appl. Phys.* 105.9 (2009), p. 093108. ISSN: 0021-8979, 1089-7550. DOI: 10.1063/1.3103777.

[19] W. L. Vos and L. A. Woldering. "Cavity Quantum Electrodynamics with Three-Dimensional Photonic Band Gap Crystals". In: *Light Localisation and Lasing: Random and Quasi-Random Photonic Structures*. Cambridge University Press, 2015, pp. 180–214. ISBN: 978-1-107-03877-6.

[20] M. Maldovan and E. L. Thomas. "Diamond-Structured Photonic Crystals". In: *Nat. Mater.* 3.9 (2004), pp. 593–600. ISSN: 1476-4660. DOI: 10.1038/nmat1201.

[21] K. M. Ho, C. T. Chan, C. M. Soukoulis, R. Biswas, and M. Sigalas. "Photonic Band Gaps in Three Dimensions: New Layer-by-Layer Periodic Structures". In: *Solid State Commun.* 89.5 (1994), pp. 413–416. ISSN: 0038-1098. DOI: 10.1016/0038-1098(94)90202-X.

[22] J. Schilling, J. White, A. Scherer, G. Stupian, R. Hillebrand, and U. Gösele. "Three-Dimensional Macroporous Silicon Photonic Crystal with Large Photonic Band Gap". In: *Appl. Phys. Lett.* 86.1 (2004), p. 011101. ISSN: 0003-6951. DOI: 10.1063/1.1842855.

[23] R. W. Tjerkstra, L. A. Woldering, J. M. van den Broek, F. Roozeboom, I. D. Setija, and W. L. Vos. "Method to Pattern Etch Masks in Two Inclined Planes for Three-Dimensional Nano- and Microfabrication". In: *J. Vac. Sci. Technol. B* 29.6 (2011), p. 061604. ISSN: 2166-2746. DOI: 10.1116/1.3662000.

[24] J. M. van den Broek, L. A. Woldering, R. W. Tjerkstra, F. B. Segerink, I. D. Setija, and W. L. Vos. "Inverse-Woodpile Photonic Band Gap Crystals with a Cubic Diamond-like Structure Made from Single-Crystalline Silicon". In: *Adv. Funct. Mater.* 22.1 (2012), pp. 25–31. ISSN: 1616-3028. DOI: 10.1002/adfm.201101101.

[25] D. A. Grishina, C. A. M. Harteveld, L. A. Woldering, and W. L. Vos. "Method for Making a Single-Step Etch Mask for 3D Monolithic Nanostructures". In: *Nanotechnology* 26.50 (2015), p. 505302. ISSN: 0957-4484. DOI: 10.1088/0957-4484/26/50/505302.

[26] M. J. Goodwin, C. A. M. Harteveld, M. J. de Boer, and W. L. Vos. "Deep Reactive Ion Etching of Cylindrical Nanopores in Silicon for Photonic Crystals". In: *Nanotechnology* (Submitted 2022).

[27] L. A. Woldering, A. P. Mosk, and W. L. Vos. "Design of a Three-Dimensional Photonic Band Gap Cavity in a Diamondlike Inverse Woodpile Photonic Crystal". In: *Phys. Rev. B* 90.11 (2014), p. 115140. DOI: 10.1103/PhysRevB.90.115140.

[28] R. Hillebrand, S. Senz, W. Hergert, and U. Gösele. "Macroporous-Silicon-Based Three-Dimensional Photonic Crystal with a Large Complete Band Gap". In: *J. Appl. Phys.* 94.4 (2003), pp. 2758–2760. ISSN: 0021-8979, 1089-7550. DOI: 10.1063/1.1593796.

[29] D. Devashish, S. B. Hasan, J. J. W. van der Vegt, and W. L. Vos. "Reflectivity Calculated for a Three-Dimensional Silicon Photonic Band Gap Crystal with Finite Support". In: *Phys. Rev. B* 95.15 (2017), p. 155141. ISSN: 2469-9950, 2469-9969. DOI: 10.1103/PhysRevB.95.155141.

[30] D. Devashish, O. S. Ojambati, S. B. Hasan, J. J. W. van der Vegt, and W. L. Vos. "Three-Dimensional Photonic Band Gap Cavity with Finite Support: Enhanced Energy Density and Optical Absorption". In: *Phys. Rev. B* 99.7 (2019), p. 075112. ISSN: 2469-9950, 2469-9969. DOI: 10.1103/PhysRevB.99.075112.

[31] S. A. Hack, J. J. W. van der Vegt, and W. L. Vos. "Cartesian Light: Unconventional Propagation of Light in a Three-Dimensional Superlattice of Coupled Cavities within a Three-Dimensional Photonic Band Gap". In: *Phys. Rev. B* 99.11 (2019), p. 115308. ISSN: 2469-9950, 2469-9969. DOI: 10.1103/PhysRevB.99.115308.

[32] M. Adhikary, R. Uppu, C. A. M. Harteveld, D. A. Grishina, and W. L. Vos. "Experimental Probe of a Complete 3D Photonic Band Gap". In: *Opt. Express* 28.3 (2020), p. 2683. ISSN: 1094-4087. DOI: 10.1364/OE.28.002683.

[33] R. Uppu, M. Adhikary, C. A. M. Harteveld, and W. L. Vos. "Spatially Shaping Waves to Penetrate Deep inside a Forbidden Gap". In: *Phys. Rev. Lett.* 126.17 (2021), p. 177402. ISSN: 0031-9007, 1079-7114. DOI: 10.1103/PhysRevLett.126.177402.

[34] M. Adhikary, M. Kozoň, R. Uppu, and W. L. Vos. "Observation of Light Propagation through a Three-Dimensional (3D) Superlattice of Cavities in a 3D Photonic Band Gap". In preparation.

[35] M. D. Leistikow, A. P. Mosk, E. Yeganegi, S. R. Huisman, A. Lagendijk, and W. L. Vos. "Inhibited Spontaneous Emission of Quantum Dots Observed in a 3D Photonic Band Gap". In: *Phys. Rev. Lett.* 107.19 (2011), p. 193903. ISSN: 0031-9007, 1079-7114. DOI: 10.1103/PhysRevLett.107.193903.

[36] S. R. Huisman, R. V. Nair, L. A. Woldering, M. D. Leistikow, A. P. Mosk, and W. L. Vos. "Signature of a Three-Dimensional Photonic Band Gap Observed on Silicon Inverse Woodpile Photonic Crystals". In: *Phys. Rev. B* 83.20 (2011), p. 205313. ISSN: 1098-0121, 1550-235X. DOI: 10.1103/PhysRevB.83.205313.

[37] M. Kozoň, A. Lagendijk, M. Schlottbom, J. J. W. van der Vegt, and W. L. Vos. "Scaling Theory of Wave Confinement in Classical and Quantum Periodic Systems". In: *Phys. Rev. Lett.* 129.17 (2022), p. 176401. ISSN: 0031-9007, 1079-7114. DOI: 10.1103/PhysRevLett.129.176401.

[38] S. G. Johnson and J. D. Joannopoulos. "Block-Iterative Frequency-Domain Methods for Maxwell's Equations in a Planewave Basis". In: *Opt. Express* 8.3 (2001), p. 173. ISSN: 1094-4087. DOI: 10.1364/OE.8.000173.

[39] P. R. Villeneuve, S. Fan, and J. D. Joannopoulos. "Microcavities in Photonic Crystals: Mode Symmetry, Tunability, and Coupling Efficiency". In: *Phys. Rev. B* 54.11 (1996), pp. 7837–7842. DOI: 10.1103/PhysRevB.54.7837.

[40] N. W. Ashcroft and N. D. Mermin. *Solid State Physics*. New York: Holt, Rinehart and Winston, 1976. ISBN: 978-0-03-083993-1.

[41] J. J. Sakurai and S. F. Tuan. *Modern Quantum Mechanics*. Rev. ed. Reading, Mass: Addison-Wesley Pub. Co, 1994. ISBN: 978-0-201-53929-5.

[42] A. S. Schulz, C. A. M. Harteveld, G. J. Vancso, J. Huskens, P. Cloetens, and W. L. Vos. "Targeted Positioning of Quantum Dots Inside 3D Silicon Photonic Crystals Revealed by Synchrotron X-ray Fluorescence Tomography". In: *ACS Nano* 16.3 (2022), pp. 3674–3683. ISSN: 1936-0851, 1936-086X. DOI: 10.1021/acsnano.1c06915.

5 Size-robust Discontinuous Galerkin Method for Light Propagation through Locally Periodic Media

5.1 Introduction

Photonic crystals are optical structures in which the permittivity, or refractive index, is periodically repeated [1]. In a photonic crystal structure, the translational symmetry gives rise via interference effects to a *photonic bandgap*, which is a range of frequencies for which light is not allowed to propagate inside the crystal irrespective of its wave vector and polarization [2, 3]. These periodic photonic structures allow for control of the propagation and emission of light [1, 4–10].

Among the plethora of applications of photonic crystals, the most prominent are the control of spontaneous emission of quantum emitters [11–14], cavity quantum electrodynamics [15], thermal emission control [16, 17], lasing [18], enhanced absorption in solar cells and thin films [19–21], and cloaking [22].

In order to properly understand the complex behavior of electromagnetic waves in photonic crystals, computational models are essential. A brief review of various relevant computational methods can be found in Ref. [8]. The most prominent of these methods are plane-wave expansions (PWE), finite-difference time-domain (FDTD) and finite element methods (FEM).

PWE is a spectral method that expands the dielectric function and the electromagnetic fields in terms of plane waves [23]. Although it is a conceptually simple method, it struggles to accurately represent sharp jumps in the dielectric function. Even more importantly, it assumes the crystal to have infinite extent, and thus it is unable to capture the surface effects occurring in realistic finitely large crystals.

FDTD, originally proposed by Ref [24], replaces continuous derivatives by finite differences [25]. In its simplest form it is very intuitive and it is particularly suitable for calculation of electromagnetic impulses passing through photonic structures and for calculation of time-dependent phenomena, such as decay of cavity resonances and cavity quality factors [26, 27]. The main drawback of FDTD are its high computational requirements, especially when dealing with large photonic structures, and the difficulty with accurate approximation of curved surfaces [8].

FEM are the most flexible of the computational methods, since they can han-

dle easily complex geometries of finite size, and they allow for local resolution enhancement [28, 29]. Their broad applicability ranges from high-accuracy time-harmonic problems [21, 30, 31] to time-domain computations [32], to topology optimization [33]. Due to its flexibility, FEM is also our method of choice in this chapter.

A major unresolved challenge in computational modeling of photonic crystals is the calculation of electromagnetic wave propagation through large but finite-sized structures surrounded by an external medium, which is the most relevant case for experiments and applications. The main hurdle comes from the fact that this is a multiscale problem: On one hand, there is the micro-scale, represented by the unit cell of the crystal. In order to capture the characteristic effects of photonic crystals on light, the wavelength must be of the same order of magnitude as the periodicity of the crystal, which means that the unit cell has to be resolved with sufficiently high accuracy. On the other hand, there is the macro-scale, representing the crystal domain as a whole. Photonic crystals utilized in the state-of-the-art research contain several thousands of unit cells [34]. It is immediately obvious that, if treated by standard computational methods, the resolution required to accurately resolve the problem on both scales is computationally intractable.

Despite the multiscale complexity of the realistic photonic crystal problem, the crystal remains locally periodic, even if only on a finite domain. Moreover, the larger the crystal is, the more the field inside it resembles that of a globally periodic, *i.e.*, infinite, crystal. The solutions of a globally periodic problem are also known as *Bloch modes* [35–37]. This observation suggests that it should be possible to use Bloch modes within a FEM to address the multiscale issue. Moreover, the quasi-periodic properties of the Bloch modes may allow to replace computations on the whole crystal by computations only on one unit cell, leading to construction of a so-called *size-robust* method, *i.e.*, a method with computational complexity independent of the size of the crystal.

Ref. [38] has proposed a way to utilize the quasi-periodicity of Bloch modes by introducing a special type of FEM multiscale basis functions, consisting of Bloch modes modulated by "macro-polynomials" of a specific degree. Subsequently, the form of these multiscale functions is used to construct the system matrix by a quadrature that depends on the crystal size only logarithmically, thus yielding an *essentially size-robust* method for photonic crystals that are finite in one dimension [39]. Refs. [38, 39] have demonstrated their method on a 2D example of a photonic crystal infinite in one direction and surrounded by an external medium in the other. Their approach, however, relies heavily on the fact that their model is finite in only one direction.

Furthermore, the macro-polynomials in Refs. [38, 39], serving as a partition of unity, were required to obtain a continuous approximation of the field. This approach has several drawbacks, the main of which is the overall complexity of the method, which is difficult to analyze and implement. Secondly, the existence of the macro-polynomials complicates the system matrix assembly to the extent that one can not have a stable quadrature completely independent of the crystal size.

In this chapter, we present a related, but different approach to the idea of Refs. [38, 39], to create a size robust method with a large degree of parallelism. By implementing Bloch basis functions within a Discontinuous Galerkin framework [40], the lack of continuity requirement at the crystal surface allows us to completely drop the macro-polynomials and thus make the system matrix calculation within the crystal domain truly size-robust. An additional benefit of dropping the macro-polynomials is the overall simplification of the method. We demonstrate the convergence of our method in numerical experiments on a physically realistic 2D photonic crystal of finite extent in both dimensions.

This chapter is divided into eight sections. In Section 5.2, we describe the Helmholtz problem and its weak formulation. Section 5.3 discusses the unit-cell problem used to obtain the Bloch modes. In Section 5.4 we describe the construction of the size-robust function space, the fundamental ingredient of our method. Section 5.5 provides the formulation of the discretized Helmholtz problem using the size-robust function space. Section 5.6 then gives details on the size-robust quadrature used to construct the system matrix for the crystal domain. In Section 5.7, we illustrate the key properties of our method by means of numerical experiments. Finally, in Section 5.8, we conclude this chapter and sketch possible directions for further research.

5.2 Problem formulation

The macroscopic behavior of light in a dielectric medium is governed by Maxwell's equations [1]:

$$\begin{aligned} \boldsymbol{\nabla}\cdot\mathbf{B}(\mathbf{r},t) &= 0, & \boldsymbol{\nabla}\times\mathbf{E}(\mathbf{r},t) + \frac{\partial\mathbf{B}(\mathbf{r},t)}{\partial t} &= 0, \\ \boldsymbol{\nabla}\cdot\mathbf{D}(\mathbf{r},t) &= \rho(\mathbf{r},t), & \boldsymbol{\nabla}\times\mathbf{H}(\mathbf{r},t) - \frac{\partial\mathbf{D}(\mathbf{r},t)}{\partial t} &= \mathbf{J}(\mathbf{r},t), \end{aligned} \tag{5.1}$$

where $\mathbf{E}, \mathbf{H}$, are the electric and magnetic intensity, and $\mathbf{D}, \mathbf{B}$, are the electric and magnetic induction fields, respectively. Free charges and current densities are denoted by ρ and $\mathbf{J}$, respectively. We denote by $\mathbf{r} \in \mathbb{R}^3, t \in \mathbb{R}$ the position vector and time, and $\boldsymbol{\nabla}$ is the nabla operator. We use the boldface notation for vectors. Here, we restrict ourselves to time-independent media with no sources of light, thus setting $\rho = 0$ and $\mathbf{J} = 0$.

The set of Eqs. (5.1) is supplemented by constitutive relations. Assuming that all the environments we are considering are isotropic and the field strengths are small enough, these relations are given by

$$\begin{aligned} \mathbf{B}(\mathbf{r},t) &= \mu_0\mu(\mathbf{r})\mathbf{H}(\mathbf{r},t) \\ \mathbf{D}(\mathbf{r},t) &= \varepsilon_0\varepsilon(\mathbf{r})\mathbf{E}(\mathbf{r},t), \end{aligned} \tag{5.2}$$

where ε_0, μ_0 are the vacuum permittivity and vacuum permeability, and $\varepsilon(\mathbf{r}), \mu(\mathbf{r})$ are the relative permittivity and relative permeability distribution within the system. We also assume that $\varepsilon(\mathbf{r})$ is purely real, *i.e.*, that all media are lossless, and that $0 < \varepsilon_{\min} \leq \varepsilon(\mathbf{r}) \leq \varepsilon_{\max} < \infty$, and neglect any frequency dependence

of the permittivity $\varepsilon(\mathbf{r})$. We also assume that $\varepsilon(\mathbf{r})$ is piecewise constant. In the following, we set $\mu(\mathbf{r}) = 1$, which is a good approximation for many dielectric materials. To simplify the notation, we will use units such that the speed of light $\nu = \varepsilon_0 = \mu_0 = 1$.

Since Maxwell's equations (5.1) are linear, one can separate the time dependence from the spatial dependence by means of the Fourier transform, leading to a family of problems for monochromatic waves with frequency ω [1, 41]. The fields then assume the time-harmonic form:

$$\begin{aligned} \mathbf{H}(\mathbf{r}, t) &= \mathbf{H}(\mathbf{r}) e^{\mathrm{i}\omega t}, \\ \mathbf{E}(\mathbf{r}, t) &= \mathbf{E}(\mathbf{r}) e^{\mathrm{i}\omega t}. \end{aligned} \tag{5.3}$$

In this chapter, we consider a 2-dimensional (2D) setting, where the fields $\mathbf{E}, \mathbf{H}$ and the permittivity ε are independent of the z-coordinate, *i.e.*, we assume that the crystal structure is homogeneously extended in the z-direction. The problem can then be split into two distinct polarizations: transverse-magnetic (TM), where the electric field points in the z-direction, $\mathbf{E}_{\mathrm{TM}}(\mathbf{r}) = u(\mathbf{r})\hat{\mathbf{e}}_{\mathbf{z}}$, and transverse-electric (TE), where the magnetic field points in the z-direction, $\mathbf{H}_{\mathrm{TE}}(\mathbf{r}) = u(\mathbf{r})\hat{\mathbf{e}}_{\mathbf{z}}$, with $\hat{\mathbf{e}}_{\mathbf{z}}$ being the unit vector in the z-direction and $u(\mathbf{r})$ the magnitude of the corresponding field. The other field can then in each case be calculated according to

$$\mathbf{H}_{\mathrm{TM}}(\mathbf{r}, t) = \frac{\mathrm{i}}{\mu_0 \omega} \boldsymbol{\nabla} \times \mathbf{E}_{\mathrm{TM}}(\mathbf{r}, t), \tag{5.4a}$$

$$\mathbf{E}_{\mathrm{TE}}(\mathbf{r}, t) = -\frac{\mathrm{i}}{\omega \varepsilon_0 \varepsilon(\mathbf{r})} \boldsymbol{\nabla} \times \mathbf{H}_{\mathrm{TE}}(\mathbf{r}, t). \tag{5.4b}$$

The Maxwell's equations (5.1) then reduce, for each polarization, to the Helmholtz equation for the field magnitude $u(\mathbf{r})$. In slight abuse of notation, we use $\mathbf{r} \in \mathbb{R}^2$ from now on and write the Helmholtz equation in polarization-independent notation as

$$\boldsymbol{\nabla} \cdot (a(\mathbf{r}) \boldsymbol{\nabla} u(\mathbf{r})) + \omega^2 b(\mathbf{r}) u(\mathbf{r}) = 0, \tag{5.5}$$

where

$$\begin{aligned} a(\mathbf{r}) &= 1, & b(\mathbf{r}) &= \varepsilon(\mathbf{r}), & &\text{for TM polarization,} \\ a(\mathbf{r}) &= \varepsilon(\mathbf{r})^{-1}, & b(\mathbf{r}) &= 1, & &\text{for TE polarization.} \end{aligned} \tag{5.6}$$

We consider a two-dimensional photonic crystal Ω^{cr} embedded in an external medium Ω^{ext}, such that $\overline{\Omega^{\mathrm{cr}}} \cup \overline{\Omega^{\mathrm{ext}}} = \overline{\Omega} \subset \mathbb{R}^2$, as illustrated in Fig. 5.1. We look for the field magnitude $u : \Omega \to \mathbb{C}$ in a chosen polarization (TM or TE), as a solution of Eq. (5.5) for all $\mathbf{r} \in \Omega$, with coefficient functions determined by Eq. (5.6).

As a source, we adopt a plane wave u^{inc} with the amplitude A^{inc} incident in the direction $\mathbf{k}_{\mathrm{ext}}$,

$$u^{\mathrm{inc}}(\mathbf{r}) = A^{\mathrm{inc}} e^{-\mathrm{i}\mathbf{k}_{\mathrm{ext}} \cdot \mathbf{r}}. \tag{5.7}$$

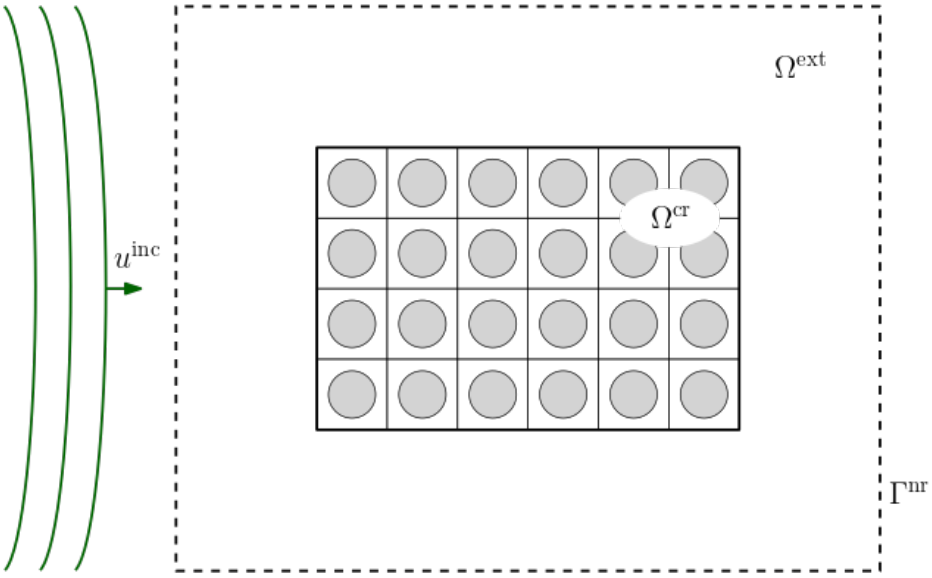

Figure 5.1: Computational domain Ω. The photonic crystal Ω^{cr} is surrounded by an external medium Ω^{ext}. At the boundary Γ^{nr}, non-reflecting boundary conditions are prescribed. As a source, we assume an incoming plane wave u^{inc}.

This wave is subsequently scattered and radiated into infinity. This radiation is expressed by the Silver-Müller radiation condition [41] at the domain boundary $\Gamma^{\text{nr}} = \partial\Omega$, *i.e.*,

$$\frac{\partial u(\mathbf{r})}{\partial \mathbf{n}} + \mathrm{i}|\mathbf{k}_{\text{ext}}|u(\mathbf{r}) = \frac{\partial u^{\text{inc}}(\mathbf{r})}{\partial \mathbf{n}} + \mathrm{i}|\mathbf{k}_{\text{ext}}|u^{\text{inc}}(\mathbf{r}), \quad \text{for } \mathbf{r} \in \Gamma^{\text{nr}}, \tag{5.8}$$

where $\mathbf{n}$ denotes the outer normal to the boundary and $\frac{\partial}{\partial \mathbf{n}} \coloneqq \mathbf{n} \cdot \boldsymbol{\nabla}$ is the normal derivative operator.

We denote the Lebesgue space of square-integrable functions on the domain Ω with values in $\mathbb{C}$ as $L^2(\Omega)$. We further denote the Sobolev space with square integrable first weak derivatives as

$$H^1(\Omega) \coloneqq \left\{ v \in L^2(\Omega) \,|\, \partial_j v \in L^2(\Omega), \text{ for } j = 1, 2 \right\}. \tag{5.9}$$

The weak formulation of problem (5.5), subject to (5.8), is

$$\text{Find } v \in H^1(\Omega), \text{ such that } \Phi(v, w) = f(w) \text{ for all } w \in H^1(\Omega), \tag{5.10}$$

where the sesquilinear form $\Phi : H^1(\Omega) \times H^1(\Omega) \to \mathbb{C}$ is defined by

$$\begin{aligned} \Phi(v, w) \coloneqq \int_\Omega a(\mathbf{r}) \boldsymbol{\nabla} v(\mathbf{r}) \cdot \boldsymbol{\nabla} \overline{w}(\mathbf{r}) \mathrm{d}\Omega - \omega^2 \int_\Omega b(\mathbf{r}) v(\mathbf{r}) \overline{w}(\mathbf{r}) \mathrm{d}\Omega \\ + \int_{\Gamma^{\text{nr}}} a(\mathbf{r}) \mathrm{i} k_{\text{ext}} v(\mathbf{r}) \overline{w}(\mathbf{r}) \mathrm{d}\Gamma, \end{aligned} \tag{5.11}$$

and the antilinear form $f : H^1(\Omega) \to \mathbb{C}$ is defined by

$$f(w) := \int_{\Gamma^{\mathrm{nr}}} a(\mathbf{r}) \left[\frac{\partial u^{\mathrm{inc}}(\mathbf{r})}{\partial \mathbf{n}} + \mathrm{i}k_{\mathrm{ext}} u^{\mathrm{inc}}(\mathbf{r}) \right] \overline{w}(\mathbf{r}) \mathrm{d}\Gamma. \tag{5.12}$$

Here, the overbar denotes the complex conjugate.

5.3 Bloch modes

The core of the method presented in this chapter lies in the approximation of the electromagnetic field in a locally periodic medium by globally periodic solutions. We next discuss the globally periodic problem, corresponding to solving the Helmholtz equation for an infinitely large crystal, without the external medium. Due to the periodicity of the coefficients in (5.5), the problem can be reduced to a family of problems on a bounded domain by the Bloch-Floquet theory (see Ref. [37]).

Let us define a lattice Λ spanned by the linearly independent *basis vectors* $\mathbf{a}_1, \mathbf{a}_2 \in \mathbb{R}^2$:

$$\Lambda := \left\{ \sum_{j=1}^{2} n_j \mathbf{a}_j \,|\, n_j \in \mathbb{Z}, j = 1, 2 \right\}. \tag{5.13}$$

In the infinite crystal, the relative permittivity ε is periodic on the lattice Λ, *i.e.*,

$$\varepsilon(\mathbf{r} + \mathbf{R}) = \varepsilon(\mathbf{r}) \qquad \text{for all } \mathbf{r} \in \mathbb{R}^2, \mathbf{R} \in \Lambda. \tag{5.14}$$

The *unit cell* of such a mesh can be defined in various ways, but the simplest definition is given by

$$\hat{\Omega} := \left\{ \sum_{j=1}^{2} s_j \mathbf{a}_j \,|\, s_j \in [0, 1], j = 1, 2 \right\}. \tag{5.15}$$

The infinite crystal can be intuitively seen as being composed of infinitely many copies of the unit cell $\hat{\Omega}$, each translated along a multiple of the lattice vectors $\mathbf{a}_1, \mathbf{a}_2$. The dual lattice to Λ is defined as

$$\Lambda^* := \left\{ 2\pi \sum_{j=1}^{2} n_j \mathbf{b}_j \,|\, n_j \in \mathbb{Z}, j = 1, 2 \right\}, \tag{5.16}$$

where the vectors $\mathbf{b}_1, \mathbf{b}_2$ are such that $\mathbf{b}_i \cdot \mathbf{a}_j = \delta_{ij}$, for $i, j = 1, 2$, and δ_{ij} is the Kronecker delta. The dual lattice gives rise to the dual unit cell, often referred to as the *first Brillouin zone*:

$$\mathcal{B} := \left\{ \sum_{j=1}^{2} s_j \mathbf{b}_j \,|\, s_j \in [-\pi, \pi], j = 1, 2 \right\}. \tag{5.17}$$

We note that, properly, the first Brillouin zone is defined as the Wigner-Seitz cell of the reciprocal lattice, see Ref. [42]. Such a definition coincides with (5.17) only for orthogonal lattice vectors, but, for our purposes of parametrization, this is irrelevant and we will refer to the unit cell defined by (5.17) as the Brillouin zone.

From the Bloch-Floquet theory (see, *e.g.*, Refs. [35–37]), it follows that the real part of the wave vector belongs to the Brillouin zone, $\mathrm{Re}\{\mathbf{k}\} \in \mathcal{B} \subset \mathbb{R}^2$. In order to account for evanescent waves, the wave vector can also have a nonzero imaginary component, thus it follows that $\mathbf{k} \in \mathcal{B} + \mathrm{i}\mathbb{R}^2$, see, *e.g.*, [43]. Moreover, the Bloch-Floquet theory shows that the field magnitude u can be expanded in Bloch modes, given by

$$u_{\mathbf{k}}^{\mathrm{Bloch}}(\mathbf{r}) \coloneqq u_{\mathbf{k}}^{\mathrm{per}}(\mathbf{r}) e^{\mathrm{i}\mathbf{k}\cdot\mathbf{r}}, \quad \text{for all } \mathbf{k} \in \mathcal{B} + \mathrm{i}\mathbb{R}^2, \tag{5.18}$$

where $u_{\mathbf{k}}^{\mathrm{per}}$ is a periodic function on Λ and is thus fully determined by its values on the unit cell $\hat{\Omega}$. Moreover, for $\mathbf{k} \in \mathcal{B} + \mathrm{i}\mathbb{R}^2$ fixed, $u_{\mathbf{k}}^{\mathrm{per}}$ is a solution to the following eigenvalue problem:

$$\begin{aligned} &\text{Find } (\omega^2, u_{\mathbf{k}}^{\mathrm{per}}) \text{ such that} \\ &-\boldsymbol{\nabla}_{\mathbf{k}} \cdot [a(\mathbf{r}) \boldsymbol{\nabla}_{\mathbf{k}} u_{\mathbf{k}}^{\mathrm{per}}(\mathbf{r})] = \omega^2 b(\mathbf{r}) u_{\mathbf{k}}^{\mathrm{per}}(\mathbf{r}), \qquad &&\text{for all } \mathbf{r} \in \hat{\Omega}, \\ &u_{\mathbf{k}}^{\mathrm{per}}(\mathbf{r} + \mathbf{a}_j) = u_{\mathbf{k}}^{\mathrm{per}}(\mathbf{r}), \qquad &&\text{and } \mathbf{r} \in \partial\hat{\Omega}, \end{aligned} \tag{5.19}$$

for $j = 1, 2$ and where $\boldsymbol{\nabla}_{\mathbf{k}} = \boldsymbol{\nabla} + \mathrm{i}\mathbf{k}$. We will refer to (5.19) as the *unit-cell problem*.

To put (5.19) into weak form, we denote the Sobolev space of periodic functions on $\hat{\Omega}$ with square integrable first weak derivatives as $H^1_{\mathrm{per}}(\hat{\Omega})$. The weak formulation of the problem (5.19) is then

$$\begin{aligned} &\text{Fix } \mathbf{k} \in \mathcal{B} + \mathrm{i}\mathbb{R}^2. \\ &\text{Find } (\omega^2, u_{\mathbf{k}}^{\mathrm{per}}) \in \mathbb{R} \times H^1_{\mathrm{per}}(\hat{\Omega}), \text{ such that} \\ &\hat{\Phi}(u_{\mathbf{k}}^{\mathrm{per}}, w) = \omega^2 (u_{\mathbf{k}}^{\mathrm{per}}, w)_b, \quad \text{for all } w \in H^1(\hat{\Omega}), \end{aligned} \tag{5.20}$$

where the sesquilinear form $\hat{\Phi} : H^1_{\mathrm{per}}(\hat{\Omega}) \times H^1_{\mathrm{per}}(\hat{\Omega}) \to \mathbb{C}$ is defined by

$$\begin{aligned} \hat{\Phi}(v, w) \coloneqq &\int_{\hat{\Omega}} a(\hat{\mathbf{r}}) \boldsymbol{\nabla} v(\hat{\mathbf{r}}) \cdot \boldsymbol{\nabla} \overline{w}(\hat{\mathbf{r}}) \mathrm{d}\hat{\Omega} + \int_{\hat{\Omega}} a(\hat{\mathbf{r}}) k^2 v(\hat{\mathbf{r}}) \overline{w}(\hat{\mathbf{r}}) \mathrm{d}\hat{\Omega} \\ &+ \int_{\hat{\Omega}} \mathrm{i} a(\hat{\mathbf{r}}) v(\hat{\mathbf{r}}) \mathbf{k} \cdot \boldsymbol{\nabla} \overline{w}(\hat{\mathbf{r}}) \mathrm{d}\hat{\Omega} - \int_{\hat{\Omega}} \mathrm{i} a(\hat{\mathbf{r}}) \mathbf{k} \cdot \boldsymbol{\nabla} v(\hat{\mathbf{r}}) \overline{w}(\hat{\mathbf{r}}) \mathrm{d}\hat{\Omega}, \end{aligned} \tag{5.21}$$

and

$$(v, w)_b = \int_{\hat{\Omega}} b(\hat{\mathbf{r}}) v(\hat{\mathbf{r}}) \overline{w}(\hat{\mathbf{r}}) \mathrm{d}\hat{\Omega}. \tag{5.22}$$

Formulation (5.20) is, however, inconvenient for us, since, to approximate the electromagnetic field generated by an incoming wave in a finite crystal by Bloch modes, these modes should have the same frequency as the incoming wave. We

thus know the frequency ω of the required modes, but need to find the corresponding wave vectors describing the light propagation. To this end, we parametrize the wave vector $\mathbf{k} = \kappa\hat{\mathbf{k}} = \kappa(\cos\theta, \sin\theta)$, with $\kappa \in \mathbb{C}$, $\hat{\mathbf{k}} = (\cos\theta, \sin\theta)$, and $\theta \in [0, \pi]$. For $\omega \in \mathbb{R}$ fixed, we thus consider the following quadratic eigenvalue problem:

$$\begin{aligned}
&\text{Find } (\kappa, u_{\mathbf{k}}^{\text{per}}) \in \mathbb{C} \times H^1_{\text{per}}(\hat{\Omega}), \text{ such that} \\
&\int_{\hat{\Omega}} a(\hat{\mathbf{r}}) \boldsymbol{\nabla} u_{\mathbf{k}}^{\text{per}}(\hat{\mathbf{r}}) \cdot \boldsymbol{\nabla} \overline{w}(\hat{\mathbf{r}}) \mathrm{d}\hat{\Omega} - \omega^2 \int_{\hat{\Omega}} b(\hat{\mathbf{r}}) u_{\mathbf{k}}^{\text{per}}(\hat{\mathbf{r}}) \overline{w}(\hat{\mathbf{r}}) \mathrm{d}\Omega \\
&+ \kappa \int_{\hat{\Omega}} \mathrm{i} a(\hat{\mathbf{r}}) u_{\mathbf{k}}^{\text{per}}(\hat{\mathbf{r}}) \hat{\mathbf{k}} \cdot \boldsymbol{\nabla} \overline{w}(\hat{\mathbf{r}}) \mathrm{d}\hat{\Omega} - \kappa \int_{\hat{\Omega}} \mathrm{i} a(\hat{\mathbf{r}}) \hat{\mathbf{k}} \cdot \boldsymbol{\nabla} u_{\mathbf{k}}^{\text{per}}(\hat{\mathbf{r}}) \overline{w}(\hat{\mathbf{r}}) \mathrm{d}\hat{\Omega} \\
&+ \kappa^2 \int_{\hat{\Omega}} a(\hat{\mathbf{r}}) u_{\mathbf{k}}^{\text{per}}(\hat{\mathbf{r}}) \overline{w}(\hat{\mathbf{r}}) \mathrm{d}\hat{\Omega} = 0.
\end{aligned} \tag{5.23}$$

We note that κ^2 here denotes the square of the complex number and not its magnitude. In the following, we will describe the utilization of the Bloch modes $u_{\mathbf{k}}^{\text{Bloch}}$ obtained by solving (5.23) to construct a size-robust approximation space for the locally periodic Helmholtz problem (5.10).

5.4 Size-robust function space

Properly choosing the approximation space for our problem is the key to obtain a size-robust method. Since the crystal Ω^{cr} is locally periodic, it should be possible to utilize this periodicity in such a way that the whole crystal can be treated with only a limited set of basis functions, independently of its size. It is immediately clear, however, that generic, commonly used FEM basis functions cannot utilize this local periodicity, and thus cannot achieve size-robustness. On the other hand, the solutions to the problem of an infinitely large crystal are relatively cheap to calculate and, for a large but finite crystal, can already be a very good approximation to the electromagnetic field inside of it. These Bloch modes, as defined by (5.18), have been proposed as a foundation for a size-robust basis by Ref. [38].

Since Bloch modes are solutions to an infinitely large crystal, they are expected to be a good approximation to the electromagnetic field deep inside a large crystal, where the surface effects are negligible. We denote the internal crystal subdomain as $\Omega^{\text{Bloch}} \subseteq \Omega^{\text{cr}}$ containing $\tilde{n}_1 \times \tilde{n}_2$ unit cells along the lattice vector directions $\mathbf{a}_1$ and $\mathbf{a}_2$, respectively. Bloch modes, however, do not necessarily well capture surface effects at the boundary of the crystal and waves in the external medium. We therefore introduce a surface domain $\Omega^{\text{surf}} \subset \Omega^{\text{cr}}$ which, together with the external domain Ω^{ext}, is discretized using elementwise polynomial basis functions, which are not necessarily continuous at element boundaries. It holds that $\overline{\Omega^{\text{cr}}} = \overline{\Omega^{\text{Bloch}}} \cup \overline{\Omega^{\text{surf}}}$. The partition of the domain Ω into the domains $\Omega^{\text{Bloch}}, \Omega^{\text{surf}}$, and Ω^{ext} is illustrated in Fig. 5.2. We note that it is also possible to choose $\Omega^{\text{surf}} = \emptyset$, in which case $\Omega^{\text{Bloch}} = \Omega^{\text{cr}}$.

Recall that the eigenvalue problem (5.23) is parametrized by $\omega > 0$ and $\theta \in [0, \pi]$. Thus, for each corresponding pair of ω and θ, we solve (5.23) and pick

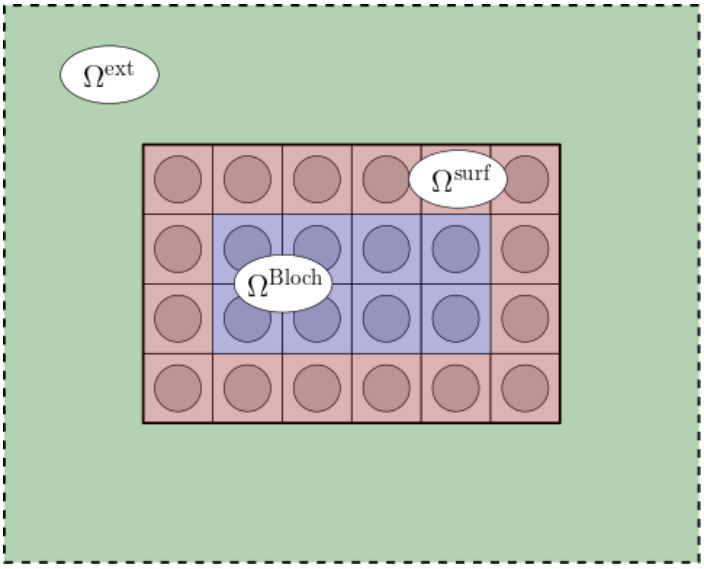

Figure 5.2: Subdivision of the domain Ω into the domains Ω^{Bloch}, Ω^{surf}, and Ω^{ext}. Here, Ω^{surf} is chosen with the depth of one unit cell along the crystal boundary. This effectively increases the approximation accuracy at the surface of the crystal without impacting the dimension of $V^{\text{Bloch}}(\Omega^{\text{Bloch}})$ defined in (5.24).

two Bloch modes corresponding to the eigenvalues $\kappa_{\theta,1}, \kappa_{\theta,2}$ with the smallest absolute value of the imaginary part $|\operatorname{Im}\{\kappa\}|$.

The photonic crystal is a scattering medium, scattering the incoming wave into all possible directions. Therefore, the propagation of light in such a crystal cannot be described by a single angle θ, but more angles are necessary. By computing the Bloch modes for N_θ different angles θ, we thus obtain in total $N^{\text{Bloch}} = 2N_\theta$ Bloch modes. Upon restricting the support of these Bloch modes to Ω^{Bloch}, they give rise to the basis of the space $V^{\text{Bloch}}(\Omega^{\text{Bloch}})$:

$$V^{\text{Bloch}}(\Omega^{\text{Bloch}}) = \operatorname{span}\left\{ u^{\text{Bloch}}_{\mathbf{k}_{i,j}} \,|\, \mathbf{k}_{i,j} = \kappa_{i,j}(\cos\theta_i, \sin\theta_i), i = 1, \dots, N_\theta, j = 1, 2 \right\}, \tag{5.24}$$

with $u^{\text{Bloch}}_{\mathbf{k}_{i,j}}$ given by (5.18).

Let us denote by $\mathcal{T}_h$ a quasi-uniform, shape-regular triangulation of the domain $\Omega^{\text{pol}} := \Omega^{\text{surf}} \cup \Omega^{\text{ext}}$. Let $\mathbb{P}^p(T)$ be the space of polynomials of degree at most $p \geq 1$ on $T \in \mathcal{T}_h$. We then define the space of broken polynomials on Ω^{pol} as

$$V_p^{\text{pol}}(\mathcal{T}_h) := \left\{ v \in L^2(\Omega^{\text{pol}}) \,|\, \forall T \in \mathcal{T}_h, v|_T \in \mathbb{P}^p(T) \right\}. \tag{5.25}$$

Finally, we combine the three approximation spaces into the space V^{SR}:

$$V^{\text{SR}} := \left\{ v \in L^2(\Omega) \,|\, v|_{\Omega^{\text{Bloch}}} \in V^{\text{Bloch}}(\Omega^{\text{Bloch}}), v|_{\Omega^{\text{pol}}} \in V_p^{\text{pol}}(\mathcal{T}_h) \right\}. \tag{5.26}$$

Note that $V^{\text{SR}} \not\subseteq H^1(\Omega)$. Therefore, we employ a nonconforming discontinuous Galerkin method in the next section.

5.5 Size-robust discretization

We approximate the weak formulation for the Helmholtz equation (5.10) in the space V^{SR}, using the Discontinuous Galerkin method in the framework of Bassi *et al.* using a lifting operator [40, 44].

5.5.1 Discontinuous Galerkin notation

Before we explicitly state the discretization, let us introduce the notation for the discontinuous Galerkin finite element method. We denote by $\mathbf{n}_T$ the outer normal to the element $T \in \mathcal{T}_h$. The set of internal faces will be denoted as $\mathcal{F}^{\mathrm{i}}$ and the set of boundary faces as $\mathcal{F}^{\mathrm{b}}$. Together, these sets yield the set of all faces $\mathcal{F} = \mathcal{F}^{\mathrm{i}} \cup \mathcal{F}^{\mathrm{b}}$. At each internal face $F \in \mathcal{F}^{\mathrm{i}}$, we arbitrarily assign the internal normal $\mathbf{n}_F$. We label the elements neighboring the face F as T_1 and T_2, such that the normal $\mathbf{n}_F$ points from T_1 to T_2. We stress that this labeling is arbitrary, but, once set, it must be obeyed. At the boundary faces $F \in \mathcal{F}^{\mathrm{b}}$ we assign the face normal $\mathbf{n}_F$ always as pointing outwards from the domain Ω. We further define at each face $F \in \mathcal{F}^{\mathrm{i}}$ the average of a function v as

$$\{\!\{v\}\!\}(\mathbf{r}) \coloneqq \frac{1}{2}\left(v|_{T_1}(\mathbf{r}) + v|_{T_2}(\mathbf{r})\right), \quad \mathbf{r} \in F, \tag{5.27}$$

and the jump of v as

$$[\![v]\!](\mathbf{r}) \coloneqq v|_{T_1}(\mathbf{r}) - v|_{T_2}(\mathbf{r}), \quad \mathbf{r} \in F, \tag{5.28}$$

with elements $T_1, T_2 \in \mathcal{T}_h$.

5.5.2 Discontinuous Galerkin formulation

We obtain the following discretized formulation of (5.10):

$$\text{Find } v_h \in V^{\mathrm{SR}}, \text{ such that } \Phi_h(v_h, w_h) = f_h(w_h), \quad \text{for all } w_h \in V^{\mathrm{SR}}, \tag{5.29}$$

where the sesquilinear form $\Phi_h : V^{\mathrm{SR}} \times V^{\mathrm{SR}} \to \mathbb{C}$ is defined as

$$\begin{aligned}
\Phi_h(v_h, w) \coloneqq & \sum_{T\in\mathcal{T}_h} \int_T a\boldsymbol{\nabla}_h v_h \cdot \boldsymbol{\nabla}_h \overline{w}\,\mathrm{d}T - \omega^2 \sum_{T\in\mathcal{T}_h} \int_T b(\mathbf{r}) v_h \overline{w}\,\mathrm{d}T \\
& - \sum_{F\in\mathcal{F}_h^i} \int_F \left(\{\!\{a\boldsymbol{\nabla}_h v_h\}\!\} \cdot \mathbf{n}_F\, [\![\overline{w}]\!] + [\![v_h]\!]\, \{\!\{a\boldsymbol{\nabla}_h \overline{w}\}\!\} \cdot \mathbf{n}_F \right) \mathrm{d}F \\
& + \sum_{F\in\mathcal{F}_h^i} \eta \int_\Omega a\, \mathbf{r}_F([\![v_h]\!]) \cdot \overline{\mathbf{r}_F([\![w]\!])}\,\mathrm{d}\Omega \\
& + \sum_{F\in\mathcal{F}_h^b} \int_F a\mathrm{i}k_{\mathrm{ext}} v_h \overline{w}\,\mathrm{d}F,
\end{aligned} \tag{5.30}$$

and the antilinear form $f_h : V^{\mathrm{SR}} \to \mathbb{C}$ is defined as

$$f_h(w) = \sum_{F \in \mathcal{F}_h^b} \int_F a \left[\frac{\partial u^{\mathrm{inc}}}{\partial \mathbf{n}} + \mathrm{i} k_{\mathrm{ext}} u^{\mathrm{inc}} \right] \overline{w} \, \mathrm{d}F. \tag{5.31}$$

Here, $\eta \geq \eta_0 > 0$ is a penalty parameter and $\mathbf{r}_F : L^2(F) \to \left[V^{\mathrm{SR}}\right]^2$ for each $F \in \mathcal{F}^{\mathrm{i}}$ the antilinear lifting operator, defined as [40]

$$\int_\Omega \mathbf{r}_F(v) \cdot \overline{\boldsymbol{\tau}_h} \mathrm{d}\Omega = \int_F \{\!\{\boldsymbol{\tau}_h\}\!\} \cdot \mathbf{n}_F \overline{v} \, \mathrm{d}F, \qquad \forall \boldsymbol{\tau}_h \in \left[V^{\mathrm{SR}}\right]^2, \tag{5.32}$$

see Appendix 5.A for implementational details.

Note that, in contrast to the standard FEM, (5.30) contains function jumps and averages across element boundaries. These terms appear due to the discontinuity of the functions in V^{SR} across these interfaces. See Appendix 5.B for the derivation of this formulation.

5.6 Size-robust quadrature

Let us denote by n_1, n_2 the number of unit cells of the crystal in the lattice directions $\mathbf{a}_1, \mathbf{a}_2$, respectively. We further denote $N^{\mathrm{SR}} = \dim V^{\mathrm{SR}}(\Omega)$, $N^{\mathrm{pol}} = \dim V_p^{\mathrm{pol}}(\mathcal{T}_h)$, $N^{\mathrm{Bloch}} = \dim V^{\mathrm{Bloch}}(\Omega^{\mathrm{Bloch}})$ and by $\{\psi_i^{\mathrm{pol}}\} \subseteq V_p^{\mathrm{pol}}(\mathcal{T}_h)$ a basis for $V_p^{\mathrm{pol}}(\mathcal{T}_h)$ and $\{\psi_i^{\mathrm{Bloch}}\} \subseteq V^{\mathrm{Bloch}}(\Omega^{\mathrm{Bloch}})$ a basis for $V^{\mathrm{Bloch}}(\Omega^{\mathrm{Bloch}})$. Then, with

$$\begin{aligned}
\mathcal{M}_{j,i}^{\mathrm{pol,pol}} &= \Phi_h(\psi_i^{\mathrm{pol}}, \psi_j^{\mathrm{pol}}), \text{ for } i,j = 1,\dots,N^{\mathrm{pol}}, \\
\mathcal{M}_{j,i}^{\mathrm{Bloch,Bloch}} &= \Phi_h(\psi_i^{\mathrm{Bloch}}, \psi_j^{\mathrm{Bloch}}), \text{ for } i,j = 1,\dots,N^{\mathrm{Bloch}}, \\
\mathcal{M}_{j,i}^{\mathrm{pol,Bloch}} &= \Phi_h(\psi_i^{\mathrm{pol}}, \psi_j^{\mathrm{Bloch}}), \text{ for } i = 1,\dots,N^{\mathrm{pol}},\ j = 1,\dots,N^{\mathrm{Bloch}}, \\
\mathcal{M}_{j,i}^{\mathrm{Bloch,pol}} &= \Phi_h(\psi_i^{\mathrm{Bloch}}, \psi_j^{\mathrm{pol}}), \text{ for } i = 1,\dots,N^{\mathrm{Bloch}},\ j = 1,\dots,N^{\mathrm{pol}},
\end{aligned} \tag{5.33}$$

the system matrix $\mathcal{M} \in \mathbb{C}^{N^{\mathrm{SR}} \times N^{\mathrm{SR}}}$ for the discrete problem (5.29) has the block structure

$$\mathcal{M} = \begin{pmatrix} \mathcal{M}^{\mathrm{pol,pol}} & \mathcal{M}^{\mathrm{pol,Bloch}} \\ \mathcal{M}^{\mathrm{Bloch,pol}} & \mathcal{M}^{\mathrm{Bloch,Bloch}} \end{pmatrix}. \tag{5.34}$$

The value of N^{Bloch} is clearly independent of the crystal sizes n_1, n_2. Since, in a finite domain, Bloch modes are not orthogonal to each other, the matrix $\mathcal{M}^{\mathrm{Bloch,Bloch}}$ is dense, with $(N^{\mathrm{Bloch}})^2$ nonzero elements. The dimension N^{pol} of the polynomial space $V_p^{\mathrm{pol}}(\mathcal{T}_h)$ depends linearly on the number of unit cells at the interface between Ω^{pol} and Ω^{Bloch}, *i.e.*, $N^{\mathrm{pol}} \propto (n_1 + n_2) \dim V_p^{\mathrm{pol}}(\hat{\mathcal{T}}_h(\hat{\Omega}))$, where $\hat{\mathcal{T}}_h(\hat{\Omega})$ is the triangulation of the unit cell $\hat{\Omega}$. Each polynomial in the discontinuous Galerkin formulation has its support limited to only one element $T \in \mathcal{T}_h$. As a result, the matrix $\mathcal{M}^{\mathrm{pol,pol}}$ is sparse, with the number of nonzero elements proportional to N^{pol}. Finally, the matrices $\mathcal{M}^{\mathrm{pol,Bloch}}$ and $\mathcal{M}^{\mathrm{Bloch,pol}}$ have the number of nonzero elements proportional to $N^{\mathrm{Bloch}} N^{\mathrm{pol}}$.

We have established that the size of $\mathcal{M}^{\text{Bloch,Bloch}}$ does not depend on the crystal sizes n_1, n_2. To obtain the elements of this matrix, we however need to integrate over the whole domain Ω^{Bloch} of the size $\tilde{n}_1 \times \tilde{n}_2 \propto n_1 \times n_2$. It is possible to alleviate the crystal-size dependence of the assembly of $\mathcal{M}^{\text{Bloch,Bloch}}$ by means of size-robust quadrature. Such a quadrature was first introduced in Ref. [38], and yielded logarithmic dependence on n_1, n_2. As we show next, by adjusting the quadrature to our DG framework, we effectively eliminate the size-dependence of the assembly of $\mathcal{M}^{\text{Bloch,Bloch}}$, resulting in a simplified, truly size-robust quadrature.

Let us define, for f periodic with respect to the lattice vectors $\mathbf{a}_1, \mathbf{a}_2$

$$T_{\lambda,i,j}[f] \coloneqq \int_{\Omega^{\text{Bloch}}} f(\mathbf{r}) D_\lambda \left(u_i^{\text{per}}(\mathbf{r}) e^{\mathrm{i}\mathbf{k}_i\cdot\mathbf{r}}\right) D_\lambda \left(\overline{u_j^{\text{per}}}(\mathbf{r}) e^{-\mathrm{i}\overline{\mathbf{k}_j}\cdot\mathbf{r}}\right) \mathrm{d}\mathbf{r}, \tag{5.35}$$

where $f(\mathbf{r})$ is a function with the same period as the crystal, $i, j = 1, \ldots, N^{\text{Bloch}}$ and $\lambda \in \{0, 1, 2\}$ is a derivative selector, such that

$$D_\lambda u \coloneqq \begin{cases} u & \text{if } \lambda = 0, \\ \partial_\lambda u & \text{if } \lambda \in \{1, 2\}. \end{cases} \tag{5.36}$$

The elements of $\mathcal{M}^{\text{Bloch,Bloch}}$ can be written as the sum of terms of the form $T_{\lambda,i,j}[f]$ for $f(\mathbf{r}) \in \{a(\mathbf{r}), b(\mathbf{r})\}$. We next show that the computation of $T_{\lambda,i,j}[f]$ can be done in a size-robust manner. We note that in our finite element discretization we treat the whole domain Ω^{Bloch} as a single finite element, regardless of the number of unit cells it contains.

The domain Ω^{Bloch} can be written as a conjunction of the translated unit-cell domains $\Omega_{\alpha\beta} = \hat{\Omega}_{11} + \mathbf{c}_{\alpha\beta}$, with the shift vector $\mathbf{c}_{\alpha\beta} = (\alpha-1)\mathbf{a}_1 + (\beta-1)\mathbf{a}_2$, such that $\Omega^{\text{Bloch}} = \bigcup_{\alpha=1}^{n_1} \bigcup_{\beta=1}^{n_2} \hat{\Omega}_{\alpha\beta}$. We denote $\hat{\Omega} = \hat{\Omega}_{11}$ and parametrize it by the vector $\hat{\mathbf{r}} \in \hat{\Omega}$. Every position vector $\mathbf{r} \in \Omega^{\text{Bloch}}$ can now be written as $\mathbf{r} = \hat{\mathbf{r}} + \mathbf{c}_{\alpha\beta}$ for some α, β, as illustrated in Fig. 5.3. We can now rewrite Eq. (5.35):

$$\begin{aligned} T_{\lambda,i,j}[f] &= \sum_{\alpha=1}^{\tilde{n}_1} \sum_{\beta=1}^{\tilde{n}_2} \int_{\Omega_{\alpha\beta}} f(\mathbf{r}) D_\lambda \left(u_i^{\text{per}}(\mathbf{r}) e^{\mathrm{i}\mathbf{k}_i\cdot\mathbf{r}}\right) D_\lambda \left(\overline{u_j^{\text{per}}}(\mathbf{r}) e^{-\mathrm{i}\overline{\mathbf{k}_j}\cdot\mathbf{r}}\right) \mathrm{d}\mathbf{r} \\ &= \sum_{\alpha=1}^{\tilde{n}_1} \sum_{\beta=1}^{\tilde{n}_2} \int_{\hat{\Omega}} f(\hat{\mathbf{r}} + \mathbf{c}_{\alpha\beta}) D_\lambda \left(u_i^{\text{per}}(\hat{\mathbf{r}} + \mathbf{c}_{\alpha\beta}) e^{\mathrm{i}\mathbf{k}_i\cdot(\hat{\mathbf{r}}+\mathbf{c}_{\alpha\beta})}\right) \\ &\qquad \times D_\lambda \left(\overline{u_j^{\text{per}}}(\hat{\mathbf{r}} + \mathbf{c}_{\alpha\beta}) e^{-\mathrm{i}\overline{\mathbf{k}_j}\cdot(\hat{\mathbf{r}}+\mathbf{c}_{\alpha\beta})}\right) \mathrm{d}\hat{\mathbf{r}}. \end{aligned} \tag{5.37}$$

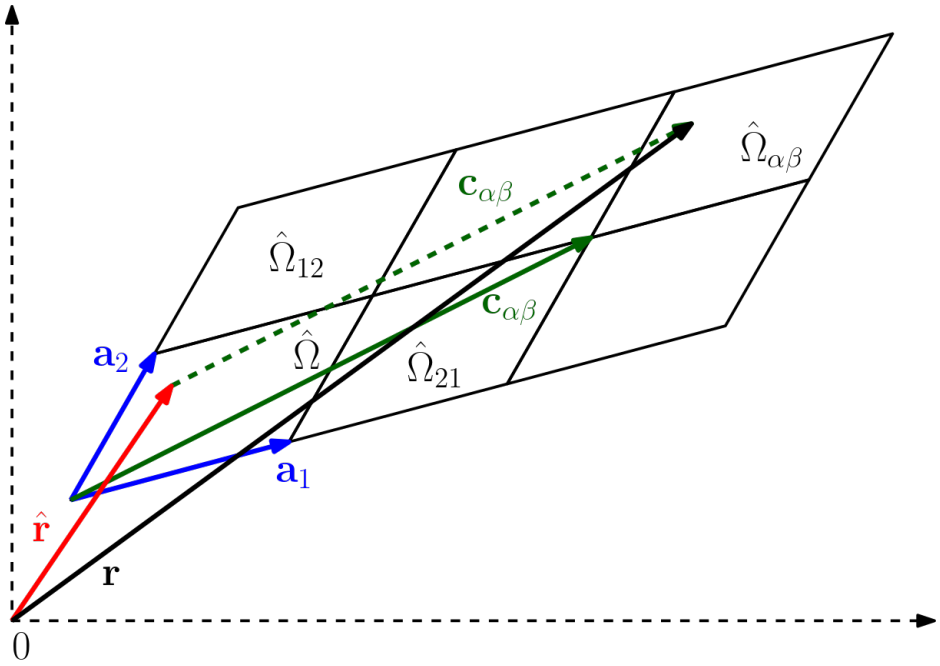

Figure 5.3: The domain Ω^{Bloch} and its parametrization. Every vector $\mathbf{r} \in \Omega_{\alpha\beta} \subset \Omega^{\text{Bloch}}$ (black), for $\alpha = 1, \dots, \tilde{n}_1$, and $\beta = 1, \dots, \tilde{n}_2$, can be parametrized by the vector $\hat{\mathbf{r}} \in \hat{\Omega}$ (blue) within the reference unit cell and the shift vector $\mathbf{c}_{\alpha\beta}$ (green).

By utilizing the periodicity of f and u_i^{per}, we further obtain

$$\begin{aligned} T_{\lambda,i,j}[f] &= \sum_{\alpha=1}^{\tilde{n}_1} \sum_{\beta=1}^{\tilde{n}_2} \int_{\hat{\Omega}} f(\hat{\mathbf{r}}) D_\lambda \left(u_i^{\text{per}}(\hat{\mathbf{r}}) e^{\mathrm{i}\mathbf{k}_i \cdot (\hat{\mathbf{r}} + \mathbf{c}_{\alpha\beta})} \right) \\ &\qquad \times D_\lambda \left(\overline{u_j^{\text{per}}}(\hat{\mathbf{r}}) e^{-\mathrm{i}\overline{\mathbf{k}_j} \cdot (\hat{\mathbf{r}} + \mathbf{c}_{\alpha\beta})} \right) \mathrm{d}\hat{\mathbf{r}} \\ &= \int_{\hat{\Omega}} f(\hat{\mathbf{r}}) D_\lambda \left(u_i^{\text{per}}(\hat{\mathbf{r}}) e^{\mathrm{i}\mathbf{k}_i \cdot \hat{\mathbf{r}}} \right) D_\lambda \left(\overline{u_j^{\text{per}}}(\hat{\mathbf{r}}) e^{-\mathrm{i}\overline{\mathbf{k}_j} \cdot \hat{\mathbf{r}}} \right) \mathrm{d}\hat{\mathbf{r}} \\ &\qquad \times \sum_{\alpha=1}^{\tilde{n}_1} \sum_{\beta=1}^{\tilde{n}_2} e^{\mathrm{i}(\mathbf{k}_i - \overline{\mathbf{k}_j}) \cdot \mathbf{c}_{\alpha\beta}}. \end{aligned} \tag{5.38}$$

Expression (5.38) now contains and integral over the unit cell $\hat{\Omega}$ multiplied by a double sum. The integral term is clearly independent of the crystal size n_1 and n_2. The only term in (5.38) that may depend on the size of Ω^{Bloch} is the term with the summation. This term can be written as

$$\begin{aligned} \sum_{\alpha=1}^{\tilde{n}_1} \sum_{\beta=1}^{\tilde{n}_2} e^{\mathrm{i}(\mathbf{k}_i - \overline{\mathbf{k}_j}) \cdot \mathbf{c}_{\alpha\beta}} &= \sum_{\alpha=0}^{\tilde{n}_1 - 1} e^{\mathrm{i}\alpha(\mathbf{k}_i - \overline{\mathbf{k}_j}) \cdot \mathbf{a}_1} \sum_{\beta=0}^{\tilde{n}_2 - 1} e^{\mathrm{i}\beta(\mathbf{k}_i - \overline{\mathbf{k}_j}) \cdot \mathbf{a}_2} \\ &= S_{n_1}(e^{\mathrm{i}(\mathbf{k}_i - \overline{\mathbf{k}_j}) \cdot \mathbf{a}_1}) S_{n_2}(e^{\mathrm{i}(\mathbf{k}_i - \overline{\mathbf{k}_j}) \cdot \mathbf{a}_2}), \end{aligned} \tag{5.39}$$

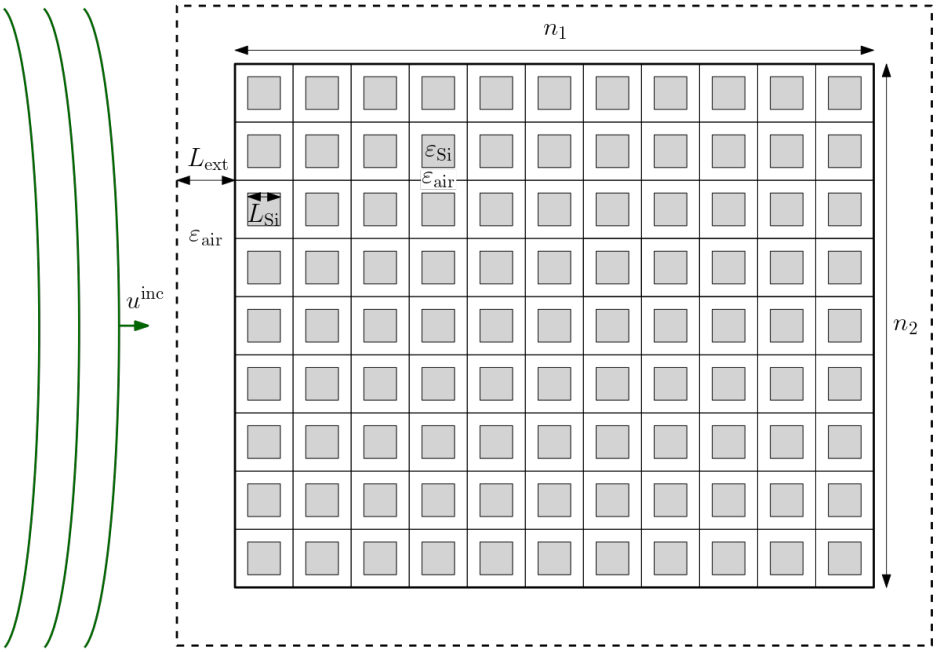

Figure 5.4: Computational domain employed for convergence analysis of our method with respect to the reference solution.

where

$$S_n(q) \coloneqq \sum_{\alpha=0}^{n-1} q^\alpha = \frac{1-q^n}{1-q}. \tag{5.40}$$

Clearly, (5.40) depends on the size of Ω^{Bloch} only weakly. The assembly of $\mathcal{M}^{\text{Bloch,Bloch}}$ is therefore size-robust, *i.e.*, except for computing powers as in (5.40), it does not depend on n_1, n_2. The calculation of the matrices $\mathcal{M}^{\text{pol,Bloch}}, \mathcal{M}^{\text{Bloch,pol}}$ depends on the crystal size only linearly, compared to standard FEM, for which $\dim V_p^{\text{pol}}(\mathcal{T}_h(\Omega)) \propto n_1 n_2 \dim V_p^{\text{pol}}(\hat{\mathcal{T}}_h(\hat{\Omega}))$. Therefore, our method yields a significant reduction in the computational complexity of computing $\mathcal{M}$.

We specifically note that the computation of the lifting operator also contains integration over Ω^{Bloch} and can also be computed using the size-robust quadrature discussed in this section. For details, see Appendix 5.A.

5.7 Numerical convergence

We illustrate the convergence properties of our method implemented in Matlab on the example depicted in Fig. 5.4.

We choose a square crystal lattice with the lattice vectors $\mathbf{a}_1 = a\hat{\mathbf{e}}_x$, $\mathbf{a}_2 = a\hat{\mathbf{e}}_y$,

with $n_1 = 11$ and $n_2 = 9$ square unit cells in each lattice direction, respectively. The crystal is surrounded by an air layer of the size of $L_{\text{ext}} = 1$ unit cell. Each crystal unit cell consists of a square silicon rod with the sides of length $L_{\text{Si}} = 0.6a$ and permittivity $\varepsilon_{\text{Si}} = 12.1$, surrounded by air with permittivity $\varepsilon_{\text{air}} = 1$. We assume an incoming plane wave of the frequency $\omega = a/\nu$ from the left and solve for TM polarization. We calculate the L^2-error with respect to a reference solution computed via standard FEM implemented by Matlab PDE Toolbox with quadratic elements and the maximum mesh edge length parameter 'Hmax' set to 0.02. The electric field of this reference solution is depicted in Fig. 5.5.

5.7.1 Varying resolution for Bloch modes

To obtain Bloch modes, we solve the eigenproblem (5.23) by standard conforming FEM with polynomials of degree $\hat{p} = 2$. We denote the degrees of freedom of this computation as $n_{\text{DOF,mic}} = N^{\text{mic}} = \dim\left(V_{\hat{p}}^{\text{pol}}\left(\hat{\mathcal{T}}_h(\hat{\Omega})\right) \cap H^1_{\text{per}}(\hat{\Omega})\right)$.

Fig. 5.6 depicts the convergence of our size-robust method for fixed number of Bloch angles $N_\theta = 23$ and N^{pol}, with quadratic polynomials $p = 2$ in V^{pol}, while varying the degrees of freedom $n_{\text{DOF,mic}}$ used to obtain the Bloch modes. We see that increasing the surface layer thickness N_{surf} enhances the accuracy of the method. This is due to the fact that Bloch modes approximate the fields inside the photonic crystal well, but are unable to capture the surface effects. For sufficiently large N_{surf}, we observe convergence of almost $\mathcal{O}(h^{-4})$ with respect to the mesh size h, until saturation is reached, most probably limited by the chosen precision N^{pol} of the Ω^{pol} discretization. It appears that by increasing the surface layer size N_{surf} by one unit cell, we gain more than one additional order of accuracy, for sufficiently good discretization. Overall, for any value of N_{surf}, we can choose a moderate number $n_{\text{DOF,mic}}$ that properly resolve the Bloch modes. Therefore, replacing the exact Bloch modes by their FEM approximations does not spoil the accuracy of the method.

5.7.2 Varying resolution in Ω^{pol}

The number of degrees of freedom for solving (5.29) is given by $n_{\text{DOF,ext}} = N^{\text{SR}} = N^{\text{pol}} + 2N_\theta$. Fig. 5.7 depicts the convergence of our method for fixed $N_\theta = 23$ and $n_{\text{DOF,mic}}$, varying the resolution of the $V_p^{\text{pol}}(\mathcal{T}_h)$ discretization with $p = 2$. Again, we observe the trend that increasing the surface layer thickness N_{surf} enhances the total achieved accuracy of the method and for sufficiently large N_{surf}, we observe convergence of almost $\mathcal{O}(h^{-4})$. As we show in the next subsection, at $N_\theta = 23$ the method is already saturated in terms of Bloch modes and adding more modes will not help increase the accuracy. We conclude that N^{pol} is well-behaved for any chosen N_{surf}.

5.7.3 Varying number of Bloch modes

Fig. 5.8 shows the convergence of our method for fixed $n_{\text{DOF,ext}}$ and $n_{\text{DOF,mic}}$, varying the number of N_θ angles. We again observe improved precision with

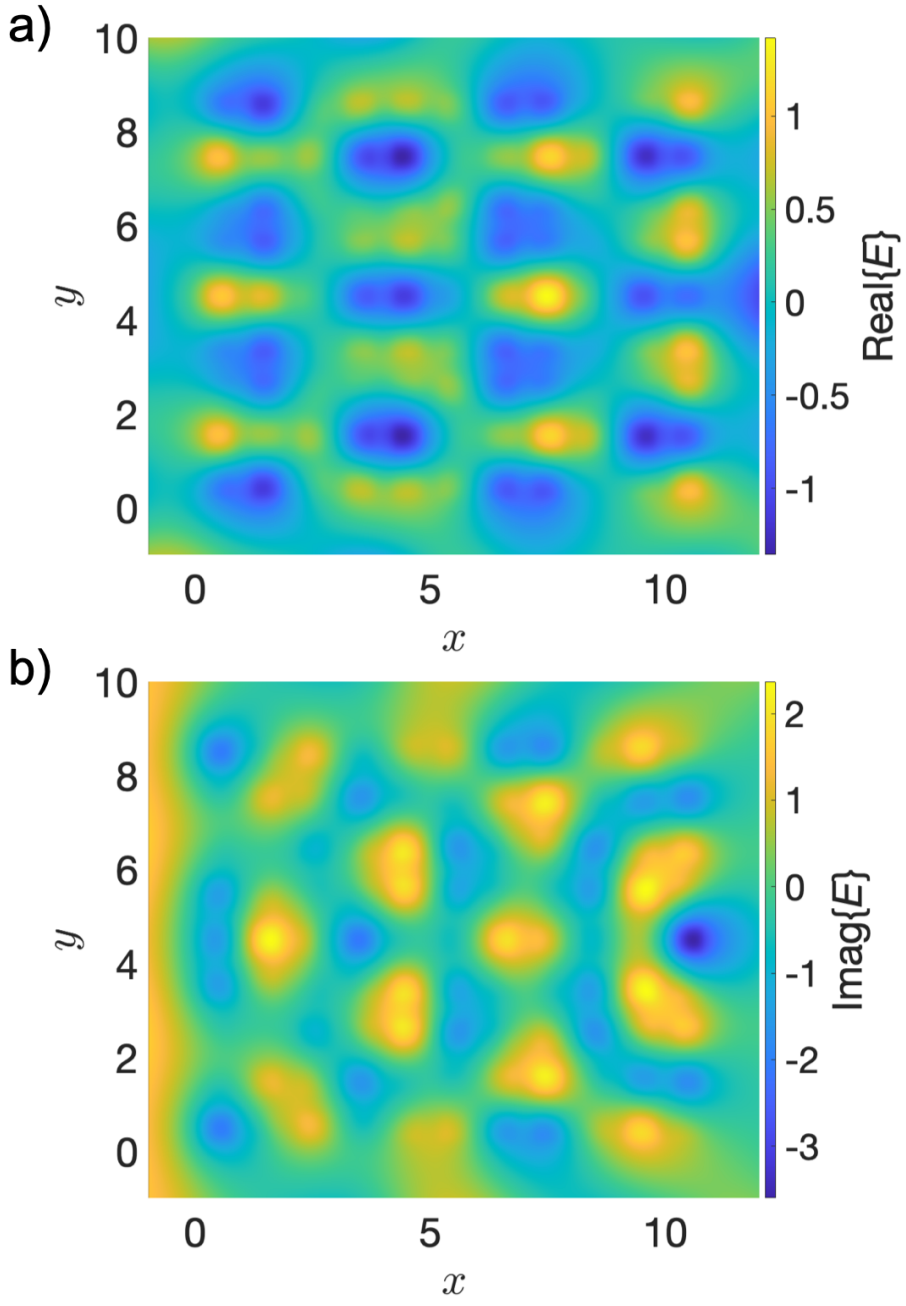

Figure 5.5: Reference solution. Electromagnetic field E in the crystal structure depicted in Fig. 5.4. a) Real part. b) Imaginary part.

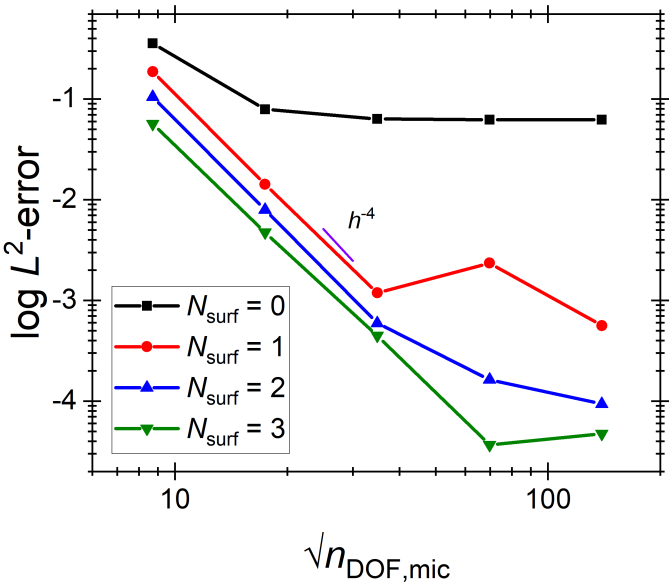

Figure 5.6: Convergence of our size-robust method with fixed Ω^{ext} discretization and varying $n_{\mathrm{DOF,mic}}$. Each line corresponds to different size of the surface layer N_{surf}, given in unit cells. Number of Bloch mode angles is $N_\theta = 23$.

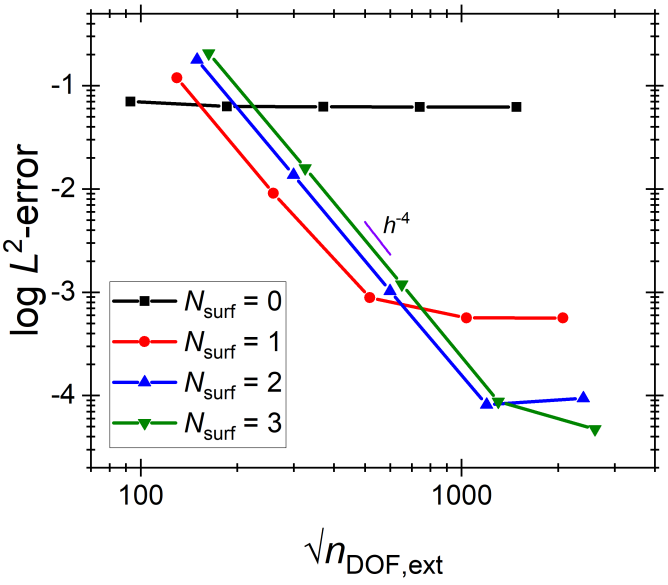

Figure 5.7: Convergence of our size-robust method with fixed $n_{\mathrm{DOF,mic}}$ and varying $n_{\mathrm{DOF,ext}}$. Each line corresponds to different size of the surface layer N_{surf}, given in unit cells. Number of Bloch mode angles is $N_\theta = 23$.

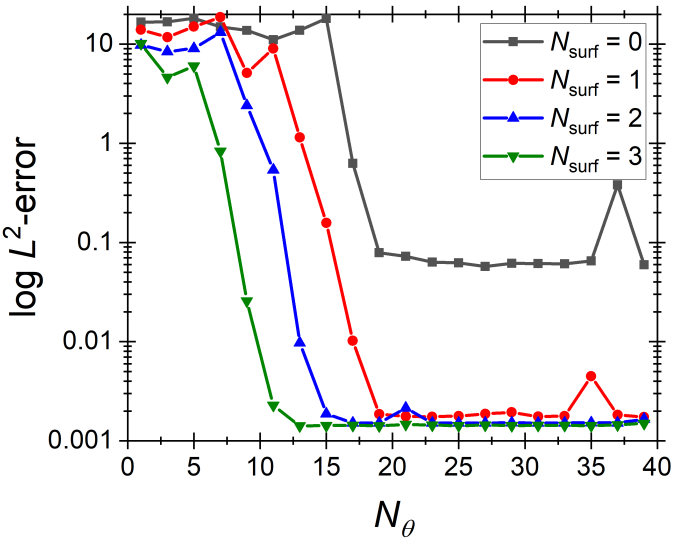

Figure 5.8: Convergence of our size-robust method with fixed $n_{\mathrm{DOF,mic}}$, constant Ω^{ext} discretization, and varying number of Bloch mode angles is N_θ. Each line corresponds to different size of the surface layer N_{surf}, given in unit cells.

higher N_{surf}, although in this case the minimum error is limited by $n_{\mathrm{DOF,ext}}$ and $n_{\mathrm{DOF,mic}}$, which were chosen lower than in previous figures to achieve a reasonable computational time. The error only starts decreasing after certain number of angles, $N_\theta > 10$, suggesting that there is a minimum number of Bloch mode angles necessary to describe the correct solution. Afterwards, the error decreases rapidly over several orders of magnitude and saturates already for $N_\theta < 20$. Further increasing the number of Bloch modes does not benefit the solution, due to the fact that the condition number of the system matrix becomes too large.

5.7.4 Varying crystal size

In this numerical experiment, we vary the size of the crystal $N = n_1 = n_2$ and calculate the resulting number of the degrees of freedom $n_{\mathrm{DOF,ext}}$. Fig. 5.9 depicts the results. We see that the number of degrees of freedom increases only linearly with the crystal size, confirming the theoretical considerations made in Section 5.6, and thus outperforming standard methods, which scale quadratically in 2D.

5.8 Conclusion

In this chapter, we presented a size-robust discontinuous Galerkin method for computation of light propagation through locally periodic media. For a crystal

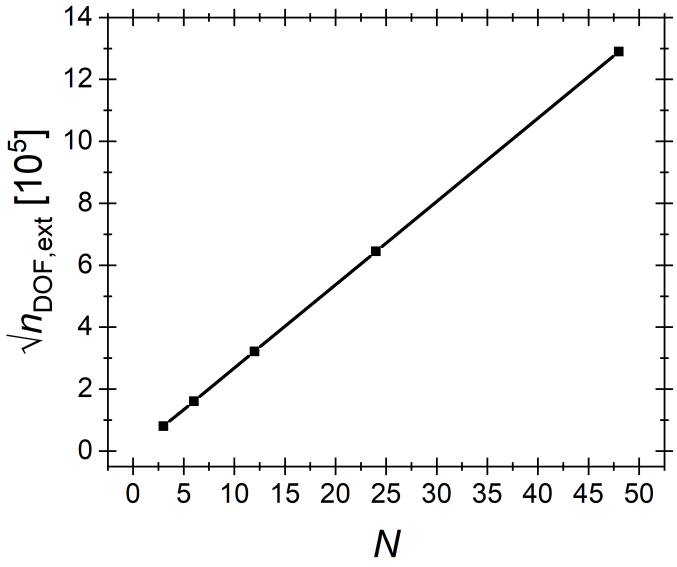

Figure 5.9: Scaling of our method with the size of the photonic crystal $N = n_1 = n_2$.

with n_1 and n_2 unit cells along the lattice directions, the computational complexity of our method scales with $n_1 + n_2$, while standard methods scale like $n_1 n_2$. We have discussed the weak formulation of the method, as well as the crucial step for constructing the size-robust function space and the size-robust quadrature. To illustrate the convergence of our method and discuss its numerical properties, we performed and analyzed several numerical experiments.

In the future, it would be beneficial to extend our method to 3D systems, where we expect an order of magnitude reduction of computational complexity compared with standard FEM. Moreover, it would be interesting to investigate if it is possible to express the surface effects of the crystal on the electromagnetic field via some family of functions in a similar manner as we now do inside the crystal with the family of Bloch modes. If such a family of surface functions is found, it would further reduce the size-dependence of our method, making it completely size-independent in 2D and only linearly size-dependent in 3D. Finally, the generalization of our method to defect superlattices by incorporating Bloch modes from both the regular and the defect unit cells should be investigated.

Appendices

5.A Implementation of the lifting operator term

The lifting operator $r_F : L^2(F) \to \left[V^{\mathrm{SR}}\right]^2$ is defined by (5.32) as

$$\int_\Omega \mathbf{r}_F(v) \cdot \overline{\boldsymbol{\tau}_h} \mathrm{d}\Omega = \int_F \{\!\{\boldsymbol{\tau}_h\}\!\} \cdot \mathbf{n}_F \overline{v} \mathrm{d}F, \qquad \forall \boldsymbol{\tau}_h \in \left[V^{\mathrm{SR}}\right]^2. \tag{5.41}$$

We can approximate each component of the lifted function using the basis functions

$$r_{F,j}(v)(\mathbf{r}) = \sum_{i \in D(F)} \hat{r}_{i,j}(v) \phi_i(\mathbf{r}), \tag{5.42}$$

where $D(F)$ is the set of indices corresponding to basis functions with nonzero support on the elements adjacent to face F, and $j = 1, 2$. Choosing $\tau_j = \phi_k$, and substituting back into Eq. (5.32), we write

$$\int_\Omega \sum_{i \in D(F)} \hat{r}_{i,j}(v) \phi_i \overline{\phi}_k \mathrm{d}\Omega = \sum_{i \in D(F)} \hat{r}_{i,j}(v) \int_\Omega \phi_i \overline{\phi}_k \mathrm{d}\Omega = \int_F \{\!\{\phi_k\}\!\} n_{F,j} \overline{v} \, \mathrm{d}F, \tag{5.43}$$

which can be written in the matrix notation

$$M \hat{\mathbf{r}}_j(v) = \mathbf{q}_j(v), \tag{5.44}$$

with mass matrix

$$M_{k,i} = \int_\Omega \phi_i \overline{\phi}_k \mathrm{d}\Omega, \tag{5.45}$$

and the k-th component of the right-hand side

$$q(v)_{k,j} = \int_F \{\!\{\phi_k\}\!\} n_{F,j} \overline{v} \mathrm{d}F, \tag{5.46}$$

where $\hat{\mathbf{r}}_j(v)$ is the vector containing $\hat{r}_{i,j}(v), i = 1, 2$. We can thus write, for $j = 1, 2$, $\hat{\mathbf{r}}_j(v) = M^{-1} \mathbf{q}_j(v)$.

Next, we would like to express the penalty term $s_h^{BRMPS}(v_h, w)$ in the derived matrix notation. We write

$$\begin{aligned}
&\sum_{F \in \mathcal{F}_h^i} \eta \int_\Omega a(\mathbf{r}) \mathbf{r}_F([\![v_h(\mathbf{r})]\!]) \cdot \overline{\mathbf{r}_F([\![w(\mathbf{r})]\!])} \mathrm{d}\Omega = \\
&= \sum_{F \in \mathcal{F}_h^i} \eta \int_\Omega a(\mathbf{r}) \sum_{j=1}^{2} \left[\sum_{i_1 \in D(F)} \hat{r}_{i_1,j}([\![v_h(\mathbf{r})]\!]) \phi_{i_1} \right] \\
&\qquad \times \left[\sum_{i_2 \in D(F)} \overline{\hat{r}_{i_2,j}([\![w(\mathbf{r})]\!]) \overline{\phi}_{i_2}} \right] \mathrm{d}\Omega \\
&= \eta \sum_{i_1, i_2 \in D(F)} \sum_{j=1}^{2} \hat{r}_{i_1,j}([\![v_h(\mathbf{r})]\!]) \, \overline{\hat{r}_{i_2,j}([\![w(\mathbf{r})]\!])} \sum_{F \in \mathcal{F}_h^i} \int_\Omega a \phi_{i_1} \overline{\phi}_{i_2} \mathrm{d}\Omega.
\end{aligned} \tag{5.47}$$

Let us define

$$\tilde{M}(f)_{k,i} = \int_\Omega f\phi_i\overline{\phi}_k. \tag{5.48}$$

It holds that $M = \tilde{M}(1)$. Now we can rewrite Eq (5.47), as

$$\begin{aligned}
&\eta \sum_{i_1,i_2\in D(F)} \sum_{j=1}^{2} \hat{r}_{i_1,j}\left(\llbracket v_h(\mathbf{r})\rrbracket\right) \overline{\hat{r}_{i_2,j}\left(\llbracket w(\mathbf{r})\rrbracket\right)} \sum_{F\in\mathcal{F}_h^i} \int_\Omega a\phi_{i_1}\overline{\phi}_{i_2}\mathrm{d}\Omega = \\
&= \eta \sum_{j=1}^{2} \overline{\hat{\mathbf{r}}_j(\llbracket w\rrbracket)}^T \tilde{M}(a)\hat{\mathbf{r}}_j(\llbracket v_h\rrbracket) \\
&= \eta \sum_{j=1}^{2} \overline{\mathbf{q}_j(\llbracket w\rrbracket)^T M^{-T}}\tilde{M}(a)M^{-1}\mathbf{q}_j(\llbracket v_h\rrbracket) \\
&= \eta \sum_{j=1}^{2} \overline{\mathbf{q}_j(\llbracket w\rrbracket)}^T M^{-1}\tilde{M}(a)M^{-1}\mathbf{q}_j(\llbracket v_h\rrbracket),
\end{aligned} \tag{5.49}$$

where in the last step we used the fact that M is Hermitian. For non-curved faces, we can write

$$q(v)_{k,j} = \left(\int_F \{\!\{\phi_k\}\!\}\,\overline{v}\mathrm{d}S\right) n_{F,j} = q(v)_k n_{F,j}, \tag{5.50}$$

with $q(v)_k$ being the k-th component of the vector $\mathbf{q}$. Now we are able to eliminate the normal $\mathbf{n}_F$ from the vectors $\mathbf{q}_j$ in Eq (5.49):

$$\begin{aligned}
&\eta \sum_{j=1}^{2} \overline{\mathbf{q}_j(\llbracket w\rrbracket)}^T M^{-1}\tilde{M}(a)M^{-1}\mathbf{q}_j(\llbracket v_h\rrbracket) = \\
&= \eta\overline{\mathbf{q}(\llbracket w\rrbracket)}^T M^{-1}\tilde{M}(a)M^{-1}\mathbf{q}(\llbracket v_h\rrbracket)\sum_{j=1}^{2} n_{F,j}^2 \\
&= \eta\overline{\mathbf{q}(\llbracket w\rrbracket)}^T M^{-1}\tilde{M}(a)M^{-1}\mathbf{q}(\llbracket v_h\rrbracket).
\end{aligned} \tag{5.51}$$

Finally, in the bilinear form we set $w = \phi_j$ and $v_h = \sum_{i=1}^{\dim(V^{\mathrm{SR}})} \hat{u}_i\phi_i$, where $\hat{u}_i$ are the coefficients of the solution u_h corresponding to the basis functions ϕ_i. We thus have, for all ϕ_j,

$$\eta \sum_{i=1}^{2} \overline{\mathbf{q}(\llbracket\phi_j\rrbracket)}^T M^{-1}\tilde{M}(a)M^{-1}\mathbf{q}(\llbracket\phi_i\rrbracket)\hat{\mathbf{u}}, \tag{5.52}$$

which can be rewritten in the matrix form

$$\eta Q^* M^{-1}\tilde{M}(a)M^{-1}Q\hat{\mathbf{u}}, \tag{5.53}$$

where Q is the matrix with columns $\mathbf{q}(\llbracket\phi_i\rrbracket)$. The matrix

$$\eta Q^* M^{-1}\tilde{M}(a)M^{-1}Q \tag{5.54}$$

thus represents the discretized penalty term. The elements of the matrices M and $\tilde{M}$ in Eq. (5.54) can be expressed via terms of the form $T_{\lambda,i,j}$ stated in Eq. (5.35) and thus they can also be computed in a size-robust manner, as described in Section 5.6.

5.B Derivation of the DGFEM formulation

In this Appendix, we adapt the derivation of the discontinuous Galerkin discretization presented in [40] to the Helmholtz equation given by (5.5) and (5.8).

We multiply (5.5) with arbitrary test functions $w \in V^{\mathrm{SR}}$ and integrate over Ω to obtain

$$\int_\Omega \boldsymbol{\nabla} \cdot (a(\mathbf{r})\boldsymbol{\nabla} u(\mathbf{r}))\, \overline{w}(\mathbf{r}) \mathrm{d}\Omega + \int_\Omega \omega^2 b(\mathbf{r}) u(\mathbf{r}) \overline{w}(\mathbf{r}) \mathrm{d}\Omega = 0. \tag{5.55}$$

We rewrite (5.55) in terms of integration over the mesh $\mathcal{T}_h$:

$$0 = \sum_{T\in\mathcal{T}_h} \int_T \boldsymbol{\nabla} \cdot (a(\mathbf{r})\boldsymbol{\nabla} u(\mathbf{r}))\, \overline{w}(\mathbf{r}) \mathrm{d}T + \sum_{T\in\mathcal{T}_h} \int_T \omega^2 b(\mathbf{r}) u(\mathbf{r}) \overline{w}(\mathbf{r}) \mathrm{d}T, \tag{5.56}$$

and apply Green's first identity to further obtain

$$\begin{aligned} 0 = &- \sum_{T\in\mathcal{T}_h} \int_T a(\mathbf{r}) \boldsymbol{\nabla} u(\mathbf{r}) \cdot \boldsymbol{\nabla} \overline{w}(\mathbf{r}) \mathrm{d}T \\ &+ \sum_{T\in\mathcal{T}_h} \int_T \omega^2 b(\mathbf{r}) u(\mathbf{r}) \overline{w}(\mathbf{r}) \mathrm{d}T \\ &+ \sum_{T\in\mathcal{T}_h} \int_{\partial T} a(\mathbf{r}) \left(\boldsymbol{\nabla} u(\mathbf{r}) \cdot \mathbf{n}_T\right) \overline{w}(\mathbf{r}) \mathrm{d}F. \end{aligned} \tag{5.57}$$

The last term in (5.57) can be rewritten as

$$\begin{aligned} \sum_{T\in\mathcal{T}_h} \int_{\partial T} a(\mathbf{r}) \left(\boldsymbol{\nabla} u(\mathbf{r}) \cdot \mathbf{n}_T\right) \overline{w}(\mathbf{r})\, \mathrm{d}F = &\sum_{F\in\mathcal{F}_h^b} \int_F a(\mathbf{r}) \frac{\partial u(\mathbf{r})}{\partial \mathbf{n}} \overline{w}(\mathbf{r})\, \mathrm{d}F \\ &+ \sum_{F\in\mathcal{F}_h^i} \int_F \left[\!\left[a(\mathbf{r}) \boldsymbol{\nabla} u(\mathbf{r}) \overline{w}(\mathbf{r}) \right]\!\right] \cdot \mathbf{n}_F\, \mathrm{d}F, \end{aligned} \tag{5.58}$$

with $\mathbf{n}_F = \mathbf{n}_{T_1} = -\mathbf{n}_{T_2}$ the normal to the face $F = \partial T_1 \cap \partial T_2$.

It is easy to see that on internal faces it holds

$$\left[\!\left[a\boldsymbol{\nabla} u \overline{w} \right]\!\right] = \left\{\!\left\{ a\boldsymbol{\nabla} u \right\}\!\right\} \left[\!\left[\overline{w} \right]\!\right] + \left[\!\left[a\boldsymbol{\nabla} u \right]\!\right] \left\{\!\left\{ \overline{w} \right\}\!\right\}. \tag{5.59}$$

Further, we apply the boundary condition (5.8) for u to the boundary term in (5.58), yielding a nonzero right-hand side. We can thus rewrite (5.57) as

$\Phi_h^{(0)}(u,w) = f_h^{(0)}(w)$, where

$$\begin{aligned}\Phi_h^{(0)}(u,w) = &- \sum_{T\in\mathcal{T}_h}\int_T a(\mathbf{r})\boldsymbol{\nabla}u(\mathbf{r})\cdot\boldsymbol{\nabla}\overline{w}(\mathbf{r})\mathrm{d}T + \sum_{T\in\mathcal{T}_h}\int_T \omega^2 b(\mathbf{r})u(\mathbf{r})\overline{w}(\mathbf{r})\mathrm{d}T \\ &+ \sum_{F\in\mathcal{F}_h^i}\int_F \left\{\!\!\left\{a(\mathbf{r})\boldsymbol{\nabla}u(\mathbf{r})\right\}\!\!\right\}\cdot\mathbf{n}_F\left[\!\left[\overline{w}(\mathbf{r})\right]\!\right] + \left[\!\left[a(\mathbf{r})\boldsymbol{\nabla}u(\mathbf{r})\right]\!\right]\cdot\mathbf{n}_F\left\{\!\!\left\{\overline{w}(\mathbf{r})\right\}\!\!\right\}\mathrm{d}F \\ &- \sum_{F\in\mathcal{F}_h^b}\int_F a(\mathbf{r})\mathrm{i}k_{\mathrm{ext}}u(\mathbf{r})\overline{w}(\mathbf{r})\mathrm{d}F,\end{aligned} \tag{5.60}$$

with

$$f_h^{(0)}(w) = -\sum_{F\in\mathcal{F}_h^b}\int_F a(\mathbf{r})\left[\frac{\partial u^{\mathrm{inc}}(\mathbf{r})}{\partial\mathbf{n}} + \mathrm{i}k_{\mathrm{ext}}u^{\mathrm{inc}}(\mathbf{r})\right]\overline{w}(\mathbf{r})\mathrm{d}F. \tag{5.61}$$

Note that we are allowed to delete the term containing $\left[\!\left[a(\mathbf{r})\boldsymbol{\nabla}u(\mathbf{r})\right]\!\right]\cdot\mathbf{n}_F$ without any effect on the consistency of our method, since the physical flux $(a\boldsymbol{\nabla}u)$ is continuous across F. After multiplying (5.60), (5.61) by (-1), we obtain

$$\begin{aligned}\Phi_h^{(1)}(u,w) = &\sum_{T\in\mathcal{T}_h}\int_T a(\mathbf{r})\boldsymbol{\nabla}u(\mathbf{r})\cdot\boldsymbol{\nabla}\overline{w}(\mathbf{r})\mathrm{d}T - \sum_{T\in\mathcal{T}_h}\int_T \omega^2 b(\mathbf{r})v_h(\mathbf{r})\overline{w}(\mathbf{r})\mathrm{d}T \\ &- \sum_{F\in\mathcal{F}_h^i}\int_F \left\{\!\!\left\{a(\mathbf{r})\boldsymbol{\nabla}u(\mathbf{r})\right\}\!\!\right\}\cdot\mathbf{n}_F\left[\!\left[\overline{w}(\mathbf{r})\right]\!\right]\mathrm{d}F, \\ &+ \sum_{F\in\mathcal{F}_h^b}\int_F a(\mathbf{r})\mathrm{i}k_{\mathrm{ext}}u(\mathbf{r})\cdot\overline{w}(\mathbf{r})\mathrm{d}F,\end{aligned} \tag{5.62}$$

and

$$f_h^{(1)}(w) = \sum_{F\in\mathcal{F}_h^b}\int_F a(\mathbf{r})\left[\frac{\partial u^{\mathrm{inc}}(\mathbf{r})}{\partial\mathbf{n}} + \mathrm{i}k_{\mathrm{ext}}u^{\mathrm{inc}}(\mathbf{r})\right]\cdot\overline{w}(\mathbf{r})\mathrm{d}F. \tag{5.63}$$

In the next step, we will make the bilinear form $\Phi_h^{(1)}(u,w)$ complex symmetric, *i.e.*, to have a form $\Phi_h^{(1)} = A + \mathrm{i}B$, with A, B Hermitian sesquilinear forms. To this end, we add the conjugate transpose of $\sum_{F\in\mathcal{F}_h^i}\int_F \left\{\!\!\left\{a(\mathbf{r})\boldsymbol{\nabla}v_h(\mathbf{r})\right\}\!\!\right\}\cdot\mathbf{n}_F\left[\!\left[\overline{w}(\mathbf{r})\right]\!\right]\mathrm{d}F$

to the DG discretization:

$$\begin{aligned}\Phi_h^{(\mathrm{cs})}(u,w) = &\sum_{T\in\mathcal{T}_h}\int_T a(\mathbf{r})\boldsymbol{\nabla}u(\mathbf{r})\cdot\boldsymbol{\nabla}\overline{w}(\mathbf{r})\mathrm{d}T\\ &-\sum_{T\in\mathcal{T}_h}\int_T \omega^2 b(\mathbf{r})u(\mathbf{r})\overline{w}(\mathbf{r})\mathrm{d}T\\ &-\sum_{F\in\mathcal{F}_h^i}\int_F \{\!\{a(\mathbf{r})\boldsymbol{\nabla}u(\mathbf{r})\}\!\}\cdot\mathbf{n}_F\,[\![\overline{w}(\mathbf{r})]\!]\,\mathrm{d}F\\ &+\sum_{F\in\mathcal{F}_h^i}\int_F [\![u(\mathbf{r})]\!]\,\{\!\{a(\mathbf{r})\boldsymbol{\nabla}\overline{w}(\mathbf{r})\}\!\}\cdot\mathbf{n}_F\,\mathrm{d}F\\ &+\sum_{F\in\mathcal{F}_h^b}\int_F a(\mathbf{r})\mathrm{i}k_{\mathrm{ext}}u(\mathbf{r})\cdot\overline{w}(\mathbf{r})\mathrm{d}F.\end{aligned} \tag{5.64}$$

Since (5.64) contains two non-positive terms, it is standard to add a stabilization term in order to maintain coercivity, at least for $b = 0$, see Refs. [40, 44]:

$$s_h^{\mathrm{BRMPS}}(v_h,w) = \sum_{F\in\mathcal{F}_h^i}\eta\int_\Omega a(\mathbf{r})\mathbf{r}_F\left([\![u(\mathbf{r})]\!]\right)\cdot\overline{\mathbf{r}_F\left([\![w(\mathbf{r})]\!]\right)}\mathrm{d}\Omega, \tag{5.65}$$

where $\eta > \eta_0 > 0$ is a penalty parameter and $\mathbf{r}_F(\cdot)$ the lifting operator defined by (5.32) as

$$\int_\Omega \mathbf{r}_F(v)\cdot\overline{\boldsymbol{\tau}_h}\mathrm{d}\Omega = \int_F \{\!\{\boldsymbol{\tau}_h\}\!\}\cdot\mathbf{n}_F\overline{v}\,\mathrm{d}F, \qquad \forall\boldsymbol{\tau}_h\in\left[V^{\mathrm{SR}}\right]^2. \tag{5.66}$$

For an elliptic problem, *i.e.*, for $b = 0$ in (5.64), it can be shown that for sufficiently large η the bilinear form containing the penalty term is coercive, see [40]. For a Helmholtz problem, the stability of the standard conforming FEM has been analyzed by Ref. [45], but, to the best of our knowledge, it still remains an open question in the case of discontinuous Galerkin framework. We therefore follow the standard penalty approach in this chapter and verify the proper convergence properties of our method by numerical experiments.

Thus, adding the term s_h^{BRMPS} to (5.64), yields the final DG formulation as in

Eq. (5.30) with sesquilinear form

$$\begin{aligned}\Phi_h(u,w) := &\sum_{T\in\mathcal{T}_h}\int_T a\boldsymbol{\nabla}_h u(\mathbf{r})\cdot\boldsymbol{\nabla}_h\overline{w}(\mathbf{r})\,\mathrm{d}T - \sum_{T\in\mathcal{T}_h}\int_T \omega^2 b(\mathbf{r})u(\mathbf{r})\overline{w}(\mathbf{r})\,\mathrm{d}T\\ &- \sum_{F\in\mathcal{F}_h^i}\int_F \{\!\{a(\mathbf{r})\boldsymbol{\nabla}_h u(\mathbf{r})\}\!\}\cdot\mathbf{n}_F\,[\![\overline{w}(\mathbf{r})]\!]\,\mathrm{d}F\\ &- \sum_{F\in\mathcal{F}_h^i}\int_F [\![u(\mathbf{r})]\!]\,\{\!\{a(\mathbf{r})\boldsymbol{\nabla}_h\overline{w}(\mathbf{r})\}\!\}\cdot\mathbf{n}_F\,\mathrm{d}F\\ &+ \sum_{F\in\mathcal{F}_h^i}\eta\int_\Omega a(\mathbf{r})\mathbf{r}_F\left([\![u(\mathbf{r})]\!]\right)\cdot\overline{\mathbf{r}_F\left([\![w(\mathbf{r})]\!]\right)}\mathrm{d}\Omega\\ &+ \sum_{F\in\mathcal{F}_h^b}\int_F aik_{\mathrm{ext}}u(\mathbf{r})\overline{w}(\mathbf{r})\,\mathrm{d}F.\end{aligned} \tag{5.67}$$

Bibliography

[1] J. D. Joannopoulos, S. G. Johnson, J. N. Winn, and R. D. Meade. *Photonic Crystals: Molding the Flow of Light*. Second. Princeton: Princeton University Press, 2008. ISBN: 978-0-691-12456-8.

[2] E. Yablonovitch. "Inhibited Spontaneous Emission in Solid-State Physics and Electronics". In: *Phys. Rev. Lett.* 58.20 (1987), pp. 2059–2062. DOI: 10.1103/PhysRevLett.58.2059.

[3] S. John. "Strong Localization of Photons in Certain Disordered Dielectric Superlattices". In: *Phys. Rev. Lett.* 58.23 (1987), pp. 2486–2489. ISSN: 0031-9007. DOI: 10.1103/PhysRevLett.58.2486.

[4] J. D. Joannopoulos, P. R. Villeneuve, and S. Fan. "Photonic Crystals: Putting a New Twist on Light". In: *Nature* 386.6621 (1997), pp. 143–149. ISSN: 0028-0836, 1476-4687. DOI: 10.1038/386143a0.

[5] C. López. "Materials Aspects of Photonic Crystals". In: *Adv. Mater.* 15.20 (2003), pp. 1679–1704. ISSN: 0935-9648, 1521-4095. DOI: 10.1002/adma.200300386.

[6] J.-M. Lourtioz, H. Benisty, V. Berger, J.-M. Gérard, D. Maystre, and A. Tchelnokov. *Photonic Crystals: Towards Nanoscale Photonic Devices*. Berlin: Springer, 2010. ISBN: 978-3-642-09704-1.

[7] M. Ghulinyan and L. Pavesi, eds. *Light Localisation and Lasing: Random and Quasi-Random Photonic Structures*. Cambridge: Cambridge University Press, 2015. ISBN: 978-1-139-83950-1. DOI: 10.1017/CBO9781139839501.

[8] K. Busch, G. von Freymann, S. Linden, S. Mingaleev, L. Tkeshelashvili, and M. Wegener. "Periodic Nanostructures for Photonics". In: *Phys. Rep.* 444.3-6 (2007), pp. 101–202. ISSN: 03701573. DOI: 10.1016/j.physrep.2007.02.011.

[9] T. Baba. "Slow Light in Photonic Crystals". In: *Nat. Photonics* 2.8 (2008), pp. 465–473. ISSN: 1749-4893. DOI: 10.1038/nphoton.2008.146.

[10] R. Moussa, S. Foteinopoulou, L. Zhang, G. Tuttle, K. Guven, E. Ozbay, and C. M. Soukoulis. "Negative Refraction and Superlens Behavior in a Two-Dimensional Photonic Crystal". In: *Phys. Rev. B* 71.8 (2005), p. 085106. ISSN: 1098-0121, 1550-235X. DOI: 10.1103/PhysRevB.71.085106.

[11] A. F. Koenderink, L. Bechger, H. P. Schriemer, A. Lagendijk, and W. L. Vos. "Broadband Fivefold Reduction of Vacuum Fluctuations Probed by Dyes in Photonic Crystals". In: *Phys. Rev. Lett.* 88.14 (2002), p. 143903. ISSN: 0031-9007, 1079-7114. DOI: 10.1103/PhysRevLett.88.143903.

[12] S. Ogawa, M. Imada, S. Yoshimoto, M. Okano, and S. Noda. "Control of Light Emission by 3D Photonic Crystals". In: *Science* 305.5681 (2004), pp. 227–229. ISSN: 0036-8075, 1095-9203. DOI: 10.1126/science.1097968.

[13] P. Lodahl, A. F. van Driel, I. S. Nikolaev, A. Irman, K. Overgaag, D. Vanmaekelbergh, and W. L. Vos. "Controlling the Dynamics of Spontaneous Emission from Quantum Dots by Photonic Crystals". In: *Nature* 430.7000 (2004), pp. 654–657. ISSN: 0028-0836, 1476-4687. DOI: 10.1038/nature02772.

[14] M. D. Leistikow, A. P. Mosk, E. Yeganegi, S. R. Huisman, A. Lagendijk, and W. L. Vos. "Inhibited Spontaneous Emission of Quantum Dots Observed in a 3D Photonic Band Gap". In: *Phys. Rev. Lett.* 107.19 (2011), p. 193903. ISSN: 0031-9007, 1079-7114. DOI: 10.1103/PhysRevLett.107.193903.

[15] W. L. Vos and L. A. Woldering. "Cavity Quantum Electrodynamics with Three-Dimensional Photonic Band Gap Crystals". In: *Light Localisation and Lasing: Random and Quasi-Random Photonic Structures*. Cambridge University Press, 2015, pp. 180–214. ISBN: 978-1-107-03877-6.

[16] J. G. Fleming, S. Y. Lin, I. El-Kady, R. Biswas, and K. M. Ho. "All-Metallic Three-Dimensional Photonic Crystals with a Large Infrared Bandgap". In: *Nature* 417.6884 (2002), pp. 52–55. ISSN: 0028-0836, 1476-4687. DOI: 10.1038/417052a.

[17] S. E. Han, A. Stein, and D. J. Norris. "Tailoring Self-Assembled Metallic Photonic Crystals for Modified Thermal Emission". In: *Phys. Rev. Lett.* 99.5 (2007), p. 053906. ISSN: 0031-9007, 1079-7114. DOI: 10.1103/PhysRevLett.99.053906.

[18] A. Tandaechanurat, S. Ishida, D. Guimard, M. Nomura, S. Iwamoto, and Y. Arakawa. "Lasing Oscillation in a Three-Dimensional Photonic Crystal Nanocavity with a Complete Bandgap". In: *Nat. Photonics* 5.2 (2011), pp. 91–94. ISSN: 1749-4885, 1749-4893. DOI: 10.1038/nphoton.2010.286.

[19] D. Zhou and R. Biswas. “Photonic Crystal Enhanced Light-Trapping in Thin Film Solar Cells”. In: *J. Appl. Phys.* 103.9 (2008), p. 093102. ISSN: 0021-8979, 1089-7550. DOI: 10.1063/1.2908212.

[20] D. M. Callahan, K. A. W. Horowitz, and H. A. Atwater. “Light Trapping in Ultrathin Silicon Photonic Crystal Superlattices with Randomly-Textured Dielectric Incouplers”. In: *Opt. Express* 21.25 (2013), p. 30315. ISSN: 1094-4087. DOI: 10.1364/OE.21.030315.

[21] D. Sharma, S. B. Hasan, R. Saive, J. J. W. van der Vegt, and W. L. Vos. “Enhanced Absorption in Thin and Ultrathin Silicon Films by 3D Photonic Band Gap Back Reflectors”. In: *Opt. Express* 29.25 (2021), p. 41023. ISSN: 1094-4087. DOI: 10.1364/OE.435412.

[22] T. Ergin, N. Stenger, P. Brenner, J. B. Pendry, and M. Wegener. “Three-Dimensional Invisibility Cloak at Optical Wavelengths”. In: *Science* 328.5976 (2010), pp. 337–339. ISSN: 0036-8075, 1095-9203. DOI: 10.1126/science.1186351.

[23] S. G. Johnson and J. D. Joannopoulos. “Block-Iterative Frequency-Domain Methods for Maxwell’s Equations in a Planewave Basis”. In: *Opt. Express* 8.3 (2001), p. 173. ISSN: 1094-4087. DOI: 10.1364/OE.8.000173.

[24] K. Yee. “Numerical Solution of Initial Boundary Value Problems Involving Maxwell’s Equations in Isotropic Media”. In: *IEEE Trans. Antennas Propagat.* 14.3 (1966), pp. 302–307. ISSN: 0018-926X. DOI: 10.1109/TAP.1966.1138693.

[25] A. Taflove and S. C. Hagness. *Computational Electrodynamics: The Finite-Difference Time-Domain Method*. 3rd ed. Artech House Antennas and Propagation Library. Boston: Artech House, 2005. ISBN: 978-1-58053-832-9.

[26] Y. D. Ho, P. S. Ivanov, E. Engin, M. F. J. Nicol, M. P. C. Taverne, Chengyong Hu, M. J. Cryan, I. J. Craddock, C. J. Railton, and J. G. Rarity. “FDTD Simulation of Inverse 3-D Face-Centered Cubic Photonic Crystal Cavities”. In: *IEEE J. Quantum Electron.* 47.12 (2011), pp. 1480–1492. ISSN: 0018-9197. DOI: 10.1109/JQE.2011.2170404.

[27] M. Minkov and V. Savona. “Automated Optimization of Photonic Crystal Slab Cavities”. In: *Sci Rep* 4.1 (2015), p. 5124. ISSN: 2045-2322. DOI: 10.1038/srep05124.

[28] J.-M. Jin. *The Finite Element Method in Electromagnetics*. Third edition. Hoboken. New Jersey: John Wiley & Sons Inc, 2014. ISBN: 978-1-118-84202-7 978-1-118-84198-3.

[29] S. Burger, R. Klose, A. Schaedle, F. Schmidt, and L. W. Zschiedrich. “FEM Modeling of 3D Photonic Crystals and Photonic Crystal Waveguides”. In: *Integrated Optoelectronic Devices 2005*. Ed. by Y. Sidorin and C. A. Waechter. San Jose, California, United States, 2005, p. 164. DOI: 10.1117/12.585895.

[30] D. Devashish, S. B. Hasan, J. J. W. van der Vegt, and W. L. Vos. "Reflectivity Calculated for a Three-Dimensional Silicon Photonic Band Gap Crystal with Finite Support". In: *Phys. Rev. B* 95.15 (2017), p. 155141. ISSN: 2469-9950, 2469-9969. DOI: 10.1103/PhysRevB.95.155141.

[31] D. Devashish, O. S. Ojambati, S. B. Hasan, J. J. W. van der Vegt, and W. L. Vos. "Three-Dimensional Photonic Band Gap Cavity with Finite Support: Enhanced Energy Density and Optical Absorption". In: *Phys. Rev. B* 99.7 (2019), p. 075112. ISSN: 2469-9950, 2469-9969. DOI: 10.1103/PhysRevB.99.075112.

[32] L. Petersson and J.-M. Jin. "A Three-Dimensional Time-Domain Finite-Element Formulation for Periodic Structures". In: *IEEE Trans. Antennas Propagat.* 54.1 (2006), pp. 12–19. ISSN: 0018-926X. DOI: 10.1109/TAP.2005.861547.

[33] P. I. Borel, A. Harpøth, L. H. Frandsen, M. Kristensen, P. Shi, J. S. Jensen, and O. Sigmund. "Topology Optimization and Fabrication of Photonic Crystal Structures". In: *Opt. Express* 12.9 (2004), p. 1996. ISSN: 1094-4087. DOI: 10.1364/OPEX.12.001996.

[34] M. Adhikary, R. Uppu, C. A. M. Harteveld, D. A. Grishina, and W. L. Vos. "Experimental Probe of a Complete 3D Photonic Band Gap". In: *Opt. Express* 28.3 (2020), p. 2683. ISSN: 1094-4087. DOI: 10.1364/OE.28.002683.

[35] P. Kuchment. "7. The Mathematics of Photonic Crystals". In: *Mathematical Modeling in Optical Science*. Ed. by G. Bao, L. Cowsar, and W. Masters. Society for Industrial and Applied Mathematics, 2001, pp. 207–272. ISBN: 978-0-89871-475-3 978-0-89871-759-4. DOI: 10.1137/1.9780898717594.ch7.

[36] P. Kuchment. "An Overview of Periodic Elliptic Operators". In: *Bull. Amer. Math. Soc.* 53.3 (2016), pp. 343–414. ISSN: 0273-0979, 1088-9485. DOI: 10.1090/bull/1528.

[37] W. Dörfler, A. Lechleiter, M. Plum, G. Schneider, and C. Wieners. *Photonic Crystals: Mathematical Analysis and Numerical Approximation*. Vol. 42. Oberwolfach Seminars. Basel: Springer Basel, 2011. ISBN: 978-3-0348-0112-6 978-3-0348-0113-3. DOI: 10.1007/978-3-0348-0113-3.

[38] H. Brandsmeier, K. Schmidt, and C. Schwab. "A Multiscale Hp-FEM for 2D Photonic Crystal Bands". In: *J. Comput. Phys.* 230.2 (2011), pp. 349–374. ISSN: 00219991. DOI: 10.1016/j.jcp.2010.09.018.

[39] H. Brandsmeier. "Standard and Generalized Hp-Finite Element Discretizations for Periodic Structures". PhD thesis. ETH Zurich, 2013, 1 Band. DOI: 10.3929/ETHZ-A-009959045.

[40] D. A. Di Pietro and A. Ern. *Mathematical Aspects of Discontinuous Galerkin Methods*. Vol. 69. Mathématiques et Applications. Berlin, Heidelberg: Springer Berlin Heidelberg, 2012. ISBN: 978-3-642-22979-4 978-3-642-22980-0. DOI: 10.1007/978-3-642-22980-0.

[41] P. Monk. *Finite Element Methods for Maxwell's Equations*. Numerical Mathematics and Scientific Computation. Oxford : New York: Clarendon Press ; Oxford University Press, 2003. ISBN: 978-0-19-850888-5.

[42] N. W. Ashcroft and N. D. Mermin. *Solid State Physics*. New York: Holt, Rinehart and Winston, 1976. ISBN: 978-0-03-083993-1.

[43] L. Novotny and B. Hecht. *Principles of Nano-Optics*. Cambridge: Cambridge University Press, 2006. ISBN: 978-0-511-81353-5.

[44] F. Bassi, S. Rebay, G. Mariotti, S. Pedinotti, and M. Savini. "A High-Order Accurate Discontinuous Finite Element Method for Inviscid and Viscous Turbomachinery Flows." In: *Proceedings of the 2nd European Conference on Turbomachinery - Fluid Dynamics and Thermodynamics*. Ed. by R. Decuypere and G. Dibelius. 1997, pp. 99–109.

[45] I. G. Graham and S. A. Sauter. "Stability and Finite Element Error Analysis for the Helmholtz Equation with Variable Coefficients". In: *Math. Comp.* 89.321 (2019), pp. 105–138. ISSN: 0025-5718, 1088-6842. DOI: 10.1090/mcom/3457.

6 Summary and Outlook

Crystals are an important type of natural or man-made materials that can be utilized for manipulation of various physical waves by their interference in the periodic structure. Waves can thus be reflected, directed, confined, or forced to interact in a specific way. The wave behavior in crystals is, however, notoriously complicated and many questions on this topic still remain unanswered. In this PhD thesis, we developed theoretical and numerical methods for the analysis of wave propagation through crystals and their confinement, allowing us to better understand these phenomena. Although our results are illustrated on and applied to mostly 3D inverse woodpile photonic crystals, many of them are directly applicable to general crystals interacting with any type of physical waves.

In Chapter 1, we introduced the topic of wave manipulation by crystals and the basics of the mathematical description of electromagnetic waves in photonic crystals. We also introduced the 3D inverse woodpile photonic crystal structure. The chapter concludes with a brief introduction into the finite element method as a tool for calculating light propagation through photonic crystals.

In Chapter 2, we introduced a general method for identification and classification of wave confinement in crystal superlattices. By observing the scaling behavior of certain quantities with respect to the supercell size, we were able to quantitatively identify the confinement dimensionality of each band in the spectrum. To our knowledge, this method surpasses any other method of confinement identification to date and can be automated easily. We illustrated our method on quantum electronic confinement in hexagonal boron nitride with a nitrogen vacancy and on a classical light confinement in a 3D inverse woodpile photonic superlattice.

Chapter 3 deals with the main limitation of our scaling method for confinement identification from Chapter 2, namely that the accuracy of the technique decreases for small supercell sizes. However, it is especially these supercell sizes that currently are both computationally feasible and experimentally interesting. We investigated unsupervised machine learning techniques, namely clustering algorithms, as either a substitute or an additional step for the scaling method. To overcome the lack of a ground truth in the confinement identification problems, we analyzed several cluster validity indices as measures of the clustering accuracy and picked the best performing one. Subsequently, we compared the results of a standard k-means++ clustering algorithm, our own model-based clustering algorithm, and the direct application of the scaling method of Chapter 2. We concluded that the best accuracy is obtained by first directly applying the scaling analysis to find the total number of different confinement dimensionalities in the spectrum of a given structure and subsequently using this number as an input to the clustering algorithm which identifies the individual confinement

dimensionalities.

In Chapter 4, we applied the methods developed in Chapters 2 and 3 to analyze the influence of the structural parameters of 3D inverse woodpile photonic superlattices on light confinement. We created so-called confinement maps, which provide the frequencies of 3D confined bands for selected combinations of the regular and the defect pore radii. We found that a certain minimum difference between the regular and defect pore radii is necessary in order for 3D confined bands to appear at all and that larger deviations of the defect pore radii from the regular radii support more 3D confined bands. Subsequently, we analyzed symmetries of chosen 3D confined bands and found that the geometry of photonic crystals provides much more variety in orbital shapes and symmetries than is the case for electronic orbitals. We also discovered that the degenerate 3D confined bands appearing in pairs are dipole analogies corresponding to the symmetry of the inverse woodpile superlattice. Finally, we investigated the relationship between the inverse woodpile structural parameters and the applicability of the given structure for cavity quantum electrodynamics (cQED) applications. We discovered that donor-like structures, *i.e.*, those where the defect pore radius is smaller than the radius of regular pores, are more suitable for cQED applications than acceptor-like structures with larger defect pores than the regular ones.

In Chapter 5, we developed and implemented a size-robust discontinuous Galerkin finite element method for light propagation through large photonic crystals. The light propagation through large photonic crystals is an extremely computationally challenging problem due to its multiscale character. To overcome this issue, we utilized the local periodicity of the crystal to construct a size-robust method in which we look for the electromagnetic fields as solutions to the Helmholtz equation in two dimensions. We then employed a size-robust quadrature to calculate the system matrix entries corresponding to the internal unit cells of the crystal. As a result, our size-robust approach only scales linearly with the crystal length and width, instead of quadratically as is the case for standard finite elements. We illustrated the numerical properties of our method by means of numerical examples.

We have several propositions for extension and continuation of our research. It would be interesting to investigate the generalization of our scaling method for confinement identification to other types of structures than superlattices, such as hyperuniform or random media. The main hurdle there would be that it is not entirely clear how to extend a nonperiodic structure to larger supercells. We thus expect that possible generalizations would have to include some kind of statistical methods, which may also allow to assess automatically the accuracy of the classification.

In our investigation of clustering algorithms for the enhancement of the accuracy of the confinement classification, we concluded that the performance of the cluster validity indices was suboptimal compared to the performance of the direct application of the scaling method when it comes to establishing the total number of confinement dimensionalities. Nevertheless, it seems possible to devise some kind of a model-based index, in a similar manner to our model-based clustering algorithm, that would measure the clustering validity not only with

respect to the geometry of the clusters, but also with respect to the underlying physical theory. Having such an index available would possibly further enhance the precision of our confinement identification method. Alternatively, one could investigate the application of a clustering algorithm that includes certain error measures, to better quantify the accuracy of the method.

In our research, we investigated the influence of various inverse woodpile structures on photonic confinement. An obvious extension here would be to include a larger dataset and to incorporate not only 3D confined, but also 2D confined bands in the analysis. Beyond that, it would be extremely interesting to investigate other photonic structures in the same manner as we did for the inverse woodpiles in this PhD thesis.

Finally, it would be beneficial for the photonics community to develop and implement a fully 3D version of our size-robust algorithm, which also requires the replacement of the scalar Helmholtz equation by the vector Maxwell's equation. Besides that, within our size-robust finite element method, the main computational bottleneck becomes the field computation in the cells on the crystal surface, which is not well approximated by Bloch modes. Nevertheless, if one could find a family of functions correctly approximating these surface states, it would be possible to treat them in a size-robust manner, similarly to how we currently handle the Bloch modes. This advancement would result in a completely size-independent method in 2D and only a linearly size-dependent method in 3D.

Nederlandse Samenvatting

Kristallen zijn een belangrijke type natuurlijke of kunstmatige materialen die gebruikt kunnen worden om diverse soorten fysieke golven te manipuleren door interferentie in de periodieke structuur. Golven kunnen daardoor worden gereflecteerd, gericht, opgesloten, of gedwongen een specifieke interactie aan te gaan. Golfgedrag in kristallen is echter notoir ingewikkeld en er zijn veel onbeantwoorde vragen op dit gebied. In dit proefschrift hebben we theoretische en numerieke methodes ontwikkeld voor de analyse van golfvoortplanting door en het opsluiten van licht in kristallen, waardoor we deze fenomenen beter kunnen begrijpen. Hoewel onze resultaten voornamelijk worden geïllustreerd met en toegepast op 3D fotonische kristallen met inversehoutstapelstructuur, zijn veel van deze resultaten direct algemener toepasbaar op de interactie tussen andere type fysieke golven en kristallen.

In Hoofdstuk 1 introduceerden we het onderwerp golfmanipulatie door kristallen en de basisprincipes voor de wiskundige beschrijving van elektromagnetische golven in fotonische kristallen. We introduceerden ook de 3D inversehoutstapelstructuur voor fotonisch kristallen. Dit hoofdstuk wordt afgesloten met een korte inleiding van de eindige elementen methode als middel voor het berekenen van de lichtvoortplanting in fotonische kristallen.

In Hoofdstuk 2 hebben we een algemene methode geïntroduceerd voor het identificeren en classificeren van golfopsluiting in kristallen met een superrooster. Door te observeren hoe bepaalde grootheden schalen met de supercelgrootte, konden we de opsluitingsdimensie van iedere band in het spectrum kwantitatief bepalen. Voor zover wij weten, overtreft deze methode tot nu toe elke andere methode voor identificatie van opsluiting, bovendien kan deze gemakkelijk worden geautomatiseerd. We hebben onze methode geïllustreerd op de kwantumelektronische opsluiting door een stikstof-vacature-centrum in een hexagonaal boronnitride kristal en op de opsluiting van klassiek licht in een superrooster van de 3D inversehoutstapelstructuur.

Hoofdstuk 3 behandelt de belangrijkste beperking van de in Hoofstuk 2 geïntroduceerde schalingsmethode voor het de identificatie van opsluiting, namelijk dat de nauwkeurigheid van de methode afneemt bij gebruik van kleinere supercellen. Dit is belangrijk gezien het juist deze kleinere supercellen waarvoor zowel berekeningen haalbaar zijn, als experimenteel interessant zijn. We hebben methodes voor ongecontroleerd machinaal leren onderzocht, specifiek voor clusteranalyse, als vervanging of ter aanvulling van onze schalingsmethode. Bij gebrek aan een ground truth voor het bepalen van de opsluitingsdimensie hebben we een aantal clustervaliditeitsindices onderzocht om te gebruiken als maat voor de nauwkeurigheid van de clustering, en hebben de beste presterende geselecteerd. Vervolgens hebben we de resultaten vergeleken van een standaard k-means++

clusteringalgoritme, ons eigen modelgebaseerde clusteringalgoritme en het directe gebruik van onze schalingsmethode uit Hoofdstuk 2. We concludeerden dat de beste nauwkeurigheid verkregen kan worden door eerst met de schalingsmethode het aantal verschillende opsluitingsdimensies te bepalen dat in het spectrum van een gegeven structuur aanwezig is, en vervolgens dit aantal te gebruiken als parameter in het clusteringalgoritme dat de opsluitingsdimensies van de individuele banden bepaalt.

In Hoofdstuk 4 hebben we de methoden uit Hoofstukken 2 en 3 gebruikt voor het analyseren van de invloed van structuurparameters van een superrooster met inversehoutstapelstructuur op lichtopsluiting. We hebben zogenaamde opsluitingsdiagrammen gemaakt, die de frequenties van 3D-opgesloten banden weergeven voor geselecteerde combinaties van straal van de reguliere en afwijkende poriën. We ontdekten dat er een ondergrens is voor het verschil tussen de straal van de reguliere en afwijkende poriën waaronder er geen 3D-opgesloten banden zijn, en dat bij een groter verschil tussen de stralen er meer 3D-opgesloten banden zijn. Vervolgens analyseerden we de symmetrieën van een aantal geselecteerde 3D-opgesloten banden en ontdekten dat de geometrie van een fotonisch kristal veel meer variatie aan symmetrieën en vormen van de orbitalen biedt dan bij de elektronische orbitalen. We ontdekten ook dat gedegenereerde 3D-opgesloten banden die in paren ontstaan dipoolanalogieën zijn die corresponderen met de symmetrie van het inversehoutstapelsuperrooster. Ten slotte hebben we ook de relatie onderzocht tussen de structuurparameters van de inverse houtstapel en de toepasbaarheid van zo'n structuur op trilholte-kwantumelectrodynamica-toepassingen (cQED). We ontdekten dat donorachtige structuren, dat wil zeggen structuren waarbij de afwijkende poriën een kleinere radius hebben dan de reguliere poriën, beter geschikt zijn voor cQED-toepassingen dan acceptor-achtige structuren, waarbij de afwijkende poriën groter zijn dan de reguliere.

In Hoofdstuk 5 hebben we een grootte-robuuste discontinue Galerkin eindige elementen methode ontwikkeld en geïmplementeerd voor het berekenen van lichtvoortplanting in grote fotonische kristallen. Het meerschalige karakter van fotonische kristallen maakt dat het berekenen van lichtvoortplanting in grote fotonische kristallen een uitdagend probleem is. Om de problemen van het meerschalige karakter te ondervangen, maken we gebruik van de lokale periodiciteit van het kristal om een grootte-robuuste methode te maken waarbij we zoeken naar de elektromagnetische velden als oplossing van de twee dimensionale Helmholtzvergelijking. Vervolgens gebruikten we een grootte-robuuste kwadratuur voor het berekenen van de elementen van de systeemmatrix die geassocieerd zijn met de interne eenheidscellen van het kristal. Als gevolg hiervan schaalt onze grootte-robuuste aanpak lineair met de lengte en breedte van het kristal, in plaats van kwadratisch zoals het geval is voor een standaard eindige elementen. We illustreren de numerieke eigenschappen van onze methode met enkele numerieke voorbeelden.

We hebben een aantal voorstellen voor de uitbreiding en voortzetting van ons onderzoek. Het zou interessant zijn om onze schalingsmethode voor het identificeren van opsluiting uit te breiden naar andere type structuren dan superroosters, bijvoorbeeld hyperuniforme en willekeurige media. De grote uitdaging daarvoor

is dat het niet duidelijk is hoe het schalen van een supercel moet werken voor een niet periodieke structuur. We verwachten daarom dat een statistische aanpak een onderdeel zal zijn van een dergelijke generalisatie, dit kan dan mogelijk ook gebruikt worden om automatisch de nauwkeurigheid van de classificatie te bepalen.

In ons onderzoek naar clusteringalgoritmes voor het verbeteren van de nauwkeurigheid van de opsluitingsclassificatie concludeerden we dat prestatie van de clustervaliditeitsindices suboptimaal is vergeleken met de prestatie van het direct toepassen van de schalingsmethode voor het bepalen van aantal verschillende opsluitingsdimensies. Desondanks lijkt het mogelijk een soort modelgebaseerde index te maken, op een manier vergelijkbaar met onze modelgebaseerde clusteralgoritme, die niet alleen de geometrische validiteit van de clustering bepaalt, maar ook de validiteit voor de onderliggende natuurkundige theorie. Het gebruik van dergelijke index zou mogelijk de nauwkeurigheid van onze opsluitingsidentificatiemethode kunnen verbeteren. Een andere optie is om het gebruik van clusteringalgoritmes te onderzoeken die naast een clustering ook een soort van foutenmarge opleveren, daarmee zou dan de nauwkeurigheid van de methode beter gekwantificeerd kunnen worden.

In ons onderzoek hebben we de invloed van diverse structuurparameters van de inversehoutstapelstructuur op fotonische opsluiting onderzocht. Een voor de hand liggende uitbreiding zou zijn om te kijken naar een grotere dataset, door naast de 3D-opgesloten banden ook 2D-opgesloten banden te analyseren. Daarnaast zou het buitengewoon interessant zijn om naast de inversehoutstapelstructuur ook andere fotonische kristalstructuren te analyseren.

Ten slotte, zou het nuttige zijn voor de fotonica-gemeenschap om een 3D versie te maken van ons grootte-robuust algoritme, dit vereist dat de scalaire Helmholtzvergelijk wordt vervangen door de vectorwaardige Maxwellvergelijkingen. Daarnaast wordt het grootste knelpunt in een dergelijke uitbreiding het berekenen van het veld in de eenheidscellen aan het kristaloppervlak, waar de Bloch-modes geen goede benadering leveren van het veld. Als men een functiefamilie kan vinden die nauwkeurig de velden aan het oppervlakte kan benaderen, dan is het mogelijk deze op grootte-robuuste manier te gebruiken net als met de Bloch-modes. Een dergelijke uitbreiding reduceert de kosten van het algoritme zodat het in 2D onafhankelijk is van de grootte van het kristal en in 3D lineair schaalt met de lengte.

Acknowledgements

I still remember Willem's words after I accepted my PhD offer: "It will be a great adventure!" And what an adventure it was! It is hard to overstate how much I have learned during the past four years. Here, I would like to thank all those who have contributed to my journey.

First of all, this thesis would not be possible at all without my supervisors **Willem**, **Jaap** and **Matthias**. It was an amazingly interesting experience to be guided by these three different personalities, who has each contributed to my PhD adventure in a unique way. Of course, it has not always been easy to make everyone happy, but it was a welcome challenge. I consider having three supervisors a privilege that not everyone gets to enjoy during their PhD and will cherish many fond memories of this time.

Thank you, **Willem**, for accepting me in such an amazing group as COPS is, and for everything that comes with it. Every time you are present in a room, your passion for science becomes obvious, which I find deeply inspiring. I am grateful to you not only for your scientific guidance, which was plentiful, but also for all the encouragment and support you have showed me during the past years.

The kindness and peace of **Jaap** have been an enormous source of reassurance for me during the more stressful periods. It always strikes me how easily you are able to solve my most perplexing problems, some even before I can finish explaining them. Even though I have been always more of a physicist than a mathematician, that never stopped you from providing excellent guidance and welcoming me in the MACS group, and I am forever grateful for that.

Thank you, **Matthias**, for dedicating so much of your time to me. You have always been available for discussion and help and your ability to rapidly provide detailed feedback on a text has become legendary by now. I could always rely on you to find a great deal of time for me, even though I know you must have been exceedingly busy. I wish you all the best with your own scientific endeavors as a young professor.

I would also like to thank my graduation committee members. **Carsten Rockstuhl**, **Femius Koenderink**, **Wilbert IJzerman**, **Ivo Vellekoop**, and **Geert Brocks**, thank you for taking the time to read and evaluate my thesis and to participate in my defense.

At this point, I would like to thank two additional people from whom I have learned a lot during my PhD. Thank you, **Ad**, for the crucial role you played in the scaling research and for the indispensable help while writing and publishing the manuscript. It was an honor working with you. I am also deeply grateful to **Lars**. In the past four years, you have been like my scientific older brother. From day one, whenever I felt lost in any topic, be it mathematics, physics, or coding, you were there for me to discuss and clarify everything. I cannot express how

much your support means to me and cannot count how many hours of searching and debugging your help has saved me. Without you, this thesis would be far from its current state right now.

My thanks belong to **Geert Brocks** and **Menno Bokdam** for arranging my access to the CMS cluster in order to perform the DFT computations crucial to illustrate the scaling method presented in Chapter 2, along with useful suggestions. I would like to thank **Christoph**, **Dietmar** and **Katrin** for the courses I attended during my PhD and for intriguing discussions. Many thanks to **Pepijn**, **Raimond** and **Victoria** for co-organizing the ANP retreat of 2019 with me. I am deeply grateful to my students **Rutger**, **Serge**, **Pelle** and **Tim** for entrusting me with the immense responsibility of supervising their theses. It has been a priceless experience for me and I hope that I was able to enrich each of you in some way. I would also like to thank the secretaries **Nicole**, **Linda W**, and **Mariëlle**, for all their administrative support and **Herbert** for his IT help.

I have been lucky enough to be part of both COPS and MACS groups, which allowed me to meet twice the standard amount of incredible colleagues. I would like to thank the COPS colleagues for all their support. Especially during the pandemic lockdowns, it was very clear what an amazing and supportive group we are. **Andreas**, thank you for the support in my PhD beginnings. **Sjoerd**, thank you for the introduction into all the important software and codes. **Manashee**, you have become an absolute legend. Thank you for your presence during most of my time here. I enjoyed every second of it. **Lars**, thank you for all the help and countless discussions over the years. **Ozan**, thank you for all your support, both scientific and personal. We need no words when we speak the language of beer. **Alfredo**, it was an honor working with you. The world needs people like you: kind, and with both strong scientific mindset and solid ethics. **Timon**, you were the perfect supplement to the group in my last year here. Thank you for all the quirky fun and conversations. **Melissa**, I am immensely glad you joined us. From bringing our crystals to new levels, to intriguing informal conversations, everything you participate in is of excellent quality and enriching in one way or the other. **Innes**, it was extraordinary to meet you and to hang out with you, from Netherlands to Czech Republic. I hope many great adventures together are yet to come. **Linda B**, it was brief but nice, hanging out with you. **João**, thanks for sharing the experience of the first half-year in the Netherlands together. **Bill**, I always enjoyed talking to you and you should definitely visit more often! **Duy**, **Pieter**, **Tim** and **Shun**, thank you for creating a pleasant working environment. **Cock**, even though I did not work in the lab, I at least got to enjoy your general presence in the group. Thank you for that, and also for the cool sailing trip! **Nicole**, thank you for all the fun and for being the one "normal" person in a group full of nerds.

Many thanks also belong to my former and current MACS colleagues. **Poorvi**, it is a pity we only had a year overlap. We had a lot of fun, especially on our London trip. **Olena**, it was nice sharing the PhD research and teaching load together. **Elena**, thank you for all the nice conversations. I also had fun teaching vector calculus with you. **Nishant**, **Kaifang**, **Fengna**, **Xiangyi**, **Hamza**, **Riccardo**, **Vincent**, **Sjoerd**, **Lars**, **Tugce**, **Fleur** and **Carlos**, thank you for

creating enjoyable atmosphere in the group.

I would like to thank my other colleagues from the Meander building, who made my time here more pleasant. **Matthijs**, it has been great knowing you and your remarkable ability to fix anything. **Reinier**, your unique saltiness is unforgettable. Thanks for all the fun times. **Mario**, I admire your technical expertise. I wish you and your 3D printer all the best. **Chris**, the lunch table would not be the same without you. Also, I would not be... For better or for worse. No, but, honestly, I learned a great deal from you and I wish one day I can be at least half as eloquent as you are. **Charlie**, I respect your quirky originality and have been enjoying our interactions to the fullest. **Malaquias**, it has been a pleasure hanging out with you. **Tristan**, **Evangelos**, **Klaas-Jan**, **Pim**, **Ben**, **Sudhir**, **Marius**, **Violetta**, **Frank**, **Jardi** and **Stefan**, thank you for providing friendly atmosphere in the Meander building. **Jelmer**, there is a lot I admire about you. Thank you for all the advice throughout the years. Finally, **Pepijn**, **Jan K.**, **Klaus**, **Peter**, **David**, **Bert** and **Carla**, your presence around has been delightful, thank you very much for that.

Many thanks to the Saive group and all the people I met through them, namely, **Frank**, **Jarco**, **Jelle**, **Lisanne**, **Mathis**, **Marnix**, **Michal K.**, **Nasim**, **Sebastian**, **Silvi**, **Willemijn**, **Wiria**, **Wladick** and **Zeinab**. Finally, **Rebecca**, thank you for all the fun, advice and conversations. It has been a pleasure. I wish you a lot of success with your growing group.

I would like to thank **Shweta** and **Ozan** for taking upon themselves the paranymph duties. The support of both of you meant a lot for me during the PhD and I am glad that I can count on it also in regard to my defense and the connected events. Furthermore, thank you, **Lars**, for translating the summary of this PhD thesis to Dutch and **Chris** for its proofreading.

My PhD time was marked by the two-year coronavirus pandemic that forced us to stay at home as much as possible. Because of this, a lot of out-of-work activities have been inaccessible. Nevertheless, during this time I have discovered a passion for working out. My deepest gratitude therefore belongs to the CrossFit Twente coaches **Chen**, **Jan vD.** and **Elwin** for teaching me how to work out correctly and safely and for all the encouragement.

My thanks belong to the few people outside of the University with whom I was fortunate to hang out with. **Sevgi**, you are such a delightful, supportive and kind person. Talking to you always makes my day brighter. **Emily**, from Leipzig to Enschede, I am glad that our paths crossed more than once. Thank you for all the support and the time together.

The most exotic group of people I used to spend time with during my PhD were definitely "The Indians". It was an immensely deep experience to hang out with and talk to you all. **Theo**, our cocktail nights have been epic. I hope many more will come yet. Also, thank you for all the delicious baking. **Sabari**, you are such a pleasant and kind person to be around. **Prachi**, **Shivam** and **Shreyasi**, thank you for all the fun and all the Indian delicacies.

The amazing advantage of this day and age is that we can digitally connect with people on regular basis despite not even living in the same countries. This way, I was able to keep in touch with the amazing people I met before I started

my PhD. **Matej** and **Xiao**, thank you for all the board games, conversations and travels. **Matej**, you have enriched my mindset already before I started the PhD, and I can see that influence up until now. Thank you for that. **Xiao**, thank you for showing me both the Chinese and the Italian culture at once. **Ioanna**, thank you for all the support, both over the distance and in person. It is not easy to find such a one-of-a-kind artistic soul as you. **Michal D.**, thanks for all the fun.

It is time to address the people in my home country of Slovakia. **Patrik**, thank you for everything, not only over the past four years but also over the last 20+ years we have known each other. I am proud to see you grow and to grow with you. **Aďa**, your life has changed so much in the last four years. I am glad that despite all the family responsibilities you now have, you always find time for a chat. Thank you for everything. **Maroš**, we had some amazing "academic" meetings online. It has been an honor to be your friend and to share the PhD path together. I also thank **Edo**, **Peťo**, **Lucia** and **Veronika** for all the time spent together and all the fun.

I am grateful to my **dad**, **mom** and **grandma** for their support of my education and for having raised me as a curious and scientifically literate person. I thank my brother **Martin** and my now sister-in-law **Kamila** for their support and for all the fun times.

And, finally, the best part. I am forever grateful to my dear **Shweta** for being in this PhD adventure with me. I cannot overstate how much I learned from you. From simply observing how you dealt with your own PhD hurdles, I already feel like I have gained two PhDs worth of experience at once. But there was much more. You trained me in presentation and speaking. You dedicated hours of time to proofreading everything from reports to important e-mails. We talked science on a daily basis. But, most important of all, you stood by me in all the difficult times and showed me that I could rely on you and trust you. I cannot imagine doing this PhD without you. Thank you.

The last four years exemplified an ultimate scientific adventure for me. A tremendous thank you again to everyone who has made it possible.